A novel RNAi screen for neurotrophin receptor internalisation and trafficking in motor neurons

Marco Terenzio

University College London

and

Cancer Research UK London Research Institute

PhD Supervisor: Giampietro Schiavo

A thesis submitted for the degree of

Doctor of Philosophy

University College London

September 2010

Declaration

I, Marco Terenzio, confirm that the work presented in this thesis is my own. Where information has been derived from other sources, I confirm that this has been indicated in the thesis.

Abstract

A primary focus of the Molecular Neuropathobiology laboratory is the investigation of the long range trafficking of neurotrophins and neurotrophin receptors in motor neurons (MNs). The goal of my project was to deepen our understanding of the nature of the cellular machinery controlling long-range neurotrophin trafficking in MNs, by discovering new players involved in this process. In order to achieve this goal I performed an siRNA screen in MNs derived from mouse ES cells to monitor the cell surface binding and internalization of two fluorescently tagged reporters: the binding fragment of the Tetanus neurotoxin (H_C), which enters an axonal transport compartment shared with neurotrophins and their receptors, and an antibody directed against the extracellular domain of the neurotrophin receptor $p75^{NTR}$. A high-throughput, lipid-based siRNA transfection method was optimised for ES cell-derived MNs and used to screen a library of siRNAs directed against a pool of genes involved in endocytosis and membrane trafficking. The primary candidate genes were subsequently validated, and one gene in particular, Bicaudal D homolog 1 (BICD1), was selected for further analyses.

BICD1 is a member of the Bicaudal D family, whose members function as molecular motor adaptors with pleiotropic roles in intracellular trafficking. *Bicd1* expression at E12.5 and 13.5 was restricted to the nervous system, suggesting an important role for BICD1 in neurons. I used gene-trapped ES cells to derive MNs depleted of the BICD1 protein (*Bicd1*$^{gt/gt}$ MNs), which, when challenged with either H_C or the $p75^{NTR}$ antibody, displayed an increased intracellular accumulation of both probes. Furthermore, I found that the level of neurotrophin receptors exposed at the plasma membrane was increased in these cells compared to their wild type counterparts, suggesting that BICD1 might be involved in the regulation of neurotrophin receptor dynamics in mammalian neurons. I also found that TrkB signalling upon stimulation with the brain-derived neurotrophic factor (BDNF) in *Bicd1*$^{gt/gt}$ MNs, was impaired. This suggests that the depletion of BICD1 not only affects the trafficking of neurotrophin receptors, but also their signalling capabilities.

In conclusion, this thesis work has demonstrated that the concept of high throughput screening can be applied to cells notoriously difficult to handle and transfect, such as MNs. This approach was successful in unravelling a new role for BICD1 in neurons, where it appears to regulate the intracellular trafficking and signalling of neurotrophin receptors. Taken together with the in vivo expression data, these data suggest that BICD1 plays an important role in the development and function of the nervous system.

Acknowledgement

I would like to thank my supervisor, Giampietro Schiavo, for offering me the opportunity to work in his lab, and all the past and present members of the MNP and SPW labs I met during these four years, particular Claire and Matthew, who helped me constantly throughout of my Ph.D.

I also would like to thank the people who made this thesis project possible, like Mike Howell, who helped me with the selection of the right transfection reagent for the screen, Ken Blight who produced the TEM data, Bradley Spencer Dene and Ian Rosewell for helping me with the mouse work. A special thanks also to Nathan, who guided me through the image analysis.

Many thanks to all the friends and people I meet in London and to the friends who still remember me in my hometown, even 10 years after I left. A special thanks of course goes to my family, my relatives and Daniela for their support.

Table of Contents

Table of figures

List of tables

Abbreviations

Akt	RAC-alpha serine/threonine-protein kinase
AraC	Cytosine arabinoside
ATP	adenosine-5'-triphosphate
BICD1/*Bicd1*	Bicaudal D homolog 1
BICD2/*Bicd*2	Bicaudal D homolog 2
BICDR1/*Bicdr1*	BICD-related protein 1
BICDR1/*Bicdr2*	BICD-related protein 2
BDNF	brain-derived neurotrophic factor
BONT	Botulinum neurotoxin
cAMP	cyclic adenosine monophosphate
cDNA	complementary DNA
CNS	central nervous system
COPI	coat protein 1
CRD	cysteine-repeats motif
CREB	cAMP response element-binding protein
DMEM	Dulbecco's modified Eagles medium
DMSO	dimethylsulphoxide
DNA	deoxyribonucleic acid
DRG	dorsal root ganglia
DRM	detergent-resistant glycolipid enriched microdomain
DTT	dithiothreitol
EB	embryoid body
EDTA	dimethylenediaminetetraacetic acid
EGF	epithelial growth factor

EGFR	EGF receptor
ELISA	enzyme-linked immunosorbent assay
ERK	extracellular signal regulated kinase
ES cells	embryonic stem cells
GDNF	glial cell-derived neurotrophic factor
GFP	green fluorescent protein
GPI	glycosylphosphatidylinositol
GSK3	glycogen synthase kinase 3
GST	glutathione-S-transferase
GTP	Guanosine-5'-triphosphate
HA	hemagglutinin
H_C	H_C fragment of the TeNT
HCS	high-content screen
HRP	horseradish peroxidase
ICD	intracellular domain
IgG	immunoglobulin G
IP3	inositol(1,4,5)trisphophate
IPTG	isopropyl-β-D-thiogalacto-pyranoside
JNK	Jun N-terminal kinase
kDa	kilo-Daltons
Kidins220	kinase D interacting substrate of 220 kDa
KIF	kinesin superfamily
LB	Luria-Bertani medium
MAPK	mitogen activated protein kinase

MN	motor neuron
MVB	multivesicular body
MW	molecular weight
NA	numerical aperture
NGF	nerve growth factor
NMJ	neuromuscular junction
NT	neurotrophin
OD	optical density
PBS	phosphate buffered saline
PC12	pheochromocytoma 12 cell line
PCR	polymerase chain reaction
PFA	paraformaldehyde
PLCγ	phospholipase C γ
$p75^{NTR}$	p75 neurotrophin receptor
RA	retinoic acid
RAB	Ras-related in brain
RISC	RNA-Induced Silencing Complex
RNA	ribonucleic acid
RNAi	RNA interference
rpm	rotations per minute
SAG	Sonic Hedgehog agonist
SDS	sodium dodecyl sulfate
SDS PAGE	SDS-polyacrylamide gel electrophoresis
Shh	Sonic Hedgehog

TeNT	Tetanus neurotoxin
TGN	trans-Golgi network
TNFR	tumor necrosis factor receptor
TRAF6	TNFR associated factor 6
Trk	tropomyosin-related kinase
s.e.m.	standard error on the mean
siRNA	short interfering RNA
SNARE	soluble *N*-ethylmaleimide-sensitive factor attachment protein receptor
SV	synaptic vesicle
VAMP2	vesicle associated protein 2

Chapter 1. Introduction

1.1 Tetanus Neurotoxin

One of the probes used extensively in this thesis work to study the intracellular trafficking of neurotrophins and neurotrophin receptors is the H_C fragment of the *Clostridium tetani* toxin of *Clostridium tetani* is able to produce a potent neurotoxin, called Tetanus Neurotoxin (TeNT), which was identified as the sole causative agent of tetanus, an often-fatal pathology characterised by spastic paralysis which can result in cardiovascular or respiratory failure.

TeNT is one of the most toxic virulence factors known, with an LD_{50} in mouse between 0.1 and 1 ng/kg of body weight. It is produced by the bacteria in lesions contaminated with toxigenic strains of *C. tetani*. In anaerobic conditions, these spores germinate, giving rise to the vegetative form of the bacteria, which synthesises TeNT. The toxin is released into the blood circulation, and is then able to bind with high affinity to the presynaptic membrane of motor neurons (MNs) at the neuromuscular junction (NMJ) (Montecucco and Schiavo, 1994). TeNT is then internalised and targeted to an axonal retrograde transport route, which enables the toxin to reach the MN soma, located in the spinal cord. Here TeNT is sorted and redirected to a transcytotic route, which results in its release into the extracellular space, where it binds to and is internalised into inhibitory interneurons. TeNT induces a block of neurotransmitter release from inhibitory interneurons, which results in the spastic paralysis characteristic of the disease (Montecucco and Schiavo, 1994).

1.1.1 Structure of Tetanus Neurotoxin

TeNT is initially synthesised by *Clostridium tetani* as an inactive polypeptide of 150 kDa, which is then cleaved by specific bacterial or host proteases into two fragments, a 100 kDa heavy chain (HC) and a 50 kDa light chain (LC) (**Figure 1.1 A**) (Montecucco and Schiavo, 1994). The two chains remain associated via a single disulfide bond and non-covalent interactions. The LC is a zinc endoprotease and it is responsible for the block of neurotransmitter release. Once in the cytosol of inhibitory interneurons, the LC cleaves a unique peptide bond in the vesicle associated membrane protein 2 (VAMP2/synaptobrevin) (Schiavo et al., 1992a) (Schiavo et al., 1992b), which is a member of the soluble *N*-ethylmaleimide-sensitive factor attachment protein receptor (SNARE) family of proteins. Different sets of SNAREs constitute the core machinery providing the driving force for membrane fusion in different cellular compartments (Jahn and Scheller, 2006). VAMP2 is involved in the fusion of synaptic vesicles (SVs), which contain the neurotransmitters, with the plasma membrane. Therefore its cleavage by TeNT prevents the fusion of SVs and results in the block of neurotransmitter release by the inhibitory interneurons.

The LC needs to be linked to the HC in order to gain access to the neuronal cytosol and cleave VAMP2. HC is, in fact, responsible for the binding to the neuronal surface and the translocation of TeNT into the cytoplasm (Lalli et al., 1999, Herreros et al., 2001), where LC cleaves its substrate. HC can be divided into two functional regions, a 50 kDa N-terminal (H_N) and a 50 kDa C-terminal fragment (H_C), which can be further subdivided in another 2 fragments of 25 kDa each, H_{CN} and H_{CC} (**Figure 1.1 A**). H_N has a loop that interacts with LC and two long α-helices and it is responsible for the translocation of LC through the endosomal membrane. Once inside the endosomal

compartment, the acidic pH is believed to cause a conformational change in H_N, which rearranges to form a membrane pore, through which the LC translocates out of the endosome and into the cytoplasm.

The precise role of the H_{CN} fragment is still unknown; however, it does not seem to play a role in the binding of TeNT to the neuronal membrane since it does not bind to rat dorsal root ganglionic cells (DRG) (Figueiredo et al., 1995) or to differentiated phaechromocytoma cells (PC12) (Herreros et al., 2001). H_{CC}, however, has a well-defined role: it is the main determinant in mediating the highly specific binding of TeNT to MN nerve terminals (Dolly et al., 1984) (Herreros et al., 2001) (Rummel et al., 2003).

1.1.2 Neurospecific binding of Tetanus Neurotoxin

TeNT binding *in vivo* is restricted to the presynaptic terminal of cholinergic nerves and to sympathetic adrenergic nerve fibers (Habermann and Dreyer, 1986). This binding has a very high affinity (sub-nanomolar range) and it is virtually irreversible. Since pre-treatment with an excess of H_C is enough to counteract the paralysis induced by the whole toxin, this fragment bears the minimum determinant for the physiological binding of TeNT (Lalli et al., 1999).

The most important binding partners of TeNT on the neuronal plasma membrane (PM) identified so far are the polysialogangliosides of the G1b series (GD1b, GT1b and GQ1b), for which the H_{CC} domain has two oligosaccharide-binding sites (Rummel et al., 2003). These gangliosides are essential for the binding and therefore the activity of the TeNT. Impairment of ganglioside biosynthesis, for example, decreases the activity of the toxin *in vivo* (Kitamura et al., 1999) (Williamson et al., 1999).

Montecucco (1986) has formulated a dual receptor model for the binding of TeNT. This model would involve a two-step process, where the initial binding is determined by the gangliosides, which are abundant on the neuronal surface and act as low affinity receptors. Once bound to gangliosides, TeNT could then come into contact with a putative high affinity protein receptor, which might mediate the subsequent endocytosis of the toxin (Montecucco, 1986, Binz and Rummel, 2009). This hypothesis is supported by the observation that TeNT has been found to be able to bind to one or more GPI-anchored protein(s) of 15 kDa (Herreros et al., 2000), and the cleavage of such GPI-anchored proteins has a protective effect on TeNT intoxication in neurons (Munro et al., 2001) (Herreros et al., 2001). One such GPI-anchored protein was identified as Thy-1 in NGF-differentiated PC12 cells, but this is unlikely to be the main protein receptor *in vivo*, since Thy1 knock-out mice are still sensitive to TeNT intoxication (Herreros et al., 2001). Interestingly, GPI-anchored proteins, cholesterol and gangliosides are all enriched in lipid rafts, which suggests that lipid microdomains might play a role in TeNT binding to the neuronal surface. Interestingly, TeNT and the closely related Botulinum toxins (BONTs) have been found associated with detergent-resistant glycolipid-enriched microdomains (DRM) (Herreros et al., 2001).

1.1.3 Endocytosis of Tetanus Neurotoxin

Synaptic activity seems to be implicated in TeNT uptake both *in vivo* and *in vitro*. TeNT was found to colocalise with SV markers in hippocampal neurons after depolarisation (Matteoli et al., 1996), and its uptake *in vivo* has been shown to be dependent on synaptic activity (Miana-Mena et al., 2002). These findings would suggest that TeNT internalisation is mediated via SV recycling. This mode of internalisation is likely to occur in hippocampal neurons, but not in MNs, where very little colocalisation

has been found between SV markers and the toxin (Lalli and Schiavo, 2002). In addition, TeNT uptake at the NMJ and its subsequent retrograde axonal transport do not appear to be affected by the inhibition of neurotransmitter release (Schiavo et al., 2000). These data were confirmed by the finding that pre-treatment with BONTs, which abolishes SV exocytocis and recycling, does not stop TeNT internalisation in MNs (Deinhardt et al., 2006a). The H_C fragment of the toxin has been found in clathrin-coated invaginations of the plasma membrane in MNs, and its internalisation was successfully prevented by overexpression of a dominant-negative mutant of dynamin and the clathrin adaptors complexes AP2 and AP180 (Deinhardt et al., 2006a). These data suggest that TeNT undergoes a clathrin-mediated dynamin-dependent endocytosis in MNs, independent of SV recycling.

1.1.4 TeNT retrograde transport

As are all neurons, MNs are extremely polarised cells, which extend long axons to make contact with their target muscles. As a result they need a tightly controlled machinery to ensure the long-range axonal transport of signalling molecules back to the cell body, which is important for their survival (Goldstein and Yang, 2000). There are two main components of axonal transport, a slow one (1-50 nm/s) for microtubules, neurofilaments, cytoplasmic proteins and metabolic enzymes, and a fast one (0.1-5 μm/s) used for vesicle and organelle transport and also for survival signals like neurotrophins and their receptors (Vallee and Bloom, 1991).

Since TeNT undergoes retrograde transport in neurons, it has been widely used to monitor this process. The compartment in which TeNT is transported has been visualised using labelled versions of the H_C fragment. Different types of carriers were

identified, including tubular vesicles with a fast and continuous movement (speed up to 3.6 μm/s) and round vesicles, which move more slowly and exhibit frequent pauses (Lalli and Schiavo, 2002).

Pharmacological disruption of the microtubule and actin cytoskeleton or inhibition of cytoplasmic dynein (Lalli et al., 2003) affects the axonal retrograde transport of H_C confirming that the transport of H_C is dynein-dependent. Another molecular motor involved in H_C axonal retrograde transport is myosin Va, as demonstrated by the fact that MNs derived from myosin Va null embryos show an overall slower transport of H_C-positive carriers (Lalli et al., 2003). These H_C-positive axonal retrograde carriers have been partially characterised. They have a neutral pH, which is crucial since an acidification of the endocytic compartment would trigger the translocation of the toxin into the cytoplasm (Lalli and Schiavo, 2002, Bohnert and Schiavo, 2005). Neurotrophins and their receptors have been found to be co-transported in H_C-positive carriers, suggesting that they use the same long-range transport pathway as TeNT (Lalli and Schiavo, 2002, Deinhardt et al., 2006b). This pathway is dependent on two small RAB GTPases, RAB5 and RAB7. In particular RAB7 seems to be responsible for the long-range axonal retrograde transport of H_C, which is abolished using a dominant-negative version of RAB7 (Deinhardt et al., 2006b) (**Figure 1.1. B**).

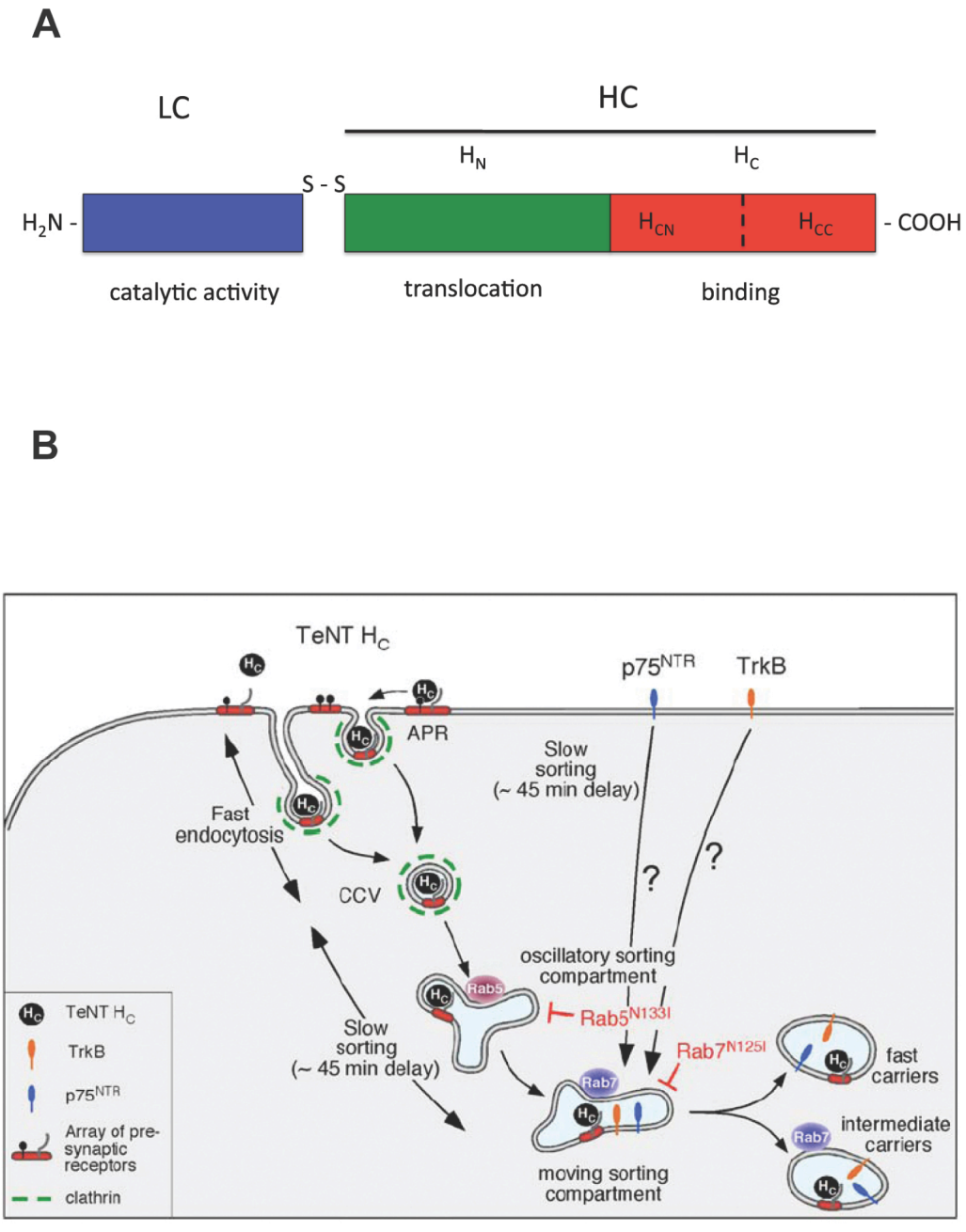

Figure 1.1. Structure of TeNT and its binding and endocytosis in MNs.
Schematic representation of the structure of TeNT. The HC fragment is further subdivided into the HCN and HCC domains (A). The main function of these domains is indicated (adapted from the Ph.D. thesis of K. Deinhardt). (B) Model of internalisation of the HC fragment of TeNT. H_C binds to the gangliosides on the neuronal plasma membrane and is internalised in a clathrin-dependent fashion. Together with neurotrophins and their receptors, H_C enters into a RAB5-positive compartment and finally undergoes axonal retrograde transport in a RAB7-positive compartment. Mutants of RAB5 (RAB5N133I) and RAB7 ($RAB7^{N125I}$) abolish the transport of H_C (taken from (Deinhardt et al., 2006b)) (B).

1.2 Neurotrophins and their receptors

In addition to the H_C fragment of TeNT, an antibody against the extracellular domain of the p75 neurotrophin receptor ($p75^{NTR}$) has been used in this thesis work to investigate the intracellular trafficking of neurotrophins and their receptors.

Neurotrophins play a critical role in the development of the nervous systems and its maintenance during adulthood. Neurotrophins are a small family of structurally related growth factors with the ability to modulate cell survival and development of most types of neurons. They were originally identified as survival factors for neurons secreted from their target tissue (Cohen et al., 1954, Levi-Montalcini and Angeletti, 1963); in particular it was proposed that during innervation neurotrophins like nerve growth factor (NGF) are released by the innervated tissue, promoting the survival of only those neurons which had made the correct connections. This would be a way of shaping the pattern of innervation of the tissue, negatively selecting away neurons that failed to make the right contacts with their target (Levi-Montalcini, 1987). Neurotrophins, however, have been implicated in a wide range of biological functions, such as the regulation of neuroblast and neural crest cell proliferation, regulation of neurite outgrowth, and synaptic modulation (Huang and Reichardt, 2001).

There are four neurotrophins, NGF, BDNF, NT-3 and NT-4/5 (Bibel and Barde, 2000, Huang and Reichardt, 2001) and their sequences are highly conserved in vertebrates. All neurotrophins are synthesised as precursors of 31-35 kDa, which are then cleaved by convertases to produce the mature forms of 13.2 – 15.9 kDa. Mature neurotrophins exist as non-covalently bound homodimers, which are released through the constitutive secretory pathway (NGF, NT-3) or a specialised regulated pathway

(BDNF) (Mowla et al., 1999, Roux and Barker, 2002). Neurons themselves can also synthesise neurotrophins (Roux and Barker, 2002). In addition, it has been documented that neurotrophin secretion in the nervous system increases after an injury (Roux and Barker, 2002).

The increasingly complex functions related to neurotrophin signalling are mediated by two classes of receptors, the tropomyosin-related kinase (Trk) tyrosine kinase receptors (TrkA, TrkB and TrKC), and $p75^{NTR}$. The Trk receptors were so named because the first reported member of the family, TrkA, was identified as a transforming oncogene, in which an unknown tyrosine kinase was fused to tropomyosin (Martin-Zanca et al., 1989). The four neurotrophins exhibit different degrees of specificity towards the different Trk receptors: NGF binds preferentially to TrkA, BDNF and NT4/5 to TrkB and NT-3 to TrkC. A certain level of crosstalk, however, has also been reported: NT-4/5 is also able to bind to TrkA and NT-3 also binds to TrkA and TrkB (Segal and Greenberg, 1996) (**Figure 1.2**). Pro-neurotrophins have a greater affinity for $p75^{NTR}$, while mature neurotrophins preferentially bind Trk receptors. For this reason the control of neurotrophin processing determines the relative contribution of $p75^{NTR}$ versus Trk receptor signalling. In addition, the selective activation of $p75^{NTR}$ by pro-neurotrophins depends on the association of the receptor with another membrane protein called sortilin (Schecterson and Bothwell, 2010).

Trk receptors are type I transmembrane proteins. Their extracellular domains contain two cysteine-rich regions, which flank a leucine–rich repeat, and two immunoglobulin (IgG)-like domains in the juxtamembrane region, which are responsible for the binding of the neurotrophins (Roux and Barker, 2002)(**Figure 1.2.**).

The binding of the ligand triggers the dimerization of Trk receptors, which then autophosphorylate, initiating their signalling cascade. In the case of TrkA, for example, this phosphorylation results in the creation of a docking site for adaptor proteins, which regulate cell growth and survival through the Ras, phosphatidylinositol 3-kinase (PI3K) and phospholipase Cγ (PLCγ) pathways (Segal and Greenberg, 1996) (Kaplan and Miller, 2000).

A number of truncated isoforms of the Trk receptors have been described, including TrkA and TrkB lacking a short amino acid region in the extracellular domain (Clary and Reichardt, 1994) (Strohmaier et al., 1996) and versions of TrkB and TrkC missing the complete intracellular kinase domain (Roux and Barker, 2002). A signalling-defective isoform of TrkC with amino acid insertions in its kinase domain has also been reported (Tsoulfas et al., 1993) (Valenzuela et al., 1993). Finally, two truncated forms of TrkB, T1 and T2, have been found, which have a cytoplasmic tail of 21-23 amino acids and are highly expressed in the adult brain (Fryer et al., 1996) (**Figure 1.2**). Truncated and inactive forms of the Trk receptors display different affinity for neurotrophins and might, therefore, act as modulators of the signalling of their full-length counterparts (Roux and Barker, 2002).

$p75^{NTR}$ is as a member of the tumour necrosis factor receptor (TNFR-SF) family of proteins (Johnson et al., 1986) (Radeke et al., 1987) and, unlike the Trk receptors, is capable of binding to all four neurotrophins. Its extracellular domain is composed of four cysteine-repeats motifs (CRD), whilst its intracellular region contains a type II death domain (**Figure 1.2**). $p75^{NTR}$ stably dimerises through a disulfide bond in the

transmembrane region of the receptor, and this linkage seems to be important to ensure effective neurotrophin-dependent signalling. (Vilar et al., 2009a, Vilar et al., 2009b).

The signalling cascades mediated by $p75^{NTR}$ is triggered by the specific interaction of its intracellular domain (ICD) and a cohort of adaptor proteins; the ICD does not contain a known catalytic domain (Roux and Barker, 2002). The binding to the neurotrophin homodimer pushes the two CRD domains of the $p75^{NTR}$ dimer close together, a movement that propagates to the intracellular domains, which are forced to spread apart, making them accessible to signalling adaptor proteins like NRIF and TRAF6 (Vilar et al., 2009a) (Vilar et al., 2009b). $p75^{NTR}$ is also sequentially cleaved by α and γ−secretases, which results in the release of its ICD into the cytoplasm, promoting NRIF signalling (Schecterson and Bothwell, 2010) (**Figure 1.2**).

1.2.1 Neurotrophin trafficking and signalling

Compared to conventional growth factor signalling, neurotrophin signalling needs to be propagated over much longer distances. Target-derived neurotrophins bind their receptors at the synaptic terminals and their downstream signals have to travel the full length of the axon before reaching the soma, where they initiate a specific gene expression response (Howe and Mobley, 2005).

Endocytosis of ligand-receptor complexes has been considered in the past as a way to down-regulate the signalling cascade (Bronfman et al., 2007). However, it is becoming evident that growth factors continue to signal from endosomes after internalisation (Bronfman et al., 2007). In the case of neurotrophin signalling, Mobley and colleagues determined that activated TrkA receptor bound to NGF could be found associated with intracellular membranes, together with PLC-γ (Grimes et al., 1996,

Grimes et al., 1997). This finding was the basis for the formulation of the "signalling endosome" hypothesis for neurotrophin signalling, which is the most widely accepted in the literature, though other theories, such as the "wave model" and the "signal effector model" have been formulated (Wu et al., 2009). According to the signalling endosome theory, neurotrophins remain bound to their activated receptors after internalisation and other signalling molecules of their cascade are recruited to the internalised endosome and activated in situ. In this context, this organelle would, then, constitute a signalling platform, which, in neurons, is retrogradely transported along the axon towards the cell soma.

There are several known routes of internalisation of activated receptors from the plasma membrane: clathrin-mediated, caveolin-mediated, clathrin- and caveolin-independent and macropinocytosis (Bronfman et al., 2007). All of these are believed to converge on one compartment, the peripheral early endosomes, also known as sorting endosomes, from which the receptors are recycled back to the plasma membrane, or targeted for lysosomal degradation via late endosomes (Di Fiore and De Camilli, 2001, Miaczynska et al., 2004). This endocytic network is orchestrated by a family of proteins called RAB GTPases, which are involved in the regulation of vesicle sorting and transport (Stenmark, 2009). For example, RAB5 controls early endosomal trafficking, RAB11 is involved in the recycling pathway and RAB7 is associated with late endosomes and lysosomes (Feng et al., 1995, Mukhopadhyay et al., 1997, Vitelli et al., 1997, Bucci et al., 2000, Lebrand et al., 2002, Jordens et al., 2005, Stenmark, 2009).

TrkA internalisation and signalling have been the most studied and best understood of the Trk receptors. TrkA internalisation depends on dynamin 1 and can

either be clathrin-mediated or occur via macropinocytosis due to the action of the chaperone protein Pincher (Shao et al., 2002). Clathrin-mediated TrkA endocytosis is connected to its signalling through ERK1/2 and the PI3-K pathway, as hinted at by the finding that, following the addition of NGF to PC12 cells, TrkA is recovered in fractions containing clathrin-coated vesicles and components of the ERK1/2 signalling pathway (Howe et al., 2001). Interestingly, PI3K influences the activity of RAB5, either acting on its effectors, such as EEA1, or on RAB5 itself, and in doing so regulates early endosomal endocytic trafficking (Seabra and Wasmeier, 2004). After stimulation of PC12 cells with NGF, TrkA internalisation is important for sustained ERK1/2 activation, as demonstrated by the fact that endosomal accumulation of TrkA induced via the over-expression of a dominant negative version of RAB7 results in potentiated ERK1/2 phosphorylation (Saxena et al., 2005a, Saxena et al., 2005b).

Macropinocytosis is a form of internalisation that is regulated by actin dynamics in areas of spreading and ruffling of the plasma membrane (Kirkham and Parton, 2005). TrkA internalisation via macropinocytosis is controlled in PC12 cells by a protein induced by NGF, Pincher (Shao et al., 2002), and it has been connected to a preferential activation of ERK5 instead of ERK1/2, which is activated upon TrkA clathrin-mediated endocytosis (Bronfman et al., 2007). Interestingly, ERK5 was found to be the preferred mitogen-activated protein kinase (MAPK) for neurotrophin receptor activation in distal axons (Watson et al., 2001).

$p75^{NTR}$ has been reported to have an effect on TrkA trafficking and signalling. In one case, $p75^{NTR}$ was found to inhibit the poly-ubiquitination of TrkA, causing its retention on the plasma membrane (Makkerh et al., 2005). These results, however, are

controversial, since another study showed that $p75^{NTR}$ was required for TrkA ubiquitination (Geetha et al., 2005). These apparently contradictory results might be explained by the existence of two ubiquitination mechanisms for TrkA, one dependent on and one independent from $p75^{NTR}$ and its effector TRAF6. Interestingly, TRAF6-induced ubiquitination of TrkA results in the activation of the TrkA signalling pathway mediated by ERK5, as demonstrated by the finding that the inhibition of TRAF6-mediated ubiquitination of TrkA causes a lower ERK5 and Akt activation (Geetha et al., 2005).

Regarding the trafficking of $p75^{NTR}$ in PC12 cells, it is known that pharmacological inhibition of clathrin-mediated endocytosis blocks the ligand-dependent internalisation of this receptor. In addition, $p75^{NTR}$ was found to accumulate in transferrin-positive recycling endosomes, where it is associated with its downstream effectors (Bronfman et al., 2003). $p75^{NTR}$ does not appear to be sorted to the degradative pathway and studies have shown that, in NGF-stimulated PC12 cells, a certain population of vesicles were positive for both TrkA and $p75^{NTR}$. TrkA has been found to follow the degradative route, even though it has also been described that a pool of the receptor is sorted to the recycling pathway. Such a $p75^{NTR}$/TrkA double-positive organelle could then either be considered as an early or a recycling endosome (Bronfman et al., 2007). Interestingly, TrkA has been shown to follow the recycling transcytotic route, dependent on RAB11 in sympathetic neurons (Ascano et al., 2009). The authors of that study speculate that during neurotrophin-mediated processes such as axon growth, guidance and neuronal survival, the demand for TrkA must be so high that the secretory pathway cannot cope. Therefore, as a backup mechanism, mature TrkA,

present on the plasma membrane of the soma is endocytosed and mobilised via RAB11-positive recycling endosomes and transported to the axonal membrane.

Surprisingly, TrkA and TrkB exhibit very different behaviours in neurosecretory cells and cortical neurons. TrkA was found to predominantly recycle back to the plasma membrane in a ligand-dependent manner, while TrKB was mainly sorted to the degradative pathway in cortical neurons (Chen et al., 2005).

In summary, NGF receptors have been found on the plasma membrane, clathrin-coated vesicles, early endosomes, late endosomes/MVBs, macropinosomes and recycling endosomes in PC12 cells, but the regulation of their trafficking is still largely unclear (**Figure 1.3**).

Studies have shown that $p75^{NTR}$ undergoes retrograde transport in neurons (Lalli and Schiavo, 2002, Chao and Lee, 2004, Deinhardt et al., 2006b), and that this receptor is internalised both in the axon and the somatodendritic region in hippocampal neurons. In addition, $p75^{NTR}$ was found in internalised vesicles together with NGF and the ganglioside GM1 and transferrin (Bronfman et al., 2003). Because of the data gathered in PC12 cells, which suggest that $p75^{NTR}$ is directed to the recycling route, it is possible that the receptor is transported along the axon in GM1-positive endosomes which are then sorted to the recycling route at the level of the cell body (Bronfman et al., 2007). Interestingly, GM1 has been described as a component of lipid rafts, and its internalisation is clathrin-dependent, as shown for the H_C, which also binds to lipid rafts and has been reported to undergo axonal retrograde transport in the same compartment as $p75^{NTR}$ (Deinhardt et al., 2006a, Deinhardt et al., 2006b).

1.2.2 Neurotrophin axonal transport

Neurotrophin trafficking in neurons is quite different from that described for PC12 cells, because neurotrophins are secreted by the target tissue and therefore need to be retrogradely transported to the cell soma, where their signalling results in a change in gene expression. Many theories have been formulated on how neurotrophin signalling is conveyed to the neuronal cell body and the hypothesis that has gathered the most experimental evidence to date seems to be the "signalling endosome" model (Bronfman et al., 2007). The initial evidence used to propose this model was the discovery that activated TrkA accumulated at the distal site of ligated rat sciatic nerve. This accumulation would imply a retrograde axonal transport of the activated receptor (Bhattacharyya et al., 1997). It was then found that dynein-mediated retrograde axonal transport of iodinated NGF in sensory neurons was dependent on the signalling of different kinases including TrkA and PI3-K (Reynolds et al., 1998), and that internalisation and activation of Trk receptors were both required for retrogradely transmitted nuclear responses (Riccio et al., 1997, Watson et al., 2001, Heerssen et al., 2004). In addition to the requirement for transport of the activated receptor, it was discovered that the ligand also had to be co-transported with the receptor in order to trigger the survival response. The need to have a functional transport of activated receptor together with its ligand was demonstrated with the use of NGF-coated microspheres, which can induce TrkA phosphorylation, but cannot be transported (Riccio et al., 1997). Riccio *et al*. found that the application of NGF microspheres to distal axons in a sympathetic neuron compartmentalised system was not sufficient for the NGF-induced survival of these neurons. Since then, more evidence supporting an endosome-based retrograde survival pathway in neurons has been found (Bronfman et

al., 2007), and some of the players regulating this process have been described. RAB5 and RAB7, for example, have been shown to control the axonal retrograde transport of neurotrophins and their receptors (Saxena et al., 2005a, Saxena et al., 2005b, Deinhardt et al., 2006b). In addition, the stability of microtubules and the actin cytoskeleton affect the axonal transport of Trk receptors and $p75^{NTR}$, and the retrograde motor dynein has been found as the main motor promoting the axonal retrograde transport of neurotrophin receptors (Yano et al., 2001, Heerssen et al., 2004, Lalli et al., 2003).

The nature of the retrogradely transported signalling organelle remains undefined. Mobley and co-workers have described that NGF and the Trk receptors are transported in RAB5-positive early endosomes (Howe et al., 2001, Delcroix et al., 2003). However, other evidence supports the hypothesis that MVBs might be the organelle involved in neurotrophin retrograde transport. For example, MVBs have been found to be the main endosomal population in sympathetic neuron cell bodies labelled with iodinated NGF (Claude et al., 1982). Other groups have found that Trk receptors are associated with MVBs (Valdez et al., 2005), suggesting that MVBs might be a stable platform for neurotrophin signalling after axonal retrograde transport. Interestingly, RAB7, which is a marker of late endosomes/MVBs, has been implicated in the control of TrkA endosomal transport and signalling through ERK1/2 in PC12 cells (Saxena et al., 2005a, Saxena et al., 2005b). RAB7 has also been described as a key player in the axonal retrograde transport of TrkB/$p75^{NTR}$ positive endosomes in motor neurons, in which dominant-negative versions of this RAB GTPase completely abolished the transport of these neurotrophin receptors (Deinhardt et al., 2006b).

If MVBs are indeed the compartment in which neurotrophins are transported, then Trk receptors must remain at the limiting membrane of the MVB in order for their tyrosine kinase domains to face the cytoplasm to remain competent for signalling. A mechanism preventing this receptor from being internalised to the inner membrane of the MVBs seems to be necessary to ensure prolonged neurotrophin signalling (Bronfman et al., 2007).

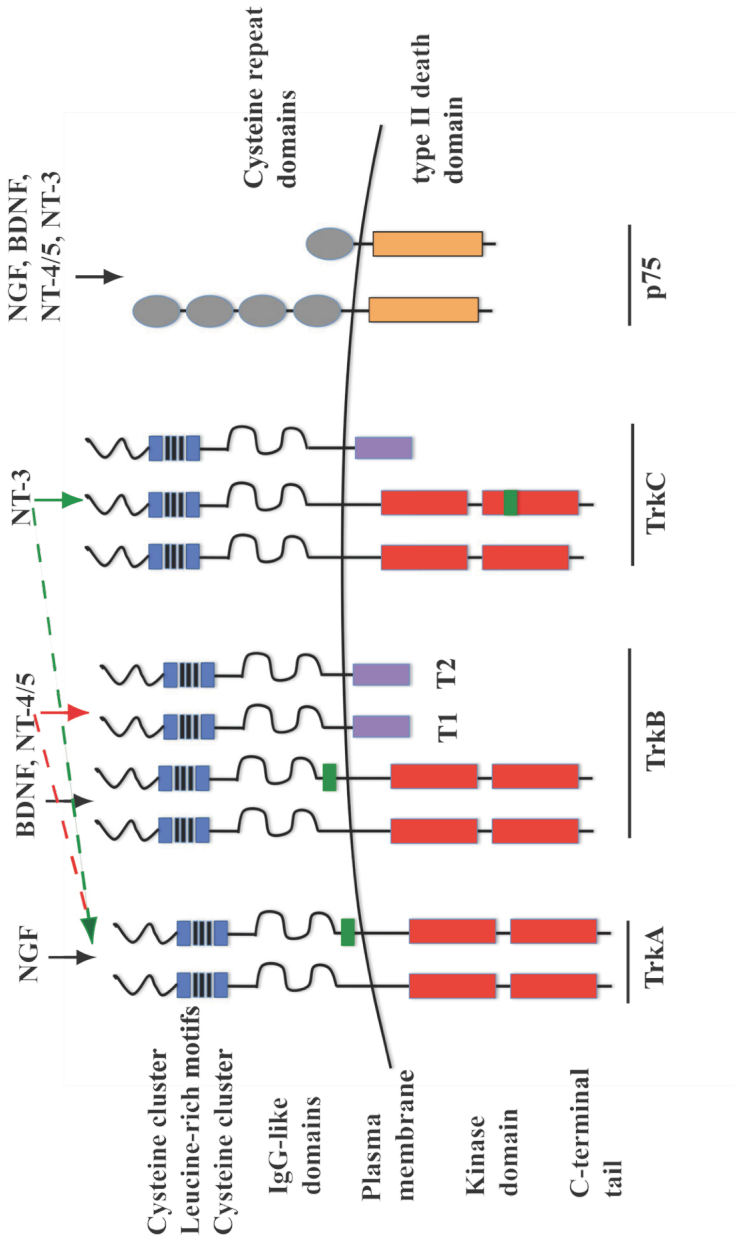

Figure 1.2. Neurotrophins and neurotrophin receptors.
Schematic representation of the different isoforms of Trk and p75NTR receptors. The neurotrophin binding specificity for each receptor is specified. Different domains have different colour codes: the intracellular kinase domains are coloured in red, the small amino acid insertions in green, the truncated intracellular domains of TrkB and TrkC in purple, the cysteine repeat domains of $p75^{NTR}$ in grey and the death domain of $p75^{NTR}$ in orange. The cysteine clusters of the Trk receptors are coloured in blue, while leucine-rich motifs are in black. Adapted from Roux & Barker, 2002 and Huang & Reichardt, 2003.

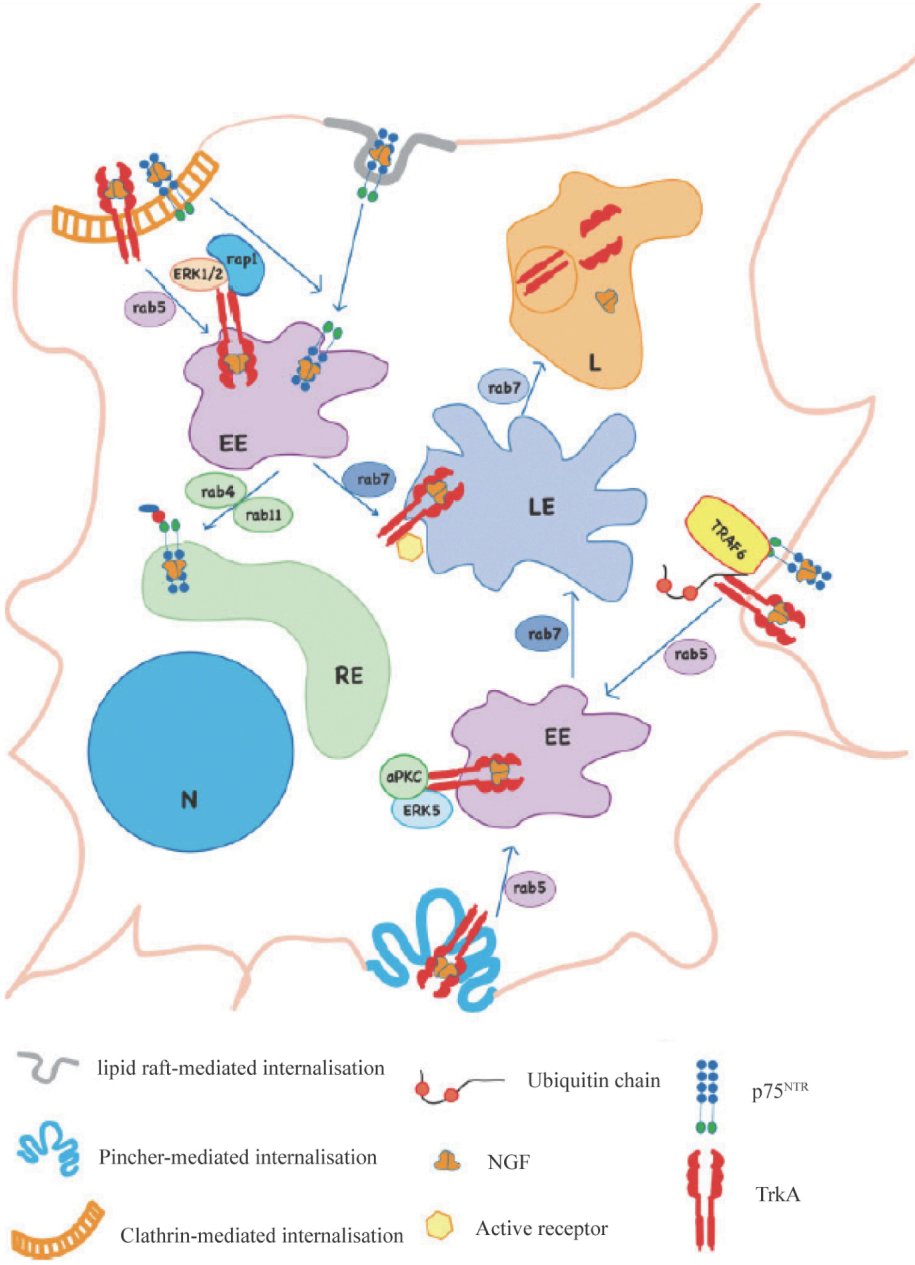

Figure 1.3. Schematic representation of the internalisation and trafficking of TrkA and p75^{NTR}. The different internalisation pathways of TrkA and p75NTR converge at the level of the early endosomes (EE). and from there different routes can be taken, one to the late endosomes (LE) and the lysosomes (L) controlled by RAB7, and the other dependent on RAB4 and RAB11, to the recycling endosomes (RE). From Bronfman et al., 2007.

1.3 High content siRNA screening

In the late 1990's, automated imaging systems started to be introduced as tools for the screening of biological/cellular processes and following that a new term, "high-content screen" (HCS), was coined. HCS can be defined as a "*multiplexed functional screening based on imaging multiple targets in the physiological context of intact cells, by extraction of multicolour fluorescence information*" (Krausz, 2007).

The HCS approach has several advantages over the traditional way of screening, such as biochemical assays or reporter genes based assays. For example, the possibility of designing a cell-based assay with high physiological relevance in which the response or "readout" is not limited to a single target, but can include the whole cell. Imaging single cells allows the ability to control for the biological heterogeneity of cell populations, and the use of multiple probes with different colours allows for the simultaneous determination of a series of subcellular parameters. For these reasons and because this data set can be integrated to produce a correlative analysis, which takes into account several parameters as opposed to concentrating on a single variable, HCS formats are generally considered to produce low false-positive and false-negative results. However, the strength of the HCS approach is also its main limitation: image-based cellular assays have more variability compared to biochemical assays or reporter gene-based assays. This is mainly due to the relatively small number of cells analysed (typically between 200 – 1000 cells per condition). Image-based screens also depend on the even distribution of cells across the field of analysis, which is critical for the microscope to sample enough cells during the automated image acquisition. Therefore,

standardisation of the cell culture conditions and the handling of the cells are critically important.

HCS is widely used in pharmaceutical companies to perform drug-based screens. However, it is also well suited to the use of RNA interference (RNAi), which has become a powerful tool allowing researchers to identify the function of genes in the context of a living cell. RNAi works by promoting specific degradation of a desired mRNA population in a living cell via the action of interfering RNA molecules, such as short interfering RNA (siRNA) oligonucleotides. Commercial sources of siRNA directed against all predicted genes in the human, mouse and rat genome are now available, together with premade siRNA libraries, which target whole gene families, such as the kinome, phosphatome, ubiquitin ligases, ubiquitinating enzymes, molecular motors and membrane proteins.

The use of siRNA induces a transient and specific silencing effect on a particular gene, which usually reaches its peak after 24 hours and then recovers by 96 hours after siRNA transfection. Although precise conditions depends on the specific gene that is knocked-down, a window of time between 48 hours to 96 hours after transfection is generally optimal to perform the screen. However, proteins with a longer half-life might fail to give a phenotype in this time frame, while depleting other proteins might significantly affect cell viability. All of these considerations have to be taken into account when deciding on the optimal time frame for the biological assay used in the screen.

Another concern is the risk of detecting false-positive hits due to off-target effects of the siRNA used. In order to tackle this issue, a set of minimal requirements

for siRNA studies in terms of controls and experimental settings has been established (Echeverri and Perrimon, 2006, Echeverri et al., 2006). There are two main approaches generally adopted by researchers interested in siRNA screens: the screen can be performed using either pools containing 3-4 siRNA duplexes (siRNA pools) or 2-4 single siRNA duplexes in separate wells for each gene. In the case of the siRNA pools, each pool needs to be done in replicates (typically 2-3) to take the experimental variability into account, while for single siRNA duplexes, at least 2 out of 3 siRNAs should give the same phenotype to exclude off-target effects. In addition, the sampling is critical: at least 200 cells per well should be covered in order to guarantee a good statistical coverage of the cell population. However, depending on the robustness and reproducibility of the biological assay, the number of cells to sample might need to be increased. If siRNA pools have been used to perform the screen, once the primary hits have been established, single siRNA duplexes contained the pool should be individually tested for all of the hits. It is common practice to consider a hit validated when 3/4 or 2/3 single siRNAs from the relevant pool produce the same phenotype. Alternatively, siRNA pools from a different supplier can be used, because the siRNA design algorithm differs among different companies and therefore the duplexes will target different parts of the transcript. The effective knock-down of the gene should also be tested by RT-PCR, Western blot and immunostaining. Finally, an elegant way to demonstrate that the phenotype observed is really due to the knock-down of the candidate gene, is to perform rescue experiments either by overexpression of the cDNA and/or by the introduction of a siRNA-resistant mutant of the gene (Krausz, 2007).

1.3.1 siRNA delivery methods for HCS

A broad range of delivery agents designed to accommodate the needs of HCS are commercially available. The most common are lipid-based transfection reagents, for which protocols for a 96- or 384-well format have now been established. However, most protocols published use a final siRNA concentration of 100 nM, which is quite high and presents a severe risk of off target effects (Moore et al., 2007). Reverse transfection strategies, in which siRNA and the transfection reagent are pre-complexed in the well before plating the cells, have been shown to achieve higher transfection efficiency at lower siRNA concentrations than the classic forward transfection protocol, in which the cells are first seeded and the transfection mixture is added the following day. In addition, reverse transfection is quicker and the manipulation of the cells is also minimised, which can be critical in case of large scale HCS. Reverse solid phase throughput transfection, which consists of spotting glass slides with transfection complexes in an array format, has also recently been optimised. The slides have a reservoir in which the cells can be plated and grown. A single slide can contain several hundred spots which minimises the quantity of transfection reagent, siRNA and cells to use and also allows fast image acquisition (Erfle et al., 2004, Wheeler et al., 2005).

Viral libraries are also available and they provide an alternative to lipid-based transfection. Viral shRNA vectors normally produce high infection rates even for cells that are notoriously difficult to transfect such as primary cells, thus opening up the possibility of screening physiologically relevant cell systems. However, these shRNA libraries are relatively more expensive than their siRNA counterparts and their stability is limited, because viruses do not tolerate repeated freeze/thaw cycles very well.

Electroporation has also been explored for HCS applications in a 96 well plate as a promising way of transfecting primary cells and cells in suspension. In general, protocols are generally empirically developed by adjusting the different parameters such as voltage, pulse duration, number of pulses and duration of the intervals between the pulses. The cells also need to be suspended in low conductivity buffers, which can affect cell viability and imposes short handling times in order to avoid damage to the cells. Finally, the cells are generally electroporated in suspension, which means that adherent cells need to be resuspended, introducing additional manipulations and a possible source of stress for the cells (Krausz, 2007).

1.3.2 Image acquisition systems for HCS

Several options are presently available for HCS image acquisition, which have to be considered in relation to the assay to be monitored, the costs and the speed of acquisition needed. One option is the use of laser scanner fluorimeters (e.g. the Acumen Explorer, which is present in the High Throughput Screening facility at CR-UK), which offer high image acquisition speed and simple reader-like handling, but have a low resolution. These scanners are characterised by a laser scanning excitation at various wavelengths combined with photomultimeter tube detection. The technology allows the acquisition of a whole plate in only a few minutes, and even though the resolution is quite low, it is still sufficient to monitor fluorescence intensity changes for assays such as cell proliferation, apoptosis, reporter gene expression, nuclear translocation and neurite outgrowth (Krausz, 2007).

A range of microscopes have been developed for HCS, which try to overcome the problems related to high-throughput image acquisition, such as the need for a robust

autofocus algorithm, rapid stage positioning across the plate, a stable light source, and high resolution imaging. One of the most widely used automated epifluorescence microscope of this type is the ARRAYSCAN from Cellomics, which has rapid automated autofocusing, a 12-bit CCD camera and a collection of dry objectives (5X, 10X, 20X and 40X magnification). Multicolour images are acquired sequentially and the system comes with a proprietary image analysis software and database. The high-throughput capability of the ARRAYSCAN is around 10,000 images per day.

Lately, the use of confocal microscopes for HCS has also been introduced, with commercial imaging systems such as IN Cell Analyser 3000 (GE Healthcare), Opera (Evotec Technologies) and ImageXpress Ultra (Molecular Devices). The major advantages offered by confocal imaging are the possibility of collecting information along the Z axis, a reduced background fluorescence and increased sensitivity obtained with the use of higher magnification and higher numerical aperture (NA) immersion objectives. Usually these confocal systems also come with proprietary image analysis software.

1.3.3 Image analysis software for HCS and interpretation of the data

A vital condition for the success of an HCS approach is the existence of image analysis software capable of processing large amounts of data in a reliable and automated way. Several software packages are offered by companies together with their automated imaging system. Typically these software are already optimised for the quantification of widespread assays such as cell cycle analysis, cytoxicity, apoptosis, receptor internalisation, protein translocation, co-localisation, cell migration and cytoskeletal rearrangements, morphological analysis or neurite outgrowth. These

analysis modules are specifically designed for their purpose and thus generally need only some minor fine-tuning to be adapted to the specific assay and cell type used.

Third party software is also available, with the capability of analysing large image datasets. One of these programs is Cell Profiler image analysis software created by a consortium started by Anne E. Carpenter and Thouis R. Jones in the laboratory of David M. Sabatini and Polina Golland (www.cellprofiler.org). Cell profiler is open-source (and thus free) and it is designed to enable researchers without training in computer programming and image analysis to quantitatively measure cellular phenotypes from large image datasets in an automated fashion. Its flexibility also allows the development of new analysis modules using the Matlab platform.

One crucial problem that needs to be considered is the storage of the data generated by the HCS. Terabytes of data should be stored and organised, a feat that can only be achieved with the creation of a laboratory information management system, which is able to store the data from the screen as well as to allow its rapid searching and evaluation. Using this informatic platform, data analysis can be run to extract metadata essential for the interpretation of the screen, such as the identification and correction of edge-effect artefacts, uneven pipetting, or the exclusion of out of focus images (Krausz, 2007). Known players in the pathway being screened should be used in each plate as internal controls for the accuracy of the assay and for the estimation of the transfection efficiency throughout the plate. These controls are essential for the normalisation of the data before statistical analysis can be applied in order to identify the hits. Finally the use of cluster analysis algorithms can assist in finding any correlation between the hits, enabling the identification of protein families involved in particular pathways.

The introduction of HCS strategies is generating an increasing mass of data, and merging functional genomics (RNAi) and the results from drug screenings has the potential to shed light on the function of a large number of genes. For that to happen, however, a systematic approach to data mining has to be undertaken. The normalisation of the intrinsic variability of biological assays by the use of more physiological cell systems, i.e. primary cultures, represents a great challenge. In particular, certain cell types are so unique that immortalised cell lines cannot effectively substitute for them. Neurons are such a cell type; the cell models commonly used to substitute for them, like PC12 or SHSY5Y cells, are very poor in accounting for specific neuronal functions, physiology and specialisation. For this reason, in order to study neurotrophin trafficking in the most physiologically relevant contest, this thesis work aims to develop a strategy to successfully apply the HCS approach to MNs.

Chapter 2. Materials and Methods

2.1 Materials

2.1.1 Chemicals and enzymes

Reagents were purchased from GE Healthcare, BDH, Biorad, Calbiochem, Clontech, Fisher Scientific, Gibco BRL, Invitrogen, Dharmacon, Qiagen, Sigma, Pierce and Stratagene. The fluorescent chemicals were purchased from Molecular Probes. Phosphate buffered saline (PBS), ethylenediaminetetraacetic acid (EDTA), Luria Bertani (LB) medium, 2YT medium, SOC medium, Hanks' buffer and Dulbecco Modified Eagle's Medium (DMEM) were provided by CRUK Central Services. The Sonic Hedgehog agonist (SAG, $C_{28}H_{28}ClN_3OS$) was purchased by Axxora (Product number 270-426-M001).

2.1.2 Antibodies

Fluorescently conjugated secondary antibodies were purchased from Invitrogen Molecular Probes and were used at a dilution of 1:200. HRP-conjugated secondary antibodies were from DAKO (dilution 1:2000).

The following primary antibodies were used at the indicated dilutions:

Table 2.1. Primary antibodies used

ANTIGEN	ANTIBODY NAME	SUPPLIER	DILUTION
Akt	9272	Cell Signalling	1:2000 WB
β−actin	AC40	Sigma	1:1000 WB
βIII tubulin	Tuj1	Covance	1:1000 IF 1:2000 WB
BICD1	2296	Dr C. Hoogenraad, Erasmus University Rotterdam, The Netherlands	1:2000 WB
Dynein Intermediate chain	74-1	Santa Cruz Biotechnology	1:2000 WB
ERK1/2	9102	Cell Signalling	1:2000 WB
GD1b	MOG-1	Dr. H. Willinson, University of Glasgow, UK	1:1000 IF 1:2000 WB
GFP	4E12	CRUK monoclonal facility	1:500 IF
MAP2	AB5622	Chemicon	1:500 IF
pAkt (S473)	D9E	Cell Signalling	1:2000 WB
pERK1/2 (Thr202/Tyr 204)	9101	Cell Signalling	1:2000 WB
Pan Trk	C14	Santa Cruz Biotechnology	1:1000 WB
p50	611002	BD Transduction Laboratories™	1:2000 WB
$p75^{NTR}$ intracellular domain	5090	Molecular Neuropathobiology Laboratory, CRUK	1:1000 WB
$p75^{NTR}$ CRD	5410	Molecular Neuropathobiology Laboratory, CRUK	1:5000 IF 1:1000 WB
VAMP2	69.1	Synaptic System	1:2000 IF 1:1000 WB

2.1.3 Transfection reagents used

All the transfection reagents used in this thesis work are listed below:

Table 2.2 Transfection reagents used

NAME	SUPPLIER
Oligofectamine	Invitrogen
TransIT siQuest	Mirus
siPORT™ Amine	Ambion
Interferin™	Polyplus
LipoRNAiMax	Invitrogen
CodeBreaker™	Promega
Dharmafect 1	Dharmacon
Dharmafect 2	Dharmacon
Dharmafect 3	Dharmacon
Dharmafect 4	Dharmacon
Lullaby	OZ Bioscience
RiboJuice™	Merck
TransIT KO	Mirus
HiPerFect	Qiagen
Genesilencer	Genlantis
NTERnanoparticle	SIGMA-Aldrich
SiPORT NeoFX	Ambion
SimPorter	Upstate
Lipofectamine 2000	Invitrogen
Santa Cruz	Santa Cruz
Metafectene	Biontex
Dreamfect Gold	OZ Bioscience
TransPass R1	New England Biolabs

2.1.4 Q-PCR primers

The primers used for PCR and Q-PCR in this thesis work are listed below:

βIII-tubulin

forward: 5’ GCGCATCAGCGTATACTACAA 3’

reverse: 5’ TTCCAAGTCCACCAGAATGG 3’

Bicd1 exons 1-2

forward: 5’ GCTGGAGGCCGAGTATGAC 3’

reverse: 5’ AGAAGGACTGCCCAAATGC 3’

Bicd1 exons 7-8

forward: 5’AAGATCGGCAGCCCTAAAA 3’

reverse: 5’ TCCCAGCTAGTTGTGAGCACT 3’

Bicd2

forward: 5’ GATGGAGCAGCTCAAAGAGG 3’

reverse: 5’ TCCTGGATCAGGCTCTCCT 3’

ChAT

forward: 5’ TGATGGCTTCATCCAGGTC 3’

reverse: 5’ GGCACCAGCCTCTGGTAA 3’

Dync1h1

forward: 5’ TGCTCCACAAGTCAGTCACAA 3’

reverse: 5’ TCCTCAGCTCGTGAACCAC 3’

HB9

forward: 5’ CTACTGCCCGCATGATCC 3’

reverse: 5’ CGTAGACCTTGTGATCCATCG 3’

p50 dynamitin

forward: 5’ GATGATGGCCAGTTCCCTTA 3’

reverse: 5’ TCACGCATCGTTGTCTGC 3’

$p75^{NTR}$

forward: 5’ ACTGAGCGCCAGTTACGC 3’

reverse: 5’ CGTAGACCTTGTGATCCATCG 3’

TrkA

forward: 5’ CCGTTTCCTCCGGTCCCACG 3’

reverse: 5’ CCAGAAGCTGCCCAAGGCCC 3’

TrkB

forward: 5’ TGCCGAGTGCTACAACCTCT 3’

reverse: 5’ GCGTCCTTCAGCGTCTTC 3’

2.1.5. Sequence of the siRNA pools used

The individual sequences of the single siRNAs of the VAMP2 siRNA pool are reported below. The sequence of the non-targeting negative siRNA control is proprietary from Qiagen (AllStars negative control siRNA, Catalog number: 1027281).

VAMP2 siRNA pool (Dharmacon)

1- sense: GUAAAUAGCCAGCUGUUAUUU

antisense: AUAACAGCUGGUAUUUACUU

2- sense: GCGCAUCCAGAUUGUAAAUU

antisense: UUUCACAAUCUGGAUGCGCUU

3 – sense: GCGCAAAUACUGGUGGAAAUU

antisense: UUUCCACCAGUAUUUGCGCUU

4 – sense: CCUCCAAACCUUACUAGUAUU

antisense: UACUAGUAAGGUUUGGAGGUU

2.1.5 Design of the molecular motors and adaptors siRNA library (Qiagen)

Table 2.3 reports the genes targeted by the pool of siRNA for each of the 96-well plates`.

Table 2.3 Layout of the siRNA library (Qiagen)
Position on the master plate, gene ID, symbol and description of the gene targeted are listed for each of the siRNA pools in the Qiagen library.

PLATE 1

row	col	geneId	symbol	description
B	2	16560	***Kif1a***	kinesin family member 1A
B	3	12121	***Bicd1***	bicaudal D homolog 1
B	4	229841	***Cenpe***	centromere protein E
B	5	13191	***Dctn1***	dynactin 1
B	6	13424	***Dync1h1***	dynein cytoplasmic 1 heavy chain 1
B	7	13426	***Dync1i1***	dynein cytoplasmic 1 intermediate chain 1
B	8	13427	***Dync1i2***	dynein cytoplasmic 1 intermediate chain 2
B	9	234663	***Dync1li2***	dynein, cytoplasmic 1 light intermediate chain 2
B	10	16563	***Kif2a***	kinesin family member 2A
B	11	16570	***Kif3c***	kinesin family member 3C
C	2	16574	***Kif5c***	kinesin family member 5C
C	3	16573	***Kif5b***	kinesin family member 5B
C	4	17300	***Foxc1***	forkhead box C1
C	5	16582	***Kifc3***	kinesin family member C3
C	6	16593	***Klc1***	kinesin light chain 1
C	7	16551	***Kif11***	kinesin family member 11
C	8	16580	***Kifc1***	kinesin family member C1
C	9	110033	***Kif22***	kinesin family member 22
C	10	17274	***Rab8a***	RAB8A, member RAS oncogene family
C	11	17912	***Myo1b***	myosin IB
D	2	17879	***Myh1***	myosin, heavy polypeptide 1, skeletal muscle, adult
D	3	17882	***Myh2***	myosin, heavy polypeptide 2, skeletal muscle, adult
D	4	17883	***Myh3***	myosin, heavy polypeptide 3, skeletal muscle, embryonic
D	5	17884	***Myh4***	myosin, heavy polypeptide 4, skeletal muscle
D	6	17888	***Myh6***	myosin, heavy polypeptide 6, cardiac muscle, alpha
D	7	140781	***Myh7***	myosin, heavy polypeptide 7, cardiac muscle, beta
D	8	17885	***Myh8***	myosin, heavy polypeptide 8, skeletal muscle, perinatal
D	9	17886	***Myh9***	myosin, heavy polypeptide 9, non-muscle
D	10	77579	***Myh10***	myosin, heavy polypeptide 10, non-muscle
D	11	546101	***EG546101***	predicted gene, EG546101
E	2	107589	***Mylk***	myosin, light polypeptide kinase
E	3	432516	***Myo1a***	myosin IA
E	4	17913	***Myo1c***	myosin IC
E	5	338367	***Myo1d***	myosin ID
E	6	71602	***Myo1e***	myosin IE
E	7	17918	***Myo5a***	myosin Va
E	8	17919	***Myo5b***	myosin Vb
E	9	17920	***Myo6***	myosin VI
E	10	17921	***Myo7a***	myosin VIIa
E	11	17922	***Myo7b***	myosin VIIb
F	2	270163	***Myo9a***	myosin IXa
F	3	17925	***Myo9b***	myosin IXb
F	4	17909	***Myo10***	myosin X
F	5	19341	***Rab4a***	RAB4A, member RAS oncogene family

F	6	271457	***Rab5a***	RAB5A, member RAS oncogene family
F	7	19344	***Rab5b***	RAB5B, member RAS oncogene family
F	8	19345	***Rab5c***	RAB5C, member RAS oncogene family
F	9	67117	***Dynlt3***	dynein light chain Tctex-type 3
F	10	21648	***Dynlt1***	dynein light chain Tctex-type 1
F	11	19349	***Rab7***	RAB7, member RAS oncogene family
G	2	56455	***Dynll1***	dynein light chain LC8-type 1
G	3	544791	***Myh13***	myosin, heavy polypeptide 13, skeletal muscle
G	4	226422	***Rab7l1***	RAB7, member RAS oncogene family-like 1
G	5	16569	***Kif3b***	kinesin family member 3B
G	6	71819	***Kif23***	kinesin family member 23
G	7	381293	***Kif14***	kinesin family member 14
G	8	19348	***Kif20a***	kinesin family member 20A
G	9	98932	***Myl9***	myosin, light polypeptide 9, regulatory
G	10	69654	***Dctn2***	dynactin 2
G	11	67268	***2900073G15Rik***	RIKEN cDNA 2900073G15 gene

PLATE 2

row	col	geneId	symbol	description
B	2	22428	***Dctn6***	dynactin 6
B	3	16562	***Kif1c***	kinesin family member 1C
B	4	73804	***Kif2c***	kinesin family member 2C
B	5	16568	***Kif3a***	kinesin family member 3A
B	6	53598	***Dctn3***	dynactin 3
B	7	667772	***Myh15***	myosin, heavy chain 15
B	8	381284	***E030010N08Rik***	RIKEN cDNA E030010N08 gene
B	9	244281	***Myo16***	myosin XVI
B	10	16565	***Kif21b***	kinesin family member 21B
B	11	16561	***Kif1b***	kinesin family member 1B
C	2	16554	***Kif13b***	kinesin family member 13B
C	3	16571	***Kif4***	kinesin family member 4
C	4	668303	***Kif26a***	kinesin family member 26A
C	5	218203	***Mylip***	myosin regulatory light chain interacting protein
C	6	235661	***Dync1li1***	dynein cytoplasmic 1 light intermediate chain 1
C	7	67665	***Dctn4***	dynactin 4
C	8	17910	***Myo15***	myosin XV
C	9	213575	***Dync2li1***	dynein cytoplasmic 2 light intermediate chain 1
C	10	0	***siControl***	
C	11	667663	***Myo3a***	myosin IIIA
D	2	17121	***Mxd3***	Max dimerization protein 3
D	3	269152	***Kif26b***	kinesin family member 26B
D	4	109242	***Kif24***	kinesin family member 24
D	5	75050	***Kif27***	kinesin family member 27
D	6	16564	***Kif21a***	kinesin family member 21A
D	7	208943	***Myo5c***	myosin VC
D	8	209737	***Kif15***	kinesin family member 15
D	9	0	***siControl***	
D	10	16559	***Kif17***	kinesin family member 17
D	11	74018	***Als2***	amyotrophic lateral sclerosis 2 (juvenile) homolog (human)
E	2	17898	***Myl7***	myosin, light polypeptide 7, regulatory
E	3	16553	***Kif13a***	kinesin family member 13A

E	4	246177	***Myo1g***	myosin IG
E	5	16578	***Kif9***	kinesin family member 9
E	6	16594	***Klc2***	kinesin light chain 2
E	7	0		
E	8	228421	***Kif18a***	kinesin family member 18A
E	9	280408	***Rilp***	Rab interacting lysosomal protein
E	10	75465	***Dynlrb2***	dynein light chain roadblock-type 2
E	11	67068	***Dynlrb1***	dynein light chain roadblock-type 1
F	2	59288	***Dctn5***	dynactin 5
F	3	73470	***Kif2b***	kinesin family member 2B
F	4	74376	***Myo18b***	myosin XVIIIb
F	5	228785	***Mylk2***	myosin, light polypeptide kinase 2, skeletal muscle
F	6	74764	***Klc4***	kinesin light chain 4
F	7	16581	***Kifc2***	kinesin family member C2
F	8	59310	***Mylc2pl***	myosin light chain 2, precursor lymphocyte-specific
F	9	67938	***Mylc2b***	myosin light chain, regulatory B
F	10	16552	***Kif12***	kinesin family member 12
F	11	64291	***Osbpl1a***	oxysterol binding protein-like 1A
G	2	231836	***EG231836***	predicted gene, EG231836
G	3	216459	***Myl6b***	myosin, light polypeptide 6B
G	4	329421	***Myo3b***	myosin IIIB
G	5	68097	***Dynll2***	dynein light chain LC8-type 2
G	6	77505	***Dnhd1***	dynein heavy chain domain 1
G	7	327954	***Dnahc2***	dynein, axonemal, heavy chain 2
G	8	232943	***Klc3***	kinesin light chain 3
G	9	319991	***Kif6***	kinesin family member 6
G	10	16576	***Kif7***	kinesin family member 7
G	11	360013	***Myo18a***	myosin XVIIIa

PLATE 3

row	col	geneId	symbol	description
B	2	17897	***Myl3***	myosin, light polypeptide 3
B	3	17916	***Myo1f***	myosin IF
B	4	18196	***Nsg1***	neuron specific gene family member 1
B	5	19325	***Rab10***	RAB10, member RAS oncogene family
B	6	23790	***Coro1c***	coronin, actin binding protein 1C
B	7	53869	***Rab11a***	RAB11a, member RAS oncogene family
B	8	67166	***Arl8b***	ADP-ribosylation factor-like 8B
B	9	67845	***Zfp364***	zinc finger protein 364
B	10	72993	***Appl1***	adaptor protein, phosphotyrosine interaction, PH domain and leucine zipper containing 1
B	11	216190	***Appl2***	adaptor protein, phosphotyrosine interaction, PH domain and leucine zipper containing 2
C	2	226421	***5430435G22Rik***	RIKEN cDNA 5430435G22 gene
C	3	0	***siControl***	
C	4	668940	***Myh7b***	myosin, heavy chain 7B, cardiac muscle, beta

Table 2.4 Sequences of the siRNAs contained in the Qiagen library
Each siRNA pool (Qiagen) contains three targeting sequences. These, as well as the sequences of the siRNA controls, are reported below., as well as the siRNA controls.

PLATE 1

symbol	siRNA 1	siRNA 2	siRNA 3
Kif1a	AAGCACCACCACTATTGTCAA	ACGGATAACTGTGACACTGTT	CAGATGCGGGTCTGAGTTGAA
Bicd1	CAGGTTGAATACGAAGGCTTA	TAGAGTCATGTTGGACTACTA	ATGGTTTATGTTTATAAAGAT
Cenpe	CTGGGAGGAAAGAACTCTTAA	CAAGGCTACAATGGTACTATA	AAGCATTGGGCTCGTGAATAA
Dctn1	CCGCATCAAGCTACCAGCTCA	CACAGTCGCCTCATCTCCTAA	AAGGCTGAAATCGAAGAGAAA
Dync1h1	ATGGCTGGGTTTAGTAAATAA	CGGCAAAGAATTCACCAGTAA	TGGCTGGGTTTAGTAAATAAA
Dync1i1	ATGGAACATATTTATTTGAAA	CCCAGTGATGCTGGAAGCCAA	CCGGACAATCCGAGTAATTGA
Dync1i2	ATGGTAGTTATCTATAAATAA	TGGGTGTATATTGTTAAGTTA	CAGGTGCTAAGCTGTCATTAA
Dync1li2	TACCATGACTTTAATGTATAA	TACCATGTTGGCAATGTTCTA	CTTGTTCTAAATGATCTTTAA
Kif2a	CGGGATTTACGTGGAGATCAA	AAGGAGTGCATCCGAGCCTTA	CTGCTGGACCATTCCATCTTA
Kif3c	CAGGGTTTCAACGGCACCGTA	ATGGATCACACCAACGAGCAA	AAGAAGCTCTATGCCAAGCTA
Kif5c	CACTGATTTGACTTAATTTAT	CGAAGTCAGTTTCCAAGATAA	CTGTACAGTAGATTTCATTAA
Kif5b	AGGGATCAAGATAATATGCAA	CAGCAAGAAGTAGACCGGATA	CACGAGCTCACGGTTATGCAA
Foxc1	AAGGATAATTTCCTAAGTAGA	CCCGGCACTCTTAGAGCCAAA	TAGGGTGATCTGCCCTGTCAA
Kifc3	CGGGCTCAGATTGCCATGTAT	CCGCACCACCGAGTTCACCAA	CAGAGGTCTGGGCTATATTTA
Klc1	CAGGGATCAGAACAAGTATAA	AGGGATCAGAACAAGTATAAA	CACCGTCACAACCACCTTGAA
Kif11	AAGGAAGAACTTGAGAATTTA	AGCAAAGAACATAATGAATAA	CACAGGAACTTTGCCAGTTAA
Kifc1	CTGCGCGGAGGTTGAAATTCA	GGCGAGTTACGTAGAGATCTA	TGCGCGGAGGTTGAAATTCAA
Kif22	AGCGAGAGTCCTCAAACCAAA	CAGCATTGAACTTCACTGCTA	AAGGGAAGGCTATGAGCTTAA
Rab8a	CGGACTCGATTGAGAAATTGA	CTCGATGGCAAGAGGATTAAA	CTGGCTCTAATCGGATGTTCA
Myo1b	TGGGATTATGTTAATAATAAA	CAGCAGAAACTTATTTATGAA	CTGGAATTAAATTGTTTCTTA
Myh1	CACAGAGCTGTTCAAGATTAA	AGGGAGAATCTGAATAAGCTA	CGGAACTACTGTAACAGTAAA
Myh2	CCGGGTCACTTTCCAGCTTAA	CAGAGCAAAGATGCAGGGAAA	CAGCTTGATGAAAGGCTCAAA
Myh3	CAGCAGGACCCTGGTGGTTAA	CAGCAGCTGGATACAAAGCTA	CACACTTTGTACGCTGTATAA
Myh4	CTGGATCAACTTGAGACGTTA	CAGGACTTGGTGGACAAACTA	CACACTAAAGTCATAAGCGAA
Myh6	CCGGGTGATCTTCCAGCTAAA	CTCGCTGTGGCCAATACACAA	CAAGCTGATGACAAACCTGAA
Myh7	AAAGAAGGACTTTGAGTTAAA	TGGGAAGACTGTCAACACTAA	TACCAAATCCTGTCTAATAAA
Myh8	CCCAAGGAGTCTTATGTGAAA	CTGGCATCAGCTGATATTGAA	CAGGACCTGGTGGACAAATTA
Myh9	CAGGGCTTATCTACACCTATT	TCCAGCAAGAATGGCTTTGAA	CTCGAGAAAGTCCACTCGGAA
Myh10	CACAAGAATAATGCACTTAAA	CAGTACTAAGACAATGTTAAA	AAGACCAGAATTCCAAATTTA
EG546101	GAGAATACAGTTCACTGTCAA	AGCAGCCAAGATGTGACTTCA	TAAGATGAAATTAGTAACTGA
Mylk	CGCAAAGGATTTCATCAGTAA	CACACTGGTGGTGGAGAACAA	CCGCGTGTCAATGTCAGAGAA
Myo1a	CAGGAGGAATACAAGAGAGAA	CCGAGTGGTGAAGCAACTCAA	CGCGGGCAAGGTGACCTACAA
Myo1c	ATCCAGAGAAACACTAAATAA	AAGACTGAAGCAAATCCTAAA	TTGGATTTGGGCAAATAAATA
Myo1d	ATGAAAGTAATTGGATTCAAA	TGGGAAATACATGGATATCAA	AAGAATTCTATGATTGCTTTA
Myo1e	TTGGTAGATTCTATCAATAAA	AACGATATTATTGATATTATT	CCCAAGCTGTACATTTATAAA
Myo5a	CCCTCGTACTGTTACCTTTAA	CAGCCTTGTATCAATCTTATA	AAGGAAGATGTTAACTGGAAA
Myo5b	CCCGCAGTTCTGCATAACTTA	AACCTGGAGTTTCTCAATGAA	TCAAACTGAGATAATATTAAA
Myo6	CAGATAATTTCCGGTATTTAA	AACCGAGATAATGAAATCTTA	CAGCAGGAGATTGACATGAAA
Myo7a	CCCAGTGATGACTAAGATCTA	CAGAGTCATTCTCCTCCAGAA	CCAGGTGTTCTTCATGAAGAA
Myo7b	CTGCTGAATTTCATTAGTCAA	CAGGTCATTCTGGCTAAGGAA	CACGATGGAGCAGGAAGAGTA
Myo9a	AACTAGGTAATCAATATTAAA	CCCGATGATGATGGTCATTCA	CTGAATTTGAATAAAGTTAAA
Myo9b	CAGCATAACTTGAATATTGAA	CACCTCCTTCCTGAAGAGTAA	CAGAGTGAAATACCAGATCAA
Myo10	CAGGACGAAGCCATCAAGATA	CAGCGCTACAAGAGAAACCAA	CCCAGACGAGAAGATATTTAA
Rab4a	TGGAATTTGGCTCAAAGATAA	ATGCGCTTACTAATTGGTTAA	CAGGTCTGTGACGAGAAGCTA

Rab5a	TAGGAATATGAAACCGATAAA	ATGAATATTGATGACATCTTA	CAAGTTTCTAATTCTGAATTA
Rab5b	CAGGAGCGATACCACAGTTTA	CTCGGGCAAAGACATGGGTAA	TATGATATTACTAATCAGGAA
Rab5c	CCCGACTGGAATCTACTCTAA	CTGGTGGTCATGGTAACCAAA	CACCTGCACCTTTCTGTACAA
Dynlt3	CAGGGAGAAATATATGAACAA	CAGAAAGTAATACATCAAATA	TACACTTGAGGTGGAATTAAA
Dynlt1	CTGTGTGATCATGCAGAAGAA	TTAGAATAATAAATTATTCAA	ATGGGAGAACAAGACCATGTA
Rab7	AGGCCGGAGCTTTGACCATAA	TCCGTTGACCCTGCGCTTCAA	TACAGAGTGTTAGAGACTCAA
Dynll1	CTCCCTTAGGTCATTCCTTTA	ACAGCTTACATTTGTATTTAT	AAGGACTGCATCCAAATTCCA
Myh13	CACGAGCCTGATAAATACCAA	AAGGATGAGGAAATCGAACAA	AAGAGGAGATTTCTGACTTAA
Rab7l1	CCCGTGTACTATAGCTAGTAT	TTGGGTGTCGTCTGTGACTTA	TCCGTTGAGAATATTCAATAT
Kif3b	CTCAAGCATCTTATTATAGAA	AACCATGACCATCCTGTTAAA	CTGCAGGATGAAGATGAGATA
Kif23	AAGGCTGAAGACTATGAAGAA	TTGTTTGAATATGATCTTTAA	TACGATCTATGAGGAAGATAA
Kif14	TTCGTGAATGCTGGAAGTAAA	CTGGCTGGAACTGGGAAATAA	CACGATGATTCAGGAAGCCAA
Kif20a	CAGGAAGTTAAAGCTGAACTA	CAGCTAGATGAAACAAGTCAA	CTCCTTTGCCTTGAAGAGTAA
Myl9	AGGGACAGTCTCTTAATACAA	CAGGGTGAGGCAGGTGCTCTA	CACCAAGGTAAAGCCACTGAA
Dctn2	CAGGAATGAGCCAGACGTTTA	CTGGCCGAGTCTAACACTGTA	TCGGATGAAGAGGCTGGGAAA
2900073G15Rik	CACGTACGCCTTTCTCTCTAA	CACAGGATTCTTTAAGCCCTA	CAGAATTGTGACCCTGCATTA

PLATE 2

symbol	siRNA 1	siRNA 2	siRNA 3
Dctn6	AGCCATGCATTTATTATGTAA	ACCATATACCATAACTAAATA	AACGACCGCTATAATTTATAT
Kif1c	CACGGACGAGCAGAAATTGAA	CAGCAGGTGTACCGAGACATA	ACCTCCATCATTAATCCCAAA
Kif2c	AGCCTCGGTACCGGAACTTAA	CGCCAATATAAGCACAGTGAA	TAGCAGAGTCGTGGTTTCCAA
Kif3a	TGGAGAGAACTCCTTAATTAA	ACGAACCTCCAAAGACATTTA	GAGACCGTAATTGATTCTTTA
Dctn3	TCCAGTGACAATAAACTTGAA	AAGGGTATAACAAGACTACAA	CAGGGTCAGGTTGACCTTAGA
Myh15	AAGGAGGAACTGGAAAGTGAA	AGCGGTGATGATGGACAAGTA	AAGGCCTAATATATCCTAGAA
E030010N08Rik	CTGGTTGAACTTAATCCGCAA	CAGGAGGTGAGTGACCTGCAA	AGGAGGAATCCTGTAAATATA
Myo16	CAGAATCAAGATGAATATAAA	AACCTCTTATTTGTAATGAAA	ACGGGTTATCTTCGGAAGAAA
Kif21b	CTGGTTGTAATTTGAGCACAA	ACCCTTGAAGTTAGGACTAAA	TAAGAGCTTGTCATAAATAAA
Kif1b	ACGAGATTTACTGAATCCCAA	TACAATGACATTGGAAAGGAA	CTCCATCTTCATGCTCACTTA
Kif13b	CACGAGAATGTCCATGAGGAA	CAGGCTGGTCTGCATGGTTAA	CAGGATGTGTCCCAAACACTA
Kif4	CAGTACCAGGATAATATTAAA	AAGAATTGGCTTGGAAATGAA	TACGATGAAATACATGGTCAA
Kif26a	ACGGCAGGAATTCTTACCAAA	CAGGCTTATTGACGAACGCAA	CAGCGGCCTCTTTCTTTATAA
Mylip	CTGCAGTATTGTAAACTATAA	CCGCCTTAAACTGAGGGTCAA	ATCGGGTGCAATACTAGCTAA
Dync1li1	TAGACTTAGTTTATAAATACA	CAGCAGGGTGGGATAATGATA	CCGCAAGTTCTGTTTACAGTA
Dctn4	AAGGATAACCCTGTAATGATA	CAGGATGACCCTGACATCGTA	AAGCAATTACATGTCATGAAA
Myo15	CAGAATGACTTTAAATTCAAA	CACCTTCATTCTGGAACTGAA	CAGAAGCATCATCAAGCAATA
Dync2li1	CTGGTCATTATTGGAAGTAAA	CTCGCTGATGTTTACCAGCAA	TTGGCATTCGGTATTGATAAA
siControl	GAGGCTGAAGATATCTACAAA	AGGCCAAACATTAGCAATTGA	AAGTGCGTGCGTGGAGAGAAA
Myo3a	AAGAGTAGTGCTGTAATAATA	CTGCACTATTATAAATGACAA	CAGGAATTCGACTACAAGAAA
Mxd3	CCCGTATATACTGCACAGTAT	CCACATGTTGAAGAGACTAAA	CCCAGGGAATTTCATGTAGCA
Kif26b	ACCATTCGAAATTAAAGTCTA	CACCAACAAGATGACCCAGAA	TTGCAGCTGAATAAATGTTAA
Kif24	CCGGGTGAAGGAACTAAAGAA	CCCAGACTGATTAGCCAACAA	CAGAGAATCCTTGGACTGAAA
Kif27	CAGGATGAAGTTTATAACACA	CACAATGTGGATCACCTGAAA	CCAGCTGAAGAGAGAACTTAA
Kif21a	AACAAGGTGATGGTCAATCAA	CAGCGCAAGCGAGATCATCAA	CCGTGTCGACATCTTATATTA
Myo5c	ATAGAACTTTATAATACTTAA	CAGCTGATGCTGGATACCAAA	AAGAATGTGCAGAGTAGCTTA
Kif15	AGGCTGGATAATGATATATTA	CAGGATTCCTACGATAACTTA	CACAATAGAATCAATGGAGAA
siControl	TGCGCTTATATCAGCATCTAA	ATCACAGAGTGTGATAAATTA	ATGGGAGCTGATGTTGATCAA
Kif17	TACCATCAACATCGAGATCTA	TCCGCAGAGACTGTAACTATA	CAGGAAGAGATCAAGAGGCTA
Als2	TCCGAGCTACTTTATAATCAA	ACCGATGGACTCAAAGAAGAA	TGCCATTGATTTCCTAAATAA
Myl7	CAGGGATGGGATCATCTGCAA	CAGGCTGAGGTCACCTCAATA	AACTCTGTGCCTGAACTAGAA
Kif13a	AAGGATCTACCTGATCGTGAA	CAGGAGCAGATGAGAAGCATA	CAGGAGGAGGGCTCTAACAAA

Myo1g	CAAGGCTATGATGATCTTGTA	TCCCATCTGTTTGCTGAGCAA	CTCGGTGTGATGGCAAGGATA
Kif9	CAGAAGCACAATTATATGAAA	CAGGAGATTGATGAGACCAAA	ATGGATATAGAAGGTAACCTA
Klc2	AAAGACGATTTGAATCTGAAA	CCGGAGAGCCCTGGAGATCTA	CAGCTGGTACAAAGCCTGTAA
siControl	AAGGACCATTACCGAAAGCTA	CAGGGTCGAGTGGCACAGCTA	AAGCTGAGGCTCAAATATGAA
Kif18a	TTCAAAGATATTGAACATTTA	TGCATTGTAAATATTGTTTAA	CAGATTTATTTGCGACAACAA
Rilp	CAGGAGCGGAATGAGCTCAAA	AGCCATGAAGGTGGCAGTCAA	GAGGAGGAAGATCAAGGCCAA
Dynlrb2	TAGGATCAGATCGAAGAAACA	CCAGCTGACCATGAAAGCCAA	ACGATGGTGGTCAATGCAGAA
Dynlrb1	CTGTGTCATTCCTTAATTTAA	CCCAAGAATAATAGTGCTAAT	ATCCAGAATCCAACTGAATAA
Dctn5	CAAGACCATTATAATGAATGA	AAGCCAGAACATCGTCCTCAA	TAAGACGAACCTGGAGATAAA
Kif2b	AGGGATGAAGTTATTCAGATA	TTGGAGAATTTACATCTTAAA	AAGGCCCAAGATTGTTCTAAA
Myo18b	CAGCAAGACGTCAATCAGCAA	CACCGGGACTTTGACGTAGAA	CTGGTCTTCCAGAATCGACAA
Mylk2	ACCGGAAATGTCAACAGTGAA	CGGGATCCTCTTCATGCACAA	CGCGCCAGATCCAAAGAACAA
Klc4	CACAGTGAACACTACTCTGAA	TCGCTGAACTACTTAAACCAA	CACACCATTGAGTGTCTGCAA
Kifc2	CCGGATCAATTCACATCAGAA	CAGGCATTTGAGAGAGGGCAA	CAGTGTCTGCATCTTCACTTA
Mylc2pl	AAGGCTGACTTCATTAAGGAA	CCAGATGTCTGTGGCAACTTA	TCGCATAAATGTCAAGAACGA
Mylc2b	CAGCATCAGGTCAGATTTAAA	AATGTTGTAAATTGTACTGAA	CACTGTGAAAGCCCAGGACAA
Kif12	AAGGGCCAGAAGGATCAGAAA	AAGGCATATTAGAAAGGGAAA	AAGGCCTCTCTTCTTGTTAAA
Osbpl1a	CACAATGCCAGTGATATTTAA	CTGGGAGAGACTTATGAATTA	CAGGTGACTGATGATGAAGAA
EG231836	CACGGAAGTATCCACCTCAAA	CAGGGAAATTGGGCACCTCAA	CAGCGCCATGTGGCAGAGCAA
Myl6b	CAAAGTGGTGATCGAGTTTAA	AAGGATGCTCCCGTGAAGAAA	CAGCAGGGCCCTCCATCTCTA
Myo3b	CTCGGAGGAAATTGAAGCAAA	AACCACCTTTCTCACAGATAA	TTCCTATTTCATGACATTATA
Dynll2	TAGGTCTGAGGTGGAAGTTAA	CTGGAACAGGTCTGAAGTATA	TAGTTAGGTCTTAGCAATCAA
Dnhd1	CAGGCTCACCTTCATTATTTA	CTGCAGGACCTTAATACTCAA	CCGGTCCTTCATGTACAATTA
Dnahc2	AACCGGGAGCTGAACAAGAAA	ATCGAGGACATCTTTCATAAA	CTCTGGAAATTTATTGACAAA
Klc3	CCCAAATGTGGCCAAGACTAA	ACGGAGGCTAGCCCAAGAGAA	GACCAGAACAAATACAAGGAA
Kif6	CAGGAGGATGATAGCCCATTA	CTGATTCTTCTTAAAGACTAA	AACGGCCTTTATGCACCTGAA
Kif7	ATGGGAGAACTGGGAAAGTAA	TCCCTGCATGAAGATGAACAA	ACAGCTTTCAATGGTGTTATA
Myo18a	CCGGCTGATGCCAAGACGGAA	GACCTGATTGATGTAAGGAAA	ACCCACCATGTTTAACCTCAT

PLATE 3

symbol	siRNA 1	siRNA 2	siRNA 3
Myl3	ACCCTGTGGCCTTATGAATAA	AAGATCGAGTTCACACCTGAA	ACAGAAGATGAGGTAGAGAAA
Myo1f	CACGTCAAAGACATAATCCTA	CAGCCGTAAGATGGACAGCAA	TACCAAGGTCTTTGTTAAGAA
Nsg1	CTGAATCTTGACATTAAAGTA	AGGGACATTTCATTAAATATA	TAGGTCAGAAATAAATGGCAA
Rab10	CTGCACTTCAGTTGTATTATA	CACCATCACAACCTCCTACTA	CTGGATTTGACTAGTCTCCAT
Coro1c	TCCGTTGAATTAATTACGTAA	CTGTGTATGTTTATAAACTAA	CAGAGGGAACTCGGTGATTAT
Rab11a	AAGGCTGTGTATAGTCCATTT	CAGATCTAAGACAACCTTAGA	TAGGACAGAATAGAACTCTAT
Arl8b	AAGAACATTCTGGACAGATAA	TGCCTGCTTTATCTAATGTAA	CCGGTCAATTCAGTGAAGATA
Zfp364	AACCCTCAACCCATAATATTA	CCCAAACTACCGGAATATATA	CCAGCTATCGAAGGAATAATA
Appl1	TAGGAACAAGATAACGATATA	CTGCTATATATTTGAATCAAA	CAGTTAATAATTATCAATTTA
Appl2	CCCATTCAGTTTGATATTGTA	CTGGATTTACAATTTGTTAAA	TGGGAGGGAGACAATAAGAAA
5430435G22Rik	CTCAATGGTATCAACATTCTA	CCGAAAGAAAGTGGACTTGAA	TTCGATGTACATTGCACTGAA
siControl	CTGCGGCAGTTGTTTATGATA	CTGTTTCTTGAAGATGATCTA	AGCAGTGTGAATATGGCTTGA
Myh7b	CTGCGACATAGCCACGAGGAA	CTGGAGTACCAGCGCATGCTA	TCCGATGGCTGGTTTCTCGAA

2.1.6 Validation rescreen

The siRNA pools used for the validation of the primary hits from the siRNA screen were purchased from Qiagen.

Table 2.5 Layout for the plate of the validation re-screen and sequences of the single siRNAs used
Position on the master plate, symbol, gene ID, and the accession number of the genes targeted are listed for each of the siRNA pool of the re-screen library.

Well	Gene Symbol	Gene Id	Accession Number	Sequence
B03	***Myh13***	544791	NM_001081250	GCGCAAAGUUAAAGAGAUG
B03	***Myh13***	544791	NM_001081250	AAUCUGAGCUUGAUCGCAA
B03	***Myh13***	544791	NM_001081250	GGAUGAGGAAAUCGAACAA
B03	***Myh13***	544791	NM_001081250	GAUAAAGAAAUGUACGUGA
B04	***Rab7l1***	226422	NM_144875	UGACACGACUCUACUAUAG
B04	***Rab7l1***	226422	NM_144875	CAAGGGAACUACAUCAAUC
B04	***Rab7l1***	226422	NM_144875	GGACAGCAAGCUCACACUA
B04	***Rab7l1***	226422	NM_144875	GCCGAGAUCACCUGUUUAA
B05	***Dctn2***	69654	NM_027151	GCAGAAGUACCAACGACUA
B05	***Dctn2***	69654	NM_027151	GAACUGGUACAGCGACUUG
B05	***Dctn2***	69654	NM_027151	GGAGGCCACUGUCCGAUGU
B05	***Dctn2***	69654	NM_027151	GAGCCAGACGUUUAUGAAA
B06	***Myl3***	17897	NM_010859	UUUGAUGCCUCCAAGAUUA
B06	***Myl3***	17897	NM_010859	CAAGGACACUGGCACGUAC
B06	***Myl3***	17897	NM_010859	GCGAGAUGAAGAUCACAUA
B06	***Myl3***	17897	NM_010859	GGUGAGAGACUGACAGAAG
B07	***Dynll1***	56455	NM_019682	GACAAGAAGUACAACCCUA
B07	***Dynll1***	56455	NM_019682	GCAGACAUGUCGGAAGAGA
B07	***Dynll1***	56455	NM_019682	UACAACAUCGAGAAGGAUA
B07	***Dynll1***	56455	NM_019682	CUUCGGUAGUUAUGUGGCA
B08	***Rab7***	19349	NM_009005	GUACAAAGCCACAAUAGGA
B08	***Rab7***	19349	NM_009005	AAACAACAUUCCUUACUUC
B08	***Rab7***	19349	NM_009005	AAACAAGAUUGACCUGGAA
B08	***Rab7***	19349	NM_009005	AAGUGGAACUGUACAAUGA
B09	***Myo9b***	17925	NM_015742	CAACCGGACACGGGAAUUA
B09	***Myo9b***	17925	NM_015742	GAACCGAAAUCGCAAAGUU
B09	***Myo9b***	17925	NM_015742	CCAAUGAGCUCAAGUUUCU
B09	***Myo9b***	17925	NM_015742	CAGGAAGACUCUAGACGUA
B10	***EG231836***	231836	XM_144611	GAGCGGACCUUUAUAUUUG
B10	***EG231836***	231836	XM_144611	GGAUACAACACGACCAUUU
B10	***EG231836***	231836	XM_144611	UGAGGGAGAUGGAACCCAA
B10	***EG231836***	231836	XM_144611	GCAGGUGACCAGUGAGGAA
B11	***Myh7b***	668940	NM_001085378	GGACAGAGCUCUUUCGACU
B11	***Myh7b***	668940	NM_001085378	ACAAAUGGCUCCCGGUCUA
B11	***Myh7b***	668940	NM_001085378	CACAAUUUCUGGCGACAAA
B11	***Myh7b***	668940	NM_001085378	GCAUGGAGGUGGACGAUCU
C03	***Myo10***	17909	NM_019472	ACAAUUCCCUGGACUACUA
C03	***Myo10***	17909	NM_019472	GCAAUGCGAAGACAGUAUA
C03	***Myo10***	17909	NM_019472	GUACAUGAAAGGUGGCUUA
C03	***Myo10***	17909	NM_019472	AGACCCAACUCAUUUGUGA

C04	***Klc2***	16594	NM_008451	GCGAGGAGAGCAAGGAUAA
C04	***Klc2***	16594	NM_008451	GGACGGGUCUUUCUGACAG
C04	***Klc2***	16594	NM_008451	CAAUGAAGAUGAACAGAGC
C04	***Klc2***	16594	NM_008451	CCACAGGAGCCUAACUCUA
C05	***Mylc2b***	67938	NM_023402	GCGCGAAAGACAAAGAUGA
C05	***Mylc2b***	67938	NM_023402	GCGCGCAACCUCCAAUGUG
C05	***Mylc2b***	67938	NM_023402	GGGAACUUCAACUACAUUG
C05	***Mylc2b***	67938	NM_023402	UCGCUUGCUUUGAUGAGGA
C06	***Rab10***	19325	NM_016676	GGAAUAGACUUUAAGAUCA
C06	***Rab10***	19325	NM_016676	CAAGAGAGUUGUACCGAAA
C06	***Rab10***	19325	NM_016676	CACAUUAGCUGAAGACAUC
C06	***Rab10***	19325	NM_016676	UAGAUGAGCAUGCCAAUGA
C07	***Bicd1***	12121	NM_009753	GAUGAAAUCCGAGAAUAUA
C07	***Bicd1***	12121	NM_009753	CCAAAUGUAUGAUGAACAA
C07	***Bicd1***	12121	NM_009753	GAAGUGAGCCAAAUAACGA
C07	***Bicd1***	12121	NM_009753	UUACAAAUGUCCAGGCAGA
C08	***Coro1c***	23790	NM_011779	GAUCAAAUCCAUAAAGGAA
C08	***Coro1c***	23790	NM_011779	GACCGAGCCUGUGGUGAUU
C08	***Coro1c***	23790	NM_011779	CAAUUGCUCUCCAUGAAAU
C08	***Coro1c***	23790	NM_011779	GAAAGUGCGAGCCCAUUAU
C09	***Dynlt3***	67117	NM_025975	CCCAUAAUAUAGUCAAAGA
C09	***Dynlt3***	67117	NM_025975	GGUGGUAACGAUUAUAAUG
C09	***Dynlt3***	67117	NM_025975	GGGGAAAGCUUACAAGUAC
C09	***Dynlt3***	67117	NM_025975	CAGAGGAGCCCGUAUGGAU
C10	***Cenpe***	229841	NM_173762	GAAGAGCUCCAUAUAAUAA
C10	***Cenpe***	229841	NM_173762	GAUUAUGAGUGCUUGAAUA
C10	***Cenpe***	229841	NM_173762	GAUAGCAAAUUGACACGAA
C10	***Cenpe***	229841	NM_173762	GAACUUAACCUUGCUCGUU
C11	***Myo16***	244281	XM_356059	GGAAACAUCCCUUUAGAUU
C11	***Myo16***	244281	XM_356059	CAUCACAACUCACGAAAUC
C11	***Myo16***	244281	XM_356059	GAGUGUAGAUCUAUGAAUC
C11	***Myo16***	244281	XM_356059	GGACUUCACCUUAAUAACU
D03	***Dync1li2***	234663	NM_001013380	GAAGAUGGUUCUGGUAAGA
D03	***Dync1li2***	234663	NM_001013380	UAAAGAAGCCAGAUCCAAA
D03	***Dync1li2***	234663	NM_001013380	GAAAGCUGGUCCAUGACAA
D03	***Dync1li2***	234663	NM_001013380	UUACAACCGUGAAGCCAGA
D04	***Kif21b***	16565	NM_019962	GGGUAAAGCUGUGGAAUUA
D04	***Kif21b***	16565	NM_019962	GAACCAGUCUCGCUAUGAA
D04	***Kif21b***	16565	NM_019962	CAACGUGGUUUCUAUCAAA
D04	***Kif21b***	16565	NM_019962	CAAACUGACUGGCCACAUU
D05	***Dync1i1***	13426	NM_010063	GGAAGGGGCUGUUGAGUUA
D05	***Dync1i1***	13426	NM_010063	GCAUUUGGAUCUAUGAUGU
D05	***Dync1i1***	13426	NM_010063	CCACAAUGCUCGCAACCUG
D05	***Dync1i1***	13426	NM_010063	GACAAUCGCAGUCAUCGAA
D06	***Kif26b***	269152	NM_177757	GCGAGGAUCUGGAGUGCUA
D06	***Kif26b***	269152	NM_177757	GAAAGCCUGUCGUCGGUGA
D06	***Kif26b***	269152	NM_177757	GAUCGCGUCGAGAGUCUUA
D06	***Kif26b***	269152	NM_177757	AAGACUAGAUUGCAUAGAU
D07	***Dynlrb2***	75465	NM_029297	GAACGAUGGUGGUCAAUGC
D07	***Dynlrb2***	75465	NM_029297	GGACAACUCCACAACGGUU
D07	***Dynlrb2***	75465	NM_029297	GAGAAUCCAGAGUCACAAA
D07	***Dynlrb2***	75465	NM_029297	AGAUCGAAGAAACAUGAAA
D08	***Kif2a***	16563	NM_008442	GUAAAGGAGUUUGGAAUUA
D08	***Kif2a***	16563	NM_008442	GAAAUGGUUUACAGGUUUA
D08	***Kif2a***	16563	NM_008442	UGAAGAAGCCAAACUAUAA

D08	***Kif2a***	16563	NM_008442	GGAAUGGCAUCCUGUGAAA
D09	***Mxd3***	17121	NM_016662	GGAGUUGACUGUACCCGAU
D09	***Mxd3***	17121	NM_016662	GCGCUCAGACUCAGACCAA
D09	***Mxd3***	17121	NM_016662	GGGCCAGGGUGCAUAUCCA
D09	***Mxd3***	17121	NM_016662	AGGAAAAGCUUCGCAGCAA
D10	***Myo1b***	17912	NM_010863	GAGCUUACCUGGAAAUCAA
D10	***Myo1b***	17912	NM_010863	GGACUCUGCUAAAGUUAAU
D10	***Myo1b***	17912	NM_010863	CAUCUAGAUUCGGCAAAUA
D10	***Myo1b***	17912	NM_010863	GAUCGGUGUUGGAGAUAUG
D11	***Kif15***	209737	NM_010620	GAACAACUGUCUCAAUUUA
D11	***Kif15***	209737	NM_010620	GAACAGACGUGUAGCAUCA
D11	***Kif15***	209737	NM_010620	GGACAACGCCAGAUUAGAA
D11	***Kif15***	209737	NM_010620	GGAUUCCUACGAUAACUUA
E03	***Osbpl1a***	64291	NM_020573	GGGAGAGACUUAUGAAUUA
E03	***Osbpl1a***	64291	NM_020573	GCACAGGACUGGAUUUAUU
E03	***Osbpl1a***	64291	NM_020573	GCAAGGAAUUACACAAAGU
E03	***Osbpl1a***	64291	NM_020573	CAACGAAGCAUACACAUGG
E04	***Kif1a***	16560	NM_008440	AGACAGAUUUCAUCCCUUA
E04	***Kif1a***	16560	NM_008440	GGAAGCACCACCACUAUUG
E04	***Kif1a***	16560	NM_008440	GAAGUGCGCGAGCUAGUUG
E04	***Kif1a***	16560	NM_008440	ACACAUAUGUCAACGGCAA
E05	***Rab8a***	17274	NM_023126	GAAUAAGUGUGAUGUGAAU
E05	***Rab8a***	17274	NM_023126	GAAGACCUGUGUCCUGUUC
E05	***Rab8a***	17274	NM_023126	GACCUACGAUUACCUGUUC
E05	***Rab8a***	17274	NM_023126	GAGCAGCCAUGGAGUCAAG
E06	***Kif12***	16552	NM_010616	CGUCGGAGCUCCUCACAUA
E06	***Kif12***	16552	NM_010616	GAACAUGCCAUAUGGGCUA
E06	***Kif12***	16552	NM_010616	GAUGUGGCGUUCCGCUUUG
E06	***Kif12***	16552	NM_010616	GCUAUUAGAUCGCGUGCAG
E07	***Kif3a***	16568	NM_008443	CAUGAUGUGUGCAAAUAUU
E07	***Kif3a***	16568	NM_008443	AGACUUAUCAGCAUAUGUA
E07	***Kif3a***	16568	NM_008443	CGACUAAUAUGAACGAGCA
E07	***Kif3a***	16568	NM_008443	CCUGAGACCGUAAUUGAUU
E08	***Kif11***	16551	NM_010615	GUAAAUGGCUGUUGUAAAG
E08	***Kif11***	16551	NM_010615	CAGCAGAGGUCUUCCAUUU
E08	***Kif11***	16551	NM_010615	GGAGAUCACUAAGAAAGUA
E08	***Kif11***	16551	NM_010615	GAAACAGGAUCUGAAACUA
E09	***Arl8c***	67166	NM_026011	GAUAGAAGCCUCUCGAAAU
E09	***Arl8c***	67166	NM_026011	UAAAGGCAACGUCACAAUA
E09	***Arl8c***	67166	NM_026011	GAUAGAUGCUGCAGAUCGA
E09	***Arl8c***	67166	NM_026011	UAGAGAAAUUUGCUGCUAU
E10	***Kif13b***	16554	XM_283218	GUACUUAGAUGCUGCCUUA
E10	***Kif13b***	16554	XM_283218	CAGCCUACCUUCUCAGAUA
E10	***Kif13b***	16554	XM_283218	GAACAUGGAUUGGUGUGGA
E10	***Kif13b***	16554	XM_283218	GUGCGGACCUCAGAGCUUA
E11	***Kif7***	16576	XM_133575	AAAGAGAGCAUCCAGAUUA
E11	***Kif7***	16576	XM_133575	GAAUGAGGCUAUCACAUGC
E11	***Kif7***	16576	XM_133575	GGUCGACACAUGUGGAUAA
E11	***Kif7***	16576	XM_133575	GAUGAUCGACGUCAGGAAA
F03	***Dctn1***	13191	NM_007835	GGACAGCGCUGCCAAGGAU
F03	***Dctn1***	13191	NM_007835	CAAAGGUCCUCAAGAGAGA
F03	***Dctn1***	13191	NM_007835	GAGCAAGCCUCCUCCGGUU
F03	***Dctn1***	13191	NM_007835	CACGAGCGCUCCUUAGAUU
F04	***Dynll2***	68097	NM_026556	ACAAAGCACUUCAUCUAUU
F04	***Dynll2***	68097	NM_026556	GCAGCUAUGUCACACACGA

F04	***Dynll2***	68097	NM_026556	AACCCUACCUGGCAUUGUA
F04	***Dynll2***	68097	NM_026556	GCCUAUAUCAAGAAGGAAU
F05	***Myh2***	17882	NM_144961	CCACGAACCCAUAUGAUUA
F05	***Myh2***	17882	NM_144961	GCGGAAAGAAGCUACCAUA
F05	***Myh2***	17882	NM_144961	CCGGUGCUGUGAUGCAUUA
F05	***Myh2***	17882	NM_144961	GCGCUGGUAUCUCAGUUAU
F06	***Dync2li1***	213575	NM_172256	GGACGGAGCUGAAAUCGGA
F06	***Dync2li1***	213575	NM_172256	GGCAUUCGGUAUUGAUAAA
F06	***Dync2li1***	213575	NM_172256	GUAGAGAAACGGAGAAGUC
F06	***Dync2li1***	213575	NM_172256	CAACCAUUAUCCUAAGGUG
F07	***Kifc3***	16582	NM_010631	GGAAGUGGCUGAGAACAAA
F07	***Kifc3***	16582	NM_010631	GGGCUCAGAUUGCCAUGUA
F07	***Kifc3***	16582	NM_010631	CACGUGAGAUUUACAAUGA
F07	***Kifc3***	16582	NM_010631	GGAAACAUCCGGGUGAUUG
F08	***Myh1***	17879	XM_354615	UGAAAGAACUCACUUAUCA
F08	***Myh1***	17879	XM_354615	GAAGCCGGAUCUAAUCGAA
F08	***Myh1***	17879	XM_354615	GCAGAGAUAUAAGGUUUUA
F08	***Myh1***	17879	XM_354615	GAACAGAAGCGCAACGUGG
F09	***Dnhd1***	77505	XM_355968	CAAUAUGUCUGUCGAAUUA
F09	***Dnhd1***	77505	XM_355968	GCAUGAGCGUCAAGUAUUU
F09	***Dnhd1***	77505	XM_355968	GCAGAUACCUAUGAAGCUA
F09	***Dnhd1***	77505	XM_355968	GGAGAAUGAUCACAGUCUA
F10	***Rab5a***	271457	NM_025887	AAACAAAGCUGACUUAGCA
F10	***Rab5a***	271457	NM_025887	GGUCAAGAACGGUAUCAUA
F10	***Rab5a***	271457	NM_025887	GCACAAGCAGCCAUAGUUG
F10	***Rab5a***	271457	NM_025887	GGCCAAAUACUGGAAAUAA

Six additional wells were used for the negative siRNA controls (B2, C2, D2 and E2 treated with a non-targeting siRNA pool and F2 and G2 left untransfected) and six were treated with 1 mM EHNA together with the two probes (B12, C12, D12 and E12 pre-treated with a non-targeting siRNA pool and F12 and G12 left untransfected before the treatment with EHNA).

2.1.7 Bacterial strains

E. coli strain:	Application:
XL-1 Blue	cloning/plasmid purification
TG1	protein expression

2.1.8 Mouse ES cell lines.

The HB9-GFP mouse ES cell line was a gift from Jessell and Wichterle (Columbia University, New York, USA) (Wichterle et al., 2002), and the homozygous and heterozygous *Bicd1* gene trapped ES cell lines were provided by Krzysztof Wicher and David Ish-Horowicz (Developmental Genetics laboratory at the CRUK, London Research Institute).

2.2 Methods

All experiments performed on mouse primary neurons followed the guidelines of the UK Home Office (Animal Scientific Procedures Act 1986) and were approved by the CRUK London Ethical Committee.

2.2.1 Bacterial cultures

2.2.1.1 Preparation of electrocompetent bacteria

Bacteria E. coli XL1Blue were grown in 5 ml of Luria Bertani (LB) medium overnight at 37°C, inoculated in an additional 800 ml of LB medium and incubated at 37°C until an optical density at 600 nm (OD_{600}) of 0.6 was reached. Bacteria were pelleted at 4°C at 5000 rpm for 20 min using a JA-10 rotor (Beckman), washed with 500 ml of ice-cold water, followed by 40 ml of ice-cold water with 10% v/v glycerol. Finally, the pellet was re-suspended in 1 volume of ice-cold water with 10% v/v glycerol and stored at -80°C.

2.2.1.2 Bacterial transformation

80 μl of competent bacteria (**section 2.2.1.1**) were transferred to a 1 mm electroporation cuvette (Flowgen) and 50 – 500 pg of DNA were added. Bacteria were then incubated at 4°C for 10 min and electroporated at 200 Ω, 25 μF and 1.8 kV. After electroporation, 400 μl of SOC medium was added to the bacteria and incubated under shaking at 37°C for 30 min. Finally, the bacteria were centrifuged at 3000 rpm using a JA-10 rotor (Beckman) for 1 minute, re-suspended in 100 μl of LB medium and transferred on LB-Agar plates containing the appropriate antibiotic.

2.2.2 Nucleic acid techniques

2.2.2.1 Reverse transcription polymerase chain reaction (RT-PCR)

The RT-PCR for TrkA (Chapter 6**, Figure 6.2**) was performed by Dr. M. Golding, Molecular NeuroPathobiology laboratory at CRUK, London Research Institute. Total RNA was extracted using the RNeasy mini kit (Qiagen) according to the manufacturer's instructions. cDNA for the RT-PCR reactions was generated from 2 μg of total RNA using the SuperScript®VILO™ cDNA synthesis kit (Invitrogen) according to the manufacturer's instructions. The PCR reaction was performed from 10 ng (equivalent to RNA) of cDNA template using the MegaMix Blue Kit (Microzone) using the following parameters:

1 cycle	denaturation	94°C 2 min
30 cycles	denaturation	94°C 30 s
	annealing/extension	72°C 40 s

2.2.2.2 Quantitative reverse transcription polymerase chain reaction (Q-PCR)

The Q-PCR experiments were performed by Dr. M. Golding, Molecular NeuroPathobiology laboratory at CRUK, London Research Institute. Total RNA was extracted using the RNeasy mini kit (Qiagen) according to the manufacturer's instructions. cDNA for the Q-PCR reactions was generated from 2 μg of total RNA using the SuperScript®VILO™ cDNA synthesis kit (Invitrogen) according to the manufacturer's instructions. The Q-PCR was performed with a 7500 Real-Time PCR system (Applied Bioscience) using the SYBR® GreenER™ Reagent System

(Invitrogen) according to the manufacturer's instructions. The data were normalised to the CT (cycle at threshold) values of the βIII tubulin control. The parameters of the Q-PCR reaction were the following:

Stage	Repetitions	Temperature	Time
Denaturation	1	95˚C	20 s
Annealing/extension	40	95˚C	03 s
		60˚C	30 s
Dissociation	1	95˚C	15 s
		60˚C	60 s
		95˚C	15 s
		60˚C	15 s

2.2.2.3 DNA agarose gel electrophoresis

Agarose gels were prepared by dissolving 1-2% agarose in Tris-acetate EDTA (TAE) buffer (40 mM Tris-OH pH 8.0, 20 mM glacial acetic acid, 1 mM EDTA) or Tris-borate EDTA (TBE) buffer (90 mM Tris-OH, 90 mM boric acid, 2 mM EDTA pH 8.0). Ethidium bromide was added to a final concentration of 0.5 μg/ml. DNA samples were mixed with 10X loading buffer (10% Ficoll 400, 25% glycerol, 10 mM Tris-HCl ph 7.6, 1 mM EDTA, 0.25% Bromophenol blue) and run at 80-150 V/cm in TAE or TBE buffer.

2.2.2.4 Isolation of plasmid DNA

Plasmid DNA was purified using the QIAprep® Spin Mini Prep Kit, or the QIAfilter™ Plasmid Maxi Kit from Qiagen® according to manufacturer's instructions.

2.2.2.5 Nucleic acid quantification

DNA was diluted in water and its optical density at 260 (OD_{260}) and 280 nm (OD_{280}) was measured using a Nanodrop® spectrophotometer (Labtech International). 1

unit of OD_{260} corresponds to 50 mg/ml of double-stranded DNA. The OD_{280} is used for quality control of the purified DNA, because proteins have their maximum absorption at 280 nm; an OD_{260}/ OD_{280} ratio below 1.8 indicates a low level of purity of the DNA preparation.

2.2.3 Protein techniques

2.2.3.1 Cell lysis

Cells were scraped on ice in phosphate buffer (PBS; 137 mM NaCl, 2.7 mM KCl, 4.3 mM Na_2HPO_4, 1.47 mM KH_2HPO_4, pH 7.6) and centrifuged at 1200 *g* for 5 min. The cell pellet was then re-suspended in lysis buffer (10 mM Tris-HCl, pH 8.0, 150 mM KCl, 1% NP-40, 1% glycerol, 1mM EDTA, 0.1 mM Dithiothreitol (DTT) and protease inhibitor cocktail (Roche), pH 7.6) and incubated at 4°C for 30 min. The extract was subsequently spun at 16,000 *g* for 20 min and the pellet was discarded.

2.2.3.2 Protein quantification

The protein concentration was determined using the BIO-RAD Protein Assay Reagent. One ml of the BIO-RAD Protein Assay Reagent diluted 1:4 in water was incubated with incremental dilutions of Bovine Serum Albumine (BSA) at room temperature for 5 min. The absorbance at 595 nm was measured with a spectrophotometer (Bio Photometer, Eppendorf) and used to create a standard curve. Samples containing 1 μg of protein were mixed with the BIO-RAD Protein Assay Reagent (1:4 in water) and incubated at room temperature for 5 min. Their absorbance at 595 nm was then measured and the protein concentration of the sample was inferred on the basis of the BSA standard curve by linear regression.

2.2.3.3 SDS-Polyacrylamide Gel Electrophoresis (SDS-PAGE)

Protein samples were diluted in sample buffer (20% glycerol, 5% β-mercaptoethanol, a pinch of Bromophenol blue, 10% SDS, 120 mM Tris-HCl pH 6.8) and incubated for 10 min at 65°C or boiled for 5 min. Samples were loaded on a pre-cast 4-12% NuPAGE® Bis-Tris minigel (Invitrogen) and the gel run at 200 V in 2-(N-Morpholino)ethanesulfonic acid sodium salt (MES) buffer (Invitrogen) for an hour. Where appropriate, gels were stained with Coomassie blue (50% methanol, 10% acetic acid, 0.1% Coomassie Brilliant Blue) for 15 min at room temperature and de-stained in water overnight.

2.2.3.4 Western Blotting

Proteins were transferred from precast 4-12% NuPAGE® Bis-Tris minigel onto a methanol-activated Polyvinylidene fluoride (PVDF) membrane (PROTEAN®) in Transfer Buffer (Invitrogen) supplemented with 20% methanol at 300 mA for an hour. PVDF membranes were subsequently stained with Ponceau S to monitor the efficiency of the protein transfer. The membrane was then de-stained in water and blocked in a solution of 5% skimmed milk (Marvel) in PBS containing 0.05% Tween-20 for 30 min at room temperature. The membrane was incubated with the primary antibody diluted in PBS containing 0.05% Tween-20 for a period of time ranging from 1 hour (room temperature) to overnight (4˚C), depending on the primary antibody used. The membrane was then washed in PBS containing 0.05% Tween-20 and incubated with the appropriate HRP-conjugated secondary antibody in 5% skimmed milk (Marvel) in PBS, 0.05% Tween-20. After extensive washing in PBS, 0.05% Tween-20, the immunoreactivity was detected using enhanced chemoluminescence (ECL, GE

Healthcare), following the manufacturer's instructions and developed on high performance chemoluminescence films (GE Healthcare).

2.2.3.5 Purification of GST-recombinant H_C

A version of H_C containing a tetracysteine tag (AEAAAREACCRECCAREAAAR, (Bohnert and Schiavo, 2005)) at its N-terminus and cloned in a pGEX-4T3 vector was electroporated into the E. coli strain TG1 (**section 2.2.1.2**) and plated on ampicillin-containing LB-Agar plates. A single transformed colony was then picked and inoculated into 200 ml of 2YT medium containing 100 μg/ml ampicillin overnight at 37°C. This preculture was then diluted to 2 L with 2YT medium containing 100 μg/ml ampicillin and grown at 37°C until an OD_{600} of 0.8 was reached. Protein expression was induced for 4 h at 30^0C by adding 1 mM isopropyl-β-D-thiogalactopyranoside (IPTG). Bacteria were subsequently pelleted by centrifugation at 1000 *g* for 10 min, resuspended in ice cold PBS and centrifuged again at 1000 *g* for 15 min. Finally, bacteria were resuspended in ice cold PBS, transferred into a 50 ml Falcon tube and pelleted again at t 1000 *g* for 15 min, snap frozen in liquid nitrogen and stored at -80˚C.

The bacterial pellet was thawed on ice and re-suspended in PBS with 0.05% Tween-20 supplemented with protease inhibitor cocktail (Roche). The mixture was then subjected to two cycles of snap-freezing and thawing and sonicated three times at maximum amplitude for 15 seconds. The resulting lysate was ultracentrifuged for 30 min at 28000 rpm using a SW40 Ti rotor (Beckman). The supernatant was absorbed onto 2.5 ml 50% glutathione-agarose beads (Sigma) per L of bacterial culture for 2 h at 4°C. Beads were then incubated at 37˚C for 10 min and washed twice with DNA K

buffer (50 mM Tris-HCl, pH 7.4, 2 mM ATP, 10 mM $MgSO_4$). The resin was further washed with PBS, 0.05% Tween-20 and with PBS, 0.05% Tween-20, 0.5 M NaCl. Finally, H_C was cleaved from the GST by incubating the resin with 100 μl of thrombin (0.8 U/mg) in 2.5 ml of TCB buffer (50 mM Tris-HCl pH 8.0, 150 mM NaCl, 0.1% β–mercaptoethanol) for 30 min at room temperature. Cleaved H_C was eluted from the beads in 2.5 ml of TCB followed by 2.5 ml of TCB, 0.5 NaCl. The eluate was pooled together, dialysed against 20 mM HEPES-NaOH pH 7.4, 150 mM NaCl, snap-frozen in liquid nitrogen and stored at -80^{0}C.

2.2.3.6 Fluorescent labelling of H_C with AlexaFluor dyes

15 nmol of purified H_C (**section 2.2.3.5**) were first added to labelling buffer (20 mM HEPES-NaOH pH 7.4, 250 mM NaCl) containing 10X molar excess of tris-(2-carboxyethyl)phosphine hydrochloride (TCEP) and then the solution was mixed with 25X molar excess of 555 AlexaFluor-maleimide (Invitrogen) in DMSO. The reaction mixture was subsequently incubated at 4^{0}C overnight. The cross-linking reaction was stopped by adding 4 mM reduced glutathione in Tris-HCl, pH 8.0 and the labelled protein was dialysed over three days against ice cold PBS at 4°C. Finally AlexaFluor conjugated H_C was aliquoted, snap-frozen in liquid nitrogen and stored at -80^{0}C.

2.2.3.7 Fluorescent labelling of the $p75^{NTR}$ antibody

$p75^{NTR}$ antibody against the extracellular domain of the receptor (batch 5410, 1.8 mg/ml) was dialysed against PBS for 48 h at 4°C; 100 μl of the dialysed antibody were then mixed with 10 μl of 1M $NaHCO_3$ and AlexaFluor488-carboxylic acid, tetrafluorophenyl (TFP) ester. The reaction mixture was left at room temperature for 1 hour and subsequently dialysed against PBS at 4°C for 24 h with frequent changes of

buffer. The conjugated AlexaFluor 488 $p75^{NTR}$ was then aliquoted and stored at 4°C.

2.2.3.8 Conjugation with 10 nm gold nanoparticles

100 μg of purified H_C (**section 2.2.3.5**) were applied drop wise to 10 ml of a suspension of 10 nm gold particles at pH 6.7, which corresponds to the pI of H_C. The solution was left stirring at 4°C for 30 min to allow the formation of aggregates and the pH was subsequently raised to 9.0 with 0.2 M $NaCO_3$. BSA was then added to a final concentration of 1% and the mixture was stirred for another 15 min at 4°C. The suspension was finally pelleted at 45000 *g* for 30 min, resuspended in 1 ml of storage buffer (20 mM Tris-OH pH 8.2, 150 mM NaCl, 1% BSA) and stored at 4°C.

2.2.4 Tissue culture techniques

2.2.4.1 Coating of the plates for motor neurons cultures

The plates and coverslips for primary and ES derived MNs were coated over night with poly-ornithine (1.5 mg/ml) diluted in milliQ water. The poly-ornithine was then removed and laminin diluted in Neurobasal medium was added for two h. Just before plating, the laminin solution was removed and MNs were plated in full medium.

2.2.4.2 Isolation of mouse spinal cord motor neurons

Spinal cord MNs were purified from E11.5 – E13.5 mouse embryos (Arce et al., 1999). Spinal cords were dissected out, removing the meninges and the dorsal horns. The ventral horns of the spinal cord were then minced and dissociated by incubation with 0.025% trypsin in PBS for 10 min at 37°C. Following dissociation, the cells were triturated in Leibovitz 15 (L-15) medium containing 0.02 mg/ml of DNAse and 0.4% of BSA. Two ml of BSA cushion (4% embryo-tested BSA in L-15) were applied with a

glass pipette at the bottom of the cell suspension, which was then spun for 5 min at 470 *g*. The resulting MN pellet was resuspended in full medium (**section 2.2.4.3**) and plated on poly-ornithine/laminin-coated dishes.

2.2.4.3 Maintenance of primary motor neuron cultures

MN cultures were maintained at 37^{o}C and 7.5% CO_2 in MN complete medium, composed of Neurobasal (Gibco-BRL), 2% v/v of B27 supplement (Gibco-BRL), 2% heat-inactivated horse serum, 1% GLUTAMAX^{TM} (Invitrogen), 25 μM β-mercaptoethanol, 10 ng/ml rat ciliary neurotrophic factor (CNTF) and 100 pg/ml rat glial-derived neurotrophic factor (GNTF) (both R&D Systems). MNs were used for experiments from day in vitro (DIV) 5 and maintained in culture for up to two weeks.

2.2.4.4 Culture of undifferentiated mouse ES cells.

ES cells are maintained in gelatinised flasks (0.1% of fish skin gelatin in distilled water applied to the flask for 10 min prior to seeding of the cells), without a feeder layer. The medium used for undifferentiated ES cell culture was composed of Glasgow MEM (GMEM), 5% ES cell-tested Foetal Bovine Serum (FBS), 5% Knockout Serum Replacement (KSR, Gicbo-BRL), 1% GLUTAMAX, 0.1 mM β-mercaptoethanol, and 1000 units/ml of leukocyte inhibitory factor (LIF).

ES cells were routinely passaged every other day due to their fast growth rate, thus avoiding acidification of the medium, overconfluency and the resulting differentiation of the ES cultures.

2.2.4.5 In vitro differentiation of ES cells into MNs

Undifferentiated ES cells were trypsinized with 0.05% Trypsin/EDTA for 5 min at room temperature. 1.5 x 10^6 cells were then centrifuged at 310 *g* per 5 min and re-suspended in differentiation (DNFK) medium (45% v/v Neurobasal, 22% v/v DMEM and F12, 1% v/v GLUTAMAX, 10% Knockout Serum Replacement, 0.1 mM β-mercaptoethanol). Resuspended cells were plated on a 10 cm Petri dish. Non tissue-culture treated plates allow the ES cells to grow in suspension and form Embryoid bodies (EBs).

The day after seeding the ES cells, the forming EBs were spun down and resuspended in 10 ml of fresh DNFK medium and plated on a new Petri dish. The following day, EBs were allowed to settle by gravity and re-suspended in fresh differentiation DFNK medium supplemented with 1 μM all-trans retinoic acid (RA) and 333 nM Sonic Hedgehog Agonist (SAG). The EBs were then maintained in DNFK medium with RA and SAG for 4 days (medium changed every other day) and finally dissociated (**section 2.2.4.6**).

2.2.4.6 Dissociation of embryoid bodies

EBs were allowed to settle down by gravity and then dissociated by incubation with 0.025% trypsin in PBS for 7 min at 37^{o}C. Following dissociation, cells were triturated in Leibovitz 15 medium (L-15) containing 0.02 mg/ml of DNAse and 0.4% of BSA. Two ml of BSA cushion (4% embryo tested BSA in L-15), were applied with a glass pipette at the bottom of the cell suspension, which was then spun for 5 min at 470*g*. The MN pellet was resuspended in full medium (**section 2.2.4.3**) supplemented with 1 μM all-trans retinoic acid and plated on poly-ornithine/laminin-coated dishes

2.2.4.7 Generation of *Bicd1*$^{gt/gt}$ ES cells.

Mouse ES cells with a gene-trap mutation in the first intron of *Bicd1* (clone RRP227) were obtained from the Mutant Mouse Regional Resource Centers. Homozygous *Bicd1*$^{gt/gt}$ cells were generated by Krzystof Wicher as previously describe (Lefebvre et al., 2001). Heterozygous cells were seeded at 30% confluency and grown in medium containing LIF and 1.5 mg/ml G418 for several days until distinct clones of antibiotic resistant cells appeared. Several clones were picked up into a drop of trypsin solution and seeded into separate wells of a 24-well plate and grown in the presence of 500 ng/ml G418. After reaching confluency, cells were trypsinised and half of them used to isolate RNA (**section 2.2.2.4**). For detection of loss of heterozygosity RT-PCR reactions were performed using the One-Step RT-PCR kit (Invitrogen), primers specific to wild type and *Bicd1*^{gt} alleles (section 2.1.4), and 35 cycles of amplification. Clones showing a 70% reduction of the wild type allele product were considered *Bicd1*$^{gt/gt}$ homozygous.

2.2.5 Imaging techniques

2.2.5.1 Immunocytochemistry and confocal imaging of fixed samples

Cells on coverslips were fixed in 4% paraformaldehyde (PFA) dissolved in PBS for 15-30 min at room temperature and then washed in PBS. After fixation, cells were permeabilised and blocked at the same time for 1 h at room temperature in a solution of 10% goat serum, 2% BSA, 0.25% fish skin gelatin, 0.1% Triton X-100 in PBS. For staining with the GD1b antibody and for the experiments performed to detect p75^{NTR} and TrkB on at the plasma membrane, cells were only blocked, without permeabilisation, in 10% goat serum, 2% BSA, 0.25% fish skin gelatin, in PBS. The

coverslips were subsequently incubated with the primary antibody diluted in 10% goat serum, 2% BSA, 0.25% fish skin gelatin, in PBS (**section 2.1.2**, for the dilutions) for 1 h to overnight at room temperature or at 4°C and then washed in PBS to remove the excess of primary antibody. Finally, coverslips were incubated with the appropriate AlexaFluor-conjugated secondary antibody diluted in 10% goat serum, 2% BSA, 0.25% fish skin gelatine, in PBS for 1 h at room temperature, washed in PBS and then in water, and mounted on Mowiol-488 prior to imaging. Cells were imaged with an upright or inverted Zeiss 510 confocal microscope using 40X or 63X oil immersion objective lenses with a numerical aperture of 1.4 and a phase contrast ring.

2.2.5.2 Immunocytochemistry and confocal images of fixed samples in a 96-well format

The plate was handled manually using a multichannel pipette. The 96-well plates were cooled on ice, acid-washed with isotonic solution at pH 2.0 (100 mM citrate-NaOH, 142 mM NaCl, pH 2.0) for 2 min and fixed with 4% PFA for 20 min, permeabilised and blocked at the same time for 1 h at room temperature in a solution of 10% goat serum, 2% BSA, 0.25% fish skin gelatin, 0.1% Triton X-100 in PBS and then washed once with PBS. The cells were then stained with a anti-rabbit AlexaFluor 647-conjugated secondary antibody diluted in 10% goat serum, 2% BSA, 0.25% fish skin gelatin, in PBS for 45 min at room temperature and then washed in PBS. Finally, each plate was sealed with a transparent plastic foil and images were acquired with an inverted 510 Zeiss Confocal microscope using the MTS macro as described in Chapter 3 (**section 3.4.1**). 16 stacks were acquired for each well.

2.2.5.3 Time-lapse imaging of H_C and $p75^{NTR}$ antibody

MNs derived from ES cells seeded on poly-ornithine and laminin-coated MatTek dishes (MatTek Corporation) at 4 days after dissociation of the EBs were incubated for 30 min at 37°C with either 20 nM AlexaFluor 555 conjugated H_C (**section 2.2.3.6**) or 0.9 μg/ml AlexaFluor 647-conjugated $p75^{NTR}$ 5410 antibody (**section 2.2.3.7**) in the presence of 100 ng/ml of NGF diluted in full medium (**section 2.2.4.3**). Cells were subsequently washed and incubated for 15 min at 37°C with imaging medium (DMEM with low bicarbonate and without phenol red, folic acid, riboflavin, penicillin and streptomycin). MatTek dishes were then placed in an environmental chamber, kept at 37^0C, and imaged with a Zeiss 510 inverted confocal microscope equipped with a 63X Plan Apochromat oil immersion objective, with a NA of 1.4. Images were collected every 4 seconds with a pinhole aperture of 1.5 μm.

2.2.5.4 Transmission electron microscopy

The handling of the samples and the acquisition of the images were performed by Ken Blight, Electron Microscopy Unit at CRUK, London Research Institute. MNs plated on coverslips were fixed in 2.5% glutaraldehyde, 4% PFA in Sorensen phosphate buffer at room temperature for 20 min. Samples were then post-fixed in osmium tetroxide, stained with tannic acid and dehydrated progressively up to 100% ethanol. Finally, coverslips were embedded in an EPON epoxy resin, cut in thin sections (70-75 nm) and stained with lead citrate. Images of the stained sections were acquired using a Tecnai Spirit Biotwin (FEI) transmission electron microscope.

2.2.6 Cell-based assays

2.2.6.1 Transfection of MNs

2.2.6.1.1 Electroporation of primary MNs

The PA-4000/PA-96 WS Pulse Agile® (Labtech) and the BTX ECM 830 (Harvard Apparatus) systems were used to electroporate primary MNs. $3x10^5$ primary MNs per well were resuspended in siPORT (Ambion) electroporation buffer and plated on a 96-well plate provided by the supplier of the electroporation apparatus (custom built to accommodate the electrodes). SiGLO siRNA (Dharmacon) was added to the cell suspension at a concentration of 1.5 μM per well. Subsequently, cells were electroporated (Chapter 3, **table 3.1** for the electroporation parameters) and left at 37°C for 12 min to recover. The cell suspension was then seeded on coverslips into a 24-well plate in a volume of 500 μl of full medium (**section 2.2.4.3**).

2.2.6.1.2 Transfection of MNs with Dharmafect 3

2.5 μl VAMP2 siRNA pool (Dharmacon) from a 20 μM stock (100 nM final concentration) were diluted in 47.5 μl of full MN medium without serum (**section 2.2.4.3**) and incubated for 5 min at room temperature. At the same time 1.5 μl of Dharmafect 3 were diluted in 48.5 μl of full MN medium without serum (**section 2.2.4.3**) and incubated for 5 min at room temperature. The two mixtures were then mixed together and incubated at room temperature for 20 min. The transfection mixture was subsequently applied drop-wise to MNs plated on poly-D-ornithine and laminin-coated coverslips in a 24-well plate (400 μl of full MN medium without serum plus 100 μl of the transfection mixture per well). The medium was changed 4-5 h later to full medium (**section 2.2.4.3**).

2.2.6.1.3 Transfection of MNs with Dreamfect Gold in a 96-well plate format

The transfection protocol described below was used with the reagents listed in **table 2.2** for transfection reagent optimisation described in Chapter 3, (**section 3.3.2**). The siRNA was diluted to a final concentration of 50 nM in 10 μl of Opti-MEM (Invitrogen) medium. 0.25 μl of Dreamfect Gold were diluted in 9.75 μl of Opti-MEM (Invitrogen) medium per well. The two mixtures were then mixed together and incubated at room temperature for 20 min to 1 h in the 96-well plate (20 μl of the transfection mixture per well). 30000 – 35000 MNs dissociated from EBs were then plated on the top of the transfection mixture in full medium with serum (**section 2.2.4.3**). The medium was not changed for 3 days until the assay for the siRNA screen was performed.

2.2.6.2 Binding of H_C

MNs plated on poly-D-ornithine and laminin-coated coverslips were cooled on ice for 15 min and incubated with with 20 nM AlexaFlour 555 conjugated H_C in full medium (**section 2.2.4.3**) for 15 min at 4°C. Unbound H_C was then removed by rinsing the cells in PBS several times. Cells were fixed in 4% PFA diluted in PBS for 20 min at 4°C and stained as described in **section 2.2.5.1**.

2.2.6.3 Internalisation assay of H_C and $p75^{NTR}$ antibody

MNs plated on poly-D-ornithine and laminin-coated coverslips were incubated in full medium (**section 2.2.4.3**) with 20 nM AlexaFlour 555 conjugated H_C together with the $p75^{NTR}$ antibody (18 μg/ml) for 15-120 min at 37°C. To remove the probes bound to the plasma membrane, cells were cooled on ice for 10 min and acid-washed

with an isotonic solution at pH 2.0 (100 mM citrate-NaOH, 142 mM NaCl, pH 2.0) for 5 min at 4°C. The acid-wash solution was then removed by rinsing the cells in PBS several times. Cells were then fixed in 4% PFA diluted in PBS for 20 min at room temperature and stained as described in **section 2.2.5.1**.

2.2.6.4 Readout of the siRNA screen

First, the 96-well plates were coated with poly-D-ornithine and laminin (**section 2.2.4.1**), then the siRNA from the master plates of the library was premixed with the Dreamfect Gold transfection reagent and added to the plates using the reverse transfection protocol previously optimised (**section 2.2.6.1.2)**. EBs derived from the HB9-GFP ES cells were then dissociated (**section 2.2.4.6**) and the resulting cell suspension was plated on top of the transfection mixture (35,000 cells per well). The plates were left in the incubator at 37°C for 72 h and then incubated in Neurobasal medium with 20 nM AlexaFlour 555 conjugated H_C together with the $p75^{NTR}$ antibody (18 μg/ml) for 2 h at 37°C. In addition to H_C and the $p75^{NTR}$ antibody, 1 mM EHNA was added to selected samples (plate layout, **Figure 4.2**) pre-treated with RISC-free siRNA control (Qiagen). After the incubation, cells were cooled on ice for 10 min and acid-washed with an isotonic solution at pH 2.0 (100 mM Citrate-NaOH, 142 mM NaCl, pH 2.0) for 2 min and immuno-stained with an AlexaFluor 647 conjugated Rabbit secondary antibody (**section 2.2.5.2**).

2.2.6.5 BDNF signalling experiments

Wild type and *Bicd1*$^{gt/gt}$ MNs were starved for 5 h in Neurobasal medium and then stimulated with 100 ng/ml of BDNF. Cells were lysed after 10, 20, 30, 45 and 60 min in lysis buffer (10 mM Tris-HCl, pH 8.0, 150 mM KCl, 1% NP-40, 1% glycerol,

1mM EDTA, 0.1 mM Dithiothreitol (DTT) and protease and phosphatase inhibitor cocktail (Roche), pH 7.6) directly in the wells at 4°C for 30 min. The extract was subsequently spun at 16,000 *g* for 20 min and the pellet was discarded. Samples were prepared by diluting in sample buffer (20% glycerol, 5% β-mercaptoethanol, 2.5 mg Bromophenol blue, 10% SDS, 120 mM Tris-HCl pH 6.8), boiled for 5 min and analysed by western blot (**section 2.2.3.4**) for their phospho ERK1/2 and phospo Akt content.

2.2.7 Mouse Techniques

2.2.7.1 X-Gal staining

Embryos were fixed at room temperature for 15-30 min in 0.1 M sodium phosphate ($NaPO_4$, pH 7.3), 0.4% PFA, 5mM EGTA, 2 mM magnesium chloride ($MgCl_2$), at room temperature. Embryos were then washed three times in 0.1 M sodium phosphate ($NaPO_4$, pH 7.3), 2 mM magnesium chloride ($MgCl_2$), 0.1% sodium deoxycholate, 0.02% NP-40. Finally, embryos were transferred into glass vial and incubated with the developing solution (100 mM $NaPO_4$, pH 7.3, 2 mM $MgCl_2$, 0.01 sodium deoxycholate, 0.02% NP-40, 5 mM $K_3Fe(CN)_6$, 5 mM $K_4Fe(CN)_6$, 1 mg/ml X-Gal), for 30 min to 5 h at 37°C in the dark. Alternatively, embryos were left developing over-night in the fridge. The reaction was stopped by rinsing the specimen several times in PBS. Embryos were be post-fixed in 4% PFA and kept in 70% ethanol.

2.2.8 Data analysis and quantification

2.2.8.1 Quantification of the axonal retrograde transport of H_C and the $p75^{NTR}$ antibody

Motion Analysis software (Kinetic Imaging) was used to manually track time-lapse videos of the axonal retrograde transport of H_C and the $p75^{NTR}$ antibody. The

distance between the positions of an axonal carrier was used to determine its speed. Only organelles that could be followed for a minimum of three consecutive frames were included in the analysis (Lalli et al., 2003) (Bohnert and Schiavo, 2005).

2.2.8.2 Quantification of immunofluorescence staining

The use of the ARRAYSCAN image analysis software and of Cell Profiler will be discussed in Chapter 3, (**section 3.2.1** & **3.4.2**). Image J software was used to quantify immunofluorescence staining in all the experiments described in this thesis work except the siRNA screen and the validation re-screen. Image J was used to threshold the fluorescence staining of interest and quantify the thresholded voxels. Staining with neuronal-specific antibodies, such as βIII−tubulin or MAP2, was used to normalise for the neuronal population. Image J was also used to perform densitometric analysis of bands in western blot.

Chapter 3. Towards the siRNA screen

3.1 Introduction.

A primary focus of the Molecular Neuropathobiology laboratory is the investigation of the long range trafficking of neurotrophins and neurotrophin receptors in MNs. Two probes have been widely used in the past to achieve this goal, the H_C fragment of the Tetanus Neurotoxin and an antibody raised against the extracellular domain of $p75^{NTR}$. Both probes are taken up at the synaptic terminae of MNs and are then transported along the axon. These probes can be conjugated to a variety of fluorescent dyes, making it possible to directly follow their intracellular trafficking in live cells. H_C binds at the plasma membrane to a protein-ligand receptor complex which includes the polysialoganglioside GD1b (Rummel et al., 2003) and is internalised in a clathrin-dependent fashion (Deinhardt et al., 2006a). In contrast, the $p75^{NTR}$ recycles back to the plasma membrane at steady state, however, upon binding to its ligands NGF and BDNF, a pool of the receptor is internalised in a clathrin-dependent manner and undergoes axonal retrograde transport (Deinhardt et al., 2006b). Importantly, neurotrophins and neurotrophin receptors follow an axonal retrograde transport route shared by H_C and controlled by the small GTPases Rab5 and Rab7 (Deinhardt et al., 2006b).

In order to discover a new cohort of players in neurotrophin trafficking an siRNA screen was set up using a customised library of siRNA pools specific for 155 genes, including molecular motors and protein adaptors.

Aim of the work presented in this chapter

- *To establish a transfection method for MNs, which is efficient and suitable for a 96 well format.*

- *To establish a reliable method for the isolation of a large quantity of MNs from mouse ES cells to be used for the RNAi screen.*

- *To design a scalable assay to monitor the trafficking of H_C and $p75^{NTR}$.*

- *To optimise a high-throughput, high resolution automatic image acquisition protocol.*

- *To optimise the use of software for the quantitative analysis of the acquired images.*

3.2 Developing the readout for the screen.

The focus of my thesis work is discovering new players in the uptake and intracellular trafficking of H_C and $p75^{NTR}$, with particular attention to regulators of axonal retrograde transport. The physiologically relevant cell system to study the trafficking of H_C is MNs. However, screening for axonal transport of our probes in MN mass cultures and with an automated imaging system was technically very challenging. This was due to the manipulations required to adapt the live imaging assay used in the laboratory to monitor axonal retrograde transport to a 96 well plate format. In addition, the transport is tracked manually by the operator and it was not feasible to design an algorithm to do it automatically, as is required to perform an siRNA screen. The use of compartmentalised microfluidic chambers, which separate axons from the cell bodies, allows to directly relate the accumulation of H_C and the $p75^{NTR}$ antibody to their axonal retrograde transport. However, they cannot be adapted to the multi-well format needed for a high-throughput screen. I decided, therefore, to shift the focus of the assay to monitor the internalisation and accumulation of H_C and $p75^{NTR}$ instead of their axonal retrograde transport.

An internalisation assay was established in which a fluorescently labelled version of H_C, together with an antibody directed against the extracellular domain of $p75^{NTR}$, was applied to the cells at 37°C. After a certain amount of time, MNs were incubated at 4°C with an acidic isotonic buffer at pH 2.0 (acid wash) in order to remove the labelled H_C and $p75^{NTR}$ antibody bound to the cell surface. Cells were then permeabilised and stained with an AlexaFluor dye conjugated secondary antibody,

which allows the detection of the internalised $p75^{NTR}$ antibody. The internalised probes were finally imaged by fluorescence microscopy.

3.2.1 Testing the ARRAYSCAN imaging system.

The aim of my project was to perform an innovative high-content imaged-based siRNA screen on MNs. To achieve this goal, I first considered the ARRAYSCAN imaging system present in the High Throughput Screening Facility at the LRI. The ARRAYSCAN is an epi-fluorescence microscope capable of acquiring several fields from each well of a 96 well plate in an automated fashion. It also operates proprietary software which is designed for multi-parametric analysis of the acquired images.

In order to determine the optimal concentration of H_C to use for the screen, the kinetics of internalisation of H_C and the $p75^{NTR}$ antibody were assessed by incubating primary MNs with different concentrations of the two probes at 37°C, then performing an acid wash, fixing the cells and staining them for the neuronal marker βIII-tubulin. The 96-well plate was then scanned by the ARRAYSCAN microscope using a 20X dry objective and the internalised probes were quantified by the software using the *neuronal profiling* and *spot count* algorithms. The *neuronal profiling* algorithm uses the βIII-tubulin antibody staining to draw a mask around the cell body and neurites which propagate from it. The software is designed to quantify the total and the average fluorescence intensity coming from this mask as well as counting the number, the length and the number of branching points of the neurites. The *spot count* algorithm identifies fluorescent spots, which represent internalised H_C or $p75^{NTR}$ antibody (**Figure 3.1**). The software is able to quantify several different parameters, such as the number, the intensity and the area of each spot. A concentration of 20 nM of the H_C and of 1.8 μg/ml

for the $p75^{NTR}$ antibody and an incubation time point of 45 minutes were chosen to test the detection limits or "range" of the assay, which enabled the ARRAYSCAN imaging system software to successfully discriminate between conditions in which the probes were internalised to conditions where their entry was prevented by incubating the cells on ice (negative control). The bigger the range, the greater the power of the system to detect subtle effects caused by knocking down candidate genes. The results of this internalisation experiment showed that the range of the assay was 4-5 fold for H_C and less than 1 fold for the $p75^{NTR}$ antibody with the *neuronal profiling* algorithm and 40 fold and 25 fold respectively using the *spot count* algorithm (**Figure 3.2**). The more sensitive *spot count* algorithm was therefore chosen for the quantification of the internalised H_C and $p75^{NTR}$ antibody.

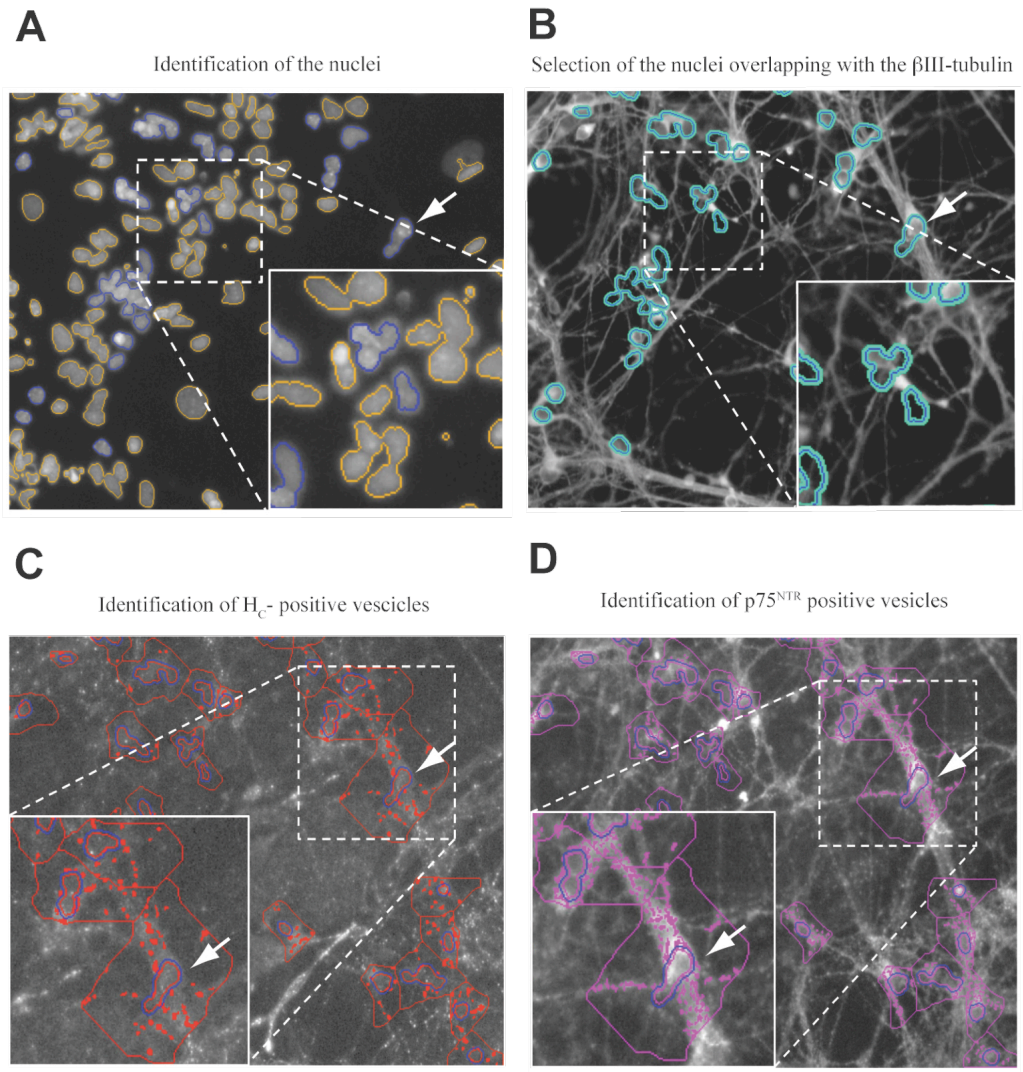

Figure 3.1. Use of the spot count algorithm to detect internalised H_C and $p75^{NTR}$ antibody.
4 images are acquired for each dataset: Hoechst, βIII tubulin, $p75^{NTR}$ antibody and H_C. Neurons are identified by combining the Hoechst and the βIII tubulin staining. All the nuclei are first identified from the Hoechst staining (B, accepted nuclei circled in blue), then a subset of nuclei corresponding to neurons are identified by overlap with the βIII tubulin staining (B, recognised neuronal nuclei in turquoise). The neuronal nuclei are then considered for the spot counting analysis. A circle of fixed diameter is drawn around each nucleus and inside this defined area vesicles positive for the individual probes are identified as spots (C for the $p75^{NTR}$ antibody, mask and identified spots in red, D for H_C, mask and identified spots in purple). An example of a nucleus recognised as belonging to a neuron is pointed to by an arrowhead. In the blown up panels in C and D it is shown how a circular mask is created around that nucleus. The identified positive vesicles are highlighted in red for $p75^{NTR}$ and violet for H_C.

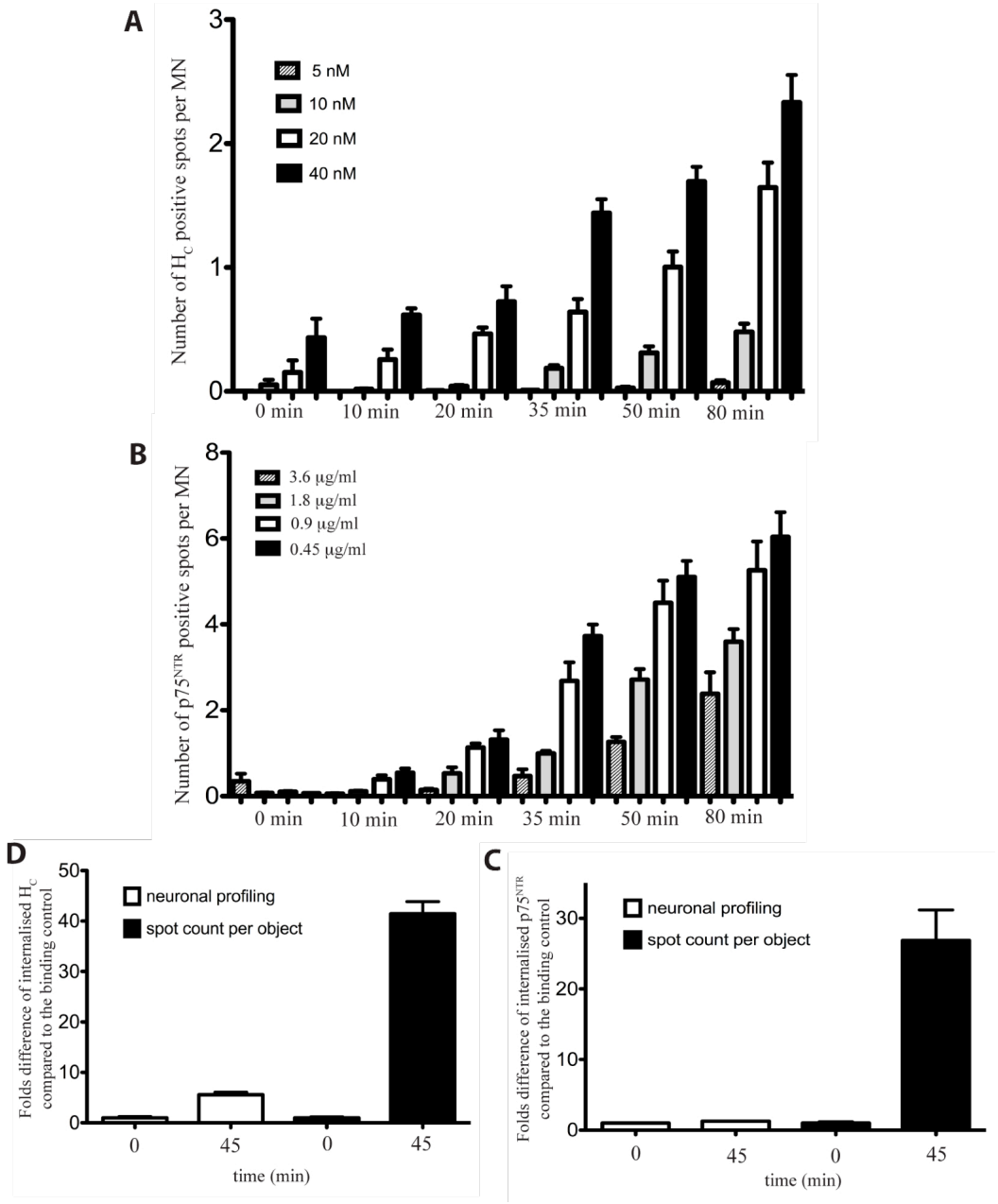

Figure 3.2. Quantification of H_C and $p75^{NTR}$ Ab internalisation with the ARRAYSCAN imaging system.

Kinetics of internalisation of H_C (A) and the $p75^{NTR}$ antibody (B) in primary MNs a 96-well plate. The probes were incubated together to simulate the conditions to be used for the screen; after each time-point the cells were acid-washed and fixed. The plate was scanned by the ARRAYSCAN imaging system and the spot count algorithm was used to quantify the amount of internalised probes for each time-point. As a negative control for internalisation MNs were incubated with H_C and $p75^{NTR}$ on ice and then acid-washed (binding control) (n=3). Two different algorithms were used to quantify the amount of internalised H_C (C) and $p75^{NTR}$ antibody (D), the neuronal profiling (white columns) and the spot count (black columns). In order to allow a direct comparison between the two quantification methods, the data were normalised to the value of the binding control. For both probes the spot count algorithm was the one with the better range (n=3).

3.3 Optimisation of transfection conditions and cell culture for the screen.

In order to perform an siRNA screen a protocol for performing RNA interference in MNs needed to be established. However, MNs are a notoriously difficult cell type to transfect. One of the best ways to achieve this goal in MNs has been to use viral transduction methodologies. Non-viral mediated transfection approaches such as lipid-based transfection reagents, or electroporation, however, have also proven to be effective in inducing RNA interference in cortical, hippocampal and sensory neurons.

Several transfection methods for MNs have been tested previously in the laboratory (Katrin Deinhardt Ph.D. thesis), including the use of lipid transfection reagents such as Lipofectamine2000, calcium phosphate and the Gene Gun (Bio-Rad), but none of these proved to be reliable or reproducible. Finally a transfection method for plasmid DNA using nuclear microinjection was established for single cell analysis (Katrin Deinhardt Ph.D. thesis). This transfection method, though, is not suitable for the format and the scope of an siRNA screen.

3.3.1 Electroporation and the use of the lipid-based transfection reagent Dharmafect 3.

Arnauld Jaquier and Georg Haase developed a siRNA electroporation technique to allow efficient knock-down of Alsin in embryonic rat spinal cord MNs. They electroporated E14 rat spinal MNs using an siRNA concentration of 4 mM, obtaining a reduction in the levels of Alsin transcript to 21% one day after transfection (Jacquier et al., 2006). Following this publication, I decided to try electroporation as a transfection method for the screen. The PA-4000/PA-96 WS Pulse Agile® (*Labtech*) and the BTX

ECM 830 (*Harvard Apparatus*) electroporation systems were tested using a panel of different parameters suggested by the suppliers, including the parameters described in the Haase's work (**Table 3.1**). Both systems are suited for a 96-well plate format and therefore had the potential of being successfully used for the screen.

To assess transfection efficiency, I monitored the internalisation of a labelled siRNA duplex from Dharmacon, the s*iGLO* RISC-free control siRNA. This siRNA does not engage the RNA-induced silencing complex (RISC) and it is stable inside the cells for several days.

The majority of the electroporation settings tested severely affected MN survival, however a set of parameters which did not affect MN viability, as confirmed by mitochondrial staining and transferrin uptake, was finally determined (200 V/cm, 5 ms pulse duration, 3 pulses with 1 s interval). Unfortunately, using these parameters no internalisation of the siGLO duplex could be observed.

Table 3.1 Set of parameters tested for electroporation.
The conditions which proved to be the best for each parameter are highlighted in grey. These parameters correspond to the ones used by Arnauld Jaquier and Georg Haase. The other parameters were suggested by the supplier and proved to be toxic for MNs.

Cell number (cells/ml)	siRNA concentration (mM)
$1.5*10^5$	4
$3*10^5$	1.5
$6*10^5$	0.1

Electric field (V/cm)	Duration (ms)	Pulses	Interval (s)
2000	0.4	1	0.5
2000	0.4	4	0.5
1500	0.4	1	0.5
1500	0.4	4	0.5
1000	0.4	1	0.5
1000	0.4	4	0.5
200	5	3	1

In light of these results, I decided to switch from electroporation to lipid –based transfection reagents. These are the most common choice for an siRNA screen, because they are relatively easy to use. Although previous data obtained by the laboratory suggested that lipid transfection reagents were toxic to MNs and impaired the efficiency of axonal retrograde transport (Deinhardt and Schiavo, 2005), these reagents are constantly improved and new, milder formulations are designed and optimised

specifically for the transfection of a variety of primary cells. Six reagents were tested in mouse MNs: Lipofectamine 2000, Oligofectamine and Dharmafect 1, 2, 3 and 4. All of them affected MN viability, with the notable exception of Dharmafect 3, which additionally did not compromise the axonal retrograde transport of H_C. MN cultures treated with Dharmafect 3 consistently showed internalisation of siGLO control siRNA, confirming the efficacy of this reagent in delivering siRNA into MNs.

To test the efficiency of silencing in MNs, I decided to attempt to knock-down the Vesicle-associated membrane protein 2 (VAMP2), a member of the synaptic SNARE family and an essential component of the neurotransmitter release machinery. This protein is several-fold more abundant in neurons than in other cell types, but its depletion does not affect neuronal viability (Schoch et al., 2001), making it a perfect candidate to assess the knock-down efficiency in MNs transfected with Dharmafect 3.

A mouse siRNA SMART pool (Dharmacon) was used to knock-down VAMP2 in mouse primary MNs. The depletion of VAMP2 was confirmed by immunofluorescence and western blot (**Figure 3.3**). Several concentrations of siRNA and Dharmafect 3 were tested. In order to maximise the knock-down efficiency, I also transfected the cells twice. These experiments indicated that VAMP2 could be efficiently depleted within 3 days using a single transfection, a concentration of 50 nM of the siRNA pool and 2 μl of Dharmafect 3 per 500 μl of total volume of medium in a 24-well plate.

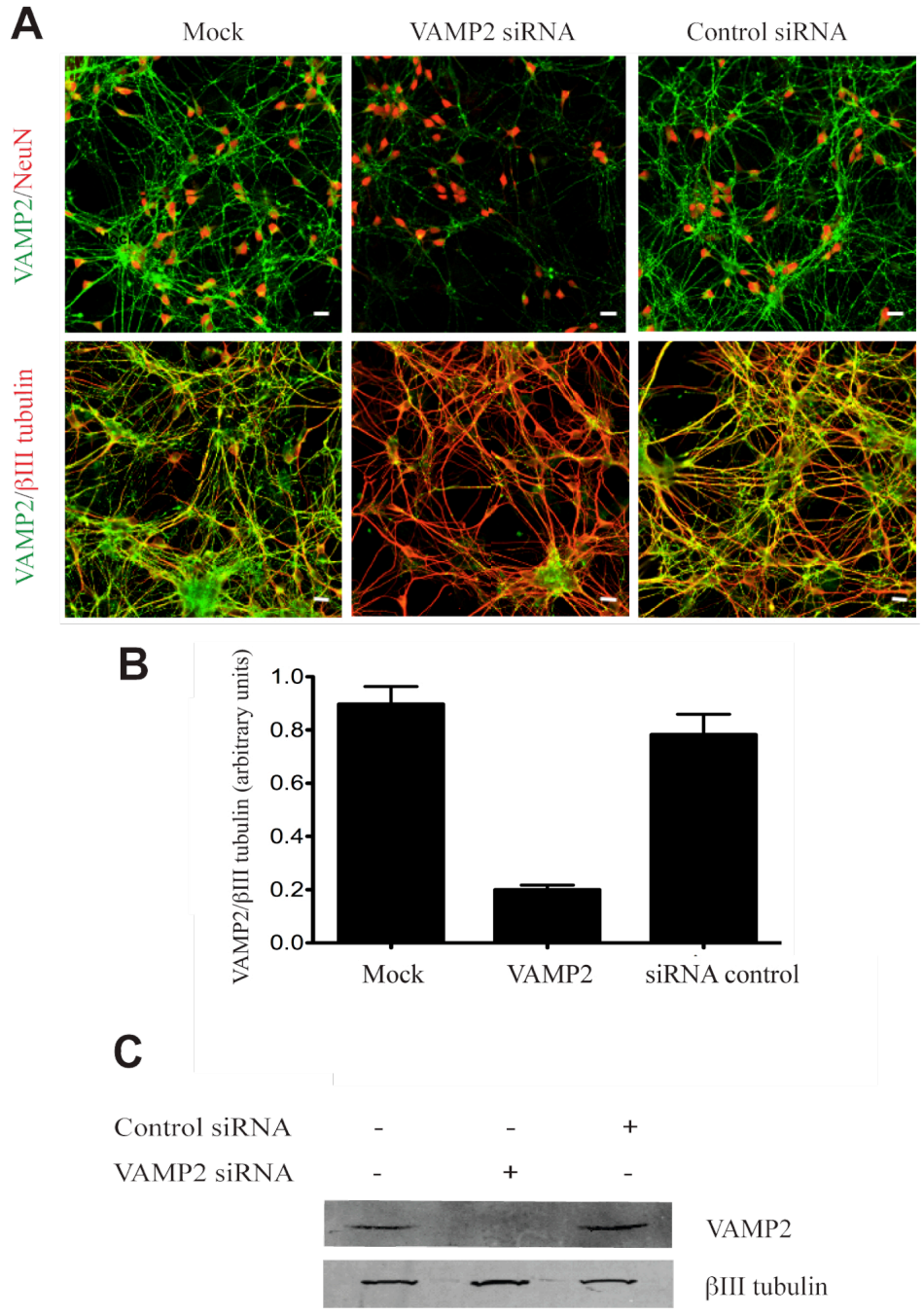

Figure 3.3. VAMP2 knock-down in primary MNs using Dharmafect 3 transfection reagent.
Three days after trasfection, the cells were fixed and immunostained for VAMP2 (green), NeuN (red, upper panel), which stains neuronal nuclei, and βIII tubulin (red, lower panel), which is a neuronal specific isoform of tubulin (A). Scale bar, 10 μm, n=3. The fluorescence intensity of VAMP2 was quantified and normalised against βIII tubulin (B) (n=3). Western blot analysis of the same experiment; βIII tubulin was used as loading control (C). The knockdown of VAMP2 proved to be very efficient both by immunofluorescence and western blot.

3.3.2 Optimisation of a transfection protocol for a 96-well plate format.

The Dharmafect 3 mediated knock-down protocol for VAMP2 was then modified for a 96-well plate, which was the format required for the screen. Unfortunately, the efficient VAMP2 silencing obtained previously could not be repeated in this new format. Since batch variability of the transfection reagent itself was suggested to be a possible explanation of this lack of reproducibility, different batches of Dharmafect 3 were tried, as well as several ratios of the concentration of siRNA and transfection reagent. Knock-down of VAMP2 was observed only after transfecting the cells twice with 0.3 μl of Dharmafect 3 in 100 μl of medium and 100 nM of siRNA per well. In addition, the transfection protocol required the use of serum free medium, which increased MN clustering in 96 well plates. The latter effect could have been due to an adaptative response of the cells to stress under such conditions.

I decided, therefore, to widen the search for a suitable transfection reagent and adopt a different approach to transfection, generally referred to as reverse transfection. In this case the lipid-based reagent and the siRNA are premixed and incubated directly into the wells of a 96 well plate. The cells are then plated in the normal complete medium with serum on top of the transfection mixture. In collaboration with the High Throughput facility, a collection of 23 different transfection reagents was screened for their ability to induce VAMP2 knock-down in primary MNs using the reverse transfection protocol (**Table 3.2**). Two concentrations of the VAMP2 siRNA were utilised for each individual reagent. The ARRAYSCAN imaging system was used to collect the images and analyse them with the spot counting algorithm (**Figure 3.4 A**). Some of the reagents were quite toxic for MNs, the toxicity being scored manually at the microscope and quantified on the basis of the viable cell count for each reagent.

Eight transfection reagents, Transit KO, Metafectene, Dreamfect Gold and Transpass R1 were for a second round of validation on the basis of their low toxicity and their ability to induce VAMP2 silencing. Dharmafect 3 was included in the screen, but, as expected on the basis of the preliminary results obtained in the 96 well format, it was not effective. An siRNA concentration of 50 nM, compared to the 100 nM required with the protocol previously established with Dharmafect 3, proved to be effective in inducing VAMP2 knockdown. This constituted an improvement over the original transfection protocol, cutting down by half the quantity of siRNA from the library needed to complete the screen.

Table 3.2 Validation of suitable transfection reagents.
The reagents selected for the next round of validation are highlighted in grey

Name	Supplier	toxicity	Efficiency of silencing
Oligofectamine	*Invitrogen*	High	Low
TransIT siQuest	*Mirus*	Low	Medium
silenAmine		Medium	High
INTERFERin™	*Polyplus*	High	Low
LipoRNAiMax	*Invitrogen*	High	Low
CodeBreaker™	*Promega*	Low	High
Dharmafect 1	*Dharmacon*	Medium	Low
Dharmafect 2	*Dharmacon*	Medium	Low
Dharmafect 3	*Dharmacon*	Medium	Low
Dharmafect 4	*Dharmacon*	Medium	Low
Lullaby	*OZ Bioscience*	Medium	Low
RiboJuice™	*Merck*	Low	High
TransIT KO	*Mirus*	Low	High
HiPerFect	*Qiagen*	High	Low
Genesilencer	*Genlantis*	Low	High
NTERnanoparticle	*SIGMA-Aldrich*	High	Low
siPORT NeoFX	*Ambion*	High	Low
SimPorter	*Upstate*	Low	High
Lipofectamine 2000	*Invitrogen*	High	Low
Santa Cruz	*Santa Cruz*	High	Low
Metafectene	*Biontex*	Low	High
Dreamfect Gold	*OZ Bioscience*	Low	High
TransPass R1	*New England Biolabs*	Low	High

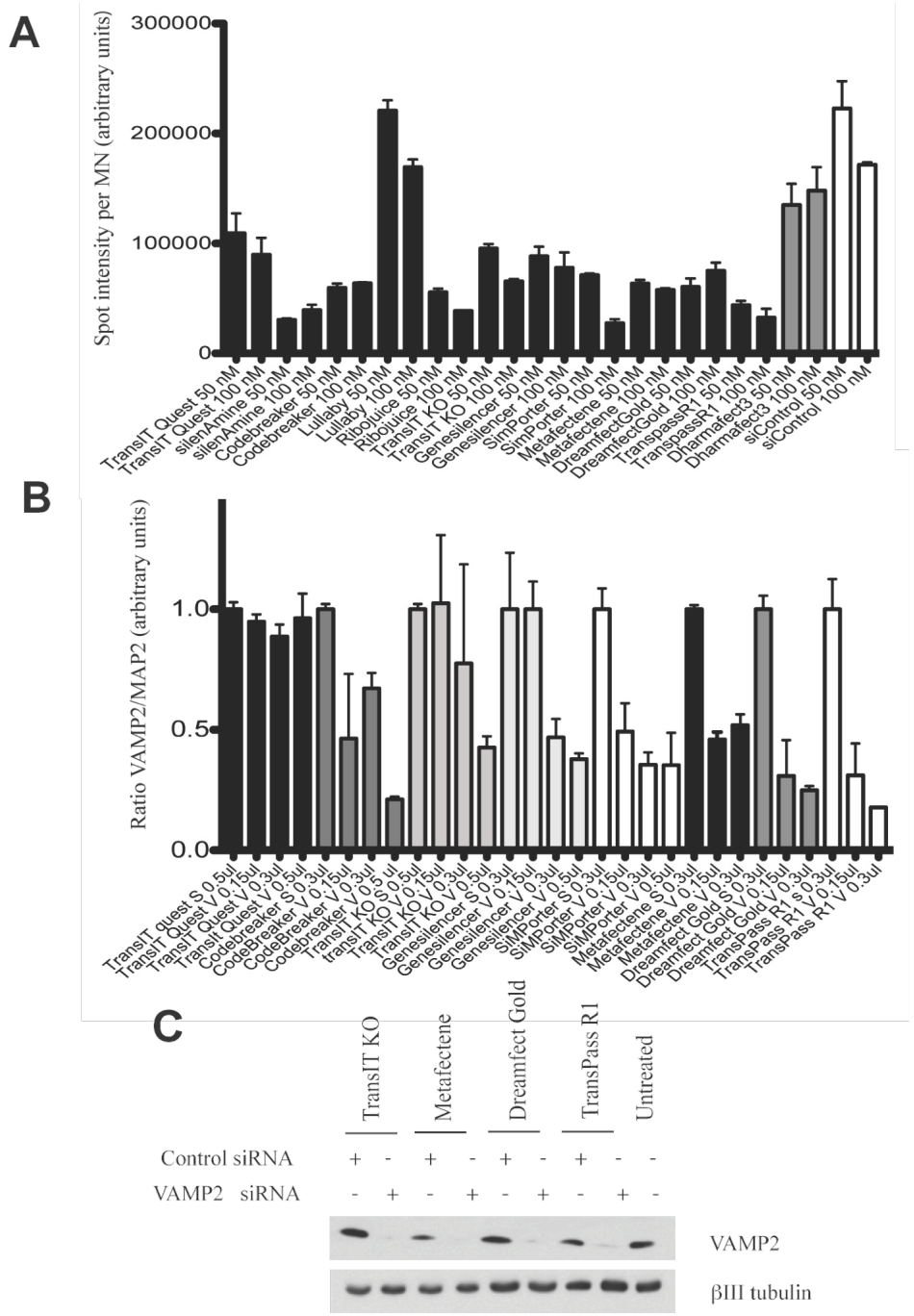

Figure 3.4. Screen for the optimal transfection reagent.
VAMP2 knockdown in primary MNs using 23 different transfection reagents in a 96 well format. The spot count for VAMP2-positive vesicles for the reagents that proved non-toxic are represented in the chart (A). The best eight reagents were re-screened using the same protocol, but using three different concentrations of each reagent. Images were taken with a 510 Zeiss confocal microscope and quantified with Image J. The quantity of each reagent used is indicated. S stands for the sample treated with the siRNA control pool, while V stands for the samples treated with the VAMP2 siRNA pool (B). The best four reagents from this re-screen were tested for their ability to induce knockdown of VAMP2 in a 96 well plate format. All four reagents proved to be effective in knocking down VAMP2 by Western blot (n=3) (C).

The 8 reagents selected from the pilot screen performed with the ARRAYSCAN imaging system were then re-screened using a glass bottom 96-well plate, which made it possible to acquire images with a Zeiss 510 confocal microscope. The advantages of using the confocal are several, including the possibility to utilise a 63X oil objective and to use phase contrast images (the ARRAYSCAN doesn't have high NA oil immersion phase contrast objectives) to assess whether the transfection reagents affected cell morphology. Primary MNs were transfected with a fixed concentration of 50 nM siRNA against VAMP2, while three different concentrations (0.15, 0.3, 0.5 μl in 100 μl of medium per well) of the reagents were tested, in order to establish the minimum effective concentration for each of them. The images were then analysed using the Image J software.

Only TransIT KO, Metafectene, Dreamfect Gold and TransPass R1 were found to be efficient in knocking down VAMP2 without affecting MN morphology. A minimum effective concentration of 0.3 μl per well for Metafectene, Dreamfect Gold and TransPass R1, and 0.5 μl per well for TransIT KO was established (**Figure 3.4 B**).

A final test was performed to detect the knock-down of VAMP2 in western blot. Again a 96-well plate was used and primary MNs were transfected with 50 nM of the VAMP2 siRNA pool using either Metafectene, Dreamfect Gold, TransPass R1 (0.3 μl per 100 μl of medium) or TransIT KO (0.5 μl per 100 μl of medium) with the reverse transfection protocol described above. MNs were scraped from the wells and lysed in the presence of NP-40, and eight wells for each condition were pooled together. All four reagents proved to be effective in inducing knock-down of VAMP2 in primary MNs.

In summary, starting with a library of 23 different transfection reagents, a new reverse transfection protocol for primary MNs in a 96-well plate was established. Four transfection reagents, Metafectene, Dreamfect Gold, TransPass R1 and TransIT KO, were identified as capable of inducing efficient silencing of VAMP2 in primary MNs under conditions suitable for performing the siRNA screen.

3.3.3 Establishment of a differentiation protocol for the derivation of MNs from mouse ES cells.

Having determined the feasibility of RNA interference in MNs, I then focused my attention on the determination of the optimal source of cells to use for the screen. Several factors had been taken into account, such as reproducibility and yield. Primary mouse embryonic MNs require a labour intensive dissection from E11.5 – E13.5 embryos and are affected by a certain degree of variability amongst preparations, due to differences in the health and the genetic background of the dissected embryos. The opportunity of finding an easier way to obtain a large quantity of MNs in a highly reproducible manner was therefore investigated.

Developmentally relevant signals can be used to induce mouse embryonic stem cells (ES cells) to differentiate into spinal progenitor cells and then into MNs *in vitro*. Wichterle and collaborators generated a transgenic ES cell line (Hb9-GFP), which expresses the enhanced green fluorescent protein (eGFP) under the control of the mouse Hb9 promoter. Hb9 is a transcription factor whose expression is restricted to MNs in the ventral horns of the spinal cord (Wichterle et al., 2002). The generation of MNs from embryoid bodies (EBs) depends on both the caudalizing action of retinoic acid (RA) and the ventralizing action of Sonic Hedgehog (Shh). One day after the addition of RA

and Shh into the growth medium, the EBs contain many neural stem cells, and after 2 – 3 days under these differentiating conditions the cells start to express MN markers. Finally, around day 5, there is a peak of expression of pan neuronal and MN specific markers like Hb9.

I decided to test the potential for using the mouse Hb9-GFP ES cells to derive MNs for the RNAi screen. Matthew Golding in the laboratory had already developed a protocol to derive MNs from monolayer cultures of mouse ES cells. This protocol was not suited for the siRNA screen because of its inherent high variability of MN yield. The original protocol for the differentiation of this mouse ES cell line into MNs established by Wichterle and colleagues (Wichterle et al., 2002) was, therefore, used as a guideline to derive MNs from ES cells. I adopted a different method of dissociation of the EBs using trypsin instead of papain and I used a synthetic agonist (SAG) of the Shh signalling pathway instead of recombinant Shh (Materials and Methods, **section 2.2.4.4 – 2.2.4.6**). This agonist was proven to be very effective in inducing MN differentiation, considerably increasing the yield of MNs obtained after 4 days (**Figure 3.5**).

It was also established that the addition of RA, to the normal growth medium after plating the dissociated EBs greatly enhanced the survival of GFP-positive MNs in culture. This is not surprising considering the known pro-survival effect of RA on MNs (Maden, 2007) .

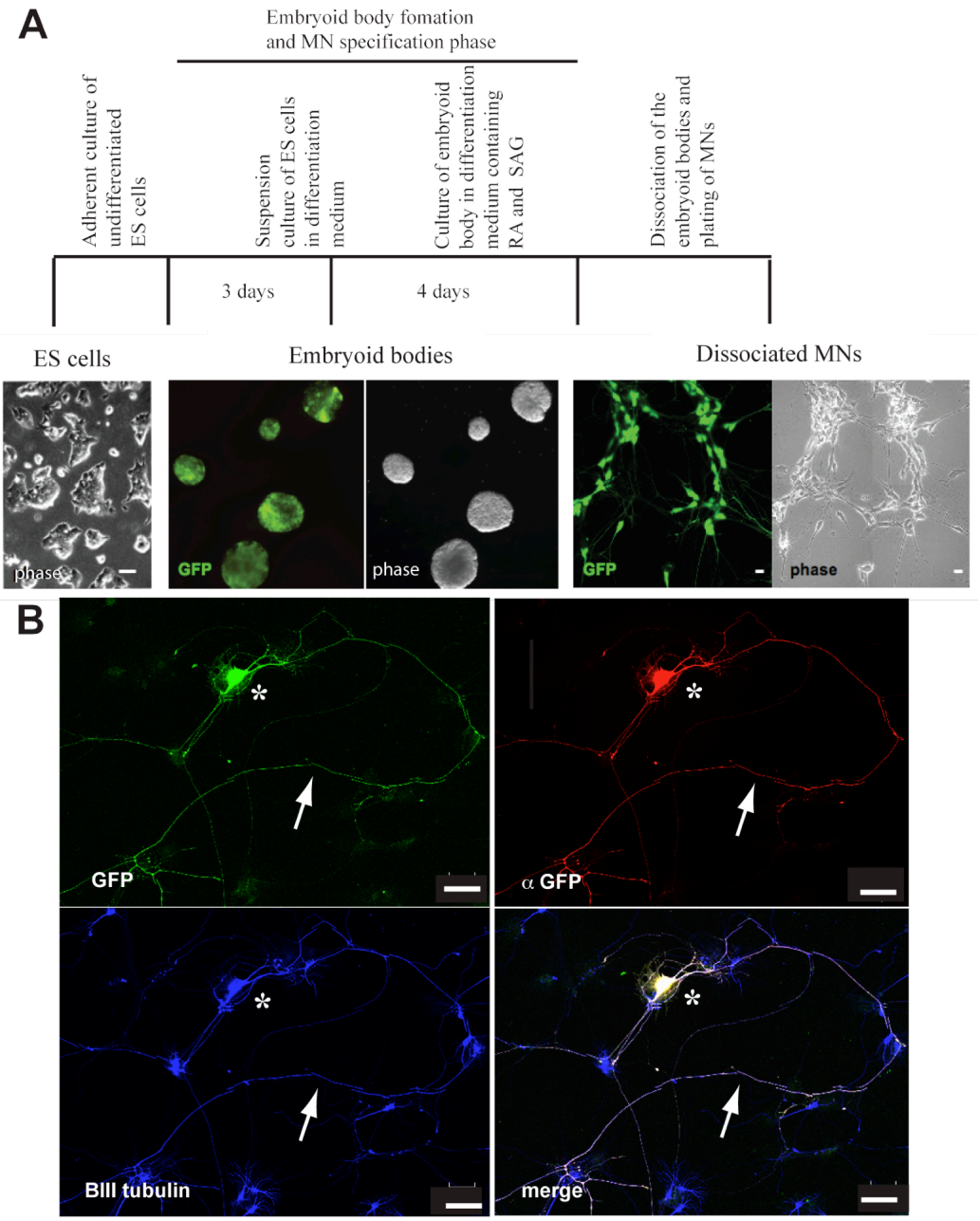

Figure 3.5. Derivation of MNs from mouse embryonic stem cells.
Flow diagram describing the protocol used for the differentiation of MNs from mouse ES cells. After growth in suspension in differentiating medium for 3 days, the ES cells form EBs. These EBs are then committed to a MN fate by the addition of RA and SAG. At the end of the 4th day in the presence of the differentiating agents, the EBs were dissociated and plated (A). Scale bar, 10 μm. An Hb9-GFP ES cell derived MN at 4 days after plating. GFP in green, GFP antibody staining in red, βIII tubulin staining in blue (B). The characteristic long axon of the MN is pointed at by an arrow head, while the soma is indicated with an asterix. Scale bar 50 μm.

3.3.4 Choice of a transfection reagent for MNs derived from mouse ES cells.

In order to use MNs derived from mouse ES cells as a cell system for the RNAi screen, it was important to determine whether they would be transfectable using the same protocol optimised for primary cultures. Metafectene, Dreamfect Gold, TransPass R1 and TransIT KO were, therefore, re-screened for their ability to transfect MNs derived from mouse ES cells.

MNs derived from mouse ES cells were transfected with 50 nM of the VAMP2 siRNA pool using the reverse transfection protocol optimised for primary MNs, and the cells were then either analysed by western blot and immunostained in parallel with the VAMP2 antibody. VAMP2 protein levels were then quantified using Image J. Dreamfect Gold was the best transfection reagent for inducing knock-down of VAMP2 in this system and this reagent was chosen to perform the RNAi screen (**Figure 3.6**).

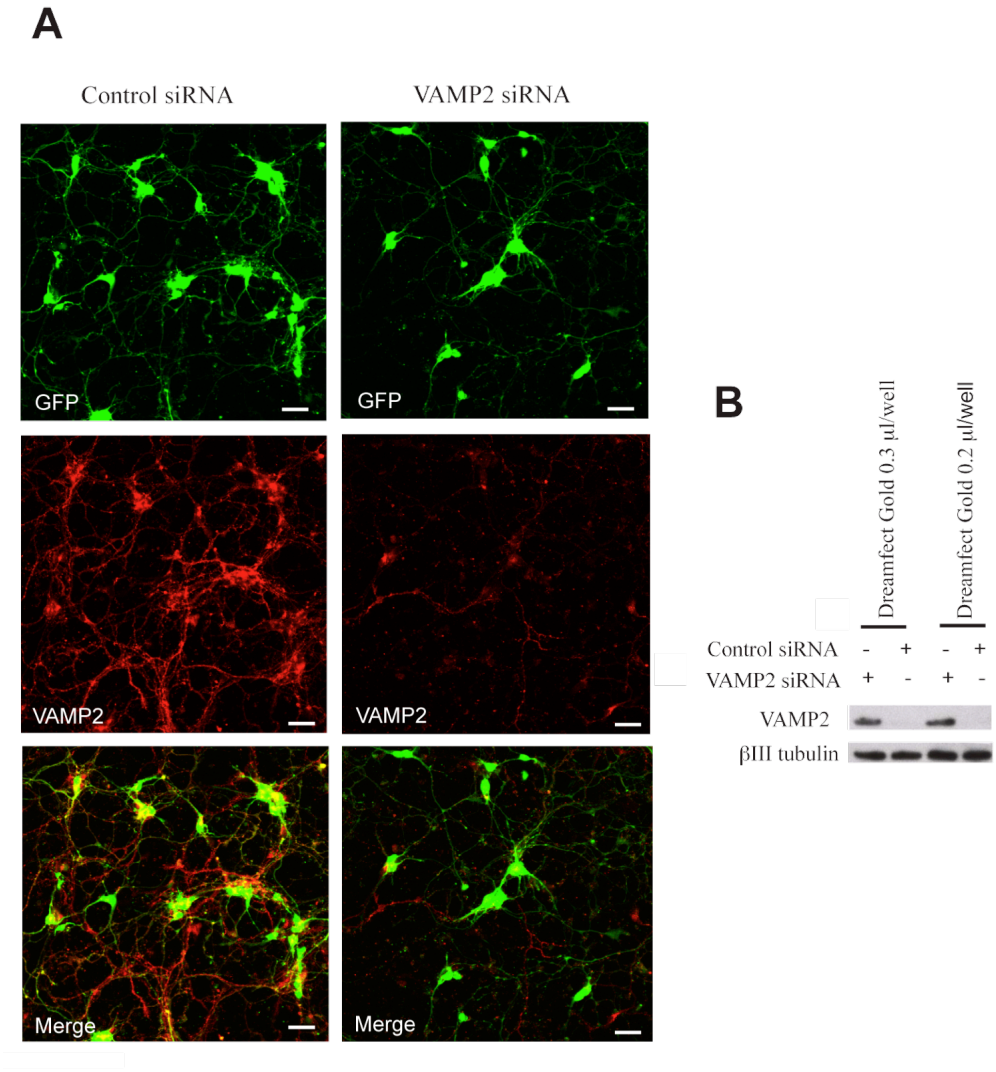

Figure 3.6. VAMP2 knock-down in MNs derived from Hb9-GFP ES cells.
Knock-down of VAMP2 (red) revealed by immunofluorescence in MNs differentiated from mouse ES cells (green) transfected with Dreamfect Gold in a 96 well plate format (A). Scale bar, 20 µm, n=3. Dreamfect Gold proven to be very effective in knocking-down VAMP2. Western blot analysis of the VAMP2 knock-down in MNs derived from ES cells transfected in a 96 well format. Dreamfect Gold induced a very effective silencing of VAMP2 (B) (n=3). These results prove that efficient knock-down can be obtained in a cell type notoriously difficult to transfect such as MNs with the reverse transfection protocol optimised for the siRNA screen.

3.4 Exploring the use of confocal microscopy for high-throughput imaging.

The ARRAYSCAN imaging system is limited to the use of dry objectives, which means that 0.75 is the maximum numerical aperture (NA) that can be achieved. The biggest problem, though, is the fact that this microscope uses an autofocus function based on the intensity levels of the nuclear staining. This is problematic when imaging cultures of MNs, as they consist of a mixture of cell populations, including an underlying layer of fibroblasts and glial cells, which provide trophic support to the neurons. There are then at least two layers of nuclei, which makes it difficult, if not impossible, for the microscope to focus on the most relevant cell population. In addition, neurons tend to aggregate in clumps, which results in an intrinsic lack of homogeneity in the density of the cultures. Several areas of the wells are, therefore, devoid of cells, making it even more difficult for the ARRAYSCAN to focus. Even though the first attempts to use the ARRAYSCAN imaging system were successful (as shown in **section 3.2.1**), it became clear that using this system for the screen was impractical because of the problems associated with the autofocus function.

I therefore decided to attempt to image the 96-well plates from the screen using a Zeiss 510 inverted confocal microscope. The use of glass bottom plates made it possible to utilise a 40X oil objective with an NA of 1.4, and the MTS macro (see next section) could be used to acquire images in an automated fashion. In summary, the major advantages of using a confocal microscope for screening purposes are: 1) its ability to autofocus on the neurons, 2) the high resolution and 3) the possibility of taking confocal Z stacks, which enables the acquisition of 3D information.

3.4.1 The Multi Field Acquisition macro.

The inverted Zeiss 510 confocal microscope has an automated stage, a feature that makes it possible to perform automated acquisition of several fields from a 96-well plate, when used in combination with the Multi Field acquisition macro (MTS) designed for the Zeiss software. The MTS macro instructs the microscope to move in a sequential manner to a series of coordinates, each one corresponding to a single well from a 96 well plate, and then to acquire a tile of 16 images or Z stacks for each coordinate. The final data output of the macro is a database where all the images from each tile are grouped together.

The MTS macro also enables the microscope to autofocus before acquiring every image or Z stacks. The autofocus function can be performed on any staining (DAPI, Hoechst, GFP or antibody staining) and it works by determining the focal plane with the maximum fluorescence intensity. The autofocus algorithm of the MTS macro proved to be more efficient in finding the optimum optical plane compared to the one from the ARRAYSCAN imaging system. In addition, even if the best optical plane was not found, the acquisition of a Z stack guaranteed that there would be at least one image in focus for each field. This was a major improvement compared with the imaging provided by the ARRAYSCAN and solved the problem associated with imaging clumps of neurons. Using the Hb9-GFP ES MNs had the major advantage of being able to instruct the MTS macro to use the GFP channel (i.e. MNs) for the autofocus function.

3.4.2 Use of the Cell Profiler software for image quantification.

Cell Profiler is a free program developed by Anne Carpenter and Thouis John in the laboratories of David M. Sabatini and Polina Golland (http://www.cellprofiler.org/).

This software was developed to analyse large image datasets and is based on a collection of modules, which can be composed into a pipeline and then executed. Basic modules allow many functions, including loading, creating, subtracting images, splitting or merging different imaging channels, identifying primary objects, creating an object mask and calculating the pixel intensity.

I decided to use the Cell Profiler software to attempt an analysis similar to the one performed with the ARRAYSCAN software. First, the best in focus image for the confocal Z stacks was chosen and loaded into the Cell Profiler software. The images were then split into the three separate RGB channels, with the GFP one used to identify the "primary objects" (i.e. MNs). With this set of information Cell Profiler could already calculate the total and mean intensity of H_C and $p75^{NTR}$ inside each MN, giving a fluorescent intensity per cell of each probe as a final output. In order to obtain something similar to the ARRAYSCAN spot count, the GFP channel was used to create a cell mask, which was then saved as an image and subtracted from the H_C and $p75^{NTR}$ channels. Finally individual H_C and $p75^{NTR}$-positive vesicles were identified and counted in the subtracted image for each channel, the final output being the average number of H_C or $p75^{NTR}$-positive vesicles per MN (**Figure 3.7**).

Using this quantification method, I tested the ability of Cell Profiler to detect a difference between control internalisation conditions and upon inhibition of the uptake of H_C and the $p75^{NTR}$ antibody. Hb9-GFP ES cell derived MNs were incubated with H_C together with the $p75^{NTR}$ antibody for 45 minutes at 37°C or at 4°C for 15 minutes. The cells were then acid-washed to remove the probes bound to the cell surface. Confocal images were acquired using a 40X oil objective and the images were then quantified

using the Cell Profiler software to score the total intensity of the two probes per cell and the number of H_C and $p75^{NTR}$-positive vesicles per MN (**Figure 3.8** for quantification). For both probes, the vesicles count algorithm is the one with the largest data point spread, allowing to detect a difference of 40-fold between the sample internalised at 37°C and the one incubated on ice and then acid-washed (**Figure 3.8** for a direct comparison of the two quantification algorithms).

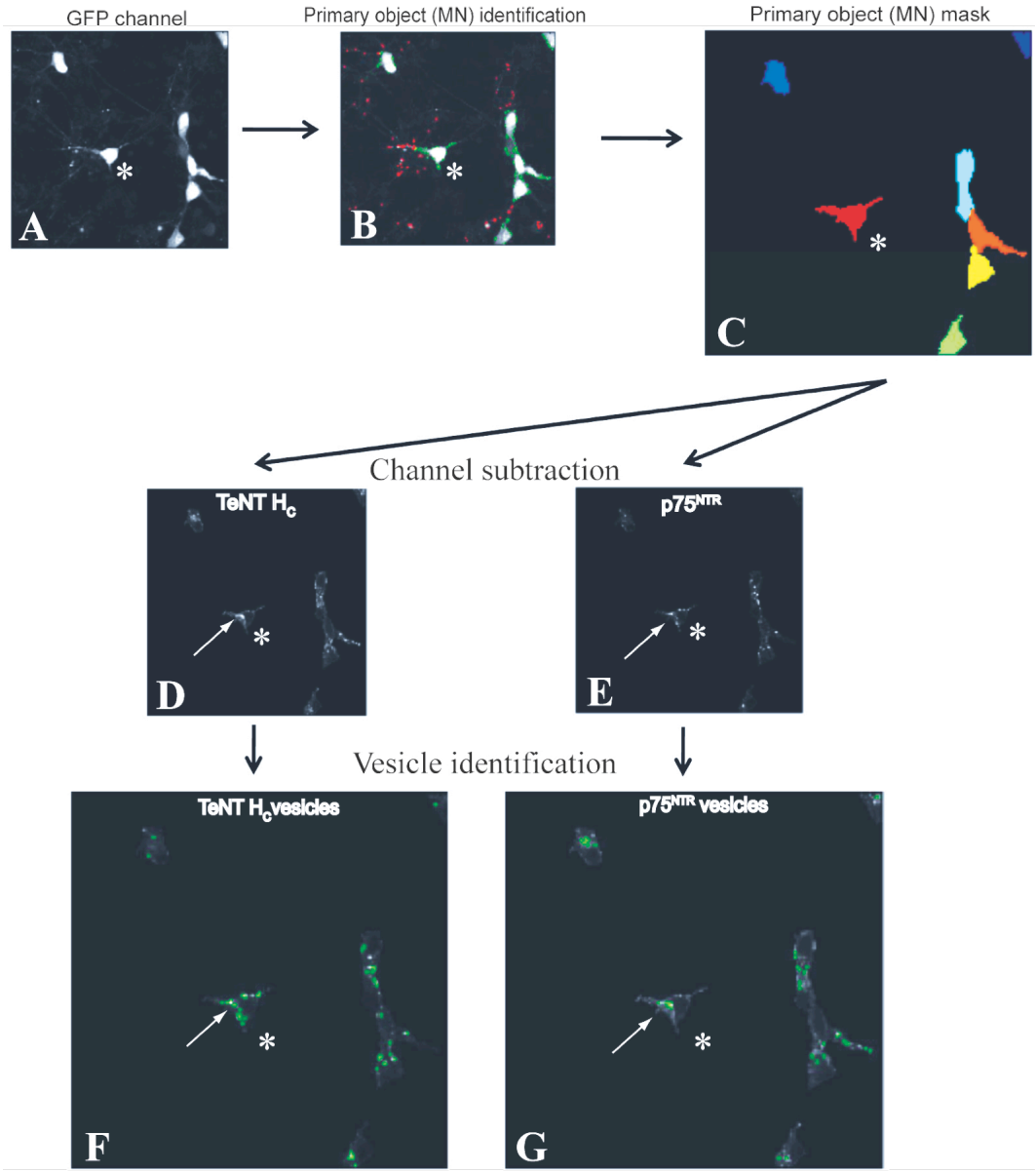

Figure 3.7 Cell Profiler quantification pipeline.
The best RGB images from each Z stack acquired with the MTS macro are split into three different channels, namely GFP (A), H_C (D) and $p75^{NTR}$ (E). Primary objects (i.e. MNs) are identified on the basis of the GFP intensity (B) and a cell mask image is created (C). At this stage the fluorescence intensity for the H_C and $p75^{NTR}$ inside each mask can be measured and quantified and expressed as mean H_C and $p75^{NTR}$ fluorescence intensity per MN (**Figure 3.8** for the quantification). Alternatively all vesicles positive for H_C and $p75^{NTR}$ inside the MN mask can be identified (F & G) and counted. The final output of the pipeline is the number of H_C and $p75^{NTR}$ vesicles per MN (**Figure 3.8** for the quantification). A single MN is indicated by an asterix; after a mask is created on the basis of the GFP staining (C), single vesicles positive for H_C (F, D) and $p75^{NTR}$ (E,G) can be identified (the identified vesicles are coloured in green, F & G) inside that mask.

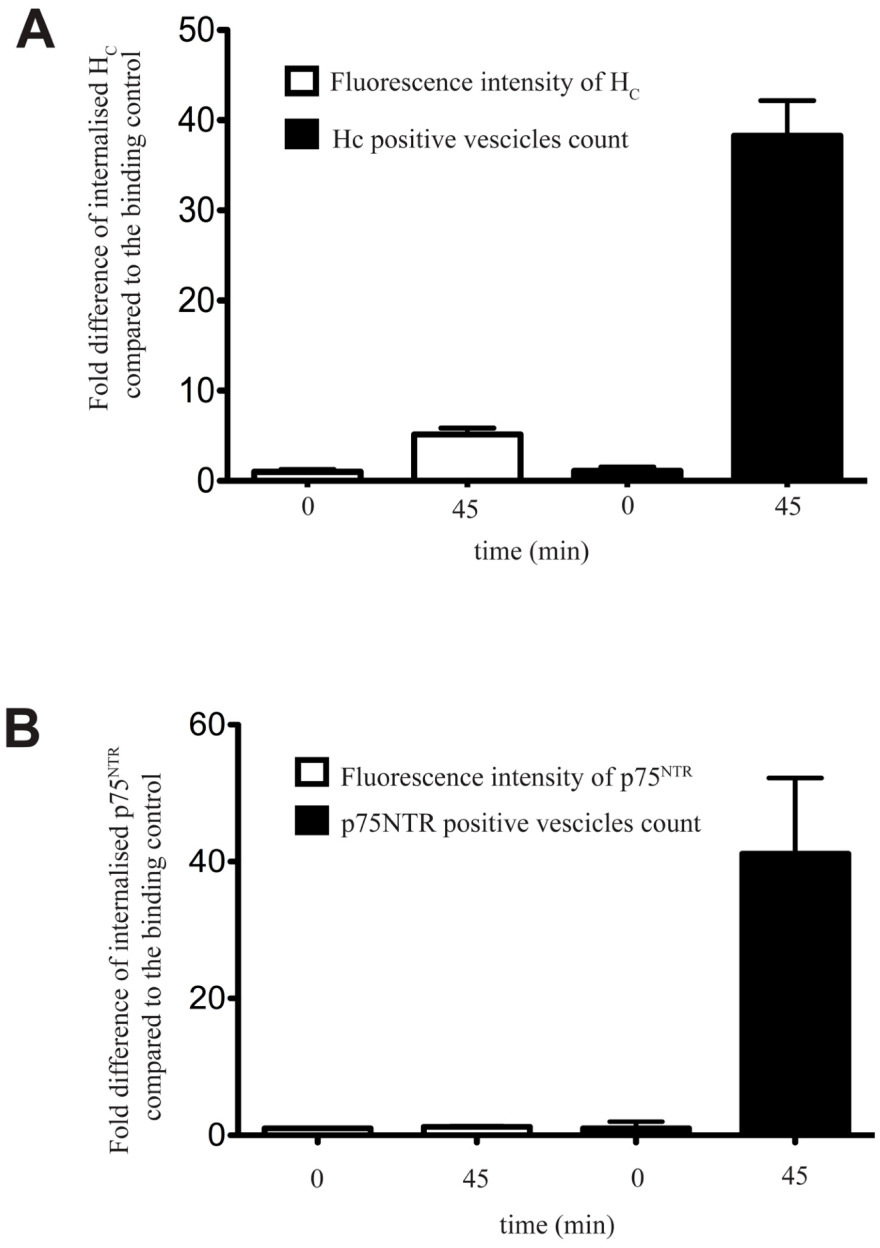

Figure 3.8. Cell profiler quantification of the internalisation of H_C and the $p75^{NTR}$ antibody.
MNs were incubated with H_C and the $p75^{NTR}$ antibody for 45 minutes at 37˚C or just on ice for 15 minutes on a 96 well plate. The cells were then acid-washed to remove the probes bound to the cell surface. The "binding control" is a control for the efficiency of the acid wash, where the internalisation is prevented and the signal corresponds to the residual background. The amount of internalised H_C (A) and $p75^{NTR}$ antibody (B) compared to the binding control was quantified with Cell Profiler in two ways, as mean fluorescence intensity of the two probes per MN (white columns) or as total number of Hc and p75NTR positive vesicles per MN (black columns). In order to allow for a direct comparison between the two quantification methods, the data were normalised to the value of the binding control. The quantification method which gives the greatest fold difference (around 40-fold for both probes) is the positive vesicles count (black columns) (n=3). This method was therefore chosen for the quantification of the siRNA screen.

Summary of the achievements presented in this chapter.

- *A protocol for the differentiation of MNs from mouse ES cells has been established, which enabled the generation of a sufficient quantity of MNs for the planned siRNA screen. In addition, the GFP expression driven by the Hb9 promoter makes it easier to identify MNs and create a specific mask during image analysis.*

- *A library of 23 different lipid-based transfection reagents was screened for their ability to induce knock-down of VAMP2 in primary and ES-derived MNs in a 96-well format. Dreamfect Gold was selected as the most effective transfection reagent.*

- *The MTS macro was optimised to enable high-resolution automated image acquisition from a 96-well plate format using a Zeiss 510 inverted confocal microscope.*

- *Using the Cell Profiler image analysis software, an algorithm was established to enable the reliable quantification of internalised H_C and $p75^{NTR}$ antibody. This quantification was then used as the readout for the siRNA screen.*

Chapter 4. The siRNA screen

4.1 Introduction

Performing an siRNA screen has become an increasingly used approach for finding new components of biological pathways. There are several siRNA libraries available that target a variety of metabolic pathways and protein families, and established protocols for transfection of several cell lines. I planned to use this approach to gather new insights into the trafficking of neurotrophins and their receptors by using an antibody against $p75^{NTR}$ and the H_C fragment of Tetanus toxin, which has been shown to traffic in the same compartment as the neurotrophins and their receptors during axonal retrograde transport (Lalli and Schiavo, 2002, Deinhardt et al., 2006b). I intended to perform a novel siRNA screen on a cell system that has not be used so far and that is believed to be physiologically relevant for the trafficking of neurotrophins. To achieve this I used MNs derived from mouse ES cells, because they resemble primary MNs as closely as possible. The screen was also made possible by developing a system for the acquisition of high resolution images and high content software image analysis.

Aims of the work presented in this Chapter

- *To establish a positive control for the H_C and the $p75^{NTR}$ antibody internalisation assay developed in Chapter 3.*

- *To perform the screen with a customised library of siRNA pools targeting 155 genes, including molecular motors and their adaptors.*

- *To analyse the data and rank the individual siRNA pools for their ability to affect the internalisation of H_C and the $p75^{NTR}$ antibody.*

- *To select the best hits from the screen for further characterisation.*

- *To validate the selected hits using siRNA pools from a different supplier.*

4.2 Developing a positive control for the readout of the screen

An siRNA screen requires a series of important internal controls. The first control is one for detecting off-target effects of the siRNA pools themselves and normally consists of a non-targeting siRNA pool (siControl) provided in the library itself. Other controls are also required: a positive one for the assay, to show that the assay has worked, and another control to show that the knockdown has worked. Normally, these last two controls are combined with the use of a previously identified "positive control" gene that when silenced is able to influence the readout of the screen. These controls make it possible to know that the assay has worked and also that the knockdown in the plate was efficient.

A first attempt was made by trying to knockdown genes that have been previously demonstrated to be involved in the internalisation of H_C, e.g. clathrin heavy chain, dynamin 1 and the AP2 clathrin adaptor complex. None of these genes, however, could be efficiently knocked-down in MNs. I decided therefore to use a different approach by blocking the internalisation of H_C and the $p75^{NTR}$ antibody using a small organic inhibitor. The inhibitor chosen was EHNA ((erythro-9-(2-Hydroxy-3-nonyl)adenine), a cell-permeable inhibitor of phosphodiesterase II (PDE II) (IC_{50} 800 nM) (Podzuweit et al., 1995), which is also known to block the retrograde motor dynein by inhibiting its ATPase activity. EHNA had already been successfully used in the laboratory by Giovanna Lalli to show that inhibition of cytoplasmic dynein abolishes the fast component of the axonal retrograde transport of H_C in primary MNs (Lalli et al., 2003).

ES cell-derived MNs were incubated at 37°C with H_C and the $p75^{NTR}$ antibody in presence of 1 mM EHNA to assess whether the drug had any effect on the internalisation and/or accumulation of these two probes. The kinetics of accumulation of H_C and the $p75^{NTR}$ antibody in the cell soma were established by detecting the extent of probe internalisation every 15 minutes up to two hours after binding at 37°C. At each time-point the cells were acid-washed to remove probes bound to the cell surface. H_C exhibited linear accumulation kinetics, which was significantly inhibited by EHNA (**Figure 4.1 A**). In contrast, the accumulation of the $p75^{NTR}$ antibody in the presence of H_C was not linear and it did not seem to differ in the presence of EHNA until 75 minutes, when the curve of the EHNA treated samples started to progressively diverge from the controls (**Figure 4.1 B**). The conclusion that can be drawn from these kinetic profiles is that EHNA inhibits the accumulation of both H_C and the $p75^{NTR}$ antibody in a progressive manner.

The maximum difference in accumulation of the two probes in the presence or absence of EHNA, was observed after two hours, which was the last time-point taken. This time point was sufficient to allow the axonal retrograde transport of the two probes to reach steady state, which according to previous data from the laboratory starts 45 minutes after binding. It is also interesting that the difference between the two accumulation curves for the $p75^{NTR}$ antibody started to be significant only after 75 minutes (**Figure 4.1 B**), contrary to what was seen for H_C (**Figure 4.1 A**). The difference in the two accumulation curves of the $p75^{NTR}$ antibody after 75 minutes indicates that the effects of EHNA are only apparent approximately 30 minutes after the onset of $p75^{NTR}$ retrograde transport. Because EHNA is a well-characterised dynein inhibitor, it is possible to speculate that in the first 75 minutes from the binding of the

$p75^{NTR}$ antibody, the intracellular accumulation of the probe is a dynein-independent process, whereas after that time point it becomes dynein-dependent (Discussion, **section 7.1.4**). Interestingly, this time point is compatible with the 45 minutes delay in the onset of axonal retrograde transport. Considering the data obtained previously(Lalli et al., 2003), it is tempting to speculate that the difference in the accumulation observed might be the result of an inhibition of the axonal retrograde transport of $p75^{NTR}$. It was therefore decided to use two hours as the end point for the assay during the screen. This would give us a chance to find genes that are effectors of both the internalisation and/or the retrograde axonal transport of the these probes.

The kinetics of internalisation of the $p75^{NTR}$ antibody alone was also tested. The intracellular accumulation of the probe overlapped with the curve obtained co-incubating the cells with the antibody and H_C in the presence of EHNA (**Figure 4.1**, Discussion, **section 7.1.4**).

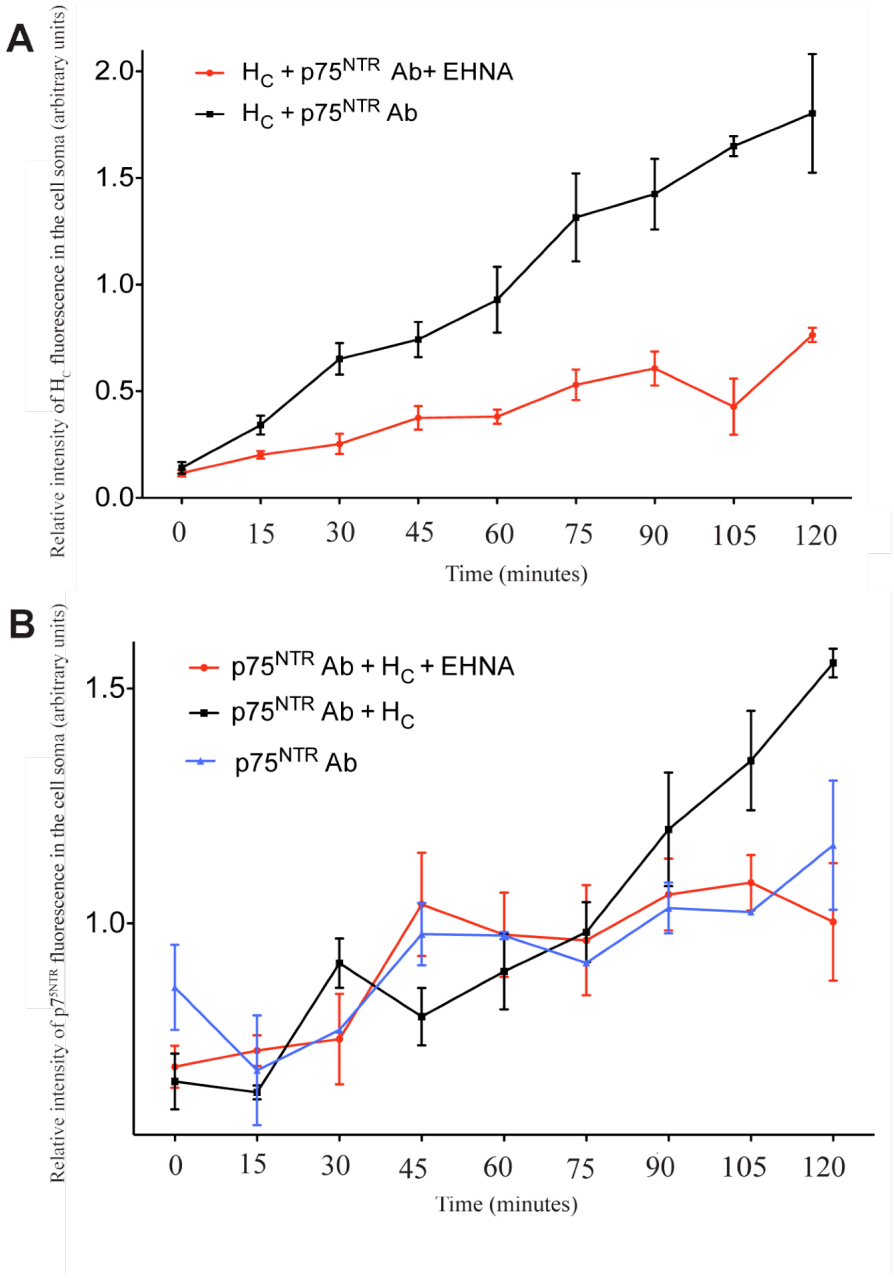

Figure 4.1 Kinetics of H_C and the p75^{NTR} antibody internalisation.
Kinetics of accumulation of H_C (A) and the p75^{NTR} antibody (B) in MNs derived from HB9-GFP ES cells in the absence (black curve) or presence (red curve) of the EHNA inhibitor (n=3). The accumulation of H_C is significantly in presence of EHNA ($p<0.0001$, two ways ANOVA). In the case of p75^{NTR} the two curves of accumulation are identical until 75 minutes when they diverge ($p<0.0001$, two ways ANOVA). The kinetics of internalisation of the p75^{NTR} antibody alone was also established (blue curve) and was found to overlap with the curve of internalisation of the p75^{NTR} antibody in presence of H_C and EHNA (B).

4.3 The siRNA screen

4.3.1 Plate design

I decided to run the siRNA screen in a 96-well plate format. The library came already aliquoted on 3 master plates (Material and Methods, **table 2.3**) and contained four internal siControls in random positions in the centre of the plate. Each gene was targeted by a pool of three siRNAs (Material and Methods, **table 2.4**).

The edges of the library plates were left empty and I decided to take advantage of them to place the controls. The EHNA inhibitor was used as a control for the accumulation of both the $p75^{NTR}$ antibody and H_C. The transfection efficiency control for VAMP2 knockdown was added in the last row of plate 1 and 2 and in the fifth row of plate 3 (**Figure 4.2**). The VAMP2 knockdown samples were analysed by Western blot compared with non-targeting siControls (**Figure 4.5** for the Western blot analysis of the plates from the screen). Four wells from each plate were used for this purpose to ensure that enough protein was harvested (the plate layouts are described in detail in **Figure 4.2**).

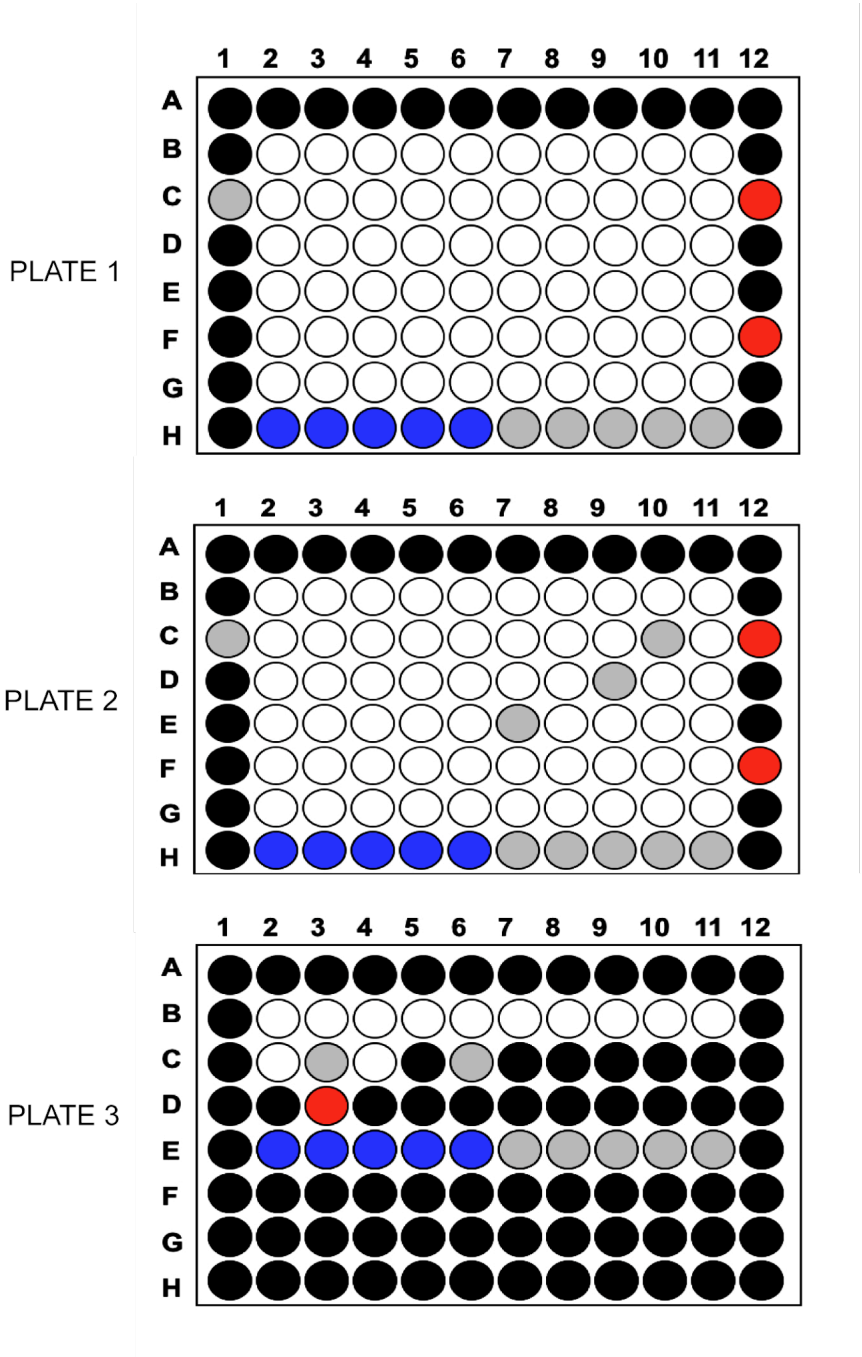

Figure 4.2 Plate design.
Layout of the three plates of the siRNA screen. The empty wells are coloured in black, those containing siRNA controls in grey, and those treated with the EHNA inhibitor in red. Finally the wells treated with the VAMP2 siRNA pool are coloured in blue.

4.4 The primary screen and its analysis with Cell Profiler

The entire library was not screened at the same time, but divided into three sessions, one for each plate of the library done in triplicate. This decision was justified by the fact that all the handling, treatment and image acquisition had to be done manually by the operator.

The screen was performed as described in **section 2.2.6.4** of Materials and Methods. Each plate was sealed with a transparent plastic foil and images were acquired with a 510 Zeiss Confocal microscope using the MTS macro as explained in Chapter 3 (**section 3.4.1**). 16 stacks were acquired for each well and the best focused image for each stack was selected. The images were analysed using the Cell Profiler imaging software as described in Chapter 3 (**section 3.4.3**).

The output of the image analysis performed with Cell Profiler was the number of intracellular vesicles positive for H_C and the $p75^{NTR}$ antibody. This raw data set was then fed to the Cell HTS software (available via the High-throughput Facility at CRUK, http://hts.cancerresearchuk.org/cellHTS/), which calculated a Z score for each well (**Table 4.1 - 4.2** for the list of the Z-scores and **Figure 4.3 - 4.4** for their visual representation). A Z-score, also called "standard" or "normal" score, is a statistical method to "normalise" or standardise a data set, where the normalisation is a way to correct for unwanted and unavoidable technical variations (for example pipetting errors and the so called edge-effects, due to the evaporation of the medium in the wells situated at the edge of the plates, which causes artefacts in cell behaviour). Mathematically, the Z-score is defined as a dimensionless quantity obtained by subtracting the population mean from an individual raw score and then dividing the

difference by the standard deviation of the population. The resulting score is a measure of how many units of standard deviation a data point is above or below the mean of the population. In the case of the readout of our screen, a positive or negative Z-score indicates that a particular siRNA pool caused an increase or decrease in the accumulation of the probe under investigation compared to the mean value of accumulation for the whole population of siRNAs present in the library. Importantly, data sets can only be allocated Z-scores when they have a Gaussian distribution.

Table 4.1 TeNT H_C Z-scores.
The Z-scores from the three replicates of each well are indicated. The "well annotation" column indicates whether the well was treated with a targeting siRNA (sample), a non-targeting siRNA control (siControls) or a positive control for the assay (EHNA treated samples). siControls are highlighted in grey, EHNA treated samples in red.

Plate	Well	Z-score	Well annotation
1	B03	2.05	sample
3	B02	2.05	sample
3	B06	1.87	sample
1	F09	1.71	sample
2	G02	1.62	sample
1	B04	1.56	sample
2	B09	1.56	sample
3	B05	1.54	sample
1	B09	1.52	sample
2	C03	1.38	sample
1	F07	1.3	sample
2	E02	1.29	sample
2	B10	1.28	sample
1	G08	1.24	sample
1	G11	1.21	sample
2	B02	1.14	sample
1	E03	1.06	sample
1	B02	1.02	sample
3	B07	0.93	sample
1	F10	0.93	sample
3	C04	0.91	sample
1	B08	0.88	sample
2	E09	0.87	sample
1	C10	0.87	sample
1	E10	0.86	sample

2	D04	0.86	sample
2	C06	0.81	sample
1	B06	0.74	sample
1	B07	0.72	sample
2	C05	0.72	sample
1	G04	0.68	sample
2	B03	0.68	sample
2	E05	0.66	sample
2	C01	0.64	siControl
2	C04	0.63	sample
2	D10	0.61	sample
1	C06	0.57	sample
2	F02	0.56	sample
2	E04	0.51	sample
1	G05	0.5	sample
1	G03	0.49	sample
1	G09	0.48	sample
2	F03	0.48	sample
2	E03	0.45	sample
2	D11	0.42	sample
1	F05	0.39	sample
2	E08	0.36	sample
1	E04	0.34	sample
3	B03	0.32	sample
2	E10	0.31	sample
2	B08	0.29	sample
1	E09	0.28	sample
1	D06	0.27	sample
1	C01	0.23	siControl
2	D09	0.22	negative
1	G07	0.22	sample
2	B04	0.15	sample
2	G07	0.14	sample
1	F04	0.13	sample
1	E07	0.1	sample
3	C03	0.07	siControl
2	F05	0.07	sample
2	B06	0.07	sample
2	B07	0.07	sample
1	E06	0.03	sample
1	D10	0.02	sample
1	F02	0.01	sample
2	F09	0.01	sample
2	G08	0	sample

1	D04	-0.03	sample
2	D06	-0.03	sample
2	G03	-0.05	sample
2	D05	-0.07	sample
2	F04	-0.07	sample
1	C11	-0.07	sample
1	D07	-0.09	sample
1	C09	-0.1	sample
1	G02	-0.1	sample
1	C02	-0.13	sample
2	C08	-0.15	sample
2	E11	-0.18	sample
2	B05	-0.2	sample
2	B11	-0.23	sample
1	B10	-0.26	sample
1	E11	-0.29	sample
2	C07	-0.3	sample
1	E08	-0.31	sample
3	B09	-0.32	sample
2	F07	-0.33	sample
1	E05	-0.34	sample
2	D07	-0.35	sample
2	D02	-0.39	sample
2	G04	-0.46	sample
1	C04	-0.46	sample
1	C08	-0.46	sample
3	C02	-0.48	sample
3	B11	-0.48	sample
2	E06	-0.53	sample
2	F06	-0.53	sample
1	F11	-0.54	sample
1	D09	-0.55	sample
2	C11	-0.55	sample
1	C07	-0.56	sample
1	F08	-0.57	sample
2	D03	-0.57	sample
1	D05	-0.58	sample
1	E02	-0.59	sample
1	G10	-0.6	sample
3	B10	-0.65	sample
2	G09	-0.67	sample
1	B11	-0.68	sample
3	B08	-0.7	sample
1	D08	-0.71	sample

3	B04	-0.71	sample
2	G11	-0.71	sample
2	C10	-0.77	siControl
1	D11	-0.79	sample
1	G06	-0.82	sample
1	C03	-0.86	sample
2	F08	-0.87	sample
1	F03	-0.91	sample
1	F06	-0.95	sample
2	G06	-0.96	sample
2	D08	-0.99	sample
1	D02	-1.04	sample
1	C05	-1.06	sample
2	C09	-1.09	sample
1	D03	-1.09	sample
2	F11	-1.18	sample
2	F10	-1.19	sample
2	G05	-1.23	sample
3	C07	-1.34	siControl
2	E07	-1.37	siControl
1	B05	-1.45	sample
2	F12	-1.53	positive
2	G10	-1.64	sample
2	C02	-1.72	sample
2	C12	-1.76	positive
3	D03	-1.91	positive
1	F12	-2.14	positive
1	C12	-2.71	positive
3	D06	-2.74	positive

Table 4.2 p75^{NTR} Z-scores.
The Z-scores from the three replicates of each well are indicated. The "well annotation" column indicates whether the well was treated with a targeting siRNA (sample), a non-targeting siRNA control (siControls) or a positive control for the assay (EHNA treated samples). siControls are highlighted in grey, EHNA treated samples in red.

Plate	Well	Z-score	Well annotation
1	G03	4.06	sample
1	G04	4.06	sample
1	G10	3.66	sample
3	B02	3.17	sample
1	G02	3.15	sample
1	F11	2.92	sample
1	F03	2.61	sample
2	G02	2.43	sample
3	C04	2.18	sample

1	F04	2.12	sample
2	E06	2.09	sample
2	F09	1.93	sample
2	C06	1.84	sample
2	D09	1.74	sample
2	B06	1.71	sample
2	E02	1.71	sample
3	B05	1.54	sample
1	G05	1.44	sample
2	C09	1.38	sample
2	F02	1.15	sample
1	B06	1.1	sample
2	G03	0.86	sample
1	E02	0.86	sample
1	B08	0.74	sample
1	C03	0.74	sample
2	F05	0.74	sample
1	D02	0.71	sample
1	E03	0.71	sample
1	G07	0.68	sample
2	F04	0.67	sample
2	G07	0.65	sample
1	D06	0.61	sample
1	D03	0.58	sample
1	G08	0.58	sample
1	F08	0.57	sample
1	B03	0.57	sample
2	C01	0.52	siControl
2	E04	0.5	sample
1	E10	0.49	sample
2	F08	0.45	sample
2	C05	0.44	sample
2	B03	0.43	sample
2	B09	0.43	sample
2	C02	0.42	sample
3	B07	0.42	sample
2	C07	0.41	sample
2	F06	0.4	sample
2	D05	0.39	sample
2	E08	0.38	sample
1	D05	0.37	sample
1	E05	0.34	sample
1	F02	0.31	sample
1	G09	0.27	sample

2	B04	0.25	sample
1	F10	0.19	sample
1	B09	0.19	sample
2	D04	0.14	sample
1	E11	0.14	sample
3	B09	0.13	sample
2	B07	0.13	sample
1	B04	0.12	sample
2	E11	0.12	sample
1	F09	0.11	sample
1	E09	0.09	sample
2	G04	0.09	sample
1	B05	0.06	sample
2	E03	0.06	sample
3	B11	0.06	sample
2	C10	0.04	siControl
1	E08	0	sample
2	G10	0	sample
2	B08	-0.03	sample
2	F03	-0.04	sample
1	D04	-0.1	sample
1	C04	-0.11	sample
1	G06	-0.11	sample
3	B04	-0.13	sample
3	C07	-0.17	siControl
2	E05	-0.17	sample
2	B02	-0.19	sample
2	D07	-0.2	siControl
2	C11	-0.23	sample
1	F05	-0.25	sample
2	C04	-0.25	sample
2	E07	-0.25	siControl
1	F07	-0.26	sample
3	B03	-0.27	sample
2	G05	-0.28	sample
2	C08	-0.28	sample
2	D06	-0.29	sample
2	E09	-0.3	sample
3	B10	-0.31	sample
1	C02	-0.32	sample
1	C01	-0.33	siControl
1	F06	-0.36	sample
1	D09	-0.38	sample
1	D10	-0.4	sample

1	E06	-0.41	sample
2	C03	-0.42	sample
2	G11	-0.42	sample
3	B06	-0.45	sample
1	D08	-0.49	sample
1	C08	-0.53	sample
2	G08	-0.54	sample
1	G11	-0.57	sample
1	C06	-0.58	sample
1	D07	-0.58	sample
2	G06	-0.59	sample
1	B11	-0.6	sample
2	B11	-0.67	sample
1	E07	-0.71	sample
3	C02	-0.74	sample
1	E04	-0.76	sample
2	D10	-0.78	sample
1	D11	-0.78	sample
2	D11	-0.79	sample
3	B08	-0.8	sample
2	F07	-0.86	sample
1	C09	-0.87	sample
3	C03	-0.89	siControl
1	C05	-0.9	sample
2	G09	-0.9	sample
1	C07	-0.97	sample
2	B05	-0.97	sample
2	F10	-0.98	sample
1	C10	-1.02	sample
1	B02	-1.11	sample
2	F11	-1.15	sample
2	D08	-1.18	sample
1	C11	-1.22	sample
2	D02	-1.23	sample
1	B10	-1.26	sample
2	E10	-1.36	sample
2	D03	-1.36	sample
1	B07	-1.47	sample
2	B10	-1.87	sample
2	F12	-2.27	positive
2	C12	-2.36	positive
1	F12	-2.5	positive
3	D02	-2.58	positive
1	C12	-2.77	positive

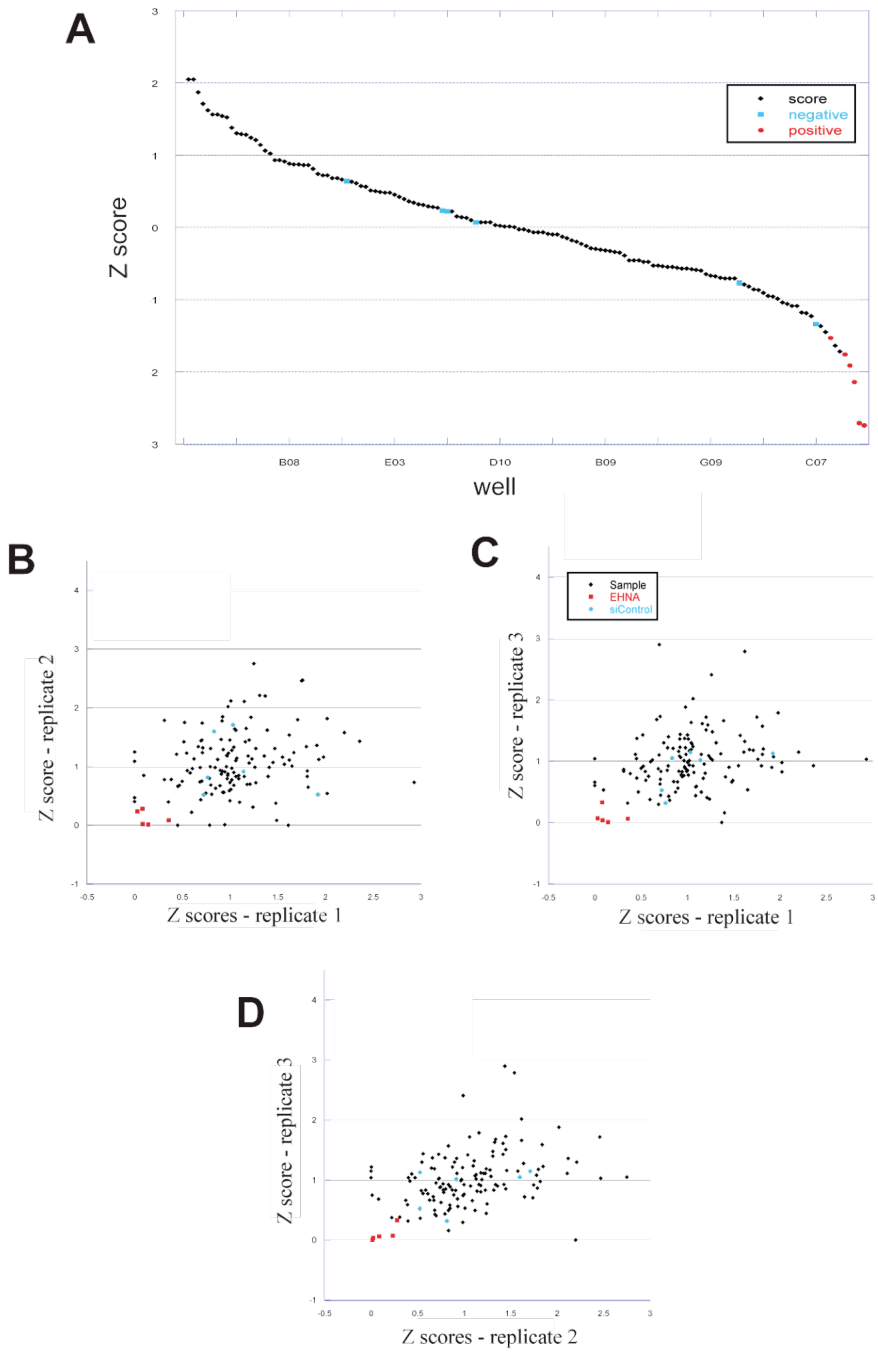

Figure 4.3 Summary of Z-scores for H_C.
The Z-scores for all the genes screened for H_C accumulation are plotted from the highest value to the lowest (A). The EHNA treated samples are highlighted in red, the siRNA controls in blue throughout the figure. The Z-scores from the first replicate of the screen are plotted against the Z-scores of the second replicate (B) and the third replicate(C). Finally the Z-scores from the second replica of the screen are plotted against the Z-scores of the third replicate (D). This representation gives an idea of how consistent the data are across the replicates. Ideally, if the data points are highly reproducible, the dot points should distribute as a diagonal line; the more the data are scattered, the less reproducible the data points were between the different replicas.

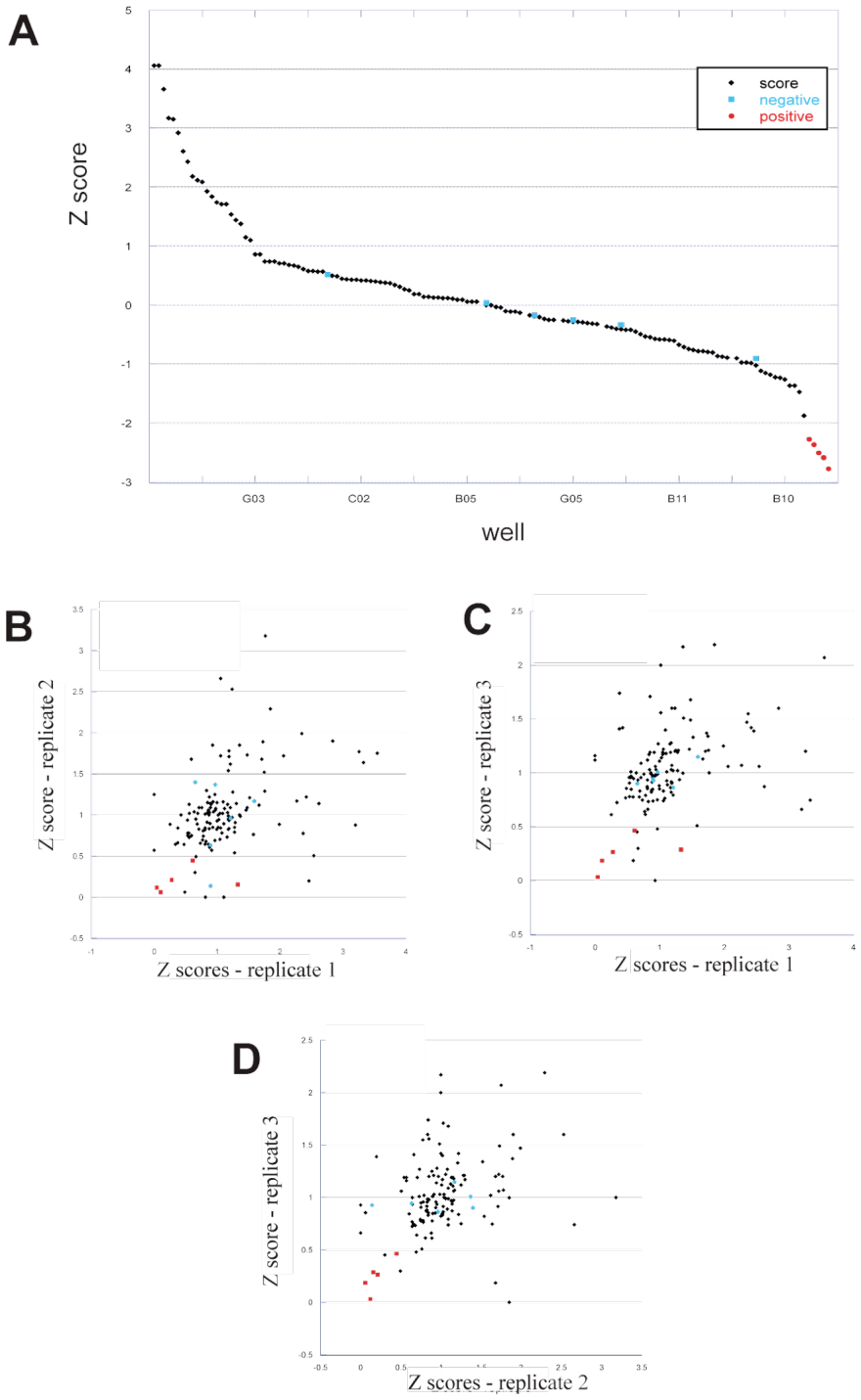

Figure 4.4 Summary of the siRNA screen for the p75^{NTR} antibody.
The Z-scores for all the genes screened for the p75^{NTR} antibody accumulation are plotted from the highest value to the lowest (A). The EHNA treated samples are highlighted in red, the siRNA controls in blue throughout the figure. The Z-scores from the first replicate are plotted against the Z-scores of the second (B) and the third (C) replicate. Finally, the Z-scores from the second replicate are plotted against the Z-scores of the third replicate (E).

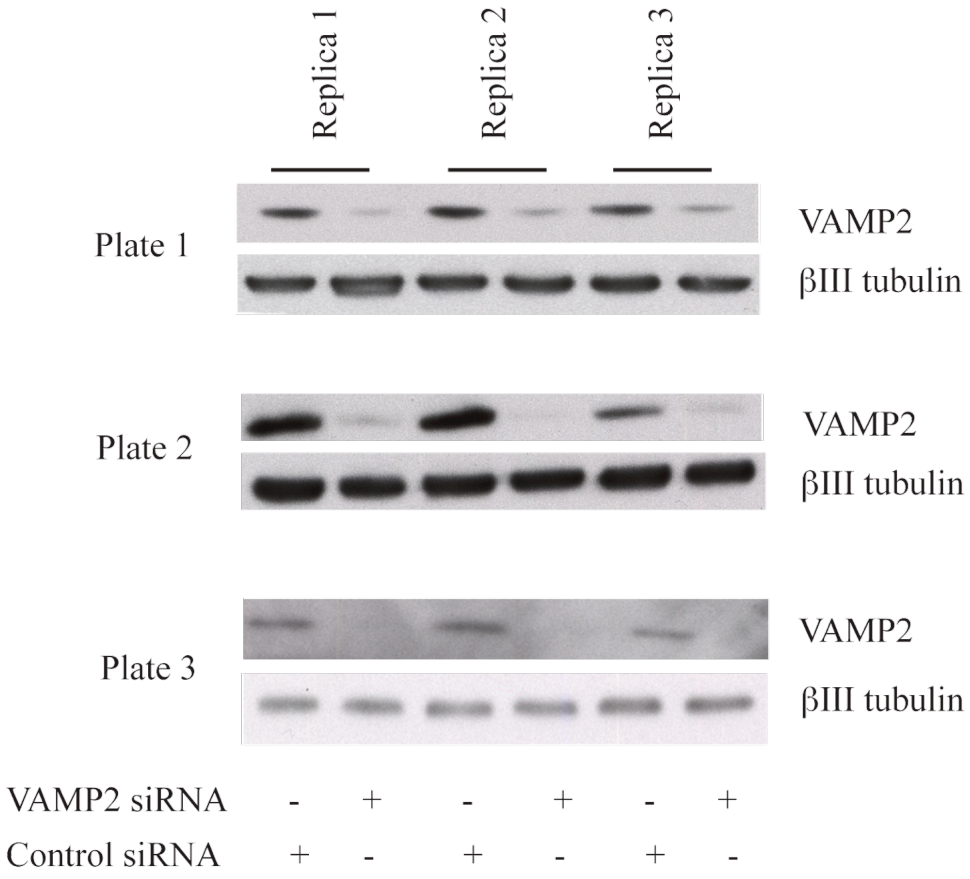

Figure 4.5 Internal control for knockdown efficiency of the siRNA screen.
Five wells from each plate were treated with siRNA control (see plate layout in **Figure 4.2**) and five with the VAMP2 siRNA pool. The protein lysates from each set of samples for each plate were pooled and analysed in Western blot to asses for knockdown efficiency. βIII tubulin was used as loading control.

4.4.1 Selecting the primary hits.

For the selection of the hits from the primary screen a threshold Z score had to be chosen. An upper limit of 1.5 standard deviations from the mean and lower limit of 0.7 for H_C and 1.5 – 0.8 for the $p75^{NTR}$ antibody was chosen (**Table 4.3, Table 4.4,** and Discussion, **section 7.1.5**).

In general, more putative negative regulators of the system have been identified, as shown by the fact that knockingdown most of the candidates resulted in an increased

rather than a decreased intracellular accumulation of the two probes. There were few hits in common for both probes. Down-regulation of the predicted gene EG231836 and Rab10 caused the increased accumulation of H_C and $p75^{NTR}$, whereas knockdown of Osbpl1a, Kif12 and Arl8b decreased the intracellular accumulation of the two probes. In addition, there seemed to be a prevalence of myosin motors amongst the genes that caused an increased accumulation of the two probes, and a prevalence of kinesin motors amongst the ones that caused a decreased accumulation (**Table 4.3 & 4.4**).

Table 4.3 TeNT H_C primary hits
All the genes that were considered hits from the primary screen are listed below together with their Z-score. The hits are divided by their ability to increase or decrease H_C accumulation. The hits common for H_C and the $p75^{NTR}$ antibody are highlighted in grey.

INCREASED INTRACELLULAR ACCUMULATION				
Z-score	**Symbol**	**Name**	**Gene ID**	**Accession number**
2.05	**BICD1**	bicaudal D homolog 1	12121	NM_009753
2.05	**MYL3**	myosin, light polypeptide 3	17897	NM_010859 XM_979450
1.87	**CORO1C**	coronin, actin binding protein 1C	23790	NM_011779
1.71	**DYNLT3**	dynein light chain Tctex-type3	67117	NM_025975
1.62	**EG231836**	predicted gene, EG231836	231836	XM_144611 XM_917042 XM_980715
1.56	**CENPE**	centromere protein E	229841	NM_173762
1.54	**MYO16**	myosin XVI	244281	NM_001081397 XM_356059 XM_906282 XM_975950 XM_976346 XM_977585
1.54	**RAB10**	RAB10, member RAS oncogene famiy	19325	NM_016676
1.52	**DYNC1LI2**	dynein, cytoplasmic 1 light intermediate chain2	234663	NM_001013380 XM_134573
DECREASED INTRACELLULAR ACCUMULATION				
Z-score	**Symbol**	**Name**	**Gene ID**	**Accession number**
-1.72	**KIF13B**	kinesin family member 13b	16554	XM_001001128 XM_001001137 XM_283218 XM_894888 XM_915018 XM_923518
-1.64	**KIF7**	kinesin family member 7	16576	XM_133575
-1.45	**DCTN1**	dynactin1	13191	NM_007835 XM_977604
-1.21	**DYNLL2**	dybein light chain LC8-type 2	68097	NM_026556

-1.17	**KIF12**	kinesin family member 12	16552	NM_010616
-1.16	**OSBPL1A**	oxysterol binding protein-like 1A	64291	NM_207530
-1.09	**MYH2**	myosin, heavy polypeptide 2	17882	NM_001039545 NM_144961
-1.09	**DYNC2LI1**	dynein cytomplasmic 2 light intermediate chain 1	213575	NM_172256 XM_984615 XM_985116
-1.06	**KIFC3**	kinesin family member C3	16582	NM_010631
-1.04	**MYH1**	myosin heavypolypeptide 1	17879	NM_030679 XM_354615
-0.99	**KIF15**	kinesin family member 15	209737	NM_010620
-0.96	**DNHD1**	dynein heavy chain domain 1	77505	XM_001000131 XM_355968 XM_908793 XM_983220
-0.95	**RAB5A**	RAB5a, member RAS oncogene family	271457	NM_025887
-0.7	**ARL8B**	Arl8b	67166	NM_026011

Table 4.4p75^{NTR} primary hits
All the genes considered hits from the primary screen are listed below together with their Z-score. The hits are divided by their ability to increase or decrease the p75^{NTR} antibody accumulation. The hits common for H_C and the p75^{NTR} antibody are highlighted in grey.

INCREASED INTRACELLULAR ACCUMULATION				
Z-score	**Symbol**	**Name**	**Gene ID**	**Accession number**
4.06	**MYH13**	myosin, heavy polypeptide 13, skeleta; muscle	544791	NM_001081250 XM_618893 XM_908247 XM_991668
4.06	**RAB7L1**	RAB7 family-like 1	226422	NM_144875
3.66	**DCTN2**	dynactin 2	69654	NM_027151
3.17	**MYL3**	myosin, light polypeptide 3	17897	NM_010859 XM_979450
3.15	**DYNLL1**	dynein light chain LC-type 1	56455	NM_019682
2.92	**RAB7**	RAB7	19349	NM_009005
2.61	**MYO9B**	myosin Ixb	17925	NM_015742
2.43	**EG231836**	predicted gene, EG231836	231836	XM_144611 XM_917042 XM_980715
2.18	**MYH7B**	myosin, heavy chain 7B	668940	XR_002269 XR_002637 XR_005103
2.12	**MYO10**	myosin X	17909	NM_019472
2.09	**KLC1**	kinesin light chain 2	16594	NM_008451
1.93	**MYHLC2B**	myosin light chain, regulatory B	67938	NM_023402
1.54	**RAB10**	RAB10	19325	NM_016676
DECREASED INTRACELLULAR ACCUMULATION				
Z-score	**Symbol**	**Name**	**Gene ID**	**Accession number**
-1.86	**KIF21B**	kinesin family member 21B	16565	NM_001039472 NM_019962
-1.47	**DYNC1I1**	dynein cytoplasimc 1 intermadiate chain 1	13426	NM_010063
-1.36	**KIF26B**	kinesin family member 21B	269152	NM_177757
-1.36	**DYNNLB2**	dynein light chain road-	75465	NM_029297

		block-type 2		
-1.26	**KIF2A**	kinesin family member 2A	16563	NM_008442
-1.22	**MXD3**	max dimerisation protein 3]	17121	NM_016662
-1.22	**MYO1B**	myosin 1B	17912	NM_010863
-1.2	**KIF15**	Kinesin family member 15	209737	NM_010620
-1.14	**OSBPL1A**	oxysterol binding protein-like 1A	64291	NM_207530
-1.11	**KIF1A**	kinesin family member 1A	16560	NM_008440
-1.02	**RAB8A**	RAB8a	17274	NM_023126 XM_981797
-0.98	**KIF12**	kinesin family member 12	16552	NM_010616
-0.98	**KIF3A**	kinesin family meber 3A	16568	NM_008443
-0.97	**KIF11**	kinesin family member 11	16551	NM_010615
-0.8	**ARL8B**	ADP-rybosilation factor-like 8B	67166	NM_026011

4.5 Hit validation

4.5.1 Validation using Dharmacon smart pools

There are several strategies commonly used to validate the hits from an siRNA screen. The idea behind the validation is to assess whether or not a particular phenotype registered in the primary screen is due to the knockdown of the gene or is instead a consequence of off-target effects. A commonly used way to assess such off-target effects is to "deconvolute" the siRNA pool for each one of the hits, i.e. to test each oligo from the pool separately. A hit will be validated as a genuine candidate if at least two out of three of the single duplexes reproduce the phenotype observed. Another way of validating the hits is to order siRNA pools from a different supplier and to test whether they result in the same phenotype as those used in the primary screen. This is because each company has its own algorithm to design siRNA duplexes, which means that siRNA pools from different suppliers tend to target different parts of the transcript.

I decided to use the second approach for the validation of the primary screen, because it allowed me to contain the size of the rescreen library to one plate and it was considerably cheaper to buy the Dharmacon SMART pools than the single Qiagen

siRNA duplexes. SMART pools from Dharmacon were, therefore, tested for each one of the primary hits. The siRNA pools came in a 96-well plate format (Materials and Methods section, **table 2.5**), and they were screened as described for the primary screen (**section 4.3.2** of this Chapter).

4.5.2 Selecting the hits from the validation re-screen

The validation re-screen with the Dharmacon siRNA pools was performed five times and the data for the replicates were pooled together for each of the individual genes and controls. As for the primary screen, the number of positive vesicles for H_C and the $p75^{NTR}$ antibody per cell body was quantified using the Cell profiler software. In the case of the primary screen, these data were fed to the Cell HTS software to calculate the Z-scores. However in the case of the validation screen, the siRNA pools are selected for their ability to affect the readout, which means that the population is not normally distributed, which is a pre-requisite for calculating the Z-scores (**section 4.3.2** of this Chapter). For this reason the data from each siRNA pool were compared to the median of the siRNA controls, instead of to the median of the whole validation siRNA library (**Figure 4.6**).

From the primary hits, only the knockdown of BICD1 was confirmed to increase the accumulation of H_C, while the knockdown of DCNT1, DYNC2LI1, KIF3C and KIF15 seemed to reduce the accumulation of this probe, in accordance with what was observed in the primary screen (see **Table 4.5** and **Figure 4.6**).

Table 4.5 H_C scores from the validation of hits obtained from the primary screen.

The score for each candidate is indicated together with the value obtained by subtracting the median of the siRNA controls from the individual score for each gene. The candidates that were considered to be genuine as "validated" are highlighted in yellow. The scores of the siControls and the EHNA-treated samples are reported and highlighted in grey. The scores are obtained by calculating the mean of the values of the five replicates for each candidate gene. A candidate is considered "validated" if its knockdown consistently showed the same effect as previously observed in the primary screen.

Mean of the siControls	**Mean of EHNA treated samples**	
1.1911315	**0.11340095**	
INCREASED INTRACELLULAR ACCUMULATION		
Candidate name	**Score**	**Score minus the median of the siControls**
BICD1	1.831421	0.6402895
MYL3	1.2197258	0.0285943
CORO1C	1.26823372	0.07710222
DYNLT3	0.66562036	-0.52551114
EG231836	1.24756302	0.05643152
MYO16	1.42768216	0.23655066
CENPE	0.8220231	-0.3691084
RAB10	0.95982068	-0.23131082
DYNC1LI2	1.1063869	-0.0847446
DECREASED IINTRACELLULAR ACCUMULATION		
Candidate name	**Score**	**Score minus the median of the siControls**
KIF13B	0.86119454	-0.32993696
KIF7	0.87835562	-0.31277588
DCTN1	0.75369896	-0.43743254
DYNLL2	1.0708651	-0.1202664
KIF12	1.1888181	-0.0023134
OSBPL1A	0.87861126	-0.31252024
MYH2	1.05655968	-0.13457182
DYNC2LI1	0.78353784	-0.40759366
KIF3C	0.70126436	-0.48986714

MYH1	1.01950226	-0.17162924
KIF15	0.71261168	-0.47851982
DNHD1	1.16207428	-0.02905722
RAB5A	1.2500167	0.0588852
ARL8C	1.31220688	0.12107538

Only the knockdown of RAB7 was confirmed to increase the intracellular accumulation of the $p75^{NTR}$ antibody, whilst the knockdown of KIF21B, MXD3 and KIF11 seemed to reduce its accumulation, consistent with the results of the primary screen (**Table 4.6**).

Table 4.6 $p75^{NTR}$ antibody scores from the validation of hits obtained from the primary screen.
The score for each candidate is indicated together with the value obtained by subtracting the median of the siRNA controls from the individual score for each gene. The candidates that were considered "validated" are highlighted in yellow. The scores of the siControls and the EHNA-treated samples are reported and highlighted in grey. The scores are obtained by calculating the mean of the values of the five replicates for each candidate gene. A candidate is considered "validated" if its knockdown consistently showed the same effect as previously observed in the primary screen regarding the $p75^{NTR}$ antibody accumulation compared to the controls.

Median of the siControls	**Median of EHNA treated samples**	
1.313071	**0.1074658**	
INCREASED INTRACELLULAR ACCUMULATION		
Candidate name	**Score**	**Score minus the median of the siControls**
MYH13	1.48087468	0.16780368
RAB7L1	0.85880744	-0.45426356
DCTN2	0.9419114	-0.3711596
MYL3	1.23503192	-0.07803908
DYNLL1	1.22249072	-0.09058028
RAB7	1.5793482	0.2662772
MYO9B	0.88561824	-0.42745276
EG231836	0.80367186	-0.50939914
MYH7B	0.50435852	-0.80871248
MYO10	0.85313542	-0.45993558
MYLC2B	1.27796624	-0.03510476

RAB10	1.15070274	-0.16236826
DECREASED INTRACELLULAR ACCUMULATION		
Candidate name	**Score**	**Score minus the median of the siControls**
KIF21B	0.73966624	-0.57340476
DYNC1I1	1.16264346	-0.15042754
KIF26B	0.90418152	-0.40888948
DYNLRB2	0.95027282	-0.36279818
KIF2A	1.13100118	-0.18206982
MXD3	0.73556886	-0.57750214
MYO1B	1.09169806	-0.22137294
KIF15	1.0111803	-0.3018907
OSBPL1A	1.12998484	-0.18308616
KIF1A	1.05208572	-0.26098528
RAB8A	1.3917102	0.0786392
KIF12	1.32336156	0.01029056
KIF3A	1.5711236	0.2580526
KIF11	0.84326322	-0.46980778
ARL8C	1.09350966	-0.21956134

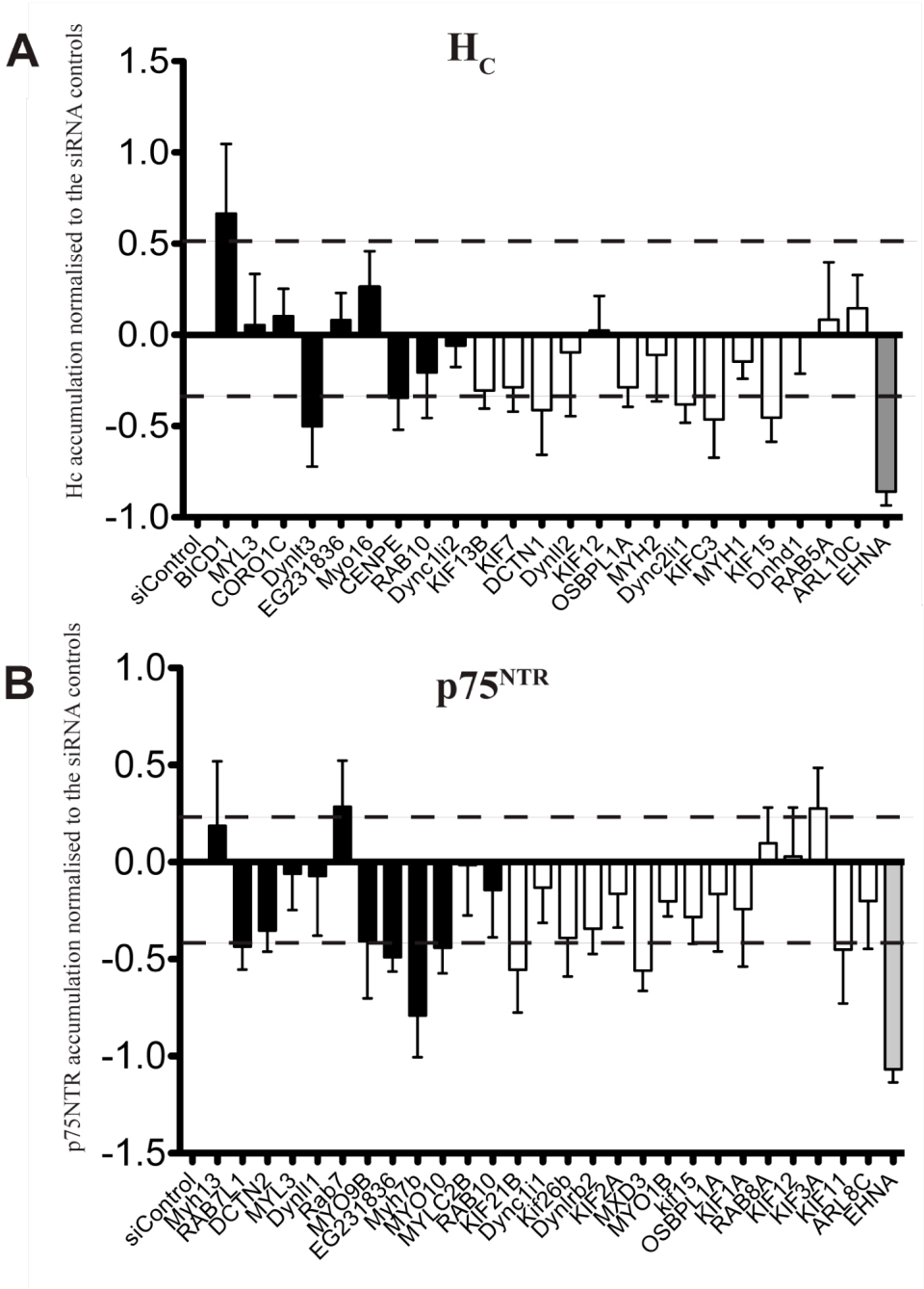

Figure 4.6. Charts of the scores of the validation screen.
The relative scores of the accumulation of Hc (A) and $p75^{NTR}$ (B) for each candidate gene are plotted (**section 4.4.1** of this Chapter). The columns corresponding to the genes that resulted in an increased intracellular accumulation of each probe in the original screen are coloured in black, while the ones corresponding to the genes that resulted in a decreased intracellular accumulation of the probes are coloured in white. They were subtracted from the median of the siRNA controls, in order to clearly visualise whether their knockdown increased or decreased the internalisation of the two probes compared to the controls. In summary, the knockdown of BICD1 increased H_C accumulation, whilst knocking-down DCNT1, DYNC2LI1, KIF3C and KIF15 caused decreased H_C accumulation consistent with what was observed in the primary screen (A). Knockdown of RAB7 was confirmed to increase $p75^{NTR}$ accumulation, and KIF21B, MXD3 and KIF11 to decrease it (B).

Summary of the achievements presented in this Chapter

- *EHNA was selected as a positive control for the internalisation assay of the two probes, because of its ability to decrease the accumulation of H_C and $p75^{NTR}$ in MNs derived from HB9-GFP ES cells.*

- *The siRNA screen was performed in triplicates with an siRNA library of molecular motors and adaptors covering 155 genes.*

- *Images were analysed using the Cell Profiler software and the resulting values were transformed into Z-scores using the Cell HTS software.*

- *A list of primary hits were chosen on the basis of the Z-score ranking and corresponding Dharmacon siRNA smart pools were used to re-screen the primary hits.*

- *The results suggested that the knockdown of **BICD1** increased H_C accumulation, whilst knocking-down **DCNT1, DYNC2LI1**, **KIF3C** and **KIF15** inhibited H_C accumulation in agreement with the results obtained in the primary screen. The data also suggested that the knockdown of **RAB7** was confirmed to increase*

*$p75^{NTR}$ accumulation, whilst **KIF21B**, **MXD3** and **KIF11** down-regulation decreased it.*

Chapter 5. BICD family of proteins

The Bicaudal-D family of proteins was originally identified in *Drosophila*, where two dominant maternal-effect mutants were characterised, in which a large proportion of the embryos presented an anterior to posterior mutation, hence the name "bicaudal", which in Latin means "two tails" (Mohler and Wieschaus, 1986). In metazoan animals the BICD protein is highly conserved, with only one isoform present in invertebrates and two (BICD1 and BICD2) in mammals, which also have two BICD-related proteins (BICD-R1 and BICD-R2) (**Figure 5.1 A**).

Mammalian BICD1 and BICD2 proteins share a good degree of homology; they both have 3 coiled-coil regions, with the C-terminal one being the most conserved between the two proteins with 93% identity. BICD-Rs, instead, have only two coiled-coil domains and their similarity to BICDs is lower than 30% (**Figure 5.1 A**).

5.1.1 Drosophila BICD

In *Drosophila* the BICD protein is essential for the correct specification of the oocyte, a process which requires a microtubule-dependent accumulation of specific mRNAs. BICD plays a role in determining the correct subcellular localisation of a certain number of mRNAs during oogenesis and embryogenesis. In order to execute this function, BICD, which has no RNA binding motifs, needs to form a complex with the Egalitarian protein (Egl) (Bullock and Ish-Horowicz, 2001). BICD has also been implicated in dynein-driven nuclear migration along microtubules in partnership with the protein Lissencephaly 1 (Lis1), and in bidirectional transport of lipid droplets in the

Drosophila blastoderm embryo (for a more comprehensive description of the roles of BICD in *Drosophila* see (Dienstbier and Li, 2009)).

Interestingly, a very recent paper pointed to a role for BICD in *Drosophila* neurons, reporting that zygotic BICD function is obligatory only in the nervous system (Li et al., 2010). BICD directly associates with clathrin heavy chain (CHC) and this association has been shown to be instrumental for the correct localisation of CHC in synaptic boutons, suggesting that BICD plays a role in dynein-mediated recycling of CHC at the synaptic plasma membrane. This function is required to maintain normal levels of neurotransmission during prolonged high-frequency electrical stimulation (Li et al., 2010) (**Figure 5.1 A**).

5.1.2 Mammalian BICDs

The first protein of the BICD family to be cloned in mammals was BICD1, whose human and murine cDNA was cloned in 1997 (Baens and Marynen, 1997). This paper established by Northern blot that BICD1 mRNA is expressed in brain, heart and skeletal muscle in both humans and mice (Baens and Marynen, 1997).

BICD2 was isolated in a yeast two-hybrid screen for interactors of the microtubule binding protein CLIP-115 (Hoogenraad et al., 2001). It was then found that BICD2 was involved in microtubule-dependent transport via its direct interaction with dynamitin (p50), a subunit of dynactin, which is part of the cytoplasmic dynein/dynactin motor complex. During interphase BICD2 localises to the Golgi and to the minus ends of microtubules together with dynactin (Hoogenraad et al., 2001).

5.1.3 BICD regulates COPI-independent Golgi to ER transport

An additional function of mammalian BICD proteins was discovered in 2002, when BICD1 was found in a yeast two-hybrid screen for interactors of Rab6 (Matanis et al., 2002). BICD1 and BICD2 are both able to bind the C-terminal domain of the GTP bound form of Rab6A through their C-terminal regions. Furthermore, BICD1 and 2 interact with the dynein complex through their N-terminal domains (Matanis et al., 2002). BICD1 and 2 were also found to colocalise with Rab6A on the trans-Golgi network (TGN) and on cytoplasmic vesicles associated with the Golgi apparatus. This cellular localisation is dependent upon Rab6A and the recruitment of cytoplasmic dynein by Rab6A-containing vesicles is enhanced by overexpression of BICD1 (Matanis et al., 2002). Overexpression of the C-terminal domain of BICD1 and BICD2, which does interact with Rab6A but not with dynein, inhibits the movement of Rab6A-positive vesicles towards the minus end of microtubules, causing their accumulation in the cell periphery. These Rab6A-positive structures contain COPI-independent ER cargoes such as β1,4-galactosyltransferase (GalTase), which suggests that the concerted action of the dynein complex, Rab6A and BICD plays a role in the regulation of the COPI-independent Golgi to ER transport (Matanis et al., 2002) (**Figure 5.1 B**).

5.1.4 BICD2 regulates the transport of Rab6 positive exocytotic carriers

In all eukaryotic cells, there is a route of transport, mediated by Golgi-derived vesicles, that leads to constitutive exocytosis of newly synthesized lipids, membrane proteins and components of the extracellular matrix. These exocytotic carriers bud off the TGN and move along microtubules towards the periphery of the cell, where they finally fuse with the plasma membrane. The knock-down of Rab6A, which was found on their surface, does not prevent their exocytosis, but affects their movement and

processivity (Grigoriev et al., 2007). Kinesin-1 (KIF5B), a plus-end microtubule motor, is also involved in the motility of Rab6A exocytotic carriers and interestingly, BICD2 was also found to interact with KIF5B. Together these observations suggest that the interaction between kinesin-1, BICD2 and Rab6A is likely to play a role in the trafficking of Rab6A exocytotic carriers from the TGN to the plasma membrane (**Figure 5.1 B**).

5.1.5 BICDs and axonal retrograde transport in neurons

BICD1 has also been found to interact with the active form of Rab6B, which is predominantly expressed in the brain (Wanschers et al., 2007). These two proteins colocalise on the Golgi apparatus and on vesicles aligned along microtubules. Furthermore, BICD1 co-localises with dynein in the neurites of differentiated SK-N-SH cells, where BICD1-associated vesicles undergo bi-directional movements. These observations suggested that BICD1 together with Rab6B might control retrograde transport of cargoes in neurons (Wanschers et al., 2007).

Interestingly BICD2 has been used as a tool to influence axonal retrograde transport (Teuling et al., 2008). There is genetic evidence, that correlates mutations of the dynein/dynactin complex with the pathogenesis of motor neuron deseases (LaMonte et al., 2002, Hafezparast et al., 2003). A transgenic mouse expressing the N-terminus of BICD2 under the control of the neuronal specific Thy 1 promoter was generated to investigate the effect of chronic impairment of the dynein/dynactin complex in neurons *in vivo*. The expression of the N-terminus of BICD2 causes an over-accumulation of dynein/dynactin complexes in the cell body of MNs and Golgi fragmentation, indicating an impairment of retrograde trafficking. Unexpectedly these transgenic mice did not

develop any sign of motor neuron degeneration or motor abnormalities (Teuling et al., 2008). These mice were also crossbred with a mouse model of amyotrophic lateral sclerosis (ALS), the SOD1-G93A strain, to determine whether impairing axonal transport would worsen the phenotype. However, these mutant mice surprisingly had an increased lifespan (Teuling et al., 2008).

5.1.6 BICDs and the centrosome

Another important function of BICD1 is associated with its localisation to the centrosome. It is known that during mitosis GSK-3β interacts with microtubules and accumulates at the centrosomes and spindle poles (Wakefield et al., 2003). GSK-3β phosphorylates BICD1, thus stabilising its interaction with the dynein complex which is required for the anchoring of the microtubules to the centrosome (Fumoto et al., 2006). The role of BICD1 in this context is likely to be the regulation of the dynein mediated transport of proteins necessary for the tethering of microtubules to the centrosome. One such protein is ninein, a minus-end capping protein essential for this process (Bornens, 2002) (Delgehyr et al., 2005). BICD1 directly interacts with ninein and its knockdown affects its centrosomal localisation, suggesting that BICD1 is an adaptor for ninein recruitment to cytoplasmic dynein (Fumoto et al., 2006) (**Figure 5.1 B**).

Recently it was shown that BICD2 influences the relative positioning of the nucleus and the centrosomes in dividing cells (Splinter et al., 2010). BICD2 was found to bind a component of the nuclear pore complex (NPC), the RAN binding protein 2 (RanBP2), during the G2 phase of the cell cycle. In this context BICD2 would be able to recruit the dynein/dynactin complex to NPCs, playing a role in the tethering of the

centrosomes to the nucleus before mitotic entry. Kinesin-1 was found to counteract the dynein complex, pushing apart the duplicated centrosomes from the nuclei in late G2. Depletion of BICD2, but not BICD1, affected not only the dynein-mediated tethering of the centrosome to the nucleus, but also prevented the kinesin-1 function. These data reveal that BICD2 is a key molecular motor adaptor, capable of regulating the action of dynein and kinesin-1 in positioning the nucleus and the centrosomes prior to mitosis. (**Figure 5.1 B**)

5.1.7 BICD1 and receptor endocytosis

Using a yeast two-hybrid screen approach, BICD1 was found to interact with the C-terminal domain of the protease-activated receptor 1 (PAR1) (Swift et al., 2010), a G protein-coupled receptor, which has been shown to be important in cancer, angiogenesis, inflammation and thrombosis (Ossovskaya and Bunnett, 2004). The internalisation of PAR1 is dynamin- and clathrin-dependent (Trejo et al., 2000). BICD1 colocalises with PAR1 and tubulin, and its silencing caused an impairment of activated PAR1 endocytosis, which suggests that BICD1 has a role in regulating the transport of the activated receptor from the plasma membrane to the endosomal compartment (**Figure 5.1 B**). Moreover, BICD1 knockdown affected PAR1 signalling, inhibiting the PAR1-driven proliferation of breast carcinoma cells. These observations link for the first time a BICD protein to the internalisation of a receptor. In addition, this effect on endocytosis also has repercussions for the signalling of the receptor itself, which highlights the fact that molecular motor adaptors might be key players in signalling as well as intracellular trafficking.

5.1.8 The trafficking of pp150 is dependent on BICD1

The tegument protein pp150 is an abundant constituent of the human cytomegalovirus (HCMV) virion, for which both nuclear and cytoplasmic localisations have been reported. Its function is still unknown: however, it is essential for the production of a fully infectious virus. BICD1 was found to interact with pp150 in a yeast two-hybrid screen (Indran et al., 2010). BICD1 knockdown caused a decreased viral yield, which could be explained by a defect in the localisation of pp150, which failed to traffic to the cytoplasmic viral assembly compartment (AC). Moreover, the overexpression of dynamitin (p50), a subunit of dynactin, which is able to disrupt the dynein complex, and the N-terminus of BICD1, which acts as a dominant-negative, caused a disruption of the AC, which resulted in a decreased viral yield. These data provide evidence that the assembly of HCMV is dynein-dependent and that the molecular motor adaptor BICD1 is instrumental in this process, determining the correct localisation and function of the tegument protein pp150.

5.1.9 BICDR-1 regulates neuritogenesis

The latest addition to the BICD family of proteins in mammals are BICD-related protein 1 (BICDR-1) and 2 (BICDR-2) (Schlager et al., 2010)(**Figure 5.1**). Murine BICDR-1 is predominantly expressed in kidney and brain, while BICDR-2 could not be detected by Northern blot or tissue dot blot. The C-terminal region of BICDR-1 interacts with Rab6A and B and BICDR-1 is also able to bind the dynein/dynactin and KIF1C motor complexes. Through its interaction with the dynein and kinesin molecular motors, BICDR-1 determines the pericentrosomal localisation of Rab6-positive secretory vesicles, preventing their secretion and also inhibiting neuritogenesis. Interestingly, the expression of BICDR-1 in mouse development is high at early stages

of embryonic development (embryonic day 10) and then drops off rapidly. A similar pattern is replicated *in vitro* in hipppocampal cultures, where BICDR-1 expression levels drop at 3 days in vitro (DIV 3). These results suggest that BICDR-1 plays a role in the temporal regulation of the secretory trafficking in neurons, sequestering Rab6 positive secretory vesicles around the centrosome (**Figure 5.1 B**). This functional block is then released when neuritogenesis has to occur by dropping the level of expression of BICDR-1.

Table 5.1 Mammalian BICDs, BICD-related proteins and their interaction partners.
Summary of the known interactors of mammalian BICD and BICD-R proteins. The interacting partner is specified together with the region of the BICD protein it interacts with (if known). Modified from (Dienstbier and Li, 2009).

BICD interacting proteins			
Interacting partner	**BICD protein**	**BICD interacting fragment**	**Reference(s)**
Kinesin 1 heavy chain	BICD2	336-595	(Grigoriev et al., 2007)
GSK-3β	BICD1	437-617	(Fumoto et al., 2006)
RAB6A	BICD2		(Matanis et al., 2002)
RAB6A, RAB6B	BICD1	673-803	(Matanis et al., 2002)
Ninein	BICD1	Full length	(Fumoto et al., 2006)
pp150	BICD1	343-835	(Indran et al., 2010)
PAR1	BICD1	Full-length	(Swift et al., 2010)
RAB6A, RAB6B	BICDR-1	382-577	(Schlager et al., 2010)
KIF1C	BICDR-1	Full-length	(Schlager et al., 2010)
Dynein-dynactin complex	BICDR-1	Full-length	(Schlager et al., 2010)
p50 dynamitin	BICD2	706-810	(Hoogenraad et al., 2001)
Dynein intermediate chain	BICD2	1-271	(Hoogenraad et al., 2001)
Dynein-dynactin complex	BICD2	1-575	(Hoogenraad et al., 2001)
RANBP2	BICD2	487-820	(Splinter et al., 2010)

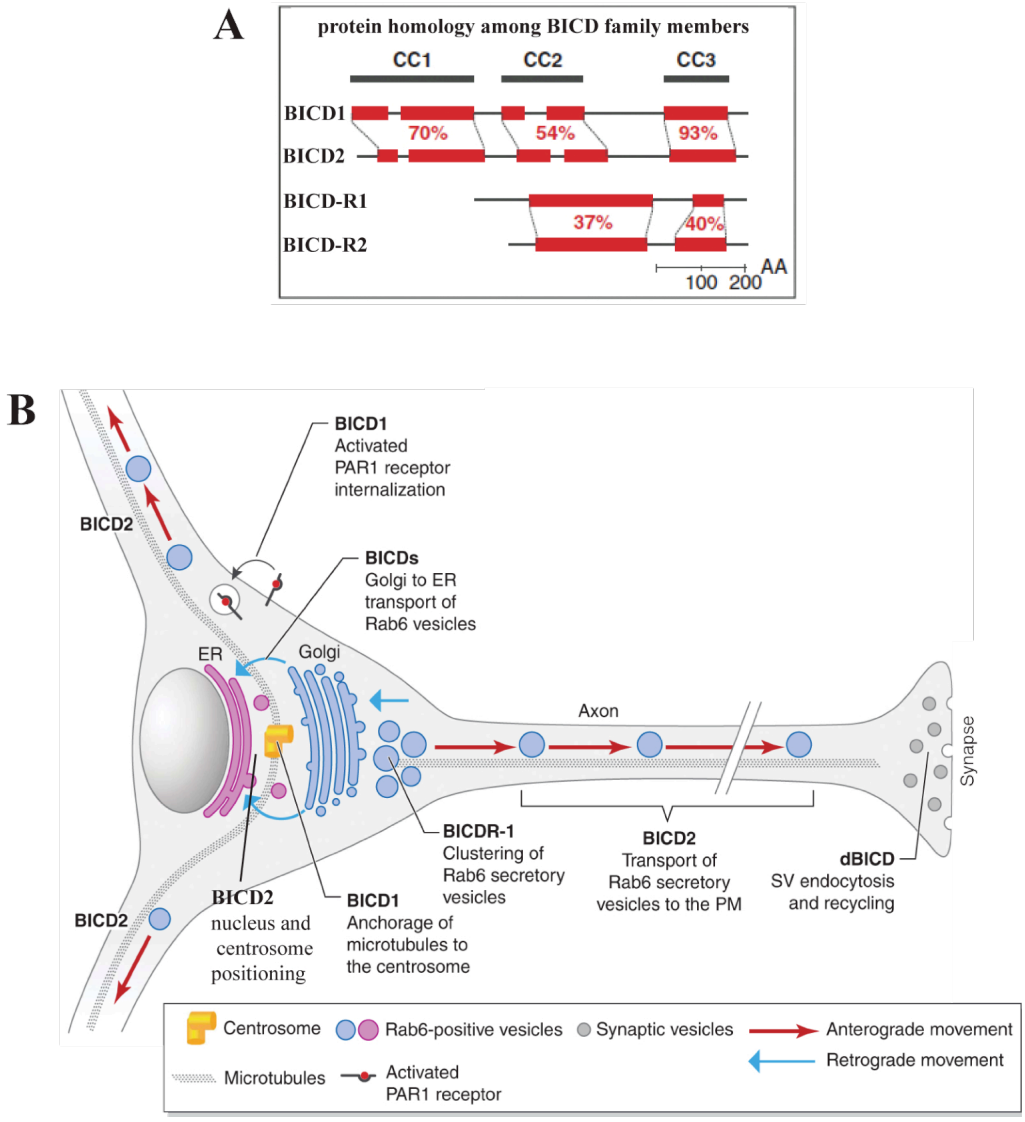

Figure 5.1 Structure and function of mammalian BICDs and their possible roles in neurons
The secondary structure of the four known members of the BICD family in mammals are reported and related to one another in terms of percentage of identity (A). BICD1 and BICD2 have three coiled-coil domains (CC, in black), which share a high percentage of identity, expecially in the C-terminal region (CC3), which is 93% identical. BICD-R1 and BICD-R2 have only two CC domains. BICDs and BICD-R share less than 30% identity (Probir Chakravarty, Cancer Research UK London Research Institute). The possibile roles of BICD family members in neurons (B). The only known role of dBICD in Drosophila neurons is also indicated (see section 1.4.1.). Both schematics are adapted from (Terenzio and Schiavo, 2010).

Chapter 6. Characterisation of the role of BICD1 in motor neurons

6.1 Introduction

BICD1 is one of the four members of the mammalian BICD family of proteins (Chapter 5, **section 5.4**), and is an adaptor for the dynein/dynactin motor complex. It also has a plethora of interactors and it has been associated with several cellular functions, such as COPI-independent Golgi to ER retrograde transport, the anchorage of dynein to the centrosome, the endocytosis of PAR1 receptor and the trafficking of the cytomegalovirus protein pp150. All of these roles have been described in cancer cell lines; however, nothing is known of the function of mammalian BICD1 in primary cells, especially in neurons. In this Chapter, a mouse ES cell line lacking the BICD1 protein was used to explore the function of BICD1 in MNs, with particular focus on the possible relationship between this protein and the trafficking of neurotrophins and their receptors.

Note: Previously when using an acronym the reference was always to the corresponding protein, however in this chapter it is necessary to refer to the gene as well. Acronyms in uppercase (i.e. BICD1) will, therefore, been used throughout this chapter to indicate the corresponding protein, whilst lowercase and italics (i.e. *Bicd1*) will refer to the gene (http://www.informatics.jax.org/mgihome/nomen/gene.shtml).

Aim of the work presented in this chapter:

- *Justification for the decision to choose the BICD1 protein as a candidate from the screen for further characterisation;*

- *To characterise MNs derived from an ES cell line gene-trapped for Bicd1 and to confirm the BICD1 knockdown phenotype observed in the screen;*

- *To further investigate the molecular basis of the phenotype observed.*

6.2 The choice of BICD1 as the candidate to characterise

I had to decide on a candidate gene from the screen to characterise further. Some of the candidates from the siRNA screen were expected, such as RAB7, for example, which we already knew was involved in the axonal retrograde transport of $p75^{NTR}$, or DCNT1, which is a component of the dynein/dynactin motor complex and is known to play a role in axonal retrograde transport and intracellular trafficking of H_C (Lalli et al., 2003).

BICD1 was a very interesting candidate, because of its well-described role as a microtubule-associated protein and more importantly as a dynein adaptor. BICD1 was also described to interact with the neuronal isoform of RAB6, RAB6B, and was proposed to play a role in axonal retrograde transport in neurons (Wanschers et al., 2007). We were intrigued by the possibility of BICD1 being an important player in the trafficking of H_C and possibly of neurotrophins and their receptors. I decided, therefore, to concentrate my efforts on this candidate.

6.3 Derivation of MNs from *Bicd1* gene-trapped mouse ES cells

6.3.1 Use of *Bicd1* gene-trapped mouse ES cells to generate MNs

The knockdown protocol perfected for Hb9-GFP ES cell derived MNs was designed to be effective in a 96-well plate format. However, it would have to be modified and adapted to other formats and to a more traditional forward transfection protocol in order to suit the needs of the molecular characterisation of BICD1. In addition, to check for off-target effects due to the siRNA technology, I wanted to verify the BICD1 phenotype observed in the screen by taking a different knockdown approach

(Discussion, **section 7.3**). I decided, then, to take advantage of the possibility of deriving MNs from mouse ES cells. Three mouse ES cell lines where used: a heterozygous gene trap ES cell line for the *Bicd1* gene (*Bicd1*$^{gt/+}$, clone RRP27) generated by the International Gene Trap Consortium (IGTC, http://www.genetrap.org/), a homozygous cell line generated from the RRP27 clone by Krzyzstof Wicher (Developmental Genetics laboratory at CRUK) (Materials and Methods, **section 2.2.4.7**), and a wild type Sv 129 mouse ES cell line kindly provided by Ian Rosewell (Transgenic Facility at CR-UK). The Sv 129 ES cell line, derived from an outbred mouse strain, was the same one used by the IGTC to generate the RRP27 ES cell clone.

The same protocol established for MN differentiation from the HB9-GFP ES cells was successfully used to generate MNs from all the three *Bicd1* genotypes (Material and Method, **section 2.2.4.5** and Chapter 3, **section 3.3.3**).

6.3.2 Gene trap technology

Gene trap technology allows the generation of transgenic ES cells through the use of a vector designed to randomly insert into a genomic sequence, intronic or a protein coding region, and interrupt the transcription of a trapped gene. In the basic version of a gene trap vector, corresponding to the one used to generate the *Bicd1* gene trapped ES cell line used for this study, the insertion cassette contains a splice acceptor site (SA), which interrupts downstream splicing of the trapped gene and instead causes transcription of the vector sequence. With this strategy the endogenous promoter of the mutated gene is used to express the gene trap vector, which usually contains a combination of a reporter and selection gene (in this case the β−galactosidase +

neomycin R genes) (**Figure 6.1 A** and **B**). The end result is the production of a truncated fusion protein containing the exons upstream of the point of insertion of the vector, followed by the vector cassette. If the insertion of the vector occurs after the first exon, it results in a functional deletion of the trapped gene. The trapped gene is identified using a PCR primer designed in the 5' region of the vector cassette to sequence the cDNA upstream of the vector (**Figure 6.1 B**).

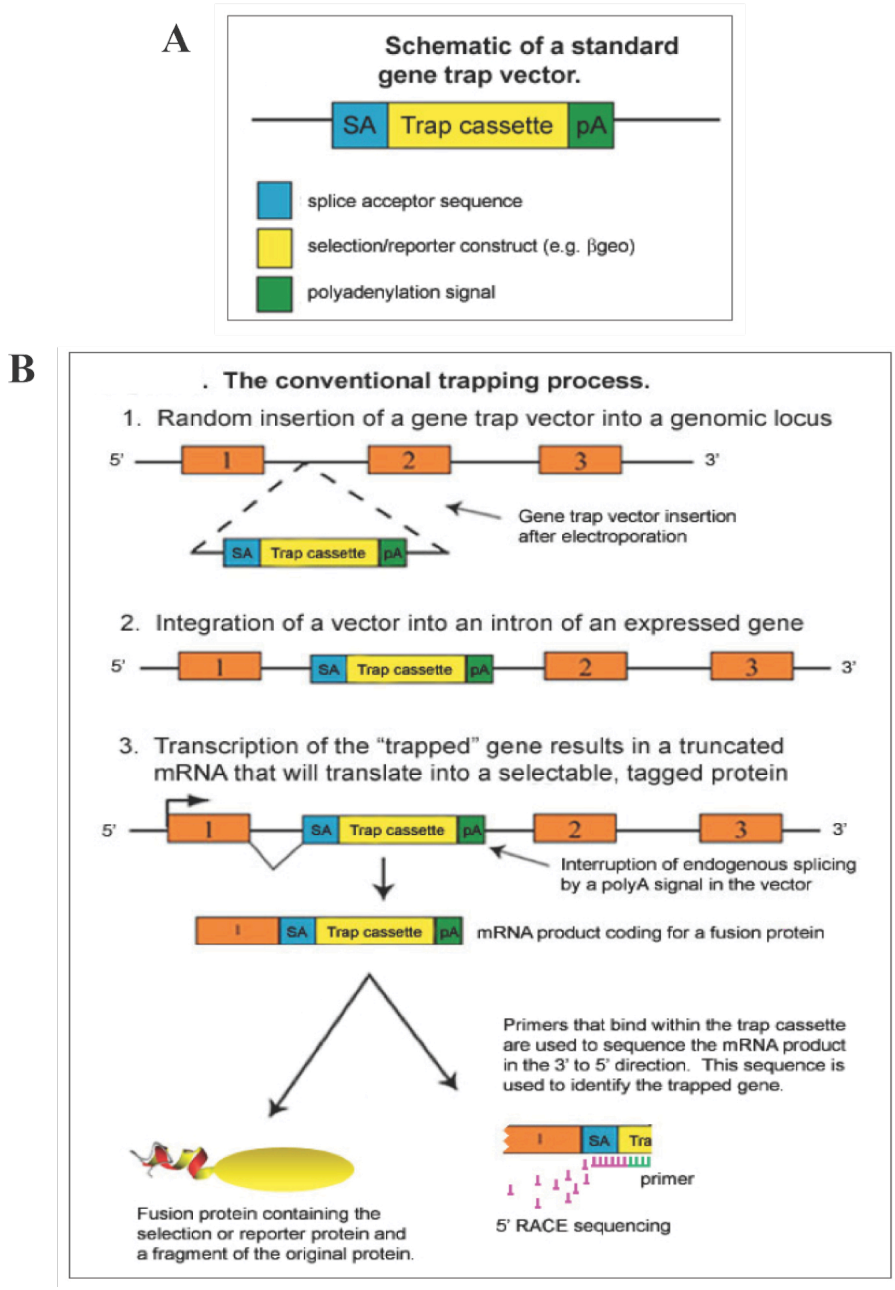

Figure 6.1. Gene trap vector and strategy.
Schematic of a standard gene trap vector, composed of a splicing acceptor site (SA), a reporter and selection gene (Trap cassette), and a poly A tail (pA), (A). Flowchart of a conventional gene trap strategy (B). Because the vector is inserted randomly in the genome, a primer located in the 5' region of the cassette is used to sequence (5' RACE sequencing) upstream of the integration site and therefore identify the gene that has been trapped. The figure is adapted from http://www.genetrap.org/tutorials/overview.html#limitations.

6.4 Characterisation of *Bicd1*$^{gt/+}$ and *Bicd1*$^{gt/gt}$ MNs

6.4.1 *Bicd1*$^{gt/+}$ and *Bicd1*$^{gt/gt}$ MNs die earlier in culture compared to wild type MNs

Morphologically, the cultures of differentiated MNs looked similar in the three genotypes. However, fewer non neuronal cells seemed to be present in *Bicd1*$^{gt/gt}$ MNs cultures. Cell survival seemed also different. Preliminary data showed that *Bicd1*$^{gt/gt}$ MNs die two weeks after dissociation from the EBs if cultured in full medium and after 9 – 10 days if cultured in the presence of arabinofuranosyl cytidine (Ara-C), a drug that selectively kills proliferating cells. Ara-C was used in order to stop the proliferation of glia, thus enriching the culture for neurons. However MNs appeared to be more fragile, possibly because they did not receive the trophic support normally provided by the glial cells. This was more evident for *Bicd1*$^{gt/gt}$ MNs, which seems to be more susceptible to cell death than wt cells. *Bicd1*$^{gt/+}$ MNs showed an intermediate life span in vitro compared to *Bicd1*$^{gt/gt}$ MNs and wild type MNs.

6.4.2 MN commitment and differentiation are not impaired in *Bicd1*$^{gt/gt}$ ES cells

Two sets of primers for quantitative polymerase chain reaction (Q-PCR) were designed, one spanning between exons 1 and 2 of the *Bicd1* gene, which is where the gene trap cassette is inserted, and the second one spanning between exons 7 and 8. Both of these Q-PCRs showed a 70% reduction of the *Bicd1* transcript in *Bicd1*$^{gt/gt}$ MNs (**Figure 6.2 C**). *Bicd1*$^{gt/gt}$ MNs should, therefore, be considered as hypomorph mutants (Discussion, **section 7.3**.).

I needed to make sure that the lack of the BICD1 protein was not affecting the differentiation potential of the gene-trapped ES cells, which might have resulted in a different neuronal population, invalidating the use of these cells for further experiments. Thus expression of well-established MN markers, like the homeobox transcriptional factor Hb9 and choline acetyltransferase (ChAT), was tested by Q-PCR by Dr. M. Golding 4 days after the dissociation of the EBs. No significant difference in expression of Hb9 and ChAT was found between *Bicd1*$^{gt/gt}$ and wild type MNs, indicating that the percentage of MNs in these cultures was very similar (**Figure 6.2 C** and Discussion, **section 7.3**).

Bicd2 expression levels were also tested by Q-PCR. Approximately 80% increased expression of Bicd2 was shown in *Bicd1*$^{gt/gt}$ MNs compared to wild type cells (**Figure 6.2 C**). This behaviour was the inverse of *Bicd1* expression and it could be explained as an attempt by *Bicd1*$^{gt/gt}$ MNs to compensate for the lack of the BICD1 protein (Discussion, **section 7.3**.).

It was important to characterise *Bicd1*$^{gt/gt}$ MNs cultures for the expression levels of the genes whose behaviour I wanted to investigate, namely the neurotrophin receptors p75^{NTR} and TrkB (Introduction, **section 1.1.2**). Dr. M. Golding in the MNP laboratory performed a set of reverse transcription polymerase chain reactions (RT-PCR) from cDNA obtained from wild type and *Bicd1*$^{gt/gt}$ MNs. The expression of TrkA, TrkB, TrkC was tested. As expected, TrkB and TrkC were expressed in both wild type and *Bicd1*$^{gt/gt}$ MNs, whilst TrkA transcript was not detectable (**Figure 6.2 A**), confirming the data previously obtained by the laboratory for wild type primary mouse MN cultures. In addition, no significant difference was shown by Q-PCR in the levels

of $P75^{NTR}$ transcript in the two genotypes (**Figure 6.3**), while TrkB seemed to be 25% less expressed in *Bicd1*$^{gt/gt}$ MNs. The levels of expression of the enzyme responsible for the synthesis of the GD1b polysialogangliosides, which determines the binding of H_C to the neuronal PM, the N-acetylgalactosaminyltransferase (GalNAcT), were also tested and no difference was found between wild type and *Bicd1*$^{gt/gt}$ MNs (**Figure 6.2 C**).

I then decided to test the protein levels of $p75^{NTR}$ in western blot, and I found that there was a 40% increase in *Bicd1*$^{gt/gt}$ MNs compared to wild type MNs (**Figure 6.2 B** and **C** for the quantification). Consistent with the data on the mRNA levels of TrkB, there was a 30% reduction of the protein levels of Trk receptors using a Pan Trk antibody (**Figure 6.2 B** and **C** for the quantification). Finally, the Q-PCR data were supported by western blot analysis as there was a 70% reduction of the BICD1 protein in *Bicd1*$^{gt/gt}$ MNs (**Figure 6.2 B** and **C** for the quantification). The residual *Bicd1* protein was supposedly due the inherent leakiness of the gene trapping technology used to generate the ES cells. For a discussion about these data please refer to **section 7.3** and **7.3.3** of the Discussion Chapter.

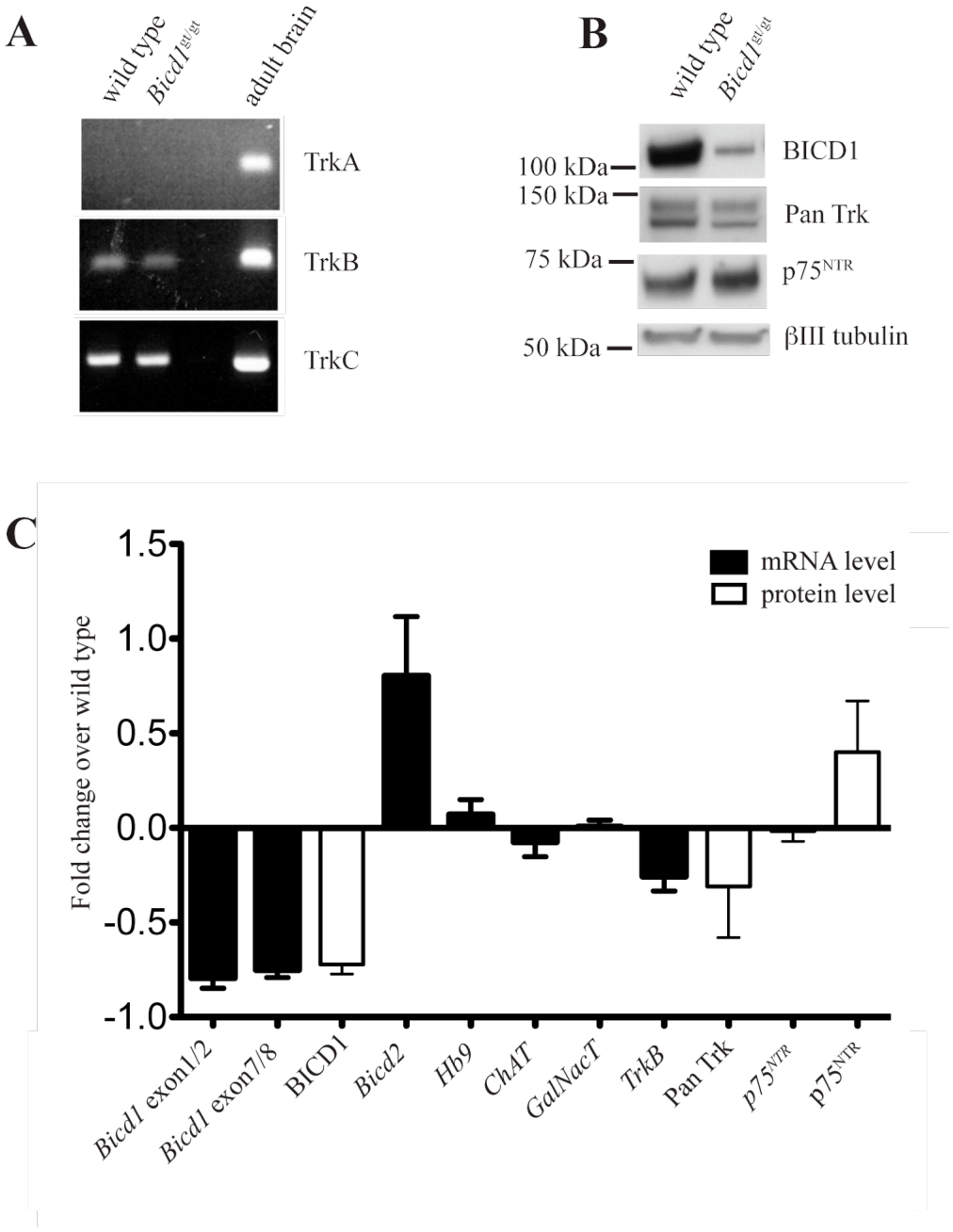

Figure 6.2 Characterisation of gene expression in *Bicd1*$^{gt/gt}$ MNs.
The presence of the neurothrophin receptors, TrkA, TrkB and TrkC was tested by PCR in *Bicd1*$^{gt/gt}$ MNs (A). As expected TrkA was not present. cDNA from adult mouse brain was used as a positive control (A). The protein levels of BICD1, Trk receptors (Pan Trk antibody) and p75^{NTR} are shown in western blot (B). The levels of transcript for each of the gene in *Bicd1*$^{gt/gt}$ MNs (C) were normalised by the value of the corresponding transcript in wt MNs. The expression levels of the indicated genes are reported as fold change over the wild type, which is set to 0 (C, black columns). The Q-PCR data are obtained from 3 independent experiments. The protein levels of BICD1, TrkB and TrkC (pan Trk antibody), and p75^{NTR} are also shown (C, white columns). The protein levels were calculated using Image J from western blots from 3 independent experiments.

6.5 Depletion of BICD1 does not affect axonal retrograde transport

A possible role for BICD1 in axonal transport was proposed by Wanschers *et al.* on the basis of the interaction of this protein with the neuronal isoform of Rab6, Rab6B, and its bidirectional transport in neurites of a differentiated human neuroblastoma cell line (SK-N-SH cells, Chapter 5, **section 5.4.5**.). Since the main aim of the siRNA screen was to find players involved in trafficking of neurotrophins and their receptors, including axonal retrograde transport, the possibility that the depletion of BICD1 might affect axonal retrograde transport was therefore tested.

MNs generated from wt, *Bicd1*$^{gt/+}$ and *Bicd1*$^{gt/gt}$ ES cells were incubated for 30 minutes either with 20 nM AlexaFluor 555-conjugated H_C or with 0.9 μg/ml AlexaFluor 647-conjugated p75^{NTR} antibody in the presence of 100 ng/ml of NGF. NGF is a physiological ligand for p75^{NTR} and specifically stimulates the internalisation of this receptor alone since TrkA is not present in this type of neurons. After incubation with either probe, the cells were washed in DMEM and imaged. H_C and p75^{NTR}-positive carriers were tracked and their instantaneous speed was determined. Speed distribution profiles of axonal retrograde transport of the two probes for MNs of the three genotypes were calculated (**Figure 6.3 A** & **B**). No statistically significant difference between the three different genotypes was observed in axonal transport of H_C (**Figure 6.3 A**) or the p75^{NTR} antibody (see **Figure 6.3 B**).

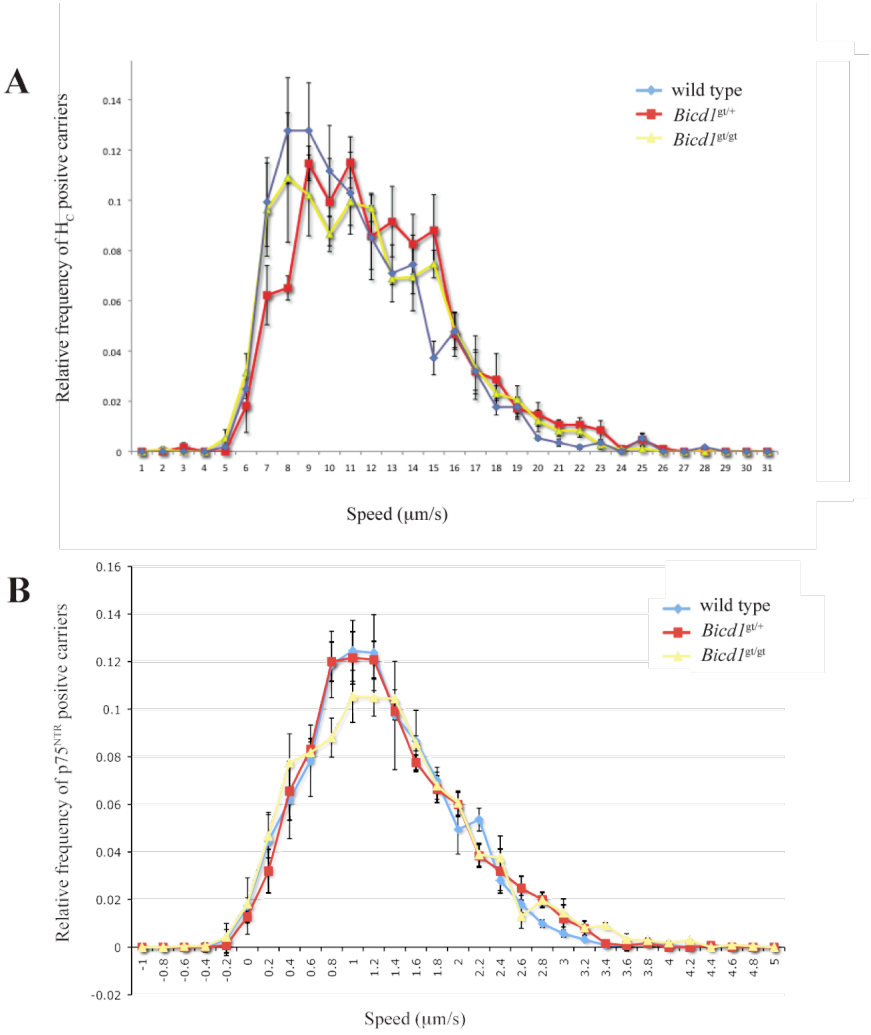

Figure 6.3 .Kinetics of axonal retrograde transport of H_C and $p75^{NTR}$ antibody in wild type, *Bicd1*$^{gt/+}$ and *Bicd1*$^{gt/gt}$ MNs.
The frequency distribution of instantaneous speeds for H_C- (A) and $p75^{NTR}$- (B) positive carriers are plotted. Four independent experiments were performed for each probe and each genotype. No statistically significant difference in the axonal transport of H_C and $p75^{NTR}$ in wt MNs compared to *Bicd1*$^{gt/+}$ and *Bicd1*$^{gt/gt}$ cells has been identified.

6.6 Internalisation of H_C and the $p75^{NTR}$ antibody in *Bicd1*$^{gt/gt}$ MNs.

6.6.1 Confirmation of the BICD1 knockdown phenotype observed in the screen using *Bicd1*$^{gt/gt}$ MNs

I sought to confirm that the depletion of BICD1 in *Bicd1*$^{gt/gt}$ MNs would induce the same phenotype that was observed in the screen, i.e. increased accumulation of H_C in MN cell bodies. MNs derived from wt, *Bicd1*$^{gt/+}$ and *Bicd1*$^{gt/gt}$ mouse ES cells were, therefore, used to assay the kinetics of internalisation of AlexaFluor 546-labelled H_C and the $p75^{NTR}$ antibody incubated together at 37°C to mimic the conditions of the siRNA screen. The extent of internalisation of both probes was assessed at fifteen, thirty and sixty minutes. The cells were acid-washed for 3 minutes at 4°C, fixed in 4% PFA, and then immunostained for $p75^{NTR}$. The internalised pool of the two probes was visualised with a confocal microscope and the intensity of fluorescence of H_C and $p75^{NTR}$ antibody quantified using the Image J software and divided by the intensity of the βIII tubulin staining for data normalisation. In the case of H_C, a statistically significant difference between wild type and *Bicd1*$^{gt/gt}$ MNs could be observed after 1h of incubation at 37°C ($p < 0.05$, pair-wise ANOVA, followed by Bonferroni post test, n = 3) (**Figure 6.4 A**), while for the $p75^{NTR}$ antibody there was a statistically significant difference between all three genotypes at this time-point ($p < 0.05$, pair-wise ANOVA, followed by Bonferroni post test, n = 3) (**Figure 6.4 B**).

These data confirmed the results obtained in the siRNA screen, where BICD1 was selected as a candidate for the accumulation of H_C. Surprisingly, an accumulation of the $p75^{NTR}$ antibody was also observed, in contrast with the results of the primary screen.

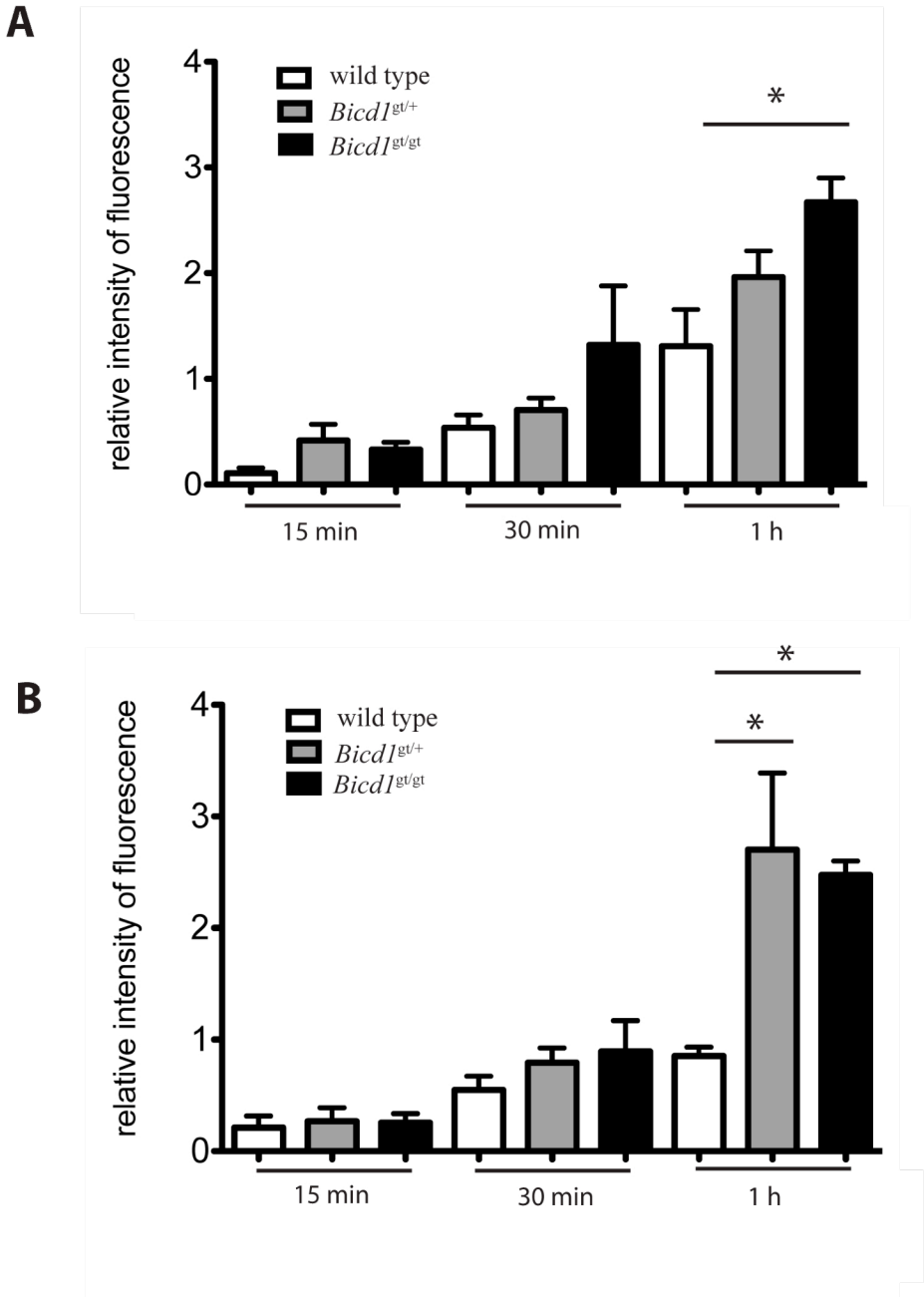

Figure 6.4 Kinetics of internalisation of H_C and $p75^{NTR}$ antibody in wild type, *Bicd1*$^{gt/+}$ and *Bicd1*$^{gt/gt}$ MNs.
MNs derived from wild type, *Bicd1*$^{gt/+}$ and *Bicd1*$^{gt/gt}$ ES cells were used to assay the kinetics of internalisation of Hc (A) and the $p75^{NTR}$ antibody (B). A statistically significant difference between wild type and *Bicd1*$^{gt/gt}$ MNs was observed after 1h of incubation for both probes. In the case of the $p75^{NTR}$ antibody a statistically significant difference between the three genotypes was observed after 1h. Statistical significance calculated using a one-way ANOVA test, followed by Bonferroni post test, n=3. Results are shown +/- s.e.m.

6.6.2 $p75^{NTR}$ accumulation in *Bicd1*$^{gt/gt}$ MNs is enhanced by BDNF stimulation.

I wanted to test whether the results obtained when co-incubating the $p75^{NTR}$ antibody with H_C could be repeated using a physiological ligand for this receptor. In MNs derived from mouse ES cells TrkA is not present, but TrkB is. I therefore decided to use BDNF, which binds to both TrkB and $p75^{NTR}$, to stimulate the internalisation of the $p75^{NTR}$ antibody. The $p75^{NTR}$ antibody was co-incubated with 100 ng/ml of BDNF at 37°C for one hour; cells were then acid-washed for 3 minutes at 4°C and fixed in 4% PFA. The intensity of fluorescence of the $p75^{NTR}$ antibody was quantified using the Image J software and divided by the intensity of the βIII tubulin staining, to normalise the data to the number of neurons (**Figure 6.5**).

A statistically significant increase in the accumulation of the $p75^{NTR}$ antibody in *Bicd1*$^{gt/gt}$ MNs compared to wild type cells was observed ($p < 0.001$). *Bicd1*$^{gt/+}$ MNs behaved like wild type cells, whist there was also a significant difference between *Bicd1*$^{gt/gt}$ and *Bicd1*$^{gt/+}$ MNs ($p < 0.001$, **Figure 6.5 B**).

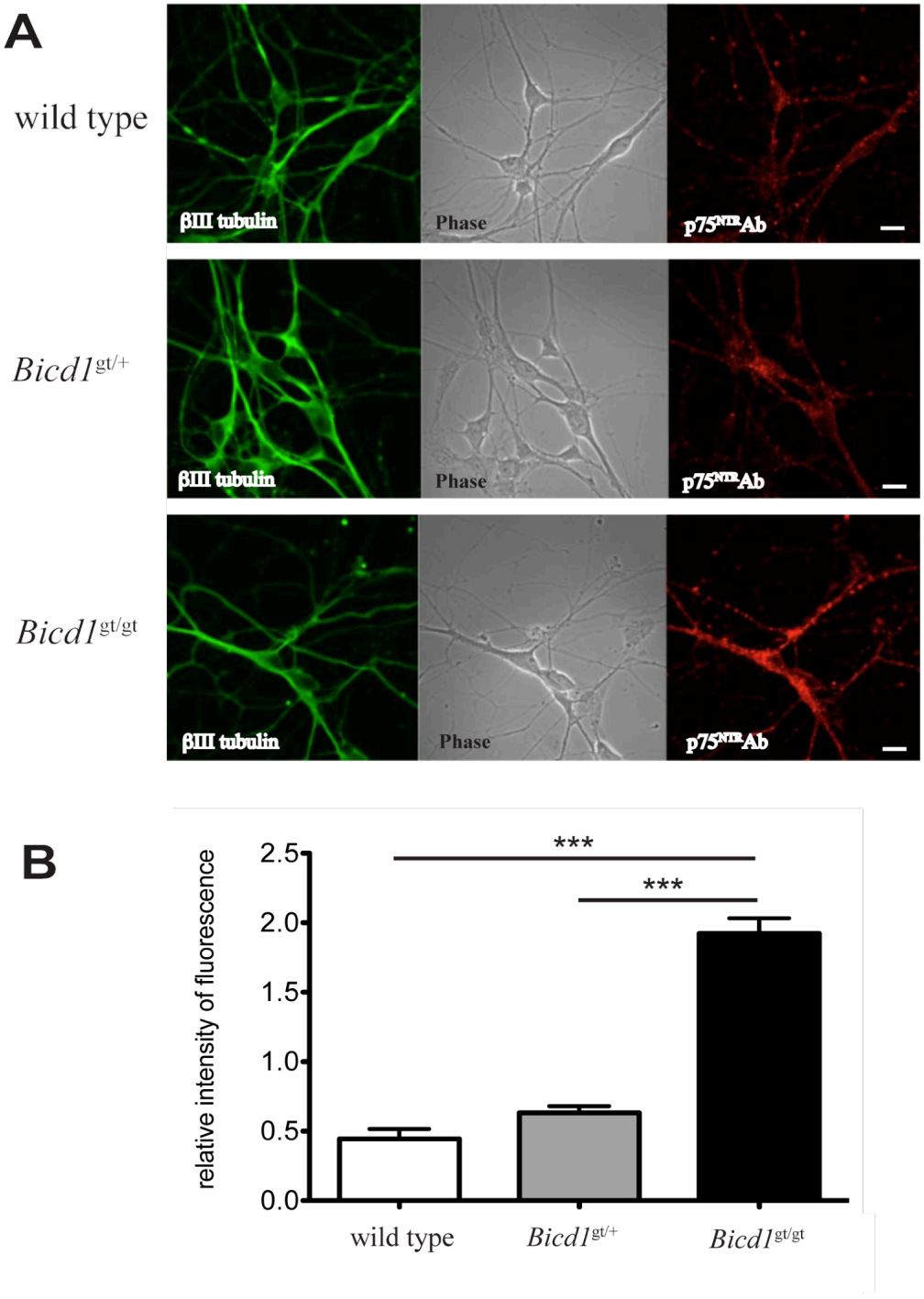

Figure 6.5 p75^{NTR} antibody internalisation upon BDNF stimulation.
MNs derived from wild type, *Bicd1*$^{gt/+}$ and *Bicd1*$^{gt/gt}$ ES cells were incubated for 1 hour with the p75^{NTR} antibody and 100 ng/ml BDNF. MNs were then acid-washed for 3 minutes and fixed in 4% PFA. βIII tubulin (in green) was used to stain the neurons; the p75^{NTR} antibody is in red (A). Scale bar, 20 μm. Quantification of three independent experiments on internalisation of the p75^{NTR} antibody for an hour upon BDNF stimulation (B). There is a statistically significant increase in the accumulation of the p75^{NTR} antibody in *Bicd1*$^{gt/gt}$ cells compared to wild type and *Bicd1*$^{gt/+}$ MNs. *** $p<0.001$ by one-way ANOVA followed by Bonferroni test, n=3. Results are shown +/- s.e.m.

6.6.3 Nature of the organelle in which H_C accumulates in *Bicd1*$^{gt/gt}$ MNs.

In order to gain a better understanding of the nature of the organelles in which H_C accumulates after one hour incubation and obtain some clues as to whether there was a block or a diversion of the normal trafficking of this protein in *Bicd1*$^{gt/gt}$ MNs, a version of this probe conjugated with 10 nM gold by Guillermo Menendez in the laboratory was used to perform transmission electro-microscopy (TEM) studies. MNs derived from wild type, *Bicd1*$^{gt/+}$ and *Bicd1*$^{gt/gt}$ ES cells were incubated with 50 nM gold-labelled H_C for an 1 hour at 37^0C and then fixed, processed, sectioned and imaged by Ken Blight from the Electron Microscopy unit at CRUK, London Research Institute.

H_C was found bound to the plasma membrane (PM), and upon internalisation accumulated predominantly in immature multi-vesicular bodies (MVBs) with low internal vesicle content; occasionally some gold could also be found in lysosomes. Compared with mutant cells, wild type MNs internalised less probe, which appeared to be dispersed within the lumen of MVBs (**Figure 6.6**), with a small amount localised to one side of the organelle. In *Bicd1*$^{gt/gt}$ MNs there seemed to be more H_C bound to the PM and a higher intracellular accumulation of the probe. As a result, more MVBs were labelled. In addition, *Bicd1*$^{gt/gt}$ MVBs contained more H_C than their wild type counterparts and the probe tended to mostly cluster in close apposition to the delimiting membrane of the organelle (**Figure 6.6**). *Bicd1*$^{gt/+}$ MNs presented an intermediate phenotype, with an increased accumulation of H_C compared to wild type cells.

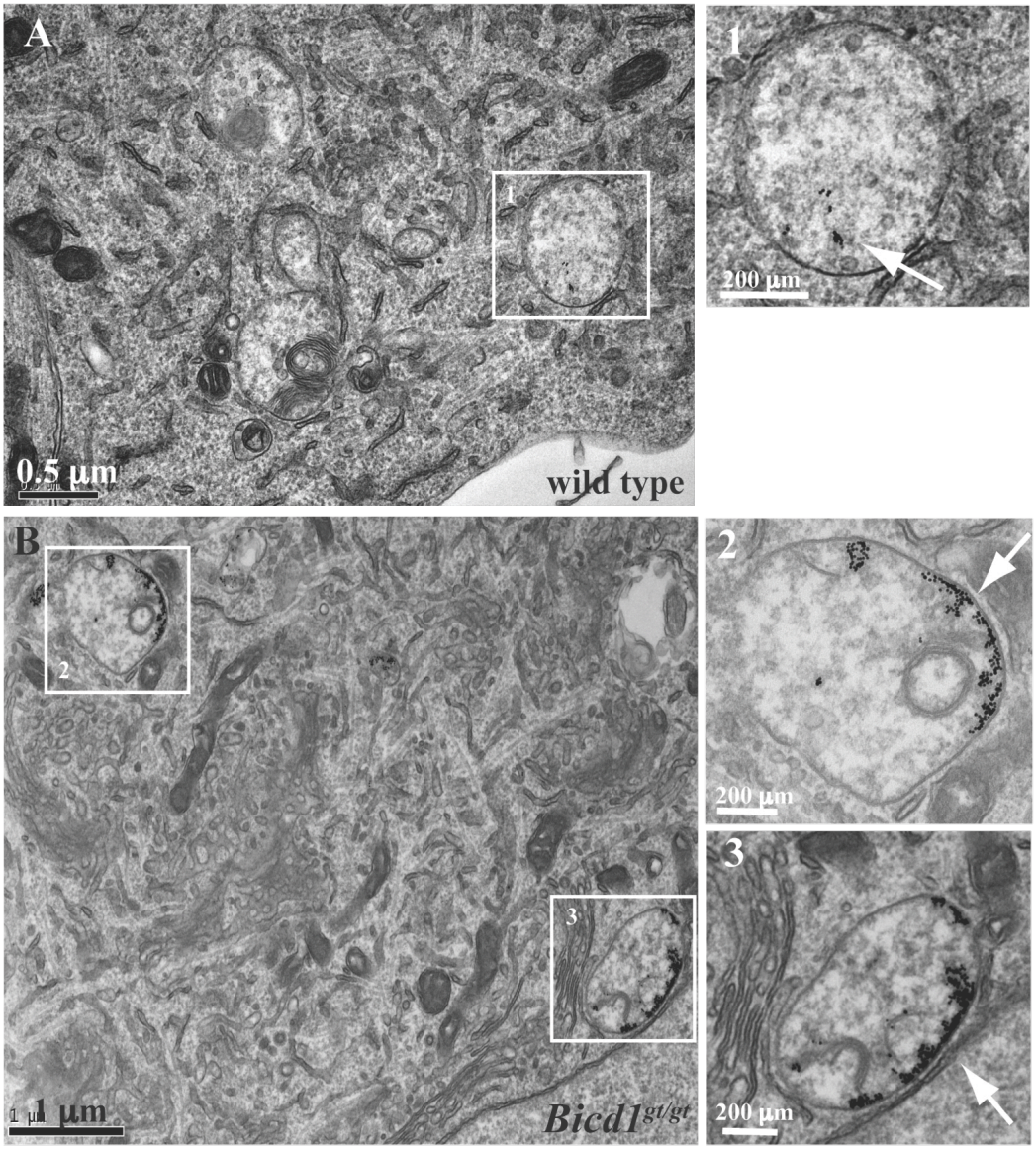

Figure 6.6 H_C accumulates in MVBs in *Bicd1*$^{gt/gt}$ MNs.
Using a gold-conjugated H_C it was determined that this probes accumulates predominantly in MVBs with a low internal vesicle content. Representative images of MVBs are shown from wild type (A, blown up panel 1) and *Bicd1*$^{gt/gt}$ MNs (B, blown up panels 2 & 3). White arrows point to the gold labelled probe. Gold labelled H_C was generally found dispersed within wild type MVBs (A, blown up panel 1). *Bicd1*$^{gt/gt}$ MVBs contained more H_C than their wild type counterparts and the probe tended to cluster in close apposition to the delimiting membrane of the organelle (B, blown up panels 2 & 3).

6.7 GD1b and neurotrophin receptor homeostasis at the plasma membrane.

6.7.1 H_C binding at the plasma membrane of *Bicd1*$^{gt/gt}$ MNs.

In light of the results discussed above (**section 6.6.1**), I sought to test whether the increased accumulation of the probe in mutant MNs was due to a block in trafficking and/or degradation, and/or to an increased binding at the PM. This was all the more important because of the EM data shown in **section 6.7**, which clearly demonstrated an increased binding of H_C to the PM, in addition to its increased intracellular accumulation.

20 nM of AlexaFluor 555-conjugated H_C was incubated at 4°C for 15 minutes with wild type, *Bicd1*$^{gt/+}$ and *Bicd1*$^{gt/gt}$ MNs. Cells were then fixed with 4% PFA and imaged with a confocal microscope (**Figure 6.7 A**). The intensity of fluorescence of bound H_C per MN was quantified from three independent experiments, and the data were normalised to the average fluorescence intensity of the probe per MN of wild type cells and plotted (**Figure 6.7 B**). The increase of H_C binding to the neuronal plasma membrane was found to be statistically significant ($p < 0.05$) in *Bicd1*$^{gt/+}$ compared to wild type MNs. The same difference was also found between *Bicd1*$^{gt/+}$ and *Bicd1*$^{gt/gt}$ MNs (**Figure 6.7 B**).

6.7.2 GD1b levels at the plasma membrane are increased in *Bicd1*$^{gt/gt}$ MNs.

Having found that H_C binding is increased in *Bicd1*$^{gt/gt}$ MNs compared to wild type cells, I sought to determine if the plasma membrane levels of GD1b, a main lipid receptor of H_C (Introduction, **section 1.1.2**), were increased in *Bicd1*$^{gt/gt}$ MNs.

MNs derived from wild type, *Bicd1*$^{gt/+}$ and *Bicd1*$^{gt/gt}$ ES cells were fixed in 4% PFA, and immuno-stained for GD1b. Images from three independent experiments were then acquired using a confocal microscope (**Figure 6.8 A**) and the fluorescence intensity of GD1b at the PM was quantified using Image J. Finally, these data were normalised to the average fluorescence intensity of GD1b per MN of wt cells and plotted (**Figure 6.8 B**). In accordance with the H_C binding data shown in **Figure 6.7**, *Bicd1*$^{gt/gt}$ MNs were found to have a statistically significant higher content of GD1b at the PM ($p < 0.001$) compared to wild type MNs. In addition, the levels of GD1b exposed at the PM in *Bicd1*$^{gt/+}$ MNs were also significantly ($p < 0.01$) increased compared to wild type cells (**Figure 6.8 B**).

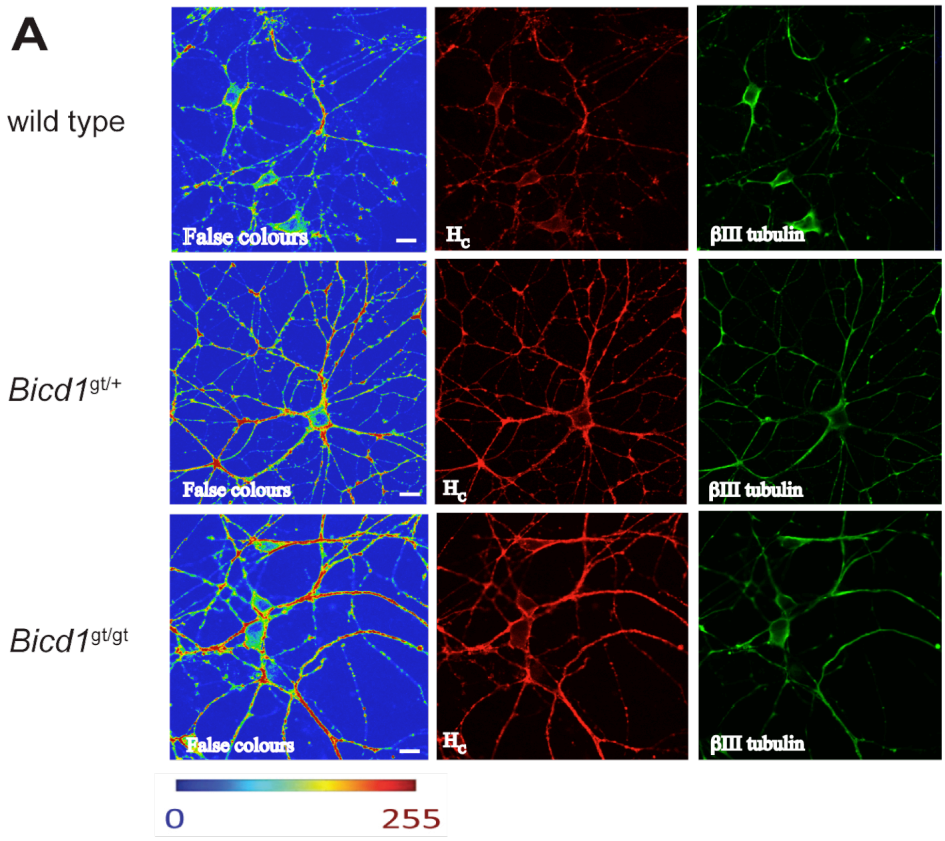

Figure 6.7 Enhanced binding of H_C to the PM of *Bicd1*$^{gt/gt}$ MNs.
Wild type, *Bicd1*$^{gt/+}$ and *Bicd1*$^{gt/gt}$ MNs were incubated with 20 nM AlexaFluor 555-conjugated H_C for 15 minutes at 40°C. Cells were then imaged with a confocal microscope (A) and the fluorescence intensity of H_C (in red) was quantified. βIII tubulin was used to identify the neurons. The H_C staining was also visualised using a rainbow palette (false colours) to better highlight the differences of intensity in the three genotypes. The lowest intensity is in blue and the highest in red as indicated by the gradient bar (A). Scale bar 20 μm. The data from three independent experiments were pooled together and the values obtained for *Bicd1*$^{gt/+}$ and *Bicd1*$^{gt/gt}$ MNs were normalised to wild type cells. Finally, the normalised fluorescence intensity of H_C bound to the PM between the three genotypes was plotted. A statistically significant difference was found between the in wild type vs *Bicd1*$^{gt/+}$ MNs and wild type vs *Bicd1*$^{gt/gt}$ MNs (B). *$p<0.05$ by one-way ANOVA followed by Bonferroni test, n=3. Results are shown +/- s.e.m.

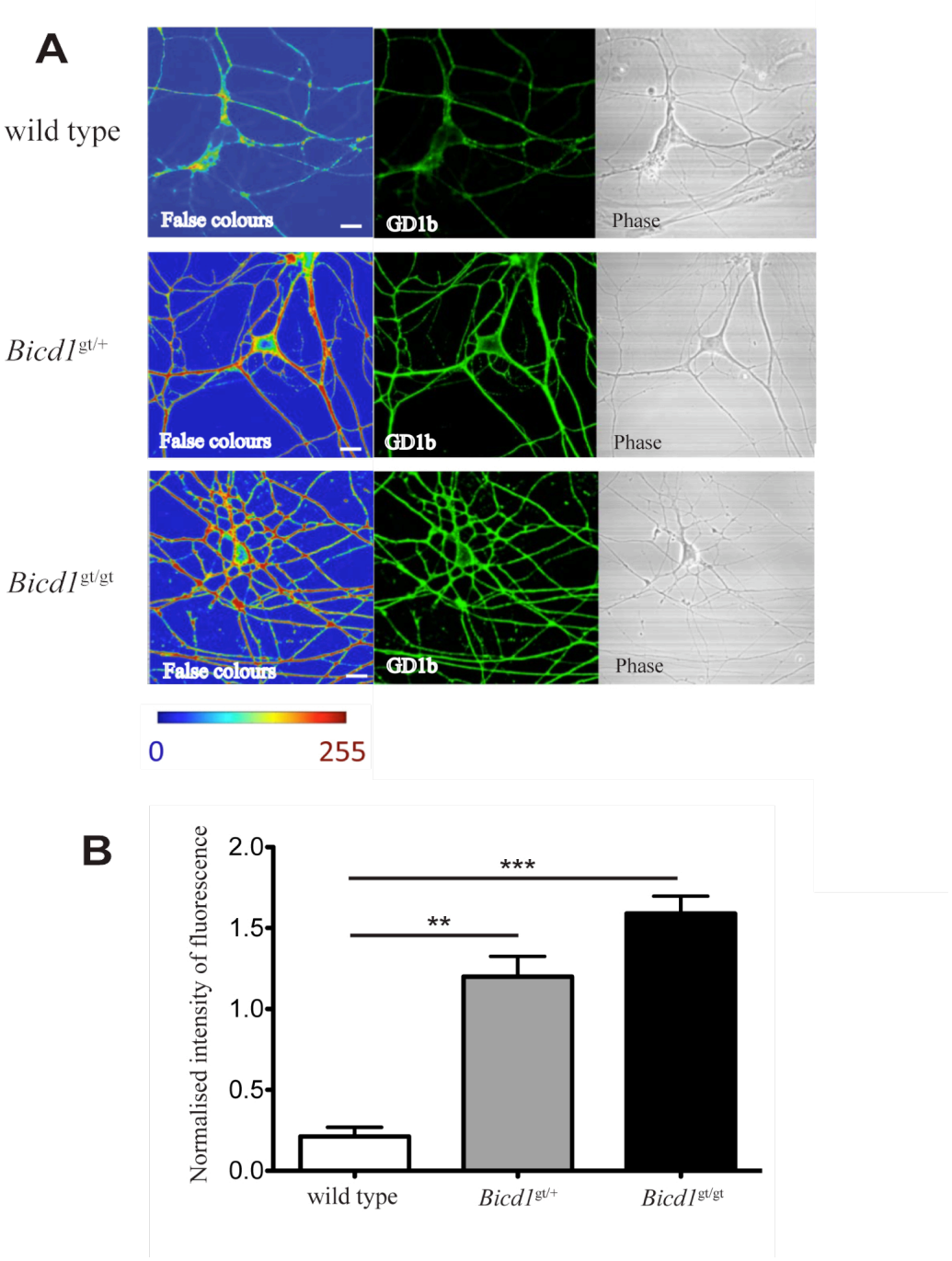

Figure 6.8 Enhanced levels of GD1b on the plasma membrane of *Bicd1*$^{gt/gt}$ MNs.
Representative pictures of wild type, *Bicd1*$^{gt/+}$ and *Bicd1*$^{gt/gt}$ MNs fixed in 4% PFA and stained for Gd1b (in green), without permeabilisation (A). The GD1b staining has also been visualised using a rainbow palette to better appreciate the difference of intensity in the three genotypes. Scale bar, 20 µm. Quantification of three independent experiments of GD1b staining in unpermeabilised MNs (B). A statistically significant increase of GD1b exposed at the plasma membrane was found in *Bicd1*$^{gt/+}$ and *Bicd1*$^{gt/gt}$ MNs compared to wild type cells. **p<0.01 and ***p<0.001 by one-way ANOVA followed by Bonferroni test, n=3. Results are shown +/- s.e.m.

6.7.3 Increased cell surface localisation of Trk receptors in *Bicd1*$^{gt/gt}$ MNs.

I then decided to also investigate the levels of p75^{NTR} on the neuronal surface. MNs derived from wild type, *Bicd1*$^{gt/+}$ and *Bicd1*$^{gt/gt}$ ES cells were fixed in 4% PFA and stained for p75^{NTR} without permeabilisation,. Images of three independent experiments were taken and the intensity of fluorescence per MN was quantified using Image J. These raw data were then normalised to the average fluorescence intensity of p75^{NTR} per MN of wt cells and plotted (**Figure 6.9 A**). *Bicd1*$^{gt/gt}$ MNs were found to have a statistically significant ($p < 0.05$) difference in cell surface p75^{NTR} compared to wild type MNs.

The data regarding the accumulation of the p75^{NTR} antibody were obtained in presence of BDNF, which meant that the internalised p75^{NTR} could have been in a complex with the TrkB receptor. It was therefore important to test whether TrkB would exhibit a similar behaviour under steady state levels of p75^{NTR} in *Bicd1*$^{gt/gt}$ MNs. MNs derived from wild type, *Bicd1*$^{gt/+}$ and *Bicd1*$^{gt/gt}$ were stained for TrkB. Images were acquired from three independent experiments and quantified in the same way described for p75^{NTR}. The intensity of fluorescence of TrkB was normalised as before and plotted (**Figure 6.10 B**). *Bicd1*$^{gt/gt}$ MNs were found to have a statistically significant ($p < 0.05$) difference in levels of TrkB at the PM compared to wild type MNs. The same difference was found between *Bicd1*$^{gt/+}$ and *Bicd1*$^{gt/gt}$ MNs (**Figure 6.10 B**).

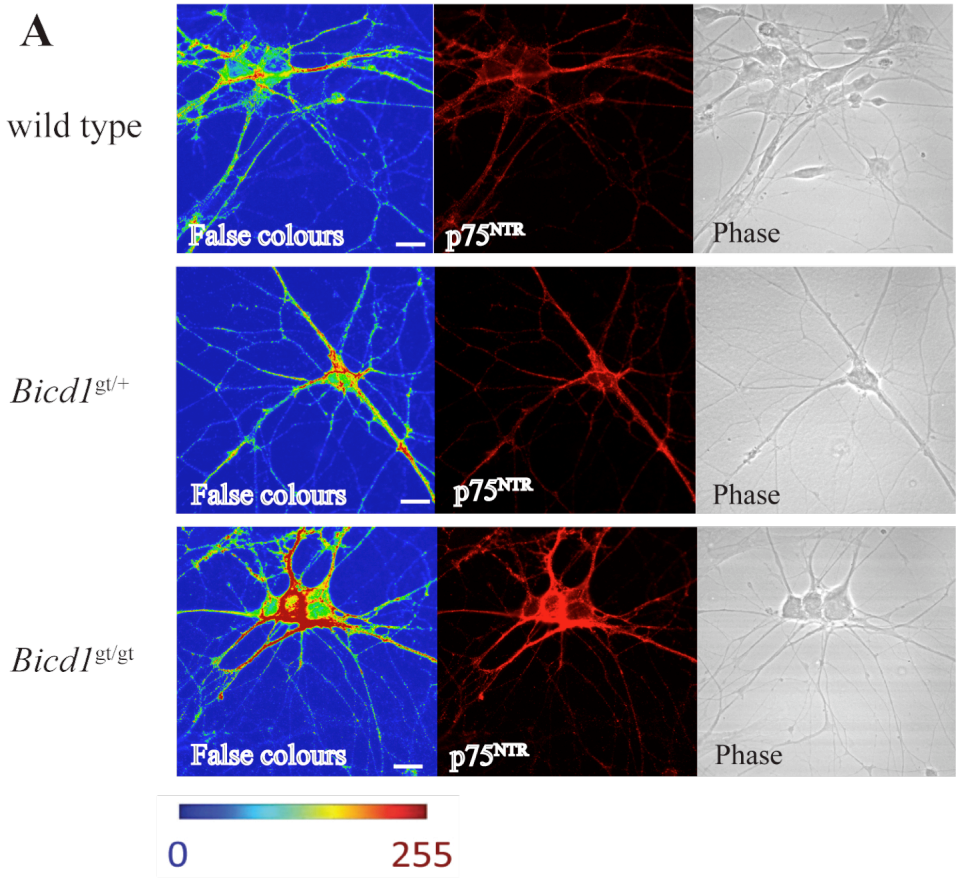

Figure 6.9 Enhanced levels of p75^{NTR} on the plasma membrane of *Bicd1*$^{gt/gt}$ MNs.
Wild type, *Bicd1*$^{gt/+}$ and *Bicd1*$^{gt/gt}$ MNs were fixed in 4% PFA and stained for p75^{NTR}. p75^{NTR} has been visualised using a rainbow palette to better appreciate the difference in intensity of this staining (A). Scale bar 20 μm. The fluorescence intensity of the two antibodies per MN was quantified and the data from three independent experiments were pooled and the values were normalised to wild type cells. Finally, the fold difference of the PM staining of p75^{NTR} between the three genotypes was plotted (B). A statistically significant difference between the level of p75NTR at the PM in wild type vs *Bicd1*$^{gt/gt}$ MNs was found (B). *p<0.05 by one-way ANOVA followed by Bonferroni test, n=3. The results are shown +/- s.e.m.

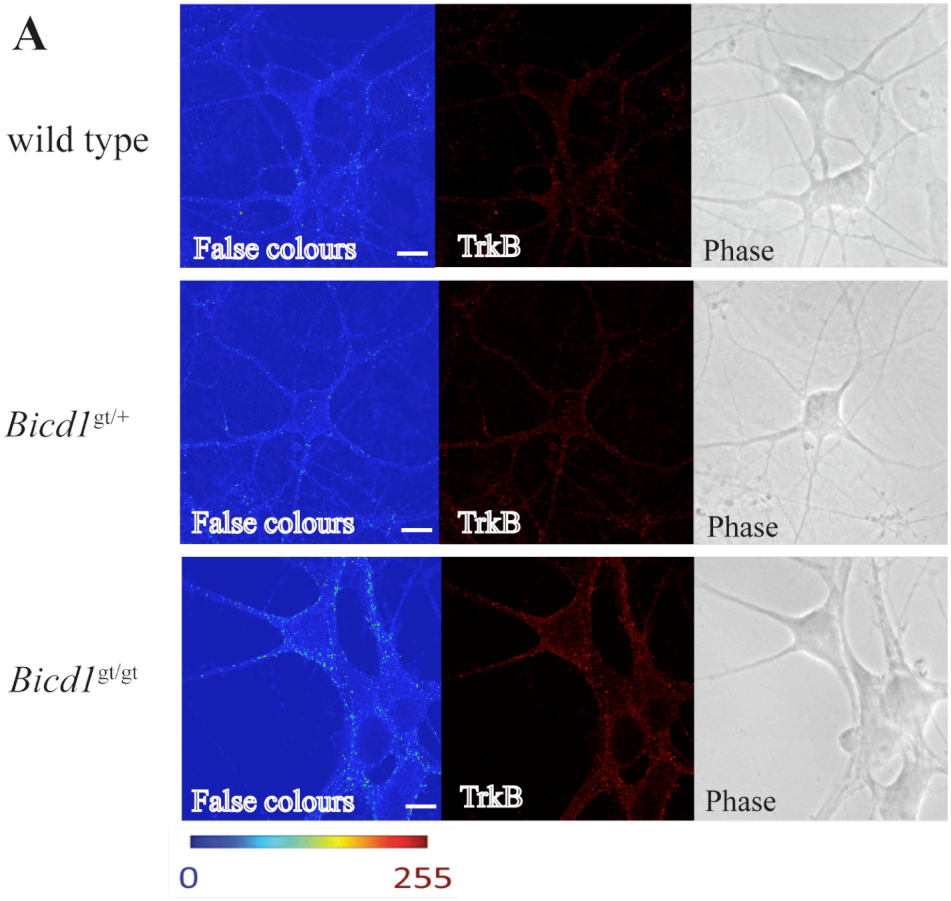

Figure 6.10 Levels of TrkB exposed at the plasma membrane in *Bicd1*$^{gt/gt}$ MNs.
Wild type, *Bicd1*$^{gt/+}$ and *Bicd1*$^{gt/gt}$ MNs were fixed in 4% PFA and stained for TrkB (in red). TrkB has also been visualised using a rainbow palette to better appreciate the difference amongst the three genotypes (A). Scale bar 20 µm. The amount of fluorescence intensity of the two antibodies per MN was quantified and the data from three independent experiments were normalised to wild type cells. Finally, the fold difference of TrkB localised to the PM amongst the three genotypes was plotted (B). A statistically significant difference was observed in the levels of TrkB at the PM between wild type and *Bicd1*$^{gt/gt}$ MNs and between *Bicd1*$^{gt/+}$ and *Bicd1*$^{gt/gt}$ (B). *p<0.05 by one-way ANOVA followed by Bonferroni test, n=3. Results are shown +/- s.e.m.

6.8 BDNF signalling in *Bicd1*$^{gt/gt}$ MNs

The finding that the levels of p75^{NTR} and TrkB at the PM are altered at steady state in *Bicd1*$^{gt/gt}$ MNs, resulting in an increased exposure of these receptors on the neuronal surface, suggests that p75^{NTR} and TrkB signalling in *Bicd1*$^{gt/gt}$ cells might also be affected. For this reason I decided to stimulate MNs derived from wild type, and *Bicd1*$^{gt/gt}$ ES cells with 100 ng/ml of BDNF and assay for the activation of ERK1/2 and Akt by western blotting.

In collaboration with Dr. M. Golding in the laboratory, the kinetic of activation of ERK1/2 and Akt upon BDNF stimulation after 5 hours of starvation were established. The levels of phosphorylation of ERK1/2 and Akt were determined (**Figure 6.11 A** & **6.12 A**) and normalised to the total levels of the corresponding protein (**Figure 6.11 B & 6.12 B**) from three independent experiments.

Akt seemed to have a peak of phosphorylation 10 minutes after stimulation with BDNF in wild type MNs; after that time point the phosphorylation decreases progressively (**Figure 6.11 B**). The same overall trend was observed in *Bicd1*$^{gt/gt}$ MNs, but the intensity of the peak at 10 minutes was less than half compared to wild type cells, and the decrease of phosphorylation was less pronounced compared to their wild type counterpart (**Figure 6.11 B**). An initial peak of ERK1/2 phosphorylation was observed at 10 minutes and then, the levels of phosphorylation decreased progressively in wild type MNs (**Figure 6.12 B**). The same overall behaviour was observed in *Bicd1*$^{gt/gt}$ MNs, however the intensity of the peak was much lower ($p < 0.05$, one-way ANOVA, followed by Bonferroni test, n=3) (**Figure 6.12 B**).

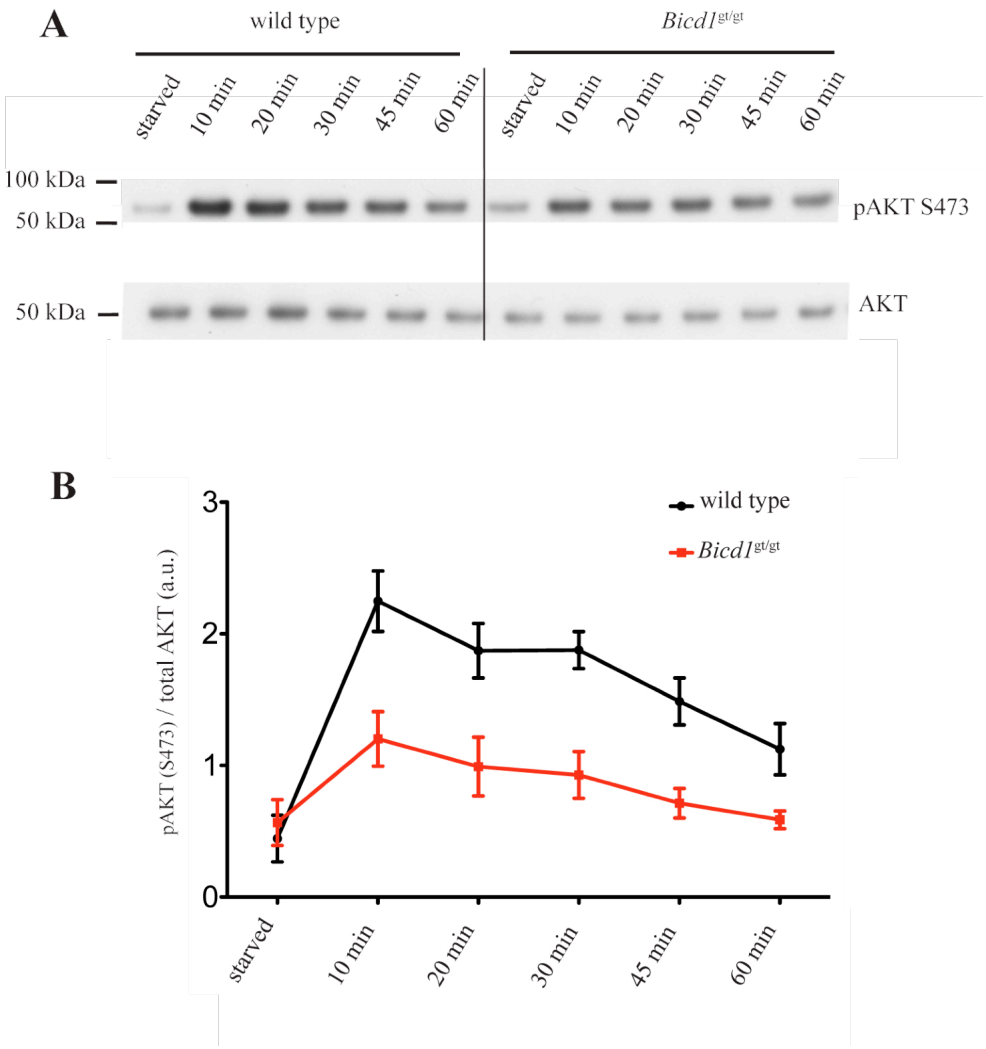

Figure 6.11. Kinetics of Akt phosphorylation in *Bicd1*$^{gt/gt}$ MNs in response to BDNF stimulation. Wild type, *Bicd1*$^{gt/+}$ and *Bicd1*$^{gt/gt}$ MNs were starved for 5 hours and stimulated with 100 ng/ml. The cells were then lysed at several time points and analysed by western blot for the levels of pAkt (S473) and total Akt (A). Densitometric analysis of pAkt bands was performed using Image J. The levels of pAkt (S473) normalised to the levels of total Akt from three independent experiments are plotted (B). The activation of pAkt (S473) in *Bicd1*$^{gt/gt}$ MNs is statistically significantly reduced compared to wild type MNs (two ways ANOVA, $p<0.0001$). Results are shown +/- s.e.m.

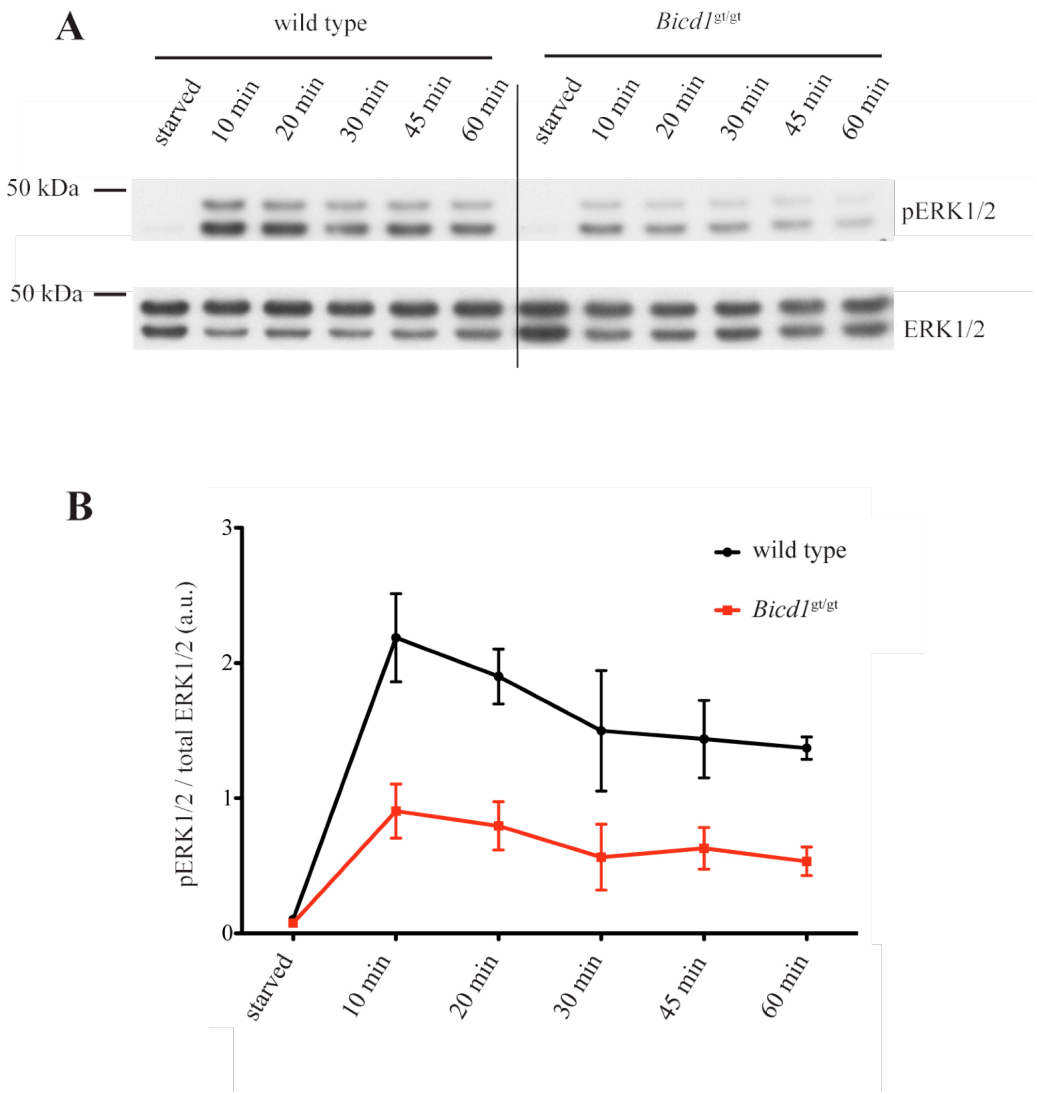

Figure 6.12 Kinetics of ERK1/2 phosphorylation in *Bicd1*$^{gt/gt}$ MNs in response to BDNF stimulation. Wild type, *Bicd1*$^{gt/+}$ and *Bicd1*$^{gt/gt}$ MNs were starved for 5 hours and stimulated with 100 ng/ml of BDNF. The cells were then lysed at several time points and analysed by western blot for the levels of pERK1/2 and total ERK1/2 (A). Densitometric analysis of pERK1/2 bands was performed using Image J. The levels of pERK1/2 normalised to the levels of total ERK1/2 from three independent experiments are plotted (B). The activation of pERK1/2 in *Bicd1*$^{gt/gt}$ MNs is reduced compared to wild type MNs (two ways ANOVA, $p<0.0001$). Results are shown +/- s.e.m.

6.9 *Bicd1* expression pattern in mouse development

I decided to try to use the *Bicd1* gene trapped mouse ES cells to derive a mouse since no mutant *Bicd1* mice have been described in the literature. The transgenic department at CR-UK performed a series of 8-cell injections using 2 lines of *Bicd1*$^{gt/+}$ mouse ES cells (the RRP27 and the C4 ES cell clones, also purchased from the International Gene Trap Consortium). Unfortunately, no viable pup was obtained with any of the ES cell clones. The 8-cell injection technique differs from a conventional ES cell transfer, because the ES cells are not injected into the blastocyst but when the embryo reaches the 8-cell stage. The result of this new approach is the generation of embryos that are entirely derived from the injected ES cells (Poueymirou et al., 2007). This feature allowed me to obtain E12.5 and E13.5 *Bicd1*$^{gt/+}$ embryos to use to test the expression pattern of *Bicd1*. X-Gal staining (Materials and Methods, **section 2.2.7.1**) was performed on 12.5 and E13.5 *Bicd1*$^{gt/+}$ embryos in collaboration with Bradley Spencer-Dene in the Histopathology unit at the CR-UK and *Bicd1* was found expressed almost exclusively in the nervous system (**Figure 6.13**). No staining could be detected earlier than E11.5, when it started to be visible, though weak. After E13.5 *Bicd1* expression was no longer detectable in the nervous system and became more diffuse.

At E11.5 and E12.5 *Bicd1* was expressed primarily in the spinal cord and in brain (**Figure 6.13 A-C**), while at E13.5, *Bicd1* expression was detected mainly in dorsal root ganglia neurons (DRG) (**Figure 6.13 D, E, F**).

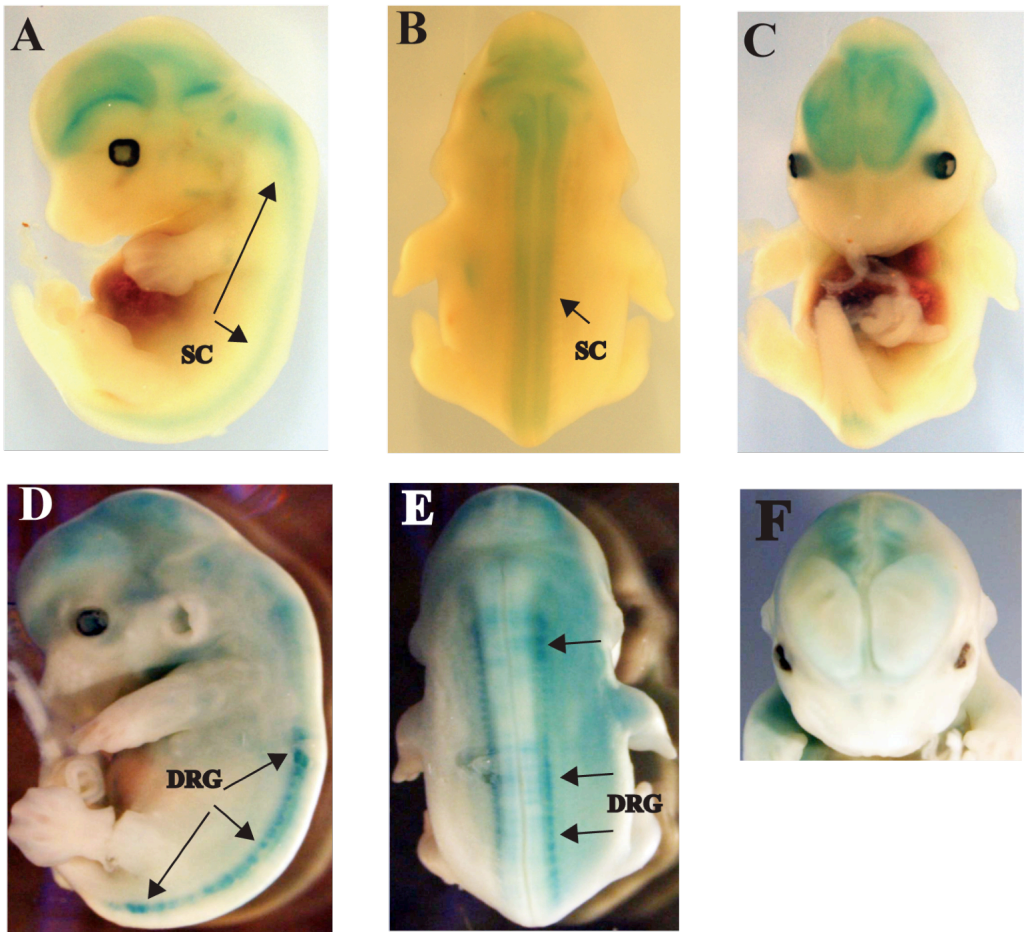

Figure 6.13 Expression pattern of *Bicd1* in mouse development.
β-gal histochemistry of mouse embryos at different embryonic days from E12.5 (A-C) to E13.5 (D-F). *Bicd1* expression seems generally to be resticted to the nervous system. Side (A), back (B) and front (C) view of an E12.5 mouse embryos generated from *Bicd1*$^{gt/+}$ ES cells . *Bicd1* is expressed in the CNS, in the spinal cord (SC, black arrow) and in the brain. At E13.5 the expression of *Bicd1* is predominant in DRG (black arrows), as it is appearent from the side (D), back (E) and front (F) view.

Summary of the achievements presented in this Chapter

- *BICD1 was selected for further investigation and MNs generated using a Bicd1 gene-trapped ES cell line were characterised;*

- *70% reduction in BICD1 protein levels did not affect the differentiation of Bicd1$^{gt/gt}$ ES cells into MNs;*

- *Bicd1$^{gt/gt}$ MNs displayed a higher intracellular accumulation of H_C and the p75^{NTR} antibody compared to wt MNs;*

- *The reduction in BICD1 protein caused an increased localisation of p75^{NTR}, TrkB and GD1b to the neuronal plasma membrane;*

- *In Bicd1$^{gt/gt}$ MNs, BDNF signalling via TrkB was altered, resulting in an decreased activation of ERK1/2 and Akt compared to wild type cells;*

- *Bicd1 was found to be expressed primarily on the nervous system between embryonic day 11.5 and 13.5.*

Chapter 7. Discussion

7.1 Set up for an RNAi screen in MNs.

RNAi screens have become increasingly popular because of the unique opportunity they offer to discover new players in a particular pathway of interest. With the introduction of complex algorithms for image analysis, it is now possible to extract more high content data from image-based screens, allowing for more refined answers. As such, an siRNA screen can be set up to look at the behaviour of several fluorescently labelled probes at the same time in accordance with several parameters, like cellular localisation, fluorescence intensity and colocalisation with different interacting partners (Krausz, 2007). A recent work constitutes an extreme example of the complexity of the image analysis available nowadays (Collinet et al., 2010). In this case, the whole genome was screened to find players involved in the endocytosis of transferrin and epidermal growth factor. The readout was provided by a complex algorithm of multiparametric image analysis, which allowed the authors to build up a map of genetic interactions on the basis of the phenotypes observed in the screen.

The goal of my thesis was to apply concept and technology of high content screening (HCS, Introduction, **section 1.3**) to investigate neurotrophin trafficking in a relevant physiological cellular system, i.e. MNs, in order to find new players in this biological process. I will discuss here some of the decisions taken when designing the siRNA screen.

7.1.1 Choice of the cell system.

Historically, the Molecular Neuropathobiology (MNP) laboratory has been interested in characterising the process of axonal retrograde transport of neurotrophins

and their receptors. They also made use of a probe, the binding fragment of TeNT (H_C), which has been shown to share the same route of axonal retrograde transport (Deinhardt et al., 2006b). The field of axonal retrograde transport has gained further importance after the formulation of the "signalling endosome" theory, whereby endosomes transported retrogradely along the axon constitute a platform for neurotrophin signalling (Grimes et al., 1997, Grimes et al., 1996). This theory provided a concept to explain the association with certain neurodegenerative diseases, such as Amyotrophic Lateral Sclerosis ALS (Strom et al., 2008) and Alzheimer's disease (Schindowski et al., 2008), with feature defects in axonal retrograde transport. A physiologically relevant cell type to investigate H_C and neurotrophin trafficking are MNs, because survival of these cells is ensured *in vivo* by the neurotrophins secreted by their target muscles, with the neurotrophins being retrogradely transported to the cell soma (Bronfman et al., 2007). In addition MNs constitute the only physiological route of infection for TeNT, which is taken up by the NMJ and transported to the spinal cord, where it enters the inhibitory interneurons and prevents neurotransmitter release (Lalli et al., 2003, Salinas et al., 2010). Consequently, I aimed to use MNs as a cellular platform to perform the siRNA screen, despite the difficulties in adapting primary cells to the format required for HCS.

The first problem to solve was to be able to generate enough cells to perform the screen and to minimise the cell heterogeneity inherent in the dissection and culture of ventral horn preparations of the spinal cord. Primary MN cultures are also "contaminated" with other neuronal populations, which makes it difficult to identify MNs, especially in the context of a high-throughput screen, where cell identification is performed by the software. Working with a mixed population of neurons is therefore far from optimal and will affect the reproducibility of the assay and ultimately diminish the

chances of generating reproducible data. To solve this problem, transgenic mouse ES cells were chosen to generate MNs for the siRNA screen. These cells were engineered by Wichterle and colleagues to express GFP under the control of the MN specific Hb9 promoter, which allows the visualisation of MNs after differentiation (Wichterle et al., 2002). Using this ES cell line it was possible to easily scale up the production of MNs with the major advantage of being able to identify a homogeneous population of fluorescent MNs for the analysis. To differentiate the Hb9-GFP ES cells into MNs, I adapted the original protocol developed by Wichterle and co-workers. In the paper the yield of MNs was around 50%, whilst using this new improved protocol, I found that more than 80% of all cells in the embryoid bodies (EBs) were expressing GFP, as quantified by cytofluorimetric (FACS) analysis. Additionally, I found that the peak of MN specification in the EBs was at 4 days after addition of SAG and retinoic acid (RA), while in the original protocol the peak was at 5 days. This acceleration in MN specification was maybe due to an increased potency of the Sonic Hedgehog agonist that we used.

7.1.2 Transfection method

In parallel with establishing a reliable protocol of differentiation of ES cells into MNs, I also optimised an efficient protocol for siRNA downregulation in MN cultures. Previous attempts in the laboratory to transfect MNs using lipid-based transfection reagents such as Lipofectamine 2000 were largely unsuccessful, resulting in a low yield of transfection, an overall high toxicity and impairment of axonal transport (Deinhardt and Schiavo, 2005). It was then decided to adopt an alternative approach, such as electroporation, which had been successfully applied to primary cells and in particular has been used for MNs by Arnauld Jacquier and colleagues (Jacquier et al., 2006). I

tried two different electroporation systems, the PA-4000/PA-96 WS Pulse Agile^{R} and the BTX ECM 830, which were designed to electoporate cells in a 96 well format. As discussed in Chapter 3 (**section 3.3.1)**, efficient transfection could never be obtained using these systems with the parameters suggested by the supplier or those used by Jacquier and colleagues (Chapter 3, **Table 3.1**). The major problem with this transfection method, especially considering its application for HCS, was the complex handling procedure, which resulted in high cell mortality. Following these results, electroporation was abandoned, because it was ineffective and impractical for the purpose of the siRNA screen. I therefore decided to test a few lipid–based transfection reagents in primary MN cultures for their ability to transfect siRNA targeting VAMP2. This protein was chosen because of its abundance in neurons and the fact that its depletion does not affect neuronal viability (Schoch et al., 2001). As discussed in Chapter 3 (**section 3.3.1)**, Dharmafect 3 initially proved to be effective in knocking-down VAMP2 in primary MNs (**Figure 3.3**) with a traditional forward transfection protocol in a 24 well plate format, and showed no toxicity. The transfection efficiency, though, dropped once the batch of reagent was changed and, when the VAMP2 knockdown was attempted in a 96 well format, Dharmafect 3 proved completely ineffective. At this point, I decided to abandon the standard forward transfection in favour of a reverse transfection protocol, which considerably reduced the handling time and better suited the needs of an siRNA screen. Together with the high throughput screening facility at CRUK, I screened 23 different lipid-based transfection reagents in primary MNs for their ability to induce knockdown of VAMP2 directly on a 96 well plate and with a reverse transfection protocol (Chapter 3, **Table 3.2**), and finally narrowed down the best transfection reagent to Dreamfect Gold (**Figure 3.6**). Wary of

past experiences, a batch of the reagent was tested and a large quantity of the same batch was ordered to cover the needs of the screen and the subsequent validation.

7.1.3 Imaging and software analysis

I wanted an image-based readout for the siRNA screen, as a way to directly visualise the intracellular trafficking of the fluorescently labelled H_C and the antibody directed against the extracellular domain of $p75^{NTR}$. In order to achieve this goal, I needed means to acquire images with high enough resolution to allow the visualisation of the probes and to develop an algorithm of image analysis to quantify the data (Chapter 3, **section 3.4.2**). I described the initial attempts I made with the ARRAYSCAN imaging system, which is a microscope expressly designed for HCS (Krausz, 2007), and discussed the reasons why the use of this system was finally abandoned in favour of a confocal microscope (Chapter 3, **section 3.4.1**).

Confocal microscopy offered very high image resolution, but acquisition times were longer than for the ARRAYSCAN imaging system. However, the size of the siRNA library I intended to use for the screen was small (155 genes), so the automated acquisition capability of the Zeiss 510 confocal was more than adequate for the task. In order to be able to utilise the 40X oil objective lens I had to resort to the using glass bottom 96 well plates and to brush the immersion oil all over the bottom of the plates. This was the only way to obtain images with an high enough resolution to enable the identification of single H_C and $p75^{NTR}$ positive endosomes with the Cell Profiler software. The confocal automatic acquisition was made possible by the use of the MTS macro, designed for this purpose (discussed in Chapter 3, **section 3.4.2**), and the GFP fluorescence of MNs derived from Hb9-GFP ES cells (Wichterle et al., 2002). The autofocus function could not rely on nuclear staining, as is usually the case in image-

based HCS, because MN cultures contain several other cell types, such as glia and fibroblasts, which grow underneath the neurons and would cause the microscope to focus on a completely irrelevant plane. In addition, MNs tended to converge in clumps, which extended in the Z axis for several planes of focus. This problem could only be solved by acquiring many series of Z-stacks, which would not have been possible with any of the standard epifluorescence image acquisition systems designed for HCS. For unknown reasons, the tendency of MNs to clump represented a serious problem in a 96 well format. Standard forward transfection seemed to stress MNs probably because of the repeated changing of the medium and the handling required, whereas the reverse transfection protocol proved to be beneficial in alleviating the clumping of MNs and had no obvious adverse effects on cell viability or morphology.

Cell Profiler was chosen as the software for image-quantification, because it proved to be excellent for the recognition of cell morphology and spot identification, and also versatile, enabling me to easily extract features from the images such as the number of endosomes positive for H_C or $p75^{NTR}$ for individual MN (for a discussion of the image-analysis pipeline see Chapter 3, **section 3.4.2**).

7.1.4 Read-out

I required an assay which would be relevant to the investigation of neurotrophin trafficking, but which would also not involve many manipulations and be easy to scale up. I therefore opted to incubate the cells with H_C and the $p75^{NTR}$ antibody for two hours at 37^0C, followed by an acid wash, in order to be able to visualise exclusively the internalised pool of the two proteins (Chapter 4, **section 4.2**). The reason for choosing an end-point of 2 hours is related to the use of the EHNA inhibitor as an internal control for the assay. EHNA is a well-established dynein inhibitor (Penningroth et al., 1982,

Reynolds et al., 1998, Lalli et al., 2003), and it served as a proof of principle that the inhibition of a retrograde molecular motor affects the readout of the screen, which was an important point, since the siRNA library I intended to use was a molecular motor and adaptor library. EHNA inhibits the accumulation of both H_C and the $p75^{NTR}$ antibody (Chapter 4, **Figure 4.1**), but while EHNA affected the accumulation of H_C from the very beginning in a progressive fashion, it did not seem to affect the accumulation of the $p75^{NTR}$ antibody until 75 minutes. The different effects on the accumulation of the two probes suggests a different mechanism of endocytosis and trafficking: in the case of H_C, dynein seemed to be involved from the very beginning, however in the case of $p75^{NTR}$ there seemed to be a dynein-independent pool that was predominant up until 75 minutes. After that time point the dynein-dependent component gave a significant enough contribution to the total accumulation of the probe to reveal a difference in EHNA-treated MNs. Interestingly, a previous study showed that the onset of axonal retrograde transport of H_C is around 45 minutes and $p75^{NTR}$ colocalizes with H_C predominantly in endosomes, which are transported along the axons, while very little localisation was seen in the somatodendritic compartment (Lalli and Schiavo, 2002). Finally, as reported in **Figure 4.1**, H_C induced a higher accumulation of the $p75^{NTR}$ antibody and the curve of accumulation of this probe in the absence of H_C overlapped with the curve of the $p75^{NTR}$ antibody incubated together with H_C and in the presence of EHNA. It is tempting to speculate that in the absence of H_C, the accumulation of the $p75^{NTR}$ antibody is indicative of the internalisation and recycling of the receptor at steady state, which is dynein-independent, while the addition of H_C triggers a dynein-mediated internalisation and transport of a different pool of $p75^{NTR}$. Previous findings from the laboratory showed that H_C is capable of eliciting the axonal retrograde

transport of the $p75^{NTR}$ antibody (Deinhardt et al., 2007); it is therefore likely that EHNA inhibits the axonal retrograde transport of the $p75^{NTR}$ and its consequent accumulation in the neuronal cell bodies.

It has been shown that H_C binds to GT1b (Rummel et al., 2003) and that $p75^{NTR}$ forms a complex with this ganglioside (Fujitani et al., 2005, Williams et al., 2008). In this light it is possible that H_C induces the clustering of GT1b, causing the accumulation of GT1b-bound $p75^{NTR}$ in H_C and GT1b-enriched clathrin-coated pits feeding to the axonal transport route. In support of this hypothesis, $p75^{NTR}$ in the absence of ligand undergoes clathrin-independent recycling at the PM (Deinhardt et al., 2007). In such conditions no axonal retrograde transport of $p75^{NTR}$ was observed (Deinhardt et al., 2007). Addition of neurotrophins, such as NGF, or H_C redirects a pool of the receptor to a dynamin and clathrin-dependent route of internalisation coupled to axonal retrograde transport (Deinhardt et al., 2007). It is plausible that the route of internalisation of H_C connected to its axonal retrograde transport and the one used by ligand stimulated $p75^{NTR}$, which are both dynamin and clathrin-dependent (Deinhardt et al., 2006a) (Deinhardt et al., 2007), are the same. TeNT would in-fact benefit from taking advantage of a pre-existent axonal retrograde transport route. In this respect the axonal retrograde transport of the $p75^{NTR}$ antibody induced by H_C would mimic the physiological process that the receptor normally undergoes when it is stimulated by its physiological ligand NGF.

7.1.5 The screen

The molecular motor and adaptor siRNA library was chosen because the laboratory is interested in molecular motors, for which the expertise and a set of reagents and constructs are already available. In addition, Qiagen offered us the

possibility to customise the library, so that many genes of interest for the laboratory could be added, including many adaptors such as some of the Rab GTPases.

The layout of the plates and the procedure of the screen have already been described in Chapter 4, **Figure 4.2**. Importantly, I set up a series of additional controls, i.e. a few wells treated with a non targeting siRNA negative control and a few treated with the EHNA inhibitor. The calculation of the Z-scores, described in **section 4.3.2**, takes into account the distribution of the whole population. The scattering of the negative controls gives an indication of the variability of the assay. Ideally, negative controls should cluster in the middle of the population curve, were the siRNAs which do not affect the read out should be located. There are no precise rules about where to set the threshold to decide which samples should be considered as hits. Generally, setting the value of the threshold Z-score depends on the range of the assay used, i.e. how many standard deviations a true hit is expected to differ from the mean of the population. Certain types of screens, i.e. those based on luciferase activity, have a range of 40-50 standard deviations from the mean, while imaged-based screens generally have a much smaller range. Ultimately, the threshold I chose for both probes was not very stringent (Chapter, **section 4.3.3.**). However, this was not problematic because of the small size of the library, which yielded only very few primary hits to validate compared to the hundreds normally expected in a HCS. Not surprisingly, therefore, only 9 candidates out of the 44 primary hits were confirmed in the validation re-screen (Chapter 4, **section 4.4.2**).

7.1.6 Validated candidates

Among the validated candidates, the only protein that seemed to increase the accumulation of H_C when knocked-down was BICD1, while the only one to have a

similar effect in the trafficking of $p75^{NTR}$ was RAB7. RAB7 is a marker of late endosomes, MVBs and lysosomes (Stenmark, 2009) and a key regulator of the trafficking to late endosomes and lysosomes (Feng et al., 1995, Mukhopadhyay et al., 1997, Vitelli et al., 1997, Bucci et al., 2000, Lebrand et al., 2002). It was also found to be crucial in the axonal retrograde transport of H_C and $p75^{NTR}$ (Deinhardt et al., 2006b), since overexpression of a dominant negative version ($RAB7^{N125I}$) inhibited the axonal retrograde transport of the two probes. In addition, RAB7 has been found to be involved in the regulation of EGF receptor (EGFR) trafficking to late endosomes and its degradation (Ceresa and Bahr, 2006). The effects caused by RAB7 knockdown observed in the screen do not seem to be due to the an interference with the axonal retrograde transport of the $p75^{NTR}$, in which case the prediction would have been a reduced accumulation in the cell soma of the probe rather than an increased one. At the same time, H_C and the $p75^{NTR}$ have been described to share the same route of axonal retrograde transport (Lalli and Schiavo, 2002) (Deinhardt et al., 2006b), therefore interfering with this process would affect the two probes equally, which is not the case, since RAB7 was found as a candidate only for the $p75^{NTR}$ antibody. It might therefore be possible that the lack of RAB7 affected the trafficking of the $p75^{NTR}$ antibody internalised in the soma and dendrites, maybe preventing the probe from being directed to lysosomal degradation, thus determining its intracellular accumulation. Similar considerations are also relevant for BICD1, which only affected H_C, and will be discussed extensively in the next sections. Interestingly, mutations of RAB7 has been involved in the pathogenesis of Charcot–Marie–Tooth type 2B (CMT2B) (Verhoeven et al., 2003, Houlden et al., 2004, Meggouh et al., 2006), an inherited neuropathy that affects peripheral nerves (Jaradeh, 2003). The molecular mechanism by which

RAB7 mutations cause the disease is still unclear. Several hypothesis, including disruption of axonal transport, however, have been formulated (Cogli et al., 2009). Intriguingly, RAB7 is ubiquitously expressed, suggesting that this protein has a set of functions specific for few neuronal subtypes, since only the peripheral nervous system is affected by the CMT2B mutants.

The knockdown of *Dcnt1*, the p150 subunit of Dynactin, caused a decrease in the accumulation of H_C, which could be linked to a role of cytoplasmic dynein as a facilitator of H_C endocytosis. This would be consistent with the inhibition of the intracellular accumulation of H_C obtained in the presence of EHNA (**Figure 4.1**). The inhibition of endocytosis after treatment with EHNA is not exclusive to H_C, but it also extends to the internalisation of the $p75^{NTR}$ antibody (**Figure 4.1)**. Again, *Dcnt1* was not picked up as a candidate affecting the trafficking of $p75^{NTR}$, suggesting that its action might be connected to the interaction with a specific component of the dynein complex, rather than interfering with the complex as a whole. Interestingly, BICD1 has been described to interact with cytoplasmic dynein (Hoogenraad et al., 2001). As described for RAB7, mutations of p150 were shown to cause neurodegenerative conditions in humans and mice, such as amyotrophic lateral sclerosis (ALS) (Munch et al., 2004) and lower motor neuron disease (Puls et al., 2003) (Levy et al., 2006, Olkkonen and Ikonen, 2006).

A few kinesin motors were found in the screen to inhibit the accumulation of H_C and the $p75^{NTR}$ antibody when knocked down. This might be due to the fact that this family of motors transports cargoes towards the cell periphery and might therefore be involved in the transport of neurotrophin receptors to the PM. Notably, a kinesin-1-dependent mechanism of anterograde transport of Trk receptors and $p75^{NTR}$ complexed

with the scaffolding protein Kidins220, has been hypothesised (Bracale et al., 2007). A decreased level of $p75^{NTR}$ exposed at the neuronal surface, caused by the impairment of a possible kinesin-dependent transport of the receptor to the PM, might explain the decreased accumulation of the $p75^{NTR}$ antibody phenotypes found in the siRNA screen. Interestingly, as for RAB7 and p150, some kinesin motors have also been implicated in the pathogenesis of neurodegenerative conditions, such as KIF1B in the case of CMT2A disease (Zhao et al., 2001) and KIF5A for hereditary spastic paraplegia (Reid et al., 2002, Olkkonen and Ikonen, 2006).

One of the strongest and most interesting candidates resulting from the screen was BICD1. Upon its down-regulation, H_C was found to accumulate in MN cell bodies in a perinuclear region. BICD1 was initially described as a microtubule-associated dynein adaptor, and was also hypothesised to play a role in axonal transport in neurons (Wanschers et al., 2007). Given its role in regulating dynein-dependent traffic, which is essential for neurotrophin axonal transport (Lalli et al., 2003) (Hafezparast et al., 2003) (LaMonte et al., 2002), I decided to concentrate my efforts on this candidate.

7.2 Characterisation of *Bicd1* gene trapped ES cells.

I had the opportunity to take advantage of a genetic model generated by Krzysztof Wicher in David Ish-Horowicz laboratory at CRUK. Krzysztof purchased the RRP27 *Bicd1* gene trapped ES clone from The Gene Trap International consortium and kept it under high G418 concentration to bring it to homozygosity (Materials and Methods, **section 2.2.4.7**). As reported in Chapter 6 (**section 6.4.2)**, $Bicd1^{gt/gt}$ MNs expressed less than 30% of the *Bicd1* transcript compared to wild type cells (**Figure 6.2 C**). The reason why a complete ablation was not obtained is due to inherent 'leakiness' of the gene trapping strategy (Stanford et al., 2001). Confirming the Q-PCR data,

approximately 30% of the BICD1 protein was still present in *Bicd1*$^{gt/gt}$ MNs (**Figure 6.2 C**). The reduction of BICD1 protein levels using this genetic model was equivalent to a robust knockdown. A caveat of this approach is that the depletion of BICD1 might compromise and/or alter the differentiation potential of the ES cells. As presented in Chapter 6 (**section 6.4.1)**, culture of MNs differentiated from *Bicd1*$^{gt/gt}$ ES cells appeared morphologically normal. However fewer glial cells were found in the mutant culture. Furthermore, *Bicd1*$^{gt/gt}$ MNs were found to have a reduced lifespan. It was essential to determine that the expression of MN specific markers such as HB9 and ChAT was unaltered in *Bicd1*$^{gt/gt}$ MNs. The Q-PCR data confirmed that this was indeed the case (**Figure 6.2 C**). Remarkably, the level of expression of *Bicd2* was substantially increased in *Bicd1*$^{gt/gt}$ MNs (**Figure 6.2 C**), suggesting these cells tried to compensate for the depletion of BICD1 up-regulating the related *Bicd2* gene. However, upregulation of *Bicd2* expression is not able to fully compensate for the reduction in BICD1 levels, suggesting that the functions of BICD1 and BICD2 are not redundant in MNs.

7.2.1 BICD1 is expressed in the nervous system during mouse development

Little is known about the expression pattern of the Bicd family during mouse development, with the exception of *Bicdr1*, a Bicd-related protein, which is highly expressed at E10. At this embryonic day its distribution seems to be restricted to the nervous system, particularly to DRG, mesencephalon and romboenchephalon (Schlager et al., 2010). Given the absence of a mouse model to study the function of BICD1 *in vivo*, I decided to take advantage of the *Bicd1* gene-trapped mouse ES cells to generate one.

The results of the siRNA screen pointed to a new function for BICD1 in the

context of intracellular trafficking and signalling of neurotrophin receptors in neurons. Reassuringly, between E12.5 and E13.5 the expression of *Bicd1* was indeed restricted to the nervous system (**Figure 6.13**). At E12.5, *Bicd1* was found in the spinal cord and in the forebrain, while at E13.5 it started to disappear from those regions and the β−gal staining labelled prevalently DRGs and the hindbrain (**Figure 6.13**). This pattern of expression suggests that BICD1 plays an important role in neurons. Importantly, what is known so far for mammalian BICD1 and BICD2 derives primarily from studies conducted on cancer cell lines, which might not be the most physiologically relevant cell type to investigate the role of BICD1. Simon Bullock's group recently published a paper on the function of *Drosophila* BICD in neurons (Li et al., 2010). Interestingly, they showed that zygotic BICD function is only obligatory in the nervous system and that BICD is involved in transporting clathrin heavy chain back to the plasma membrane at synaptic sites in order to sustain synaptic vesicle recycling under prolonged electrical stimulation. This function of BICD might be conserved in mammalian cells, however it is probably not related to the phenotype I observed in the screen, because neither of the probes I used, H_C and $p75^{NTR}$, has been described to enter MNs via synaptic vesicle recycling. Also the study of Li and colleagues showed that BICD function becomes essential under conditions of sustained stimulation (Li et al., 2010), while the MN cultures I used were maintained in resting conditions. In addition, Li and colleagues showed that depletion of BICD determined an inhibition of endocytosis, which contrasts with my study where down-regulation of BICD1 during the screen and in *Bicd1*$^{gt/gt}$ MNs caused an accumulation of H_C and the $p75^{NTR}$ antibody (**Figure 6.4 & 6.5**), indicating that the endocytosis of the probes was not impaired. Finally, there is also the possibility that the function described by Li and colleagues in

Drosophila is played in mammalian neurons by BICD2 and not BICD1.

7.2.2 BICD1 depletion does not affect axonal retrograde transport.

Wanschers and colleagues hypothesised a role for mammalian BICD1 in retrograde transport on the basis of their finding that BICD1 – RAB6B double positive vesicles underwent bidirectional movements in neurites of differentiated SK-N-SH neuroblastoma cells (Chapter 5, **section 5.4.5**, (Wanschers et al., 2007)). It is tempting to speculate that BICD1 might have a role in axonal transport because it is an adaptor for the dynein-dynactin complex, which is essential for neurotrophin and H_C axonal retrograde transport (Hafezparast et al., 2003, Lalli et al., 2003) (LaMonte et al., 2002). However, the increased accumulation of H_C after knockdown of *Bicd1* was unlikely to be related to defects in axonal retrograde transport, as a decreased accumulation of the probe travelling from the periphery of the neuronal network would be expected in this case.

Axonal retrograde transport of H_C or NGF-stimulated $p75^{NTR}$ in wild type, *Bicd1*$^{gt/+}$ and *Bicd1*$^{gt/gt}$ MNs was analysed. However, no difference in the speed distribution curves of these probes was noticeable (**Figure 6.3**). This finding also offers a further confirmation that the neuronal populations derived from ES cells from the three genotypes were indeed similar. Consequently, it does not appear that BICD1 has a role in axonal retrograde transport, unless the residual levels of this protein were sufficient to support this process. Alternatively, the increased levels of BICD2 might be able to compensate for the lack of BICD1 in this context. Interestingly, BICD2 has been related to the anterograde transport of RAB6A positive vesicles (Grigoriev et al., 2007), however no interaction with the neuronal RAB6B isoform has been described to date.

7.2.3 BICD1 depletion induces accumulation of H_C and $p75^{NTR}$ and H_C accumulates in immature MVB in *Bicd1*$^{gt/gt}$ MNs

The H_C accumulation phenotype observed in the siRNA screen was confirmed in *Bicd1*$^{gt/gt}$ MNs (**Figure 6.4 A**). Interestingly, *Bicd1*$^{gt/+}$ MNs also showed a tendency to accumulate H_C at higher levels than the wild type cells, but this was not statistically significant (**Figure 6.4 A**). Strickingly, the $p75^{NTR}$ antibody when co-incubated with H_C, was also found to accumulate more in *Bicd1*$^{gt/+}$ and *Bicd1*$^{gt/gt}$ MNs (**Figure 6.4 B**). This result is not consistent with what was observed during the siRNA screen, where the knockdown of BICD1 did not affect the trafficking of the $p75^{NTR}$ antibody. This difference might be the result of a greater depletion of BICD1 in the case of the gene-trapped model compared to the siRNA knockdown.

In order to make a comparison with the trafficking of $p75^{NTR}$ triggered by a physiological ligand, the intracellular accumulation of the antibody upon BDNF stimulation was tested, and it was found to be 3 fold higher in *Bicd1*$^{gt/gt}$ than in wild type MNs (**Figure 6.5 B**). This finding suggests that BICD1 might play a role in the intracellular trafficking of the $p75^{NTR}$ upon stimulation with its physiological ligand in MNs. After internalisation, $p75^{NTR}$ is thought to prevalently recycle back to the PM ((Bronfman et al., 2003) (Deinhardt et al., 2006b), **Figure 7.1**), while TeNT undergoes sorting in MN cell bodies and is redirected to the plasma membrane to be transcytosed ((Salinas et al., 2010), **Figure 7.1**). It is possible that BICD1 depletion causes an accumulation of the two probes because of a modification of a normal endosomal sorting mechanism. In this light, our EM data demonstrated an increased accumulation of gold-labelled H_C in immature MVBs, with a low content of intraluminal vesicles, in *Bicd1*$^{gt/gt}$ MNs (**Figure 6.6**). The number and the size of these immature MVBs were

increased in *Bicd1*$^{gt/gt}$ MNs, suggesting that the depletion of BICD1 inhibited the maturation of this organelle (**Figure 7.2**), causing the intracellular accumulation of these structures and of the probe inside them. Interestingly, H_C displayed a polarised distribution inside *Bicd1*$^{gt/gt}$ MVBs, clustering on one side of the delimiting membrane. This distribution is maybe an indication of the probe accumulating in preparation for a potential sorting back to the plasma membrane (**Figure 7.2**).

Although the EM data have been obtained using H_C, it is possible to speculate that what appears to be a general inhibition of the maturation of MVBs would also affect the intracellular trafficking of p75^{NTR} and TrkB. TrkB has been described to mainly be sorted to the degradative route, while a smaller pool of the receptor enters the recycling pathway ((Chen et al., 2005) (Bronfman et al., 2007, Huang et al., 2009), **Figure 7.1**). Depletion of BICD1 might prevent the maturation of the MVBs resulting in an inhibition of the degradative pathway and a consequent intracellular accumulation of the pool of TrkB receptor destined for degradation. In the absence of ligands, p75^{NTR} has been described to mainly undergo recycling back to the plasma membrane in PC12 cells (Bronfman et al., 2007) and in neurons ((Deinhardt et al., 2007), **Figure 7.1**). However, p75^{NTR} internalisation becomes clathrin-dependent upon binding with its ligand or when incubated with H_C and in MNs this results in the retrograde transport of the receptor in the same compartment as H_C ((Deinhardt et al., 2007), **Figure 7.1**). It is therefore possible that p75^{NTR} accumulation upon stimulation with NGF in *Bicd1*$^{gt/gt}$ MNs is caused by an MVB maturation defect caused by the depletion of BICD1, which might prevent p75^{NTR} from undergoing its physiological trafficking and sorting (**Figure 7.2**). Interestingly, MVBs have been found to be the main endosomal population in sympathetic neuron cell bodies labelled with iodinated NGF (ligand of both TrkA and

p75^{NTR}) (Claude et al., 1982), and Trk receptors were found associated with MVBs (Valdez et al., 2005).

7.2.4 BICD1 depletion affects the levels of TrkB and p75^{NTR} on the PM and alters TrkB signalling

Ligand-bound p75^{NTR} and TrkB, which are unable to progress along the degradative route in *Bicd1*$^{gt/gt}$ MNs are likely to be redirected on the PM. To confirm this hypothesis, the levels of TrkB and p75^{NTR} exposed at the PM were indeed found to be significantly higher in *Bicd1*$^{gt/gt}$ MNs (Chapter 6, **section 6.8.3**, **Figure 6.9** and **6.10**). This is particularly relevant for TrkB, because it is expressed at lower levels in *Bicd1*$^{gt/gt}$ MNs than in wild type cells (**Figure 6.2 C**), which indicates that a higher proportion of TrkB must be redirected to the PM in mutant cells. In the case of p75^{NTR}, the depletion of BICD1 is expected to affect only the pool of the receptor that undergoes ligand-triggered internalisation, because this receptor is already thought to undergo mainly the recycling route to the PM in the absence of ligands. Surprisingly, though, p75^{NTR} levels on the PM in *Bicd1*$^{gt/gt}$ MNs were double that of wild type cells even without the addition of BDNF. However, MN cultures also contain glial cells, which are likely to secrete neurotrophins into the medium (Levi-Montalcini et al., 1996) (Roux and Barker, 2002), and neurons themselves secrete neurotrophins (Roux and Barker, 2002). Consequently, p75^{NTR} ligand-triggered internalisation and redirection to the degradative route might happen normally in culture, resulting in a increased exposure of the receptor on the *Bicd1*$^{gt/gt}$ MN surface compared to wild type cells, determined by the redirection of the ligand-bound pool of the receptor (**Figure 6.9**). This hypothesis could be tested by analysing the conditioned media from MN cultures for secreted neurotrophins such as BDNF. Intriguingly, p75^{NTR} protein levels of at steady state were higher in *Bicd1*$^{gt/gt}$

MNs (**Figure 6.2 B**), yet the gene was expressed at wild type levels (**Figure 6.2. C**), supporting the idea that the degradative pathway of the receptor is impaired. Interestingly, RAB7 was found to induce increased accumulation of the $p75^{NTR}$ antibody in the siRNA screen (**section 7.1.6**), suggesting that blocking late endosome maturation does indeed cause the intracellular accumulation of $p75^{NTR}$. No further characterization was done for RAB7, but it will be important to check whether RAB7 knockdown phenocopies BICD1 depletion in terms of an increased exposure of the $p75^{NTR}$ on the PM.

I wanted to test if the altered intracellular distribution of $p75^{NTR}$ and TrkB in *Bicd1*$^{gt/gt}$ MNs would also affect TrkB signalling. In collaboration with Matthew Golding in the laboratory, we assessed the phosphorylation kinetics of Akt and ERK1/2 upon BDNF stimulation. A decrease in activation of these proteins was observed in *Bicd1*$^{gt/gt}$ MNs compared to the wild type control (**Figure 6.11** and **6.12**). An alteration of TrkB signalling due to changes in its intracellular localisation is reported in the literature: overexpression of hepatocyte growth factor-regulated tyrosine kinase substrate (Hrs) in PC12 cells causes the redirection of TrkB to the recycling route, determining a more sustained ERK1/2 activation upon BDNF stimulation (Huang et al., 2009). A similar behaviour has also been described for another Trk receptor, TrkA, in that inhibiting the degradative pathway of the receptor resulted in endosomal accumulation of TrkA with a consequent increase in ERK1/2 activation (Saxena et al., 2005a, Saxena et al., 2005b). The difference between our data and what has been reported in the literature might be due to different signalling mechanics in PC12 cells compared to neurons. In favour of this hypothesis, work from a colleague in the laboratory, Guillermo Menedez, showed that in DRG neurons the knockdown of RAB7

or the overexpression of a dominant negative form of this protein reduces the activation of CREB induced by NGF (Guillermo Menendez, Ph.D thesis). CREB phosphorylation is induced by the activation of TrkA, and this suggests that inhibiting the degradative pathway of TrkA might have the opposite effect on signalling in neurons than what has been previously described for PC12 cells (Saxena et al., 2005a, Saxena et al., 2005b). In addition, a potential reduction of the survival signal elicited by TrkB could explain the decreased viability of *Bicd1*$^{gt/gt}$ MNs in culture (Chapter 6, **section 6.4.1**).

An interesting observation is that, while the exposure of p75^{NTR} at the PM is two folds higher in *Bicd1*$^{gt/gt}$ MNs compared to wild type cells (Chapter 6, **Figure 6.9**), TrkB is only 45% more exposed at the PM in of *Bicd1*$^{gt/gt}$ MNs (Chapter 6, **Figure 6.10**). This difference might result in an excess of p75^{NTR}, which would then sequester BDNF preventing it from activating TrkB. Alternatively, an altered ratio between p75^{NTR} and TrkB at the PM might affect the integration of the signals coming from these receptors. Hyperactivation of p75^{NTR}, for example, could give rise to a feedback loop, which might decrease TrkB signalling. In order to test this hypothesis the signalling of p75^{NTR} through NF-kB and JNK (Roux and Barker, 2002) (Chen et al., 2009) would need to be tested; the prediction would be that the signalling through these pathways should be increased in *Bicd1*$^{gt/gt}$ MNs.

An increased binding of H_C was also observed in *Bicd1*$^{gt/gt}$ MNs, which could be explained by the increased levels of the polysialogangliosides GD1b on the PM, to which H_C binds ((Halpern and Neale, 1995, Schiavo et al., 2000, Rummel et al., 2003), **Figure 6.8**). I have not yet investigated whether the depletion of BICD1 affects the intracellular trafficking of this molecule or if the overall content of GD1b in these cells is increased. In future experiments I plan to attempt to purify these lipids using thin

layer chromatography (TLC) to quantify the GD1b content of *Bicd1*$^{gt/gt}$ MNs. The only indirect data we have in this regard is that the expression level of the enzyme responsible for the synthesis of this lipid, GalNacT, is the same in the two genotypes (**Figure 6.2 C**).

7.3 Conclusion and future experiments

BICD1 is a microtubule associated protein and a dynein adaptor, which has been associated with several cellular functions (**Figure 5.1**), the best known in mammalian cells being the Golgi to ER COPI-independent retrograde transport (Matanis et al., 2002). I have identified a novel role of this molecule in MNs. Notably, the only study linking a BICD protein to neurons was performed in *Drosophila* (Li et al., 2010), while BICDR-1, a BICD related protein, was found to be involved in neurite extension in hippocampal neurons (Schlager et al., 2010). In this thesis work, I have shown that the depletion of BICD1 alters the intracellular trafficking of neurotrophin receptors, possibly by impairing MVB maturation, resulting in an increased recycling of p75^{NTR} and TrkB back to the PM (**Figure 7.2**). The recycling of p75^{NTR} could be assayed by incubating *Bicd1*$^{gt/gt}$ MNs with a fluorescently conjugated version of the p75^{NTR} antibody for an amount of time sufficient to allow receptor internalisation, followed by a brief acid-wash and then allow enough time for p75^{NTR} to recycle back to the PM. The recycled receptor could then be visualised by staining with a differently coloured fluorescent secondary antibody (Deinhardt et al., 2007).

The signalling induced by BDNF via TrkB was decreased in *Bicd1*$^{gt/gt}$ MNs. It should be established whether this is also the case for p75^{NTR} signalling through NF-kB and JNK. In addition, it would be interesting to verify whether the initial defect in Akt

and ERK1/2 activation in $p75^{NTR}$ MNs translates to a defect in the activation of a downstream effector of the MAPK pathway, like the transcriptional factor CREB. The knockdown of RAB7, another candidate of the siRNA screen, gives a similar phenotype in terms of $p75^{NTR}$ intracellular accumulation and TrkA signalling in DRG neurons (Guillermo Menendez, PhD thesis) and should also be tested. Finally, the opportunity of using the *Bicd1*$^{gt/gt}$ ES cells to generate a homozygous mouse should be explored, in order to determine the *in vivo* phenotype. The heterozygous ES cells never gave rise to any offspring, suggesting that the gene is haploid insufficient, even though no obvious defect were noted in heterozygous embryos up to E14.5, which was the latest development stage analysed. Interestingly, while *Bicd1*$^{gt/+}$ MNs mostly behaved like wild type MNs, they showed a behaviour similar to *Bicd1*$^{gt/gt}$ cells in the assays involving H_C internalisation (**Figure 6.4**) and binding (**Figure 6.7**). A possible explanation could be provided by the observation that the levels of GD1b on the PM, a major determinant of H_C binding to the neuronal surface, are similar in *Bicd1*$^{gt/+}$ and *Bicd1*$^{gt/gt}$ MNs (**Figure 6.8**). The level of depletion of BICD1 in *Bicd1*$^{gt/+}$ MNs seems sufficient to cause an increased exposure of GD1b at the PM, while not affecting the behaviour of $p75^{NTR}$ and TrkB. Further studies will be needed to unravel the mechanism underlying this observation.

In conclusion this thesis work has demonstrated that a high content screen approach can be applied to motor neurons, which are notoriously difficult to handle and transfect. This approach has been successful in unravelling a new role for BICD1 in mammalian neurons. I was also able to show the pattern of expression of *Bicd1* in E12.5 and E13.5 mouse embryos, and gather data that points to a role for this protein in the trafficking and signalling of neurotrophin receptors, which might be extremely relevant

during the development of the nervous system.

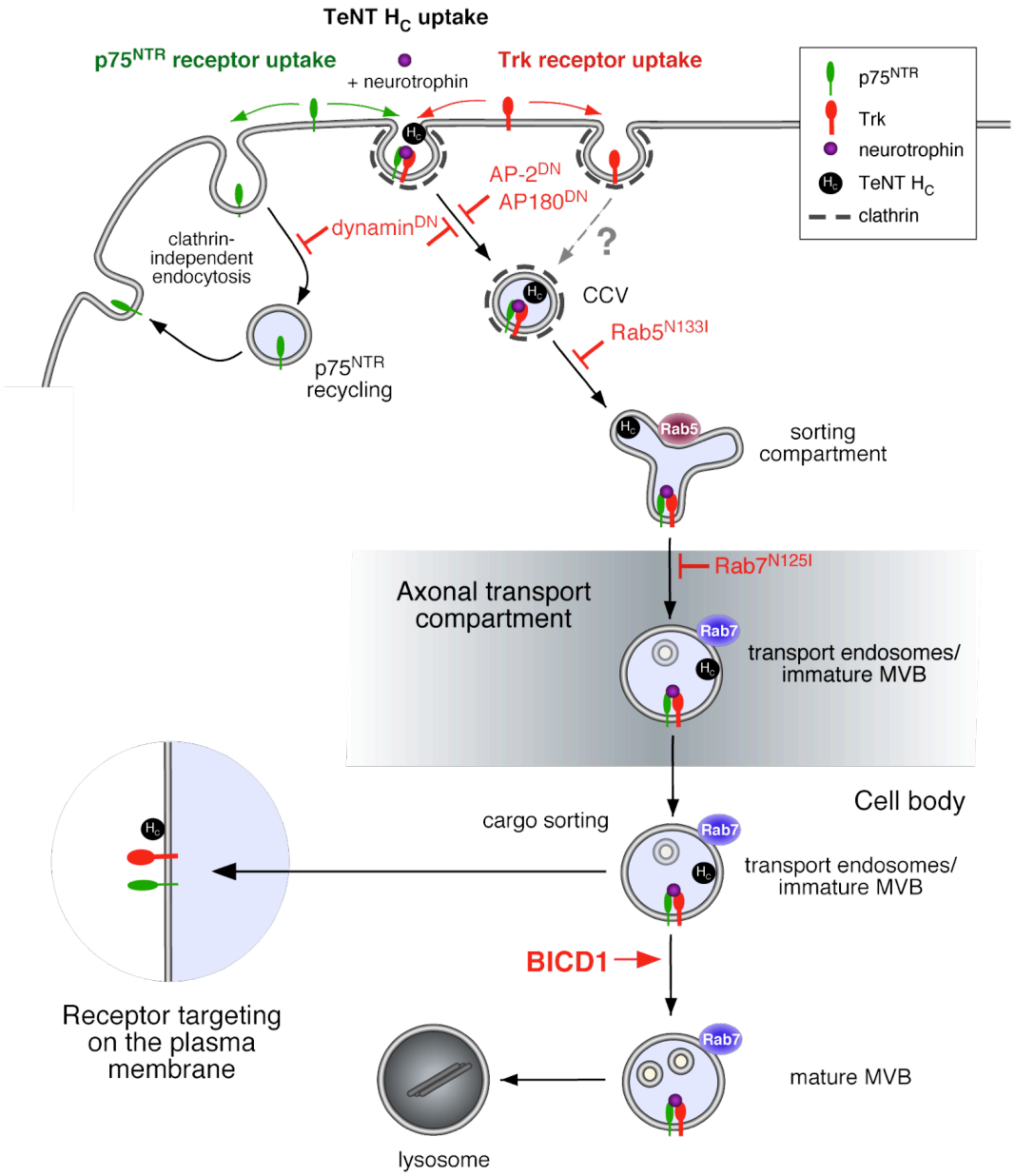

Figure 7.1 Intracellular trafficking of H_C, TrkB and p75^{NTR}
Schematic representation of the trafficking of neurotrophin receptors and H_C in wild type MNs. In conditions of non stimulation TrkB is mainly directed to a degradative route (lysosome), while p75^{NTR} mostly recycles back on the PM (Chen et al., 2005, Deinhardt et al., 2007). Upon neurotrophin binding both receptors undergo clathrin-mediated endocytosis, similar to H_C, and are redirected to a common retrograde axonal transport route. This process is dependent on Rab5 and Rab7, because dominant negative forms of these two proteins prevent H_C, p75^{NTR} and TrkB axonal retrograde transport (Deinhardt et al., 2006b). After axonal transport to the cell body H_C is found in multivescicular bodies (MVB). It is likely that p75^{NTR} and TrkB also end up in MVBs, since they are transported together with H_C. From this sorting platform H_C, p75^{NTR} and TrkB can undergo recycling or degradation. From the data gather in this thesis work BICD1 is likely to play a role in MVB maturation (**Figure 7.2**). Modified from (Deinhardt et al., 2006b).

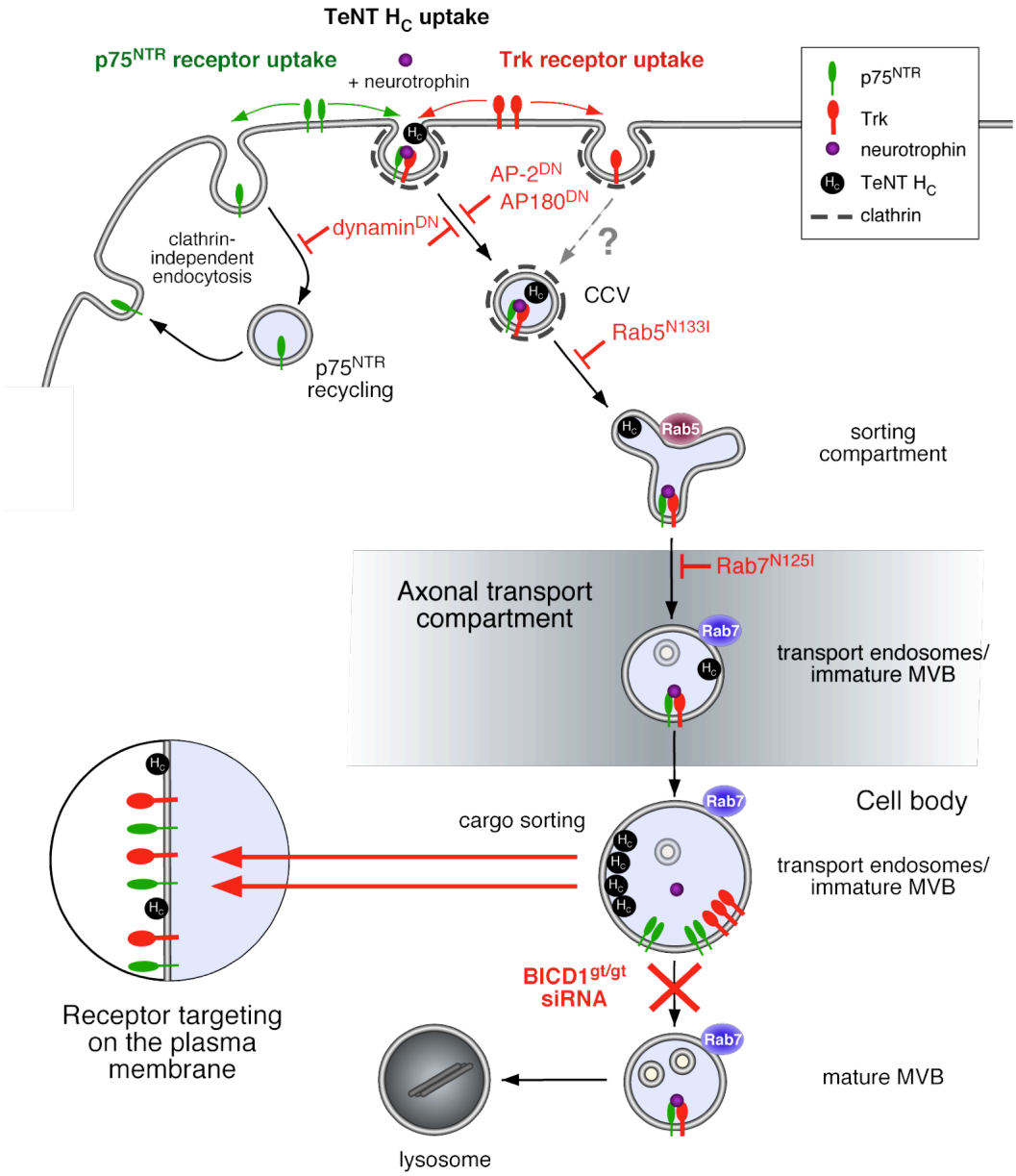

Figure 7.2 Model of the putative function of BICD1 in the intracellular trafficking of TrkB and p75^{NTR}

Schematic representation of the possible role of the BICD1 protein in the trafficking of neurotrophin receptors based on the evidence gathered in this thesis work. The depletion of BICD1 by inhibiting the maturation of the MVBs could interfere with the degradation of endocytosed TrkB and p75^{NTR}. This might result in a redirection of both receptors to the PM, with the net effect of increasing their concentration on the PM.

Reference List

ARCE, V., GARCES, A., DE BOVIS, B., FILIPPI, P., HENDERSON, C., PETTMANN, B. & DELAPEYRIERE, O. (1999) Cardiotrophin-1 requires LIFRbeta to promote survival of mouse motoneurons purified by a novel technique. *J Neurosci Res,* 55**,** 119-26.

ASCANO, M., RICHMOND, A., BORDEN, P. & KURUVILLA, R. (2009) Axonal targeting of Trk receptors via transcytosis regulates sensitivity to neurotrophin responses. *J Neurosci,* 29**,** 11674-85.

BAENS, M. & MARYNEN, P. (1997) A human homologue (BICD1) of the Drosophila bicaudal-D gene. *Genomics,* 45**,** 601-6.

BHATTACHARYYA, A., WATSON, F. L., BRADLEE, T. A., POMEROY, S. L., STILES, C. D. & SEGAL, R. A. (1997) Trk receptors function as rapid retrograde signal carriers in the adult nervous system. *J Neurosci,* 17**,** 7007-16.

BIBEL, M. & BARDE, Y. A. (2000) Neurotrophins: key regulators of cell fate and cell shape in the vertebrate nervous system. *Genes Dev,* 14**,** 2919-37.

BINZ, T. & RUMMEL, A. (2009) Cell entry strategy of clostridial neurotoxins. *J Neurochem,* 109**,** 1584-95.

BOHNERT, S. & SCHIAVO, G. (2005) Tetanus toxin is transported in a novel neuronal compartment characterized by a specialized pH regulation. *J Biol Chem,* 280**,** 42336-44.

BORNENS, M. (2002) Centrosome composition and microtubule anchoring mechanisms. *Curr Opin Cell Biol,* 14**,** 25-34.

BRACALE, A., CESCA, F., NEUBRAND, V. E., NEWSOME, T. P., WAY, M. & SCHIAVO, G. (2007) Kidins220/ARMS is transported by a kinesin-1-based

mechanism likely to be involved in neuronal differentiation. *Mol Biol Cell,* 18**,** 142-52.

BRONFMAN, F. C., ESCUDERO, C. A., WEIS, J. & KRUTTGEN, A. (2007) Endosomal transport of neurotrophins: roles in signaling and neurodegenerative diseases. *Dev Neurobiol,* 67**,** 1183-203.

BRONFMAN, F. C., TCHERPAKOV, M., JOVIN, T. M. & FAINZILBER, M. (2003) Ligand-induced internalization of the p75 neurotrophin receptor: a slow route to the signaling endosome. *J Neurosci,* 23**,** 3209-20.

BUCCI, C., THOMSEN, P., NICOZIANI, P., MCCARTHY, J. & VAN DEURS, B. (2000) Rab7: a key to lysosome biogenesis. *Mol Biol Cell,* 11**,** 467-80.

BULLOCK, S. L. & ISH-HOROWICZ, D. (2001) Conserved signals and machinery for RNA transport in Drosophila oogenesis and embryogenesis. *Nature,* 414**,** 611-6.

CERESA, B. P. & BAHR, S. J. (2006) rab7 activity affects epidermal growth factor:epidermal growth factor receptor degradation by regulating endocytic trafficking from the late endosome. *J Biol Chem,* 281**,** 1099-106.

CHAO, M. V. & LEE, F. S. (2004) Neurotrophin survival signaling mechanisms. *J Alzheimers Dis,* 6**,** S7-11.

CHEN, Y., ZENG, J., CEN, L., WANG, X., YAO, G., WANG, W., QI, W. & KONG, K. (2009) Multiple roles of the p75 neurotrophin receptor in the nervous system. *J Int Med Res,* 37**,** 281-8.

CHEN, Z. Y., IERACI, A., TANOWITZ, M. & LEE, F. S. (2005) A novel endocytic recycling signal distinguishes biological responses of Trk neurotrophin receptors. *Mol Biol Cell,* 16**,** 5761-72.

CLARY, D. O. & REICHARDT, L. F. (1994) An alternatively spliced form of the nerve growth factor receptor TrkA confers an enhanced response to neurotrophin 3. *Proc Natl Acad Sci U S A,* 91**,** 11133-7.

CLAUDE, P., HAWROT, E., DUNIS, D. A. & CAMPENOT, R. B. (1982) Binding, internalization, and retrograde transport of 125I-nerve growth factor in cultured rat sympathetic neurons. *J Neurosci,* 2**,** 431-42.

COGLI, L., PIRO, F. & BUCCI, C. (2009) Rab7 and the CMT2B disease. *Biochem Soc Trans,* 37**,** 1027-31.

COHEN, S., LEVI-MONTALCINI, R. & HAMBURGER, V. (1954) A Nerve Growth-Stimulating Factor Isolated from Sarcom as 37 and 180. *Proc Natl Acad Sci U S A,* 40**,** 1014-8.

COLLINET, C., STOTER, M., BRADSHAW, C. R., SAMUSIK, N., RINK, J. C., KENSKI, D., HABERMANN, B., BUCHHOLZ, F., HENSCHEL, R., MUELLER, M. S., NAGEL, W. E., FAVA, E., KALAIDZIDIS, Y. & ZERIAL, M. (2010) Systems survey of endocytosis by multiparametric image analysis. *Nature,* 464**,** 243-9.

DEINHARDT, K., BERNINGHAUSEN, O., WILLISON, H. J., HOPKINS, C. R. & SCHIAVO, G. (2006a) Tetanus toxin is internalized by a sequential clathrin-dependent mechanism initiated within lipid microdomains and independent of epsin1. *J Cell Biol,* 174**,** 459-71.

DEINHARDT, K., REVERSI, A., BERNINGHAUSEN, O., HOPKINS, C. R. & SCHIAVO, G. (2007) Neurotrophins Redirect p75NTR from a clathrin-independent to a clathrin-dependent endocytic pathway coupled to axonal transport. *Traffic,* 8**,** 1736-49.

DEINHARDT, K., SALINAS, S., VERASTEGUI, C., WATSON, R., WORTH, D., HANRAHAN, S., BUCCI, C. & SCHIAVO, G. (2006b) Rab5 and Rab7 control endocytic sorting along the axonal retrograde transport pathway. *Neuron,* 52**,** 293-305.

DEINHARDT, K. & SCHIAVO, G. (2005) Endocytosis and retrograde axonal traffic in motor neurons. *Biochem Soc Symp***,** 139-50.

DELCROIX, J. D., VALLETTA, J. S., WU, C., HUNT, S. J., KOWAL, A. S. & MOBLEY, W. C. (2003) NGF signaling in sensory neurons: evidence that early endosomes carry NGF retrograde signals. *Neuron,* 39**,** 69-84.

DELGEHYR, N., SILLIBOURNE, J. & BORNENS, M. (2005) Microtubule nucleation and anchoring at the centrosome are independent processes linked by ninein function. *J Cell Sci,* 118**,** 1565-75.

DI FIORE, P. P. & DE CAMILLI, P. (2001) Endocytosis and signaling. an inseparable partnership. *Cell,* 106**,** 1-4.

DIENSTBIER, M. & LI, X. (2009) Bicaudal-D and its role in cargo sorting by microtubule-based motors. *Biochem Soc Trans,* 37**,** 1066-71.

DOLLY, J. O., BLACK, J., WILLIAMS, R. S. & MELLING, J. (1984) Acceptors for botulinum neurotoxin reside on motor nerve terminals and mediate its internalization. *Nature,* 307**,** 457-60.

ECHEVERRI, C. J., BEACHY, P. A., BAUM, B., BOUTROS, M., BUCHHOLZ, F., CHANDA, S. K., DOWNWARD, J., ELLENBERG, J., FRASER, A. G., HACOHEN, N., HAHN, W. C., JACKSON, A. L., KIGER, A., LINSLEY, P. S., LUM, L., MA, Y., MATHEY-PREVOT, B., ROOT, D. E., SABATINI, D. M., TAIPALE, J., PERRIMON, N. & BERNARDS, R. (2006) Minimizing the

risk of reporting false positives in large-scale RNAi screens. *Nat Methods,* 3**,** 777-9.

ECHEVERRI, C. J. & PERRIMON, N. (2006) High-throughput RNAi screening in cultured cells: a user's guide. *Nat Rev Genet,* 7**,** 373-84.

ERFLE, H., SIMPSON, J. C., BASTIAENS, P. I. & PEPPERKOK, R. (2004) siRNA cell arrays for high-content screening microscopy. *Biotechniques,* 37**,** 454-8, 460, 462.

FENG, Y., PRESS, B. & WANDINGER-NESS, A. (1995) Rab 7: an important regulator of late endocytic membrane traffic. *J Cell Biol,* 131**,** 1435-52.

FIGUEIREDO, D., TURCOTTE, C., FRANKEL, G., LI, Y., DOLLY, O., WILKIN, G., MARRIOTT, D., FAIRWEATHER, N. & DOUGAN, G. (1995) Characterization of recombinant tetanus toxin derivatives suitable for vaccine development. *Infect Immun,* 63**,** 3218-21.

FRYER, R. H., KAPLAN, D. R., FEINSTEIN, S. C., RADEKE, M. J., GRAYSON, D. R. & KROMER, L. F. (1996) Developmental and mature expression of full-length and truncated TrkB receptors in the rat forebrain. *J Comp Neurol,* 374**,** 21-40.

FUJITANI, M., KAWAI, H., PROIA, R. L., KASHIWAGI, A., YASUDA, H. & YAMASHITA, T. (2005) Binding of soluble myelin-associated glycoprotein to specific gangliosides induces the association of p75NTR to lipid rafts and signal transduction. *J Neurochem,* 94**,** 15-21.

FUMOTO, K., HOOGENRAAD, C. C. & KIKUCHI, A. (2006) GSK-3beta-regulated interaction of BICD with dynein is involved in microtubule anchorage at centrosome. *EMBO J,* 25**,** 5670-82.

GEETHA, T., JIANG, J. & WOOTEN, M. W. (2005) Lysine 63 polyubiquitination of the nerve growth factor receptor TrkA directs internalization and signaling. *Mol Cell,* 20**,** 301-12.

GOLDSTEIN, L. S. & YANG, Z. (2000) Microtubule-based transport systems in neurons: the roles of kinesins and dyneins. *Annu Rev Neurosci,* 23**,** 39-71.

GRIGORIEV, I., SPLINTER, D., KEIJZER, N., WULF, P. S., DEMMERS, J., OHTSUKA, T., MODESTI, M., MALY, I. V., GROSVELD, F., HOOGENRAAD, C. C. & AKHMANOVA, A. (2007) Rab6 regulates transport and targeting of exocytotic carriers. *Dev Cell,* 13**,** 305-14.

GRIMES, M. L., BEATTIE, E. & MOBLEY, W. C. (1997) A signaling organelle containing the nerve growth factor-activated receptor tyrosine kinase, TrkA. *Proc Natl Acad Sci U S A,* 94**,** 9909-14.

GRIMES, M. L., ZHOU, J., BEATTIE, E. C., YUEN, E. C., HALL, D. E., VALLETTA, J. S., TOPP, K. S., LAVAIL, J. H., BUNNETT, N. W. & MOBLEY, W. C. (1996) Endocytosis of activated TrkA: evidence that nerve growth factor induces formation of signaling endosomes. *J Neurosci,* 16**,** 7950-64.

HABERMANN, E. & DREYER, F. (1986) Clostridial neurotoxins: handling and action at the cellular and molecular level. *Curr Top Microbiol Immunol,* 129**,** 93-179.

HAFEZPARAST, M., KLOCKE, R., RUHRBERG, C., MARQUARDT, A., AHMAD-ANNUAR, A., BOWEN, S., LALLI, G., WITHERDEN, A. S., HUMMERICH, H., NICHOLSON, S., MORGAN, P. J., OOZAGEER, R., PRIESTLEY, J. V., AVERILL, S., KING, V. R., BALL, S., PETERS, J., TODA, T., YAMAMOTO, A., HIRAOKA, Y., AUGUSTIN, M., KORTHAUS, D., WATTLER, S.,

WABNITZ, P., DICKNEITE, C., LAMPEL, S., BOEHME, F., PERAUS, G., POPP, A., RUDELIUS, M., SCHLEGEL, J., FUCHS, H., HRABE DE ANGELIS, M., SCHIAVO, G., SHIMA, D. T., RUSS, A. P., STUMM, G., MARTIN, J. E. & FISHER, E. M. (2003) Mutations in dynein link motor neuron degeneration to defects in retrograde transport. *Science,* 300**,** 808-12.

HALPERN, J. L. & NEALE, E. A. (1995) Neurospecific binding, internalization, and retrograde axonal transport. *Curr Top Microbiol Immunol,* 195**,** 221-41.

HEERSSEN, H. M., PAZYRA, M. F. & SEGAL, R. A. (2004) Dynein motors transport activated Trks to promote survival of target-dependent neurons. *Nat Neurosci,* 7**,** 596-604.

HERREROS, J., LALLI, G., MONTECUCCO, C. & SCHIAVO, G. (2000) Tetanus toxin fragment C binds to a protein present in neuronal cell lines and motoneurons. *J Neurochem,* 74**,** 1941-50.

HERREROS, J., NG, T. & SCHIAVO, G. (2001) Lipid rafts act as specialized domains for tetanus toxin binding and internalization into neurons. *Mol Biol Cell,* 12**,** 2947-60.

HOOGENRAAD, C. C., AKHMANOVA, A., HOWELL, S. A., DORTLAND, B. R., DE ZEEUW, C. I., WILLEMSEN, R., VISSER, P., GROSVELD, F. & GALJART, N. (2001) Mammalian Golgi-associated Bicaudal-D2 functions in the dynein-dynactin pathway by interacting with these complexes. *EMBO J,* 20**,** 4041-54.

HOULDEN, H., KING, R. H., MUDDLE, J. R., WARNER, T. T., REILLY, M. M., ORRELL, R. W. & GINSBERG, L. (2004) A novel RAB7 mutation associated with ulcero-mutilating neuropathy. *Ann Neurol,* 56**,** 586-90.

HOWE, C. L. & MOBLEY, W. C. (2005) Long-distance retrograde neurotrophic signaling. *Curr Opin Neurobiol,* 15**,** 40-8.

HOWE, C. L., VALLETTA, J. S., RUSNAK, A. S. & MOBLEY, W. C. (2001) NGF signaling from clathrin-coated vesicles: evidence that signaling endosomes serve as a platform for the Ras-MAPK pathway. *Neuron,* 32**,** 801-14.

HUANG, E. J. & REICHARDT, L. F. (2001) Neurotrophins: roles in neuronal development and function. *Annu Rev Neurosci,* 24**,** 677-736.

HUANG, S. H., ZHAO, L., SUN, Z. P., LI, X. Z., GENG, Z., ZHANG, K. D., CHAO, M. V. & CHEN, Z. Y. (2009) Essential role of Hrs in endocytic recycling of full-length TrkB receptor but not its isoform TrkB.T1. *J Biol Chem,* 284**,** 15126-36.

INDRAN, S. V., BALLESTAS, M. E. & BRITT, W. J. (2010) Bicaudal D1-dependent trafficking of human cytomegalovirus tegument protein pp150 in virus-infected cells. *J Virol,* 84**,** 3162-77.

JACQUIER, A., BUHLER, E., SCHAFER, M. K., BOHL, D., BLANCHARD, S., BECLIN, C. & HAASE, G. (2006) Alsin/Rac1 signaling controls survival and growth of spinal motoneurons. *Ann Neurol,* 60**,** 105-17.

JAHN, R. & SCHELLER, R. H. (2006) SNAREs--engines for membrane fusion. *Nat Rev Mol Cell Biol,* 7**,** 631-43.

JARADEH, S. S. (2003) Hereditary neuropathies. *J Clin Neuromuscul Dis,* 5**,** 72-80.

JOHNSON, D., LANAHAN, A., BUCK, C. R., SEHGAL, A., MORGAN, C., MERCER, E., BOTHWELL, M. & CHAO, M. (1986) Expression and structure of the human NGF receptor. *Cell,* 47**,** 545-54.

JORDENS, I., MARSMAN, M., KUIJL, C. & NEEFJES, J. (2005) Rab proteins, connecting transport and vesicle fusion. *Traffic,* 6**,** 1070-7.

KAPLAN, D. R. & MILLER, F. D. (2000) Neurotrophin signal transduction in the nervous system. *Curr Opin Neurobiol,* 10**,** 381-91.

KIRKHAM, M. & PARTON, R. G. (2005) Clathrin-independent endocytosis: new insights into caveolae and non-caveolar lipid raft carriers. *Biochim Biophys Acta,* 1746**,** 349-63.

KITAMURA, M., TAKAMIYA, K., AIZAWA, S. & FURUKAWA, K. (1999) Gangliosides are the binding substances in neural cells for tetanus and botulinum toxins in mice. *Biochim Biophys Acta,* 1441**,** 1-3.

KRAUSZ, E. (2007) High-content siRNA screening. *Mol Biosyst,* 3**,** 232-40.

LALLI, G., GSCHMEISSNER, S. & SCHIAVO, G. (2003) Myosin Va and microtubule-based motors are required for fast axonal retrograde transport of tetanus toxin in motor neurons. *J Cell Sci,* 116**,** 4639-50.

LALLI, G., HERREROS, J., OSBORNE, S. L., MONTECUCCO, C., ROSSETTO, O. & SCHIAVO, G. (1999) Functional characterisation of tetanus and botulinum neurotoxins binding domains. *J Cell Sci,* 112 (Pt 16)**,** 2715-24.

LALLI, G. & SCHIAVO, G. (2002) Analysis of retrograde transport in motor neurons reveals common endocytic carriers for tetanus toxin and neurotrophin receptor p75NTR. *J Cell Biol,* 156**,** 233-9.

LAMONTE, B. H., WALLACE, K. E., HOLLOWAY, B. A., SHELLY, S. S., ASCANO, J., TOKITO, M., VAN WINKLE, T., HOWLAND, D. S. & HOLZBAUR, E. L. (2002) Disruption of dynein/dynactin inhibits axonal

transport in motor neurons causing late-onset progressive degeneration. *Neuron,* 34**,** 715-27.

LEBRAND, C., CORTI, M., GOODSON, H., COSSON, P., CAVALLI, V., MAYRAN, N., FAURE, J. & GRUENBERG, J. (2002) Late endosome motility depends on lipids via the small GTPase Rab7. *EMBO J,* 21**,** 1289-300.

LEFEBVRE, L., DIONNE, N., KARASKOVA, J., SQUIRE, J. A. & NAGY, A. (2001) Selection for transgene homozygosity in embryonic stem cells results in extensive loss of heterozygosity. *Nat Genet,* 27**,** 257-8.

LEVI-MONTALCINI, R. (1987) The nerve growth factor 35 years later. *Science,* 237**,** 1154-62.

LEVI-MONTALCINI, R. & ANGELETTI, P. U. (1963) Essential role of the nerve growth factor in the survival and maintenance of dissociated sensory and sympathetic embryonic nerve cells in vitro. *Dev Biol,* 7**,** 653-9.

LEVI-MONTALCINI, R., SKAPER, S. D., DAL TOSO, R., PETRELLI, L. & LEON, A. (1996) Nerve growth factor: from neurotrophin to neurokine. *Trends Neurosci,* 19**,** 514-20.

LEVY, J. R., SUMNER, C. J., CAVISTON, J. P., TOKITO, M. K., RANGANATHAN, S., LIGON, L. A., WALLACE, K. E., LAMONTE, B. H., HARMISON, G. G., PULS, I., FISCHBECK, K. H. & HOLZBAUR, E. L. (2006) A motor neuron disease-associated mutation in p150Glued perturbs dynactin function and induces protein aggregation. *J Cell Biol,* 172**,** 733-45.

LI, X., KUROMI, H., BRIGGS, L., GREEN, D. B., ROCHA, J. J., SWEENEY, S. T. & BULLOCK, S. L. (2010) Bicaudal-D binds clathrin heavy chain to promote its transport and augments synaptic vesicle recycling. *EMBO J,* 29**,** 992-1006.

MADEN, M. (2007) Retinoic acid in the development, regeneration and maintenance of the nervous system. *Nat Rev Neurosci,* 8**,** 755-65.

MAKKERH, J. P., CENI, C., AULD, D. S., VAILLANCOURT, F., DORVAL, G. & BARKER, P. A. (2005) p75 neurotrophin receptor reduces ligand-induced Trk receptor ubiquitination and delays Trk receptor internalization and degradation. *EMBO Rep,* 6**,** 936-41.

MARTIN-ZANCA, D., OSKAM, R., MITRA, G., COPELAND, T. & BARBACID, M. (1989) Molecular and biochemical characterization of the human trk proto-oncogene. *Mol Cell Biol,* 9**,** 24-33.

MATANIS, T., AKHMANOVA, A., WULF, P., DEL NERY, E., WEIDE, T., STEPANOVA, T., GALJART, N., GROSVELD, F., GOUD, B., DE ZEEUW, C. I., BARNEKOW, A. & HOOGENRAAD, C. C. (2002) Bicaudal-D regulates COPI-independent Golgi-ER transport by recruiting the dynein-dynactin motor complex. *Nat Cell Biol,* 4**,** 986-92.

MATTEOLI, M., VERDERIO, C., ROSSETTO, O., IEZZI, N., COCO, S., SCHIAVO, G. & MONTECUCCO, C. (1996) Synaptic vesicle endocytosis mediates the entry of tetanus neurotoxin into hippocampal neurons. *Proc Natl Acad Sci U S A,* 93**,** 13310-5.

MEGGOUH, F., BIENFAIT, H. M., WETERMAN, M. A., DE VISSER, M. & BAAS, F. (2006) Charcot-Marie-Tooth disease due to a de novo mutation of the RAB7 gene. *Neurology,* 67**,** 1476-8.

MIACZYNSKA, M., PELKMANS, L. & ZERIAL, M. (2004) Not just a sink: endosomes in control of signal transduction. *Curr Opin Cell Biol,* 16**,** 400-6.

MIANA-MENA, F. J., ROUX, S., BENICHOU, J. C., OSTA, R. & BRULET, P. (2002) Neuronal activity-dependent membrane traffic at the neuromuscular junction. *Proc Natl Acad Sci U S A,* 99**,** 3234-9.

MOHLER, J. & WIESCHAUS, E. F. (1986) Dominant maternal-effect mutations of Drosophila melanogaster causing the production of double-abdomen embryos. *Genetics,* 112**,** 803-22.

MONTECUCCO, C. (1986) How do tetanus and botulinum toxins bind to neuronal membranes? *Trends in Biochemical Sciences,* 11**,** 314-317.

MONTECUCCO, C. & SCHIAVO, G. (1994) Mechanism of action of tetanus and botulinum neurotoxins. *Mol Microbiol,* 13**,** 1-8.

MOORE, K. G., SPECKMANN, W. & HERZIG, R. P. (2007) The use of siRNA to validate immunofluorescence studies. *Methods Mol Biol,* 356**,** 245-51.

MOWLA, S. J., PAREEK, S., FARHADI, H. F., PETRECCA, K., FAWCETT, J. P., SEIDAH, N. G., MORRIS, S. J., SOSSIN, W. S. & MURPHY, R. A. (1999) Differential sorting of nerve growth factor and brain-derived neurotrophic factor in hippocampal neurons. *J Neurosci,* 19**,** 2069-80.

MUKHOPADHYAY, A., FUNATO, K. & STAHL, P. D. (1997) Rab7 regulates transport from early to late endocytic compartments in Xenopus oocytes. *J Biol Chem,* 272**,** 13055-9.

MUNCH, C., SEDLMEIER, R., MEYER, T., HOMBERG, V., SPERFELD, A. D., KURT, A., PRUDLO, J., PERAUS, G., HANEMANN, C. O., STUMM, G. & LUDOLPH, A. C. (2004) Point mutations of the p150 subunit of dynactin (DCTN1) gene in ALS. *Neurology,* 63**,** 724-6.

MUNRO, P., KOJIMA, H., DUPONT, J. L., BOSSU, J. L., POULAIN, B. & BOQUET, P. (2001) High sensitivity of mouse neuronal cells to tetanus toxin requires a GPI-anchored protein. *Biochem Biophys Res Commun,* 289**,** 623-9.

OLKKONEN, V. M. & IKONEN, E. (2006) When intracellular logistics fails--genetic defects in membrane trafficking. *J Cell Sci,* 119**,** 5031-45.

OSSOVSKAYA, V. S. & BUNNETT, N. W. (2004) Protease-activated receptors: contribution to physiology and disease. *Physiol Rev,* 84**,** 579-621.

PENNINGROTH, S. M., CHEUNG, A., BOUCHARD, P., GAGNON, C. & BARDIN, C. W. (1982) Dynein ATPase is inhibited selectively in vitro by erythro-9-[3-2-(hydroxynonyl)]adenine. *Biochem Biophys Res Commun,* 104**,** 234-40.

PODZUWEIT, T., NENNSTIEL, P. & MULLER, A. (1995) Isozyme selective inhibition of cGMP-stimulated cyclic nucleotide phosphodiesterases by erythro-9-(2-hydroxy-3-nonyl) adenine. *Cell Signal,* 7**,** 733-8.

POUEYMIROU, W. T., AUERBACH, W., FRENDEWEY, D., HICKEY, J. F., ESCARAVAGE, J. M., ESAU, L., DORE, A. T., STEVENS, S., ADAMS, N. C., DOMINGUEZ, M. G., GALE, N. W., YANCOPOULOS, G. D., DECHIARA, T. M. & VALENZUELA, D. M. (2007) F0 generation mice fully derived from gene-targeted embryonic stem cells allowing immediate phenotypic analyses. *Nat Biotechnol,* 25**,** 91-9.

PULS, I., JONNAKUTY, C., LAMONTE, B. H., HOLZBAUR, E. L., TOKITO, M., MANN, E., FLOETER, M. K., BIDUS, K., DRAYNA, D., OH, S. J., BROWN, R. H., JR., LUDLOW, C. L. & FISCHBECK, K. H. (2003) Mutant dynactin in motor neuron disease. *Nat Genet,* 33**,** 455-6.

RADEKE, M. J., MISKO, T. P., HSU, C., HERZENBERG, L. A. & SHOOTER, E. M. (1987) Gene transfer and molecular cloning of the rat nerve growth factor receptor. *Nature,* 325**,** 593-7.

REID, E., KLOOS, M., ASHLEY-KOCH, A., HUGHES, L., BEVAN, S., SVENSON, I. K., GRAHAM, F. L., GASKELL, P. C., DEARLOVE, A., PERICAK-VANCE, M. A., RUBINSZTEIN, D. C. & MARCHUK, D. A. (2002) A kinesin heavy chain (KIF5A) mutation in hereditary spastic paraplegia (SPG10). *Am J Hum Genet,* 71**,** 1189-94.

REYNOLDS, A. J., BARTLETT, S. E. & HENDRY, I. A. (1998) Signalling events regulating the retrograde axonal transport of 125I-beta nerve growth factor in vivo. *Brain Res,* 798**,** 67-74.

RICCIO, A., PIERCHALA, B. A., CIARALLO, C. L. & GINTY, D. D. (1997) An NGF-TrkA-mediated retrograde signal to transcription factor CREB in sympathetic neurons. *Science,* 277**,** 1097-100.

ROUX, P. P. & BARKER, P. A. (2002) Neurotrophin signaling through the p75 neurotrophin receptor. *Prog Neurobiol,* 67**,** 203-33.

RUMMEL, A., BADE, S., ALVES, J., BIGALKE, H. & BINZ, T. (2003) Two carbohydrate binding sites in the H(CC)-domain of tetanus neurotoxin are required for toxicity. *J Mol Biol,* 326**,** 835-47.

SALINAS, S., SCHIAVO, G. & KREMER, E. J. (2010) A hitchhiker's guide to the nervous system: the complex journey of viruses and toxins. *Nat Rev Microbiol,* 8**,** 645-55.

SAXENA, S., BUCCI, C., WEIS, J. & KRUTTGEN, A. (2005a) The small GTPase Rab7 controls the endosomal trafficking and neuritogenic signaling of the nerve growth factor receptor TrkA. *J Neurosci,* 25**,** 10930-40.

SAXENA, S., HOWE, C. L., COSGAYA, J. M., STEINER, P., HIRLING, H., CHAN, J. R., WEIS, J. & KRUTTGEN, A. (2005b) Differential endocytic sorting of p75NTR and TrkA in response to NGF: a role for late endosomes in TrkA trafficking. *Mol Cell Neurosci,* 28**,** 571-87.

SCHECTERSON, L. C. & BOTHWELL, M. (2010) Neurotrophin receptors: Old friends with new partners. *Dev Neurobiol,* 70**,** 332-8.

SCHIAVO, G., BENFENATI, F., POULAIN, B., ROSSETTO, O., POLVERINO DE LAURETO, P., DASGUPTA, B. R. & MONTECUCCO, C. (1992a) Tetanus and botulinum-B neurotoxins block neurotransmitter release by proteolytic cleavage of synaptobrevin. *Nature,* 359**,** 832-5.

SCHIAVO, G., MATTEOLI, M. & MONTECUCCO, C. (2000) Neurotoxins affecting neuroexocytosis. *Physiol Rev,* 80**,** 717-66.

SCHIAVO, G., POULAIN, B., ROSSETTO, O., BENFENATI, F., TAUC, L. & MONTECUCCO, C. (1992b) Tetanus toxin is a zinc protein and its inhibition of neurotransmitter release and protease activity depend on zinc. *EMBO J,* 11**,** 3577-83.

SCHINDOWSKI, K., BELARBI, K. & BUEE, L. (2008) Neurotrophic factors in Alzheimer's disease: role of axonal transport. *Genes Brain Behav,* 7 Suppl 1**,** 43-56.

SCHLAGER, M. A., KAPITEIN, L. C., GRIGORIEV, I., BURZYNSKI, G. M., WULF, P. S., KEIJZER, N., DE GRAAFF, E., FUKUDA, M., SHEPHERD, I.

T., AKHMANOVA, A. & HOOGENRAAD, C. C. (2010) Pericentrosomal targeting of Rab6 secretory vesicles by Bicaudal-D-related protein 1 (BICDR-1) regulates neuritogenesis. *EMBO J,* 29**,** 1637-51.

SCHOCH, S., DEAK, F., KONIGSTORFER, A., MOZHAYEVA, M., SARA, Y., SUDHOF, T. C. & KAVALALI, E. T. (2001) SNARE function analyzed in synaptobrevin/VAMP knockout mice. *Science,* 294**,** 1117-22.

SEABRA, M. C. & WASMEIER, C. (2004) Controlling the location and activation of Rab GTPases. *Curr Opin Cell Biol,* 16**,** 451-7.

SEGAL, R. A. & GREENBERG, M. E. (1996) Intracellular signaling pathways activated by neurotrophic factors. *Annu Rev Neurosci,* 19**,** 463-89.

SHAO, Y., AKMENTIN, W., TOLEDO-ARAL, J. J., ROSENBAUM, J., VALDEZ, G., CABOT, J. B., HILBUSH, B. S. & HALEGOUA, S. (2002) Pincher, a pinocytic chaperone for nerve growth factor/TrkA signaling endosomes. *J Cell Biol,* 157**,** 679-91.

SPLINTER, D., TANENBAUM, M. E., LINDQVIST, A., JAARSMA, D., FLOTHO, A., YU, K. L., GRIGORIEV, I., ENGELSMA, D., HAASDIJK, E. D., KEIJZER, N., DEMMERS, J., FORNEROD, M., MELCHIOR, F., HOOGENRAAD, C. C., MEDEMA, R. H. & AKHMANOVA, A. (2010) Bicaudal D2, dynein, and kinesin-1 associate with nuclear pore complexes and regulate centrosome and nuclear positioning during mitotic entry. *PLoS Biol,* 8**,** e1000350.

STANFORD, W. L., COHN, J. B. & CORDES, S. P. (2001) Gene-trap mutagenesis: past, present and beyond. *Nat Rev Genet,* 2**,** 756-68.

STENMARK, H. (2009) Rab GTPases as coordinators of vesicle traffic. *Nat Rev Mol Cell Biol,* 10**,** 513-25.

STROHMAIER, C., CARTER, B. D., URFER, R., BARDE, Y. A. & DECHANT, G. (1996) A splice variant of the neurotrophin receptor trkB with increased specificity for brain-derived neurotrophic factor. *EMBO J,* 15**,** 3332-7.

STROM, A. L., GAL, J., SHI, P., KASARSKIS, E. J., HAYWARD, L. J. & ZHU, H. (2008) Retrograde axonal transport and motor neuron disease. *J Neurochem,* 106**,** 495-505.

SWIFT, S., XU, J., TRIVEDI, V., AUSTIN, K. M., TRESSEL, S. L., ZHANG, L., COVIC, L. & KULIOPULOS, A. (2010) A novel protease-activated receptor-1 interactor, Bicaudal D1, regulates G protein signaling and internalization. *J Biol Chem,* 285**,** 11402-10.

TEULING, E., VAN DIS, V., WULF, P. S., HAASDIJK, E. D., AKHMANOVA, A., HOOGENRAAD, C. C. & JAARSMA, D. (2008) A novel mouse model with impaired dynein/dynactin function develops amyotrophic lateral sclerosis (ALS)-like features in motor neurons and improves lifespan in SOD1-ALS mice. *Hum Mol Genet,* 17**,** 2849-62.

TREJO, J., ALTSCHULER, Y., FU, H. W., MOSTOV, K. E. & COUGHLIN, S. R. (2000) Protease-activated receptor-1 down-regulation: a mutant HeLa cell line suggests novel requirements for PAR1 phosphorylation and recruitment to clathrin-coated pits. *J Biol Chem,* 275**,** 31255-65.

TSOULFAS, P., SOPPET, D., ESCANDON, E., TESSAROLLO, L., MENDOZA-RAMIREZ, J. L., ROSENTHAL, A., NIKOLICS, K. & PARADA, L. F. (1993)

The rat trkC locus encodes multiple neurogenic receptors that exhibit differential response to neurotrophin-3 in PC12 cells. *Neuron,* 10**,** 975-90.

VALDEZ, G., AKMENTIN, W., PHILIPPIDOU, P., KURUVILLA, R., GINTY, D. D. & HALEGOUA, S. (2005) Pincher-mediated macroendocytosis underlies retrograde signaling by neurotrophin receptors. *J Neurosci,* 25**,** 5236-47.

VALENZUELA, D. M., MAISONPIERRE, P. C., GLASS, D. J., ROJAS, E., NUNEZ, L., KONG, Y., GIES, D. R., STITT, T. N., IP, N. Y. & YANCOPOULOS, G. D. (1993) Alternative forms of rat TrkC with different functional capabilities. *Neuron,* 10**,** 963-74.

VALLEE, R. B. & BLOOM, G. S. (1991) Mechanisms of fast and slow axonal transport. *Annu Rev Neurosci,* 14**,** 59-92.

VERHOEVEN, K., DE JONGHE, P., COEN, K., VERPOORTEN, N., AUER-GRUMBACH, M., KWON, J. M., FITZPATRICK, D., SCHMEDDING, E., DE VRIENDT, E., JACOBS, A., VAN GERWEN, V., WAGNER, K., HARTUNG, H. P. & TIMMERMAN, V. (2003) Mutations in the small GTP-ase late endosomal protein RAB7 cause Charcot-Marie-Tooth type 2B neuropathy. *Am J Hum Genet,* 72**,** 722-7.

VILAR, M., CHARALAMPOPOULOS, I., KENCHAPPA, R. S., REVERSI, A., KLOS-APPLEQUIST, J. M., KARACA, E., SIMI, A., SPUCH, C., CHOI, S., FRIEDMAN, W. J., ERICSON, J., SCHIAVO, G., CARTER, B. D. & IBANEZ, C. F. (2009a) Ligand-independent signaling by disulfide-crosslinked dimers of the p75 neurotrophin receptor. *J Cell Sci,* 122**,** 3351-7.

VILAR, M., CHARALAMPOPOULOS, I., KENCHAPPA, R. S., SIMI, A., KARACA, E., REVERSI, A., CHOI, S., BOTHWELL, M., MINGARRO, I., FRIEDMAN,

W. J., SCHIAVO, G., BASTIAENS, P. I., VERVEER, P. J., CARTER, B. D. & IBANEZ, C. F. (2009b) Activation of the p75 neurotrophin receptor through conformational rearrangement of disulphide-linked receptor dimers. *Neuron,* 62**,** 72-83.

VITELLI, R., SANTILLO, M., LATTERO, D., CHIARIELLO, M., BIFULCO, M., BRUNI, C. B. & BUCCI, C. (1997) Role of the small GTPase Rab7 in the late endocytic pathway. *J Biol Chem,* 272**,** 4391-7.

WAKEFIELD, J. G., STEPHENS, D. J. & TAVARE, J. M. (2003) A role for glycogen synthase kinase-3 in mitotic spindle dynamics and chromosome alignment. *J Cell Sci,* 116**,** 637-46.

WANSCHERS, B. F., VAN DE VORSTENBOSCH, R., SCHLAGER, M. A., SPLINTER, D., AKHMANOVA, A., HOOGENRAAD, C. C., WIERINGA, B. & FRANSEN, J. A. (2007) A role for the Rab6B Bicaudal-D1 interaction in retrograde transport in neuronal cells. *Exp Cell Res,* 313**,** 3408-20.

WATSON, F. L., HEERSSEN, H. M., BHATTACHARYYA, A., KLESSE, L., LIN, M. Z. & SEGAL, R. A. (2001) Neurotrophins use the Erk5 pathway to mediate a retrograde survival response. *Nat Neurosci,* 4**,** 981-8.

WHEELER, D. B., CARPENTER, A. E. & SABATINI, D. M. (2005) Cell microarrays and RNA interference chip away at gene function. *Nat Genet,* 37 Suppl**,** S25-30.

WICHTERLE, H., LIEBERAM, I., PORTER, J. A. & JESSELL, T. M. (2002) Directed differentiation of embryonic stem cells into motor neurons. *Cell,* 110**,** 385-97.

WILLIAMS, G., WOOD, A., WILLIAMS, E. J., GAO, Y., MERCADO, M. L., KATZ, A., JOSEPH-MCCARTHY, D., BATES, B., LING, H. P., AULABAUGH, A., ZACCARDI, J., XIE, Y., PANGALOS, M. N., WALSH, F. S. & DOHERTY, P.

(2008) Ganglioside inhibition of neurite outgrowth requires Nogo receptor function: identification of interaction sites and development of novel antagonists. *J Biol Chem,* 283**,** 16641-52.

WILLIAMSON, L. C., BATEMAN, K. E., CLIFFORD, J. C. & NEALE, E. A. (1999) Neuronal sensitivity to tetanus toxin requires gangliosides. *J Biol Chem,* 274**,** 25173-80.

WU, C., CUI, B., HE, L., CHEN, L. & MOBLEY, W. C. (2009) The coming of age of axonal neurotrophin signaling endosomes. *J Proteomics,* 72**,** 46-55.

YANO, H., LEE, F. S., KONG, H., CHUANG, J., AREVALO, J., PEREZ, P., SUNG, C. & CHAO, M. V. (2001) Association of Trk neurotrophin receptors with components of the cytoplasmic dynein motor. *J Neurosci,* 21**,** RC125.

ZHAO, C., TAKITA, J., TANAKA, Y., SETOU, M., NAKAGAWA, T., TAKEDA, S., YANG, H. W., TERADA, S., NAKATA, T., TAKEI, Y., SAITO, M., TSUJI, S., HAYASHI, Y. & HIROKAWA, N. (2001) Charcot-Marie-Tooth disease type 2A caused by mutation in a microtubule motor KIF1Bbeta. *Cell,* 105**,** 587-97.